Novel Molecular and Metallo-Supramolecular Nano-Materials: Design, Synthesis, Processing and Functional Aspects

A Thesis Submitted for the Degree of

DOCTOR OF PHILOSOPHY

BY

Supratim Basak

School of Chemistry
University of Hyderabad
Hyderabad-500 046
INDIA

Nov 2013

Devoted to my beloved parents

CONTENTS

DECLARATION

I hereby declare that the matter embodied in this thesis is the result of investigations carried out by me in the School of Chemistry, University of Hyderabad, Hyderabad under the supervision of Assoc. Prof. Dr. Rajadurai Chandrasekar.

In keeping with the general practice of reporting scientific observations, due acknowledgements have been made wherever the work described is based on the findings of other investigators. Any omission or error that might have crept in is regretted.

Supratim Basak

CERTIFICATE

This is to certify that the work described in this thesis entitled **"Novel Molecular and Metallo-Supramolecular Nano-Materials: Design, Synthesis, Processing and Functional Aspects"** has been carried out by Mr. Supratim Basak (Reg. No. 08CHPH30), under my supervision and the same has not been submitted elsewhere for any degree.

Prof. M. V. Rajasekharan
Dean
School of Chemistry
University of Hyderabad
Hyderabad 500 046

Assoc. Prof. Dr. R. Chandrasekar
(Thesis Supervisor)
School of Chemistry
University of Hyderabad
Hyderabad 500 046

ACKNOWLEDGEMENTS

It is indeed a great opportunity for me to express my sincere gratitude and profound respect to my guru, Assoc. Prof. Dr. Rajadurai Chandrasekar, for his constant guidance, ceaseless encouragement and continuous support during my research work. I have been motivated most by his immense dedication to the research, plethora of innovative ideas and a very high degree of discipline and sincerity. Any discussion with him has always been very enriching and rejuvenating. I am indebted to him for the freedom he gave me in carrying out my research and the time he spent in trying to explain various facts and concepts. My association with him is a memorable one.

I thank present and former Deans and faculty members of the School of Chemistry for their support and help on various occasions. I thank all the faculty members for their co-operation whenever required. I thank all non-teaching staff, School of Chemistry for their cooperation.

I am grateful to Prof. Dr. Klaus Müllen, Prof. Dr. Martin Baumgarten (Max-Planck-Institut für Polymerforschung), Prof. S. N. Kaul and Prof. M Ghanashyam Krishna (School of Physics, University of Hyderabad) for their support in my research work. I also sincerely acknowledge Dr. Ahamad Mohiddon for his valuable and timely assistance during various microscope/Raman imaging measurements.

I thank CSIR, New Delhi, for providing the financial support; Center for Nanotechnology for the TEM, SNOM, and CLSM.

I am deeply indebted to all my teachers right from my school to the University for the excellent training I received throughout my academics.

It is a great pleasure to thank my lab mate and wife Ms. Pramiti Hui, for her excellent support, encouragement, companion, keeping ebullient atmosphere and timely help both inside and outside the lab. I am extremely thankful to NC, Narayana, Ajay, Krishna and Ramudu for their support help and cooperation and maintaining a lively environment in the lab. I thank all research scholars of School of chemistry and friends for the cheerful and enlivening atmosphere they maintained and for making my stay in the campus unforgettable.

I am at a loss of words to express gratitude to my parents and my wife. The way I grew up, the values I imbibed, the education I received and the person I am now is all due to them. I am grateful to my caring and loving brother who has always been an ardent listener and a strong support to me. I would like to acknowledge all my relatives for their love and encouragement.

Supratim Basak

LIST OF ACRONYMS

μm	micrometer
^{1}H	proton
AAO	anodized aluminum oxide
AFM	atomic force microscope
$CDCl_3$	deuterated chloroform
CH_2Cl_2	dichloromethane
CH_3CN	acetonitrile
$CHCl_3$	chloroform
cm	centimeter
CT	charge transfer
CuI	copper iodide
CW	continuous wave
D	deuterium
DCM	dichloromethane
DMSO	dimethyl sulfoxide
DSC	differential scanning calorimetry
EBL	electron beam lithography
EDTA	ethylenediaminetetraacetic acid
EDXS	energy dispersive x-ray spectroscopy
EtOH	ethanol
$Eu(tta)_3$	tris[4,4,4-trifluoro-1-(2-thienyl)-1,3-butanediono]europium
$Fe(ClO_4)_2$	iron perchlorate
FESEM	field emission scanning electron microscope
FRET	förster resonance energy transfer
H_2O	water
Hz	hertz
hυ	light
IR	infrared
ISC	intersystem crossing
K_2CO_3	potassium carbonate
kDa	kilo dalton
KOH	potassium hydroxide
LB	langmuir-blodgett
LCW	lithographically controlled wetting
LED	light emitting diode
lm W^{-1}	lumens per watt
LPEF	long pass edge filter
M	molecular weight
M.P	melting temperature
MeOH	methanol

MHz	megahertz
MIMIC	micro moulding in capillaries
M_n	number average molecular weight
MSP	metallo-supramolecular polymers
M_w	weight average molecular weight
nm	nanometer
nM	nanomolar
NMR	nuclear magnetic resonance spectroscopy
ns	nanosecond
$Pd(PPh_3)_4$	tetrakis(triphenylphosphine)palladium (0)
PL	photoluminescence
PS	polystyrene
PVD	physical vapor deposition
RPM	revolutions per minute
RT	room temperature
SAED	selected area electron diffraction
SCO	spin crossover
SEM	scanning electron microscope
SERS	surface-enhanced Raman spectroscopy
SPR	surface plasmon resonance
ST	spin transition
STM	scanning tunneling microscopy
T	temperature
t	time
TEM	transmission electron microscope
Terpy	terpyridine
TGA	thermogravimetric analysis
THF	tetrahydrofuran
Tol.	toluene
UV	ultraviolet
UV-Vis	ultraviolet-visible
WOLED	White organic light-emitting diode
WPLED	White polymer organic light-emitting diode
X_n	number-average degree of polymerization
$Zn(ClO_4)_2$	zinc perchlorate
Δ	heat
δ	nmr chemical shift reported in ppm
$\Delta\lambda$	change in wavelength of emission or absorption
λ	wavelength
λmax	wavelength of emission or absorption maximum
π-π	pi-pi

1.1 Introduction to Nanoscience and Nanotechnology:

Nanoscience and Technology is an important discipline of 21st century. Nanoscience is the understanding of behavior and phenomena of the nanoscale world and nanotechnology deals with the capability to manipulate, control, assemble, produce and manufacture things at atomic precision. Nanoscience and technology is inherently interdisciplinary in nature involving many major disciplines such as chemistry, physics,

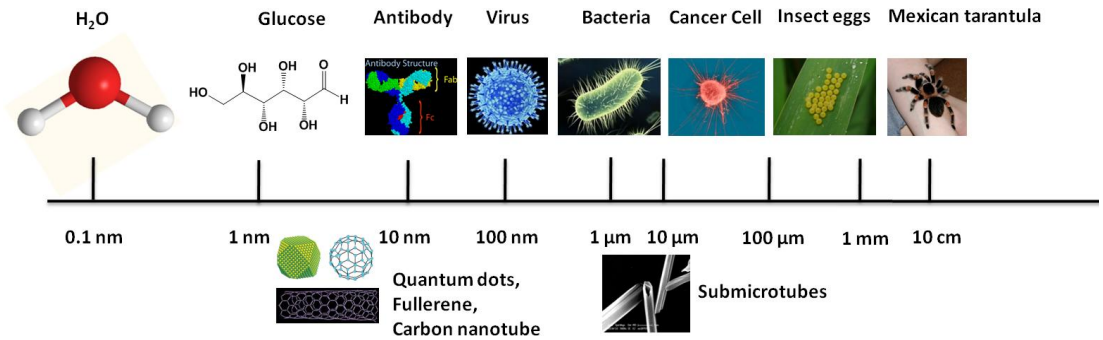

Figure 1.1 Comparison of the size domains of naturally existing and manmade systems.

biology, engineering, computation, and medicine. A comparison of the size domains of various naturally existing and manmade systems is presented in Fig. 1.1. The word 'nano' is originated from the Greek "νανοσ", meaning 'dwarf.' Lohmann used the prefix 'nano' for the first time in 1908, to address small organisms having size in the order of ~200 nm scale.[1] The visionary idea of controlling matter in the nanoscale regime was proposed by Nobel laureate Richard P. Feynman, in his famous lecture entitled "There's Plenty of Room at the Bottom", delivered at California Institute of Technology, in 1959.[2] In his talk, he outlined the theoretical concept of manipulating matter in the atomic/molecular level and the potential applications of nanoscale systems. In the famous talk he told…

"The principles of physics, as far as I can see, do not speak against the possibility of maneuvering things atom by atom. It is not an attempt to violate any laws; it is something, in principle, that can be done; but in practice, it has not been done because we are too big"

1.2 Historical Perspective of Nanoscience:

The first nano sized gold in colloidal state was prepared by Michael Faraday in 1857.[3] In nature a lot of biological processes are accompanied by nanoparticles. It was the

German bacteriologist Robert Koch, who found that compounds made with gold inhibited the growth of bacteria in 1890, which brought him the Nobel Prize for medicine in 1905. The use of gold in medicine is not new, Indian medical system *Ayurveda* used gold in several preparations. In 3150 BC the Egyptians used gold in dentistry. Colloidal gold has been incorporated in glasses and vases to furnish them colour, which has been found in many European cathedrals. The use of gold and silver nanoparticles in dichroic glass is found in the *Lycurgus cup* made by the Romans in 4 A. D. (Fig. 1.2). If light source is kept inside the cup it appears red from the outside (transmitted light) and green from the inside (reflected light). Modern study shows it contains very small amounts of gold (about 40 ppm) and silver (about 300 ppm) in the form of nanoparticles. *Magnetosperillum magnetotacticum*, a bacterium is known to produce Magnetite (Fe_3O_4) particles of nanometer size. It is also established that the bacteria make nanoparticles of specific morphology. The magnetism caused by the particles helps in finding a direction favorable for its growth. The familiar bacterium called *lactobacillus*, which grows in curd can uptake metal ions from the curd and reduce them in nanoparticles inside the cell. The formation of nanoparticles are not only restricted to bacteria, but also has been found in fungi and viruses.

Figure 1.2 The Lycurgus cup (a) reflecting and (b) transmitted light.

Although nanomaterials have existed for a long time, systematic scientific discussion about them was initiated only in 1959, after Richard Feynman prophetic lecture at the annual meeting of the American Physical Society. At the beginning of 1900 the development of nanoscience and technology was crippled by the resolution. Because according to Abbe's theory the ability to resolve detail in an object was limited approximately by the wavelength of the light used in imaging, which limits the resolution of an optical microscope to a few hundred nanometers ~ 250 nm.

$$d = \frac{\lambda}{2NA} \qquad \ldots\ldots \; 1.1$$

λ = Wavelength of light used for imaging

NA = Numerical apperture of the objective

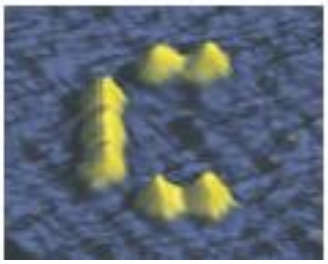

Fig 1.3 Seven carbon monooxide molecule forming the letter 'C' positioned with the tip of a scanning tunneling microscope. (Image taken from http://www.physics.ubc.ca/~stm/)

The development of Transmission Electron Microscopy (TEM) in 1928, Atomic Force Microscopy (AFM) in 1980 and Scanning Tunneling Microscopy (STM) in 1981 paved a way to characterize nano objects down to atomic resolution. Now it is not only possible to see atoms/molecules but also to manipulate them in a desired pattern. For example positioning of CO molecules in a "C" shaped arrangement has been done by using a STM tip (Fig. 1.3). Later development of fullerene, carbon nanotubes, semiconducting quantum dots, and graphene revolutionized the era of science and technology. Nano science and nanotechnology mainly focuses in the size region 1-100 nm. As the quantum confinement effect arises in the size domain 1-50 nm, nonmaterials show a very different physical and chemical properties compared to their bulk counterparts or from their atomic/molecular constituents in terms of color, solubility, reactivity, magnetic, optical, mechanical and electrical properties. Recently the interfaces of nanoscience have been extended to nanobiology, nanosensors, nanomedicines, molecular nanomachines and nanotribology.

1.3 Classification of Nanomaterials:

Nanomaterials can be classified based on their chemical nature, properties and also applications in areas such as metals, ceramics, semiconductors, composites and polymers. These can be further subdivided into biomaterials, catalytic materials, coatings, glasses, magnetic and electronic materials; another way to visualize families of nanomaterials is based on their building blocks–atoms, ions, small molecules or macromolecules. If the nanomaterial is made of small molecules or macromolecules they are often called molecular nanomaterial. The molecular nanomaterials shows completely different properties compared to the nanomaterials made of atoms and ions. As the field of nanostructure materials has evolved, many names and labels have been used. For e.g. a cluster is a collection of atoms or reactive units of up to around 50 units. A colloid is a stable solution of particles ~ 1-1000 nm. Nanoparticles are solid particles in the range of a few tens of nanometers that could be amorphous, aggregates of crystallites or single

crystalline. Quantum dot (or Q-particles) is a particle that shows a size quantization effect and emits different colour light depending upon its sizes in at least one of the dimension.

Based on dimension, nanomaterials can be classified as zero-dimensional (0-D), one-dimensional (1-D), two-dimensional (2-D), and three-dimensional (3-D) materials. 0-D nanomaterials are those where all the dimensions are measured within the nanoscale. The most common representation of zero-dimensional nanomaterial is nanoparticles. In case of 1-D material one of the dimensions is outside the nanoscale (even up to several microns). This includes nanotubes, nanorods, and nanowires. 2-D materials are those where two of the dimensions are not confined to the nanoscale viz. nanofilms, nanolayers, and nanocoatings. Three dimensional materials are not confined to the nanoscale in any dimension. These materials are thus characterized by having three arbitrarily dimensions above 100 nm.

Nanomaterials can be fabricated by two major approaches called the *top-down* and *bottom-up* methods. In the former method essentially a structure or pattern is *imposed* on the substrate being processed. e.g., lithography, writing, stamping, etc. The latter method guides the assembly of atomic and molecular constituents into organized surface structures through processes inherent in the manipulated system.

1.4 Assembly of Nanomaterials:

In order to realize the integration of nanoscale materials into devices that have practical significance, nanoscale patterning techniques that are scalable, massively parallel, low-cost, and high throughput must be developed. Although 1-D nanowires/tubes are of great interest for applications, their disordered structures seem to be problematic for use in device fabrication (for example, microelectronics and photonics) that often requires well-aligned and highly ordered architectures.[4] Recently, the group of Yang have studied and reviewed nanocrystal and nanowire assembly of metallic and inorganic nanostructures by the Langmuir−Blodgett (LB) method;[5] they have shown the optical responses of a silver nanoparticle film, which can be tuned using LB assembly. Müllen and co-workers have used Zone casting to produce large area anisotropic uniaxial alignment of the HBC) film,[6] which they have successfully integrated into an organic field-effect transistor device.[7] Assembly of nanoparticles in desired fashions can be made by designing molecular nano-architectures by fine tuning of molecular building blocks and engaging them in programmable/ predefined interactions,

which can lead to directed self-assembly.[8] Self-assembled nanofibers of a phthalocyanine derivative are oriented by applying electric field under photoexcitation.[9] Murphy et al. have self assembled gold nano rods in a stacked fashion in presence of adipic acid. The assembly and disassembly of gold nano rods can be triggered by varying the pH of the solution.[10] They have also shown a preferentially end-to-end assembly of gold nanorods by *biotin streptavidin* connectors.[11] L. M. Liz-Marzán and coworkers have used carbon nanotube as a template to align gold nano rods. Paul Malvaney and coworkers have used electric field to direct the growth of gold nanorods in aqueous solution containing cetyltrimethylammonium bromide (CTAB) as surfactant. M. A. El-Sayed and coworkers have presented a simple method through vertical dipping of TEM grid into a nanoparticle solution. They have anticipated the packing of nanoparticles on the substrate could be a result of the hydrodynamic pressure of water stream and the lateral capillary forces.[12] Carsten Sönnichsen et al. have presented a general strategy to stabilize gold nanorod suspensions with mono- and bifunctional polyethylene glycol (PEG) and to attach a controlled number of nanoparticles or biomolecules.[13] Yan reported a feasible approach for the linear assembly of Au nanorods using glutathione and cysteine in aqueous solutions without the addition of organic solvents. Thomas and co workers have studied the longitudinal surface plasmon resonance (SPR) of end-to-end coupled Au nanorods and observed a red-shift as the number of rods in the chain increased.[14]

Chattopadhyay et al. introduce a new lithographic method for the generation of 2-D patterns of composite nanoparticles (NPs) of Ag and Au through galvanic replacement by taking recourse to combine top-down and bottom-up approaches using commercially available compact disks (CDs) and digital versatile disks (DVDs) as templates.[15] They also used top-down and bottom-up approaches to fabricate a fluorescent yellow pattern. In their work they have reported a new form of lithography that involves a reaction between a H_2S gas and a Cd^{2+} ions embedded in a polymer film using a transmission electron microscope grid as a mask.[16] In a separate work they also report the formation of linear assemblies of citrate-stabilized spherical gold nanoparticles in the presence of acetanilide in aqueous medium. In a systematic they have analyzed the dependency of acetanilide concentration on the effective surface areas and catalytic properties of the gold nanoparticles array.[17]

T. Pradeep et al. developed a technique combining the seed mediated growth and the electrochemical deposition in which they formed oriented gold nanotriangles on

indium tin oxide (ITO) coated conducting glass surfaces.[18] In another work a synthesized fluorescent, porphyrin-anchored, Au_{22} cluster was fabricated to form fluorescent patterns by soft lithography technique.[19] They have also developed a facile and reversible method for assembling and disassembling gold nanorods using a common chelating agent, ethylenediaminetetraacetic acid (EDTA).[20]

When a lower dimensional structure such as quantum dots or quantum wires forms a periodic structure of layers of two (or more) materials they are called super-lattice. Talapin and co workers have shown that the colloidal inorganic nanoparticles can self-assemble into binary periodic superlattices.[21]

Although it is very easy to form self assembled nano/micro structures from small organic molecules, dendrimers and polymers, but the assembly of nano/micro structures in a desired pattern is still remains a challenging task. If the nanostructures are susceptible to magnetic field they can be aligned by applying the magnetic field.[22] This method is mostly applicable for magnetic nano structures and can be extended to prepare aligned single walled carbon nanotube.[23] Electrical force or dielectrophoresis is another method to assemble electrically charged objects.[24] But this technique is also restricted to metallic nanowires and can be extended to large-scale directed assembly[25] of single-walled carbon nanotubes devices.[26] Another economical and domestic method to align nanowires/tubes

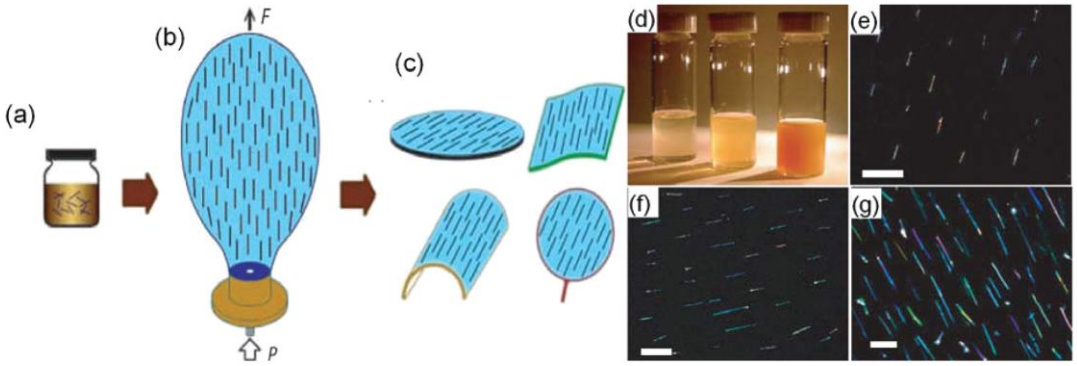

Figure 1.4 Illustration of blown-bubble film (BBF) process. (a) NW/NT polymer suspension, (b) bubble expansion over a circular die, and (c) films transferred to crystalline wafers, plastics, curved surfaces, and open frames. Nitrogen gas at pressure P flows through the die and expands a bubble from the NW/NT–epoxy suspension (dark-blue color) on the top of the die while a stable vertical force, F is applied by means of a wire-ring connected to a controlled speed motor. Black straight lines represent aligned NWs/NTs embedded in the bubble film. (d–g) Control of aligned NW density in BBFs. (d) Photograph of 0.01, 0.03, and 0.15 wt % (left to right) epoxy suspensions of Si NWs. (e–g) Dark-field optical images recorded from 0.01 (e), 0.03 (f), and 0.15 (g) wt % Si NW-BBFs, respectively. The scale bars in e, f, and g are 50, 20, and 10 mm, respectively. Adapted from ref. 27b.

is "Bubble-Blowing Process". The bubble-blowing assembly strategy is a general and scalable method that has been recently developed for uniformly aligned and controlled-density nanowires and nanotubes films by controlling bubble expansion of homogeneous polymer suspensions containing 1-D nanomaterials. In this method first, the functionalized nanowires were dispersed in a controlled concentration polymer to form a homogeneous and stable suspension. Then expansion of the polymer suspension occurs, using a circular die to form a bubble at controlled pressure, and expansion rate, where stable vertical expansion is achieved by using an external vertical force. Lieber and coworkers have first developed this method and shown the fabrication of flexible plastics sheets of dimensions of at least $225 \times 300\ mm^2$ over a highly curved surfaces (Fig. 1.4).[27]

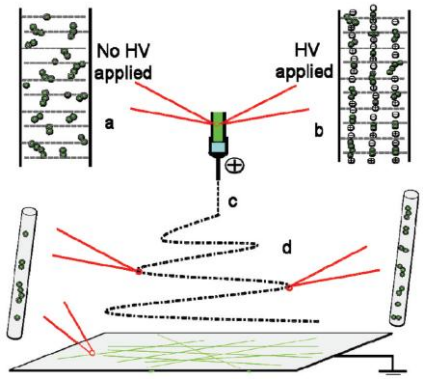

Figure 1.5 Simplified schematic representation of the formation of chain-like arrays of Ag NP aggregates within PVA nanofibers. (a) Random dispersion of Ag aggregates in PVA solution before a high voltage was applied. (b) after a high voltage was applied. Fig adapted from ref. 28.

Electrospinning is another method to fabricate highly aligned microstructures. In this method a polymer solution or melt is pumped through a thin nozzle with an inner diameter of the order of 100 μm. The nozzle also serves as an electrode, to which a high electric field of 100−500 kV m^{-1} is applied, and the distance to the counter electrode is 10−25 cm in laboratory systems. Electrospinning mainly makes use of the electrostatic repulsions between surface charges to reduce the diameter of a viscoelastic jet or a glassy filament. Yu and coworkers have used poly(vinylalcohol) (PVA) to fabricate high SERS-active Ag dimers or aligned aggregates, which are assembled within nanofibers with chainlike arrays. In this way they have successfully developed a free-standing and flexible surface-enhanced Raman scattering (SERS) substrate via the electrospinning technique (Fig. 1.5).[28]

The LB technique which was traditionally used to fabricate amphiphilic molecule monolayers onto a water surface is now has been shown to be a high-throughput, low-cost, and easily integrated method to assemble nanosized building blocks to fabricate both closely packed nano superstructures and well-defined patterns with low density.[29] In this method, at first the nanomaterials to be processed was dissolved in an immiscible volatile solvent and spread onto a water-supported surface using a microsyringe. After solvent

evaporation, the sample was compressed slowly while the surface pressure was monitored and a Langmuir thin film consisting of a nanostructure monolayer can be obtained. The monolayers can be repeatedly deposited in a layer-by-layer fashion onto a solid substrate through vertical-dipping (Langmuir−Blodgett) or horizontal-lifting (Langmuir−Schaefer) techniques. Plenty of integrated logic circuits,[30] one-dimensional functional networks[31] and programmable nanowire nanoprocessors[32] have been fabricated by using this technique. Recently hydrophilic Te nanostructures have also been arranged by using a non aqueous solvent like DMF/$CHCl_3$.[29c]

Assembly by mechanical force is one of the emerging areas. Since Controlled and uniform assembly of nanowire materials with high order and large area can be obtained by this method which is one of the criteria for electronic applications. Contact-printing method,[33] the knocking-down method,[34] strain-release assembly[35] are to name quite a few, which are driven by mechanical force. Lieber et al. have used the contact-printing method, to directly transfer regular arrays of semiconductor NWs from donor to patterned receiver substrates, to assemble both single and highly dense parallel arrays of NWs on substrates and in large scale. Weak interactions between the chemically unmodified NWs and surface chemical modification of the receiver substrate play an important role in the assembly process.[33a] Knocking–down method was first developed by Patolsky and co-workers. In this method, at first a typical vertical nanowire array was formed by the simple top-down sculpting of an appropriate substrate. Then followed by manual rolling of the elastomer-based roller, made of poly(dimethylsiloxane) (PDMS), teflon, or other elastomers with different rigidity and surface properties, over the nanowire-array substrate. Compared with the contact-printing method, nanowire elements are directly grown on the final device substrate, which is advantageous over transferring the nano-wires from a "donor" substrate.[34] Lei et al. reported a two-step knock-down method for successful fabrication over large-area and well-aligned arrays of ZnO nanowires and high density along their c-axis on a flexible

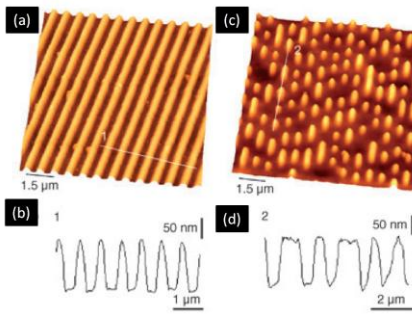

Figure 1.6 (a) AFM image of a Mn_{12}–poly carbonate (PC) replica exhibiting a sequence of grooves replicating the blank DVD master. b) AFM image of a Mn_{12}–PC replica of a recorded DVD, c) AFM image of a Mn_{12}–PC replica of a recorded DVD, which exhibits a structured sequence of bits of information as protrusions. b) Topographical line profile along the white line 1 drawn in (a). d) Topographical line profile along the white line 2 drawn in (c).

substrate.[36] First, a modified chemical vapor deposition (CVD) process is initially used for synthesizing vertical ZnO NW arrays perpendicular to the donor substrate surface. Then, the manual contact-printing method was introduced to knock the nanowires down and transfer them to a receiver substrate with well patterns.[36] Interestingly, nano and micro patterning of functional metal complexes and organic solids are still in its infancy with only a few examples. For example, Cavallini and coworkers used LCW (lithographically controlled wetting) and MIMIC (micro molding in capillaries) techniques to fabricate Mn_{12}-based single molecular magnet (Fig 1.6),[37] oligothiophene fibers with enhanced functional properties,[38] and spin state switchable Fe(II) spin cross-over arrays.[39]

1.5 1-D Organic Materials:

After the discovery of carbon nano-tubes by Iijima in 1991,[40] various kinds of 1-D semi-conducting nanomaterials,[41] including nanorods, nanowires, nanotubes and nanobelts, have been attracted considerable attention among scientist, because their two-dimensional quantum confinement effect.[42] 1-D nanomaterials are promising building blocks for miniaturized devices, and used as chemical sensors,[43] light emitting diodes,[44] field-effect transistors,[45] solar cells,[46] and so on.[47] Most of the reported literatures focused mainly on inorganic based 1-D materials, whereas organic materials are not much studied although the organic functional molecules have been playing important roles in various optoelectronic applications.[48] Organic macromolecules such as polymers, biomolecules, dendrimers, etc., have been under active investigation during the past couple of years.[49] For instance, conductive polymers, such as polyaniline[50] and polypyrrole,[51] have been fabricated into 1-D nanostructure owing to their good electrical conductivity, redox properties, environmental stability, and potential applications in sensors, biomedicine, actuators, etc. Polymers can be fabricated into 1-D nanostructures via electrochemical deposition,[52] electrospinning,[53] and the template method.[54]

1-D organic nanomaterials can be fabricated by liquid and vapor phase based *bottom-up* methods. In this method, the tendency to form 1-D material is inherent in the molecular system. It is a facile and reliable strategy, using mild conditions.[55] More importantly, composite nanostructures of organic materials can be readily achieved with this method,[56] by physical vapor deposition (PVD) organic 1-D nanomaterials with high crystallinity can be achieved.[57] Doped organic materials using highly efficient organic or

inorganic light emitting materials as dopant to generate multicolor emission[58] and white light emission have also been realized recently by using physical vapor deposition (PVD) techniques.[59] There is another universal method to fabricate 1-D nano structure which called template method. It is a *top-down* method. This method can be applied in most of the organic molecular materials that cannot form 1-D structure through liquid-phase or vapor-phase methods described before. The idea behind the template method is to fill organic molecules into 1-D nanosized vacancies, which are often referred as ‘‘templates’’ in nano fabrication techniques. If the template induce the 1-D growth of organic aggregates by the hydrophilic and hydrophobic interactions with solvents and molecules they are called soft template. Soft templates are often made up with surfactant solutions. Various shapes, like spherical or rod-like soft templates can be made depending on the surfactants. Scientist has also realized the formation of nano structures of various shape form a single organic molecule by only changing the reactant/surfactant ratio.[60] As a hard template ordered porous membranes like anodized aluminum oxide (AAO), silica, nanochannel glass, and iontrack-etched polymers are often used. After filling the pores with organic molecules the templates are often treated thermally to increase the crystallinity of the nanostructure.[61]

One dimensional nano and micro scale organic solid structures are potential components for miniaturized devices. The most fascinating aspect of 1-D organic nanomaterial is their opto-electronic and photonic properties, which are fundamentally different from their inorganic counterparts. The luminescence efficiency, energy levels can also be fine tuned by rational design of small organic building block. The weak intermolecular interactions between the molecules can also be manifested into the photo-physical and photo-chemical processes, including energy transfer, charge transfer, exciton coupling and diffusion.

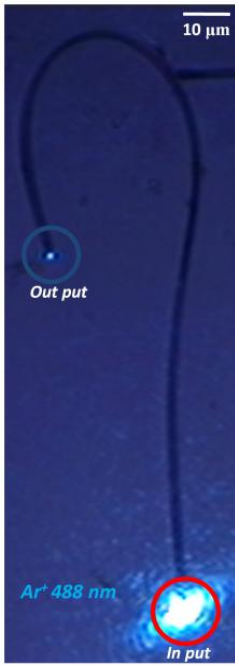

Figure 1.7 Passive optical wave guiding behavior of a bent organic submicro tube illuminated with 488 nm laser source. Adapted from ref. 64.

1-D organic solids are promising candidates to manipulate and guide optical waves in the nano/submicro/micro domains, because the refractive index (*n*) of the organic solid is usually higher than the surrounding medium.[62] Based on the type of light a 1-D solid propagates, organic optical wave guides are classified into *active* and

passive-waveguides. In active wave guides,[63] the molecular building block of the organic solid is electronically excited and the coupled exciton-polariton propagates to the opposite end of the elongated wave guide. Here, the wave length of the output light is longer than the input light due to electronic excitation of molecular building blocks and resultant fluorescence. There are quite a few excellent examples reported for this type of exciton-polariton based wave guides.[63] On the other hand, passive organic wave guides function almost similar to commercial optical fibers, i.e., here the input light directly propagates along the organic medium to the output end.[64] Most of the π-conjugated organic molecules have absorbance window in the range of ultra-violet (UV) light. The use of laser light energy in the range of the absorbance window of the molecule leads to electronic excitation and subsequent fluorescence. Hence to create passive organic wave guides, Chandrasekar and coworkers have used visible lasers (Ar^+ 488; Nd:YAG 532 and He:Ne 633) to avoid the unwanted fluorescence light generation in their light-organic tube interaction studies (Fig. 1.7). For their surprise, orthogonal illumination of laser light at one of the open end (input) of a linear tube showed propagation of the laser to the opposite exit end of the tube. They have also observed similar results for the bent tubes and *directional coupling* behavior in X-crossed tubes. Chandrasekar et al. have also confirmed the weak interaction of the propagating laser light with the organic tube building block molecules by Raman spectroscopy/mapping technique. Organic optical wave guide also exploited to electronically excite a meso-tetratolylporphyrin molecular nano-sheet kept ca. 20 μm away from the main 488 nm laser source (Fig. 1.8).

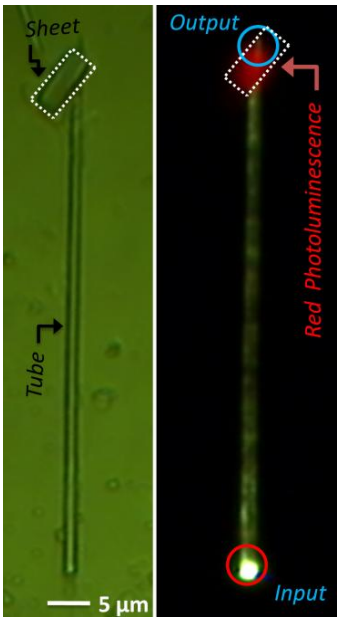

Figure 1.8 Remote electronic excitation of a phorphyrin derivative nano-sheet located at ca. 60 μm away from the 488 nm laser source through a linear submicro tubular waveguide. Adapted from ref. 64.

Other than the organic optical wave guiding property the 1-D nanowires can be used for optically pumped laser with the increase of the excitation power,[65] and multicolour emission.[66] Yao and co workers used the organic 1-D structures extensively for tunable emission from a nanowire containing two components through FRET,[67] waveguide modulators,[68] electroluminescent device,[69] heterojunction solar

cells,[70] and also as chemical sensors.[71]

1.6 Historical Perspective of a Building Block Molecule: Bispyrazolyl Pyridine (BPP):

After the first synthesis of 2,6-bispyrazolyl pyridine (BPP) by Goldsby et al. in 1990, BPP has attracted a great attention among the inorganic chemist due to its structural

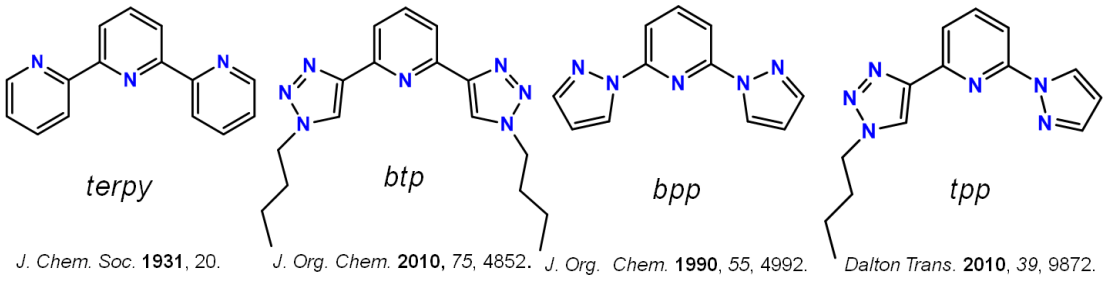

Figure 1.9 Tridentate ligands available in the literature.

resemblance to a well-known terpyridine (terpy) ligand. Recently, 2,6-bistriazolyl pyridine (btp) and 2,6-triazolylpyrazolylpyrdines (tpp) were also added into the club of tridentate ligands (Fig. 1.10). Due to its moderate ligand field strength BPP shows unique magnetic phenomenon such as spin crossover (SCO) effect with Fe(II) ion.[74] Eleven years after the discovery of BPP, Halcrow et al. have shown its coordinating ability as a tridentate ligand with Ni(II), Co(II) and Cu(II) metal ions.[72] As the chemistry of tridentate ligand like terpyridine reached its saturation level, more and more scientists turned towards BPP. In 2002 Brunet and co workers have first synthesized water soluble macrocyclic chelates by connecting diethylenetriaminepentaacetic acid to 2,6-bis-pyrazolylpyridine. The chelates shows high luminescence properties upon binding with Eu(III) and Tb(III) metal ions. They also proposed the energy transfer from ligand (BPP) to lanthanide metal centre.[73] In the same year Halcrow et al. have reported the temperature dependent reversible spin crossover property (High-spin; S=2 ↔ Low-spin; S=0) of an octahedral

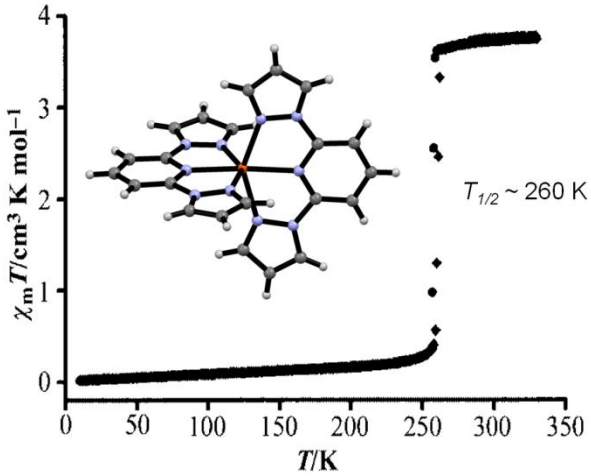

Figure 1.10 The first spin-crossover Fe(II) complex of BPP. Adapted from ref. 74.

$[Fe^{II}(BPP)_2](BF_4)_2$ complex displaying $T_{1/2}$ at 260 K (Fig. 1.10).[74] BPP ligand also form redox active metal complex Ru(II) ion.[75] BPP and its derivative 2,6-bis(3,5-dimethylpyrazol-1-yl)pyridine (Me_4BPP) also form coordination complexes with Ni(II)[76] Ru(II) ions.[75]

In 2005 Giorgio et al. have developed a one-pot synthetic route that allows functionalization of the BPP backbone in the 4- and 4"-pyrazole carbons by direct H(4)-pyrazole halogen exchange. The symmetrically substituted di-iodo derivative provides easy access to additional functionalities through both Sonogashira and Grignard exchange reactions. In 2006 Chandrasekar and co workers have synthesized a 1-D supramolecular head-to-tail N^+-H···N-type hydrogen-bonded chain of the complex $[Fe^{II}(L)_2H](ClO_4)_3$ MeOH [where, *L* = 4′-(4‴-pyridyl)-1,2′:6′1″-bis(pyrazolyl)pyridine] which exhibits a reversible, thermally driven spin transition at $T_{1/2}$ = 286 K with a hysteresis loop ($\Delta T_{1/2}$) of ca. 2 K (Fig. 1.11). In the same year Halcrow and coworkers functionalized the 4-pyridyl carbon of BPP with nucleobase substituents, and also first time synthesized the back-to-back coupled BPP having a CH_2-CH_2 spacer.[77] In 2007, Chandrasekar and coworkers have reported the synthesis of a back-to-back coupled BPP ligand bridged by a phenyl spacer and its 1-D metallo-supramolecular polymer with Fe(II) ions exhibiting $T_{1/2}$ = at 323 K with a ca. 10 K wide hysteresis loop. Several SCO complexes and their $T_{1/2}$ dependency on lattice solvent,[78] guest desorption have also been studied.[79] Oshio et al. have synthesized an Fe(II) complex using a BPP ligands carrying

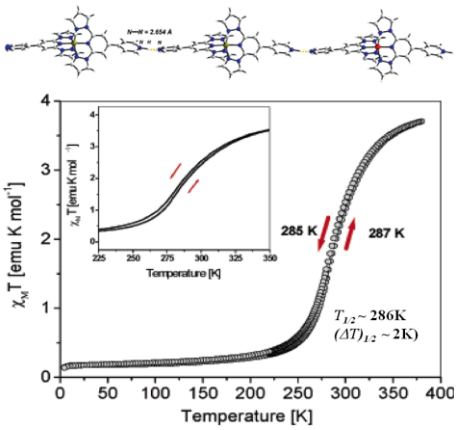

Figure 1.11 χ_MT vs T plot for the polycrystalline complex (↓ cooling mode and ↑ heating mode) with an applied dc magnetic field of 0.1 Tesla. The inset shows the hysteresis loop ($\Delta T_{1/2}$~2K). Figure adapted from ref. 146.

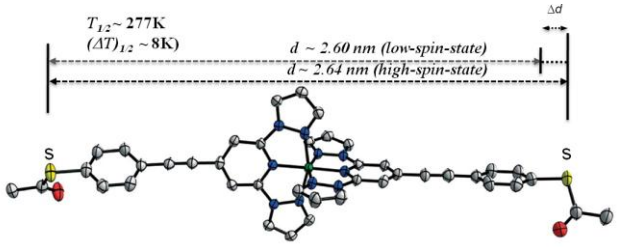

Figure 1.12 A novel iron(II) coordination complex $[Fe^{II}(L)_2](ClO_4)_2$ [L = S-(4-{[2,6-(Dipyr- azol-1-yl)pyrid-4-yl]ethynyl}phenyl) ethane-thioate] carrying terminal acetyl-protected thiol anchoring groups exhibits reversible spin transition at 277 K with a ca. 8 K wide hysteresis loop. thiol anchoring SCO molecule for single molecule conductivity studies. Adapted from ref. 81.

doublet state nitronyl nitroxide radicals, to study the interplay between bulk magnetism (exchange coupling) and SCO effect.[80] In 2008, BPP attached to thiol anchoring groups and its SCO Fe(II) compound was synthesized for single molecule conductivity studies (Fig. 1.12).[81] From 2009 onwards a lot of chemistry developed towards the functionalization of BPP unit. Kadjane and coworkers synthesized a nona-coordinating precursor using a regioselective strategy for nucleophilic aromatic substitution on polyfluoropyridines. The nonacoordinating BPP ligand upon coordinating with rare earth metals like Tb, Eu, Yb afforded numerous applications for near-IR emission, two-photon absorption spectroscopy, or the formation of luminescent gels.[82] Light induced excited state spin trapping (LIESST) property of BPP based Fe(II) complexes displaying SCO effect has also been demonstrated.[83]

In 2010 for the first time Chandrasekar et al. have exploited the BPP derivatives to fabricate fluorescent nanotapes and nearly monodispersed submicrotubes in a controlled manner via a supramolecular bottom-up self-assembly approach.[84] Holliday et al. have developed a conductive metallopolymer from thiophene appended bispyrazolyl pyridine coordinated to Ru(II) ion by electropolymerisation method (Fig. 1.13).[85] His group further reported on the synthesis of a red luminescent nine-coordinated Eu(III) complex of BPP and its photo-physical properties. The solid-state structure of complex has been determined by single-crystal X-ray crystallography and shows the geometry of the local coordination environment around the Eu(III) ion to be a slightly distorted tricapped trigonal prism (see chapter 4).[86] Ye and co workers have developed a dual-BPP based chelating ligand. The ligand shows weak luminescence on chelating with Tb(III) ion, but can be selectively and strongly enhanced upon reaction with Zn(II) ions. The Tb(III) chelate-based luminescent chemosensor is highly selective and sensitive towards the detection of Zn(II) ions in living cells.[87] In 2011 Nishihara and co workers have designed and synthesized bispyrazolyl pyridine decorated with stilbene and its Fe(II) complex exhibiting a visible light photoisomerization from *Z*-2 to *E*-2, both in solution and in solid phases. The *Z*- isomer remains in the high-spin state in temperature range between 2-300K, whereas *E*-2 displayed a SCO phenomenon between

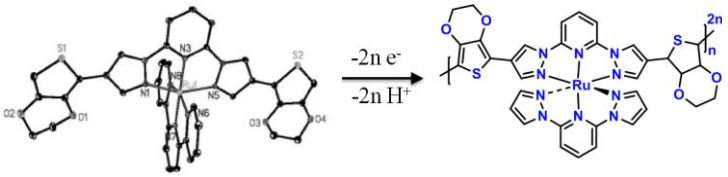

Figure 1.13 BPP based electropolymer, synthesized by Holliday et al. Figure adapted from ref. 85.

100 K and 300 K.[88] Oshio et al. have prepared Fe(II) complexes with neutral and oxidized tetrathiafulvalene (TTF). X-ray crystallographic analyses, magnetic and electrical resistivity measurements of this complex suggested the influence of SCO effect on electrical conductivity.[89] Ruben and co workers have synthesized two BPP functionalized with pyrene moieties through linkers of different lengths. In one of the ligand the pyrene group is directly connected to the BPP moiety via a C–C single bond, while in the other ligand it is separated by a benzyl ester group involving a flexible butanoic chain. The flexible chain of ligand in Fe(II) complexes prevents structural constraints allowing for reversible spin transitions, but in other one where pyrene is directly attached with BPP is blocked in its high spin state due to constraints caused by a strong intermolecular π-π stacking in its structure.[90] In 2012 Chandrasekar and co workers synthesized a series of nitronyl-nitroxide (NN), oxoverdazyl (OVZ) based mono-, and bi-radicals attached to 4-phenyl-2,6-bispyrazolylpyridine coupling unit and studied their intramolecular spin-spin coupling behavior by cryogenic electron spin resonance (ESR) spectroscopy and by computational analysis.[91] At the same time Ziessel and coworkers have prepared lanthanide complexes of ligands constructed from a BPP core bearing various chelating arms with anionic mixed carboxylate/phosphonate substituents. They reported these ligands to form particularly stable complexes with Eu(III) and Tb(III) which display outstanding spectroscopic properties suitable for bio-labeling.[92]

1.7 Metallo-Supramolecular Polymers (MSP):

Supramolecular materials[93] have attracted attention and grown tremendously over the last two decades after the Nobel Prize winning work of Lehn, Pederson, and Cram in 1987 on "*molecular structure specific interactions studies"*.[94] Now it is well known that hydrogen bonding (5–30 kJ/mol),[95] π-π interactions (8–12 kJ/mol),[96] and metal coordination (29–46 kJ/mol)[97] offer supramolecular interactions. The weak interactions among the supramolecular polymers differ from conventional polymers as the noncovalent interactions can be reversible in nature which has led to their use as stimuli-responsive materials. The stimuli-responsive materials are susceptible to various environmental factors such as temperature, pressure light, chemical interactions and so on.

If the supramolecular polymer contains a metal which is held by coordination bond the resulting polymer is called metallo-supramolecular (MSP) polymer. MSPs are

attractive because they combine the mechanical properties and processability of polymers with the inherent functionalities of metal ions. Depending upon the position of metal-ligand complex in the polymer chain the MSP can be classified as main-chain,[98] side-chain,[99] branched,[100] crosslinked,[101] star-shaped,[102] dendritic,[103] or helical polymer.[104]

1.7.1 ***Main-Chain Metallosupramolecular Polymers:*** Main chain MSPs contains directly incorporated metal-ligand moiety into the polymer chain. This type of polymers can be obtained by addition of the appropriate metal-ions to a ditopic ligand end-capped monomer in a 1:1 ratio resulting a MSP with many metal-ligand complexes along the polymer backbone. Rehahn and coworkers have first prepared a main-chain MSP by adding Ag(I) or Cu(I) to a solution of ditopic phenanthroline ligand derivatives (Fig 1.14).[105] Schubert and coworkers have reported the synthesis and characterization of a series of main-chain MSPs by combining a ditopic terpyridine end-capped poly(ethylene glycol) with a variety of

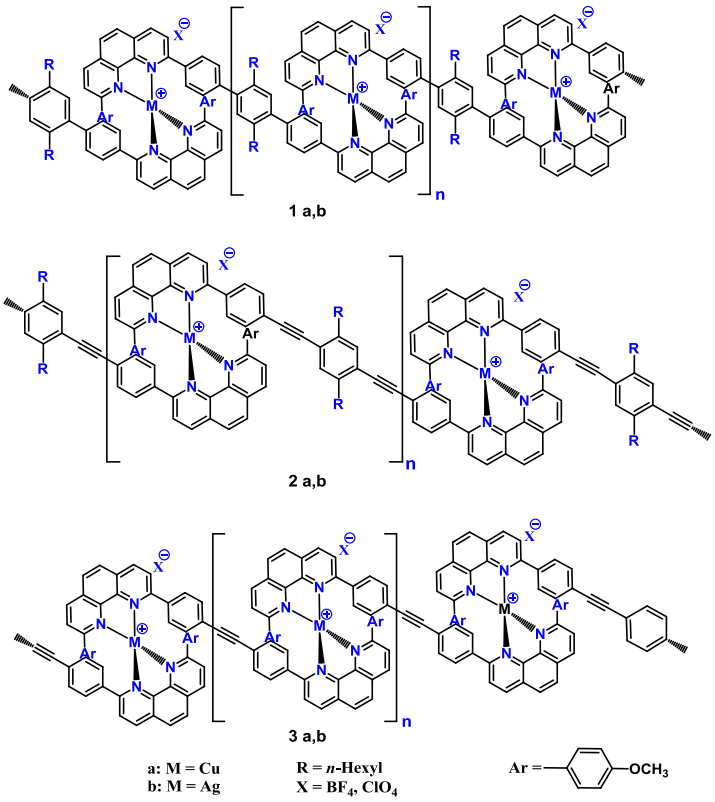

Figure 1.14 Main Chain metallo-supramolecular polymers synthesized by Rehahn et al. Figure adapted from ref. 105.

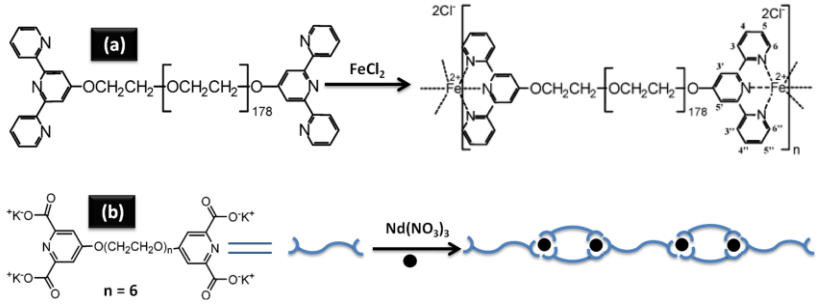

Figure 1.15 (a) Ditopic terpyridine end-capped poly(ethylene glycol) metallo-supramolecular polymer prepared by Schubert et al. (b) Water-Soluble reversible Nd(III) branched coordination polymers synthesized by Stuart et al. Figures adapted from ref. 106 and 107.

transition metal-ions to achieve high molecular weight polymers (Fig 1.15a).[106] Cohen Stuart and coworkers have prepared multiple examples of water-soluble and highly branched or cross-linked Nd^{3+} containing MSPs by using a short poly(ethylene glycol) chains end-capped with pyridine-2,6-dicarboxylate ligands (Fig. 1.15b).[107]

Currently, much attention has been directed towards the creation and exploitation of MSPs as functional materials. Swager and coworkers have reported the use of an Co(II) based electropolymerizable MSPs as a sensor for nitric oxide (NO) monitored by polymer conductivity.[108] Terech and coworkers have prepared a small molecular weight gelator comprised of two different types of metal-ion receptor sites terpyridine end-groups with a cyclam core. The gel formed by complexation of Co(II) or Ni(II) show stimuli-responsive property including mechanically-induced gel-sol transitions (thixotropic) and electrical stimulus.[109] Rowan and coworkers developed benzimidazol based MSP exhibiting diverse properties such as, multi-responsive gels,[110] thermo-,

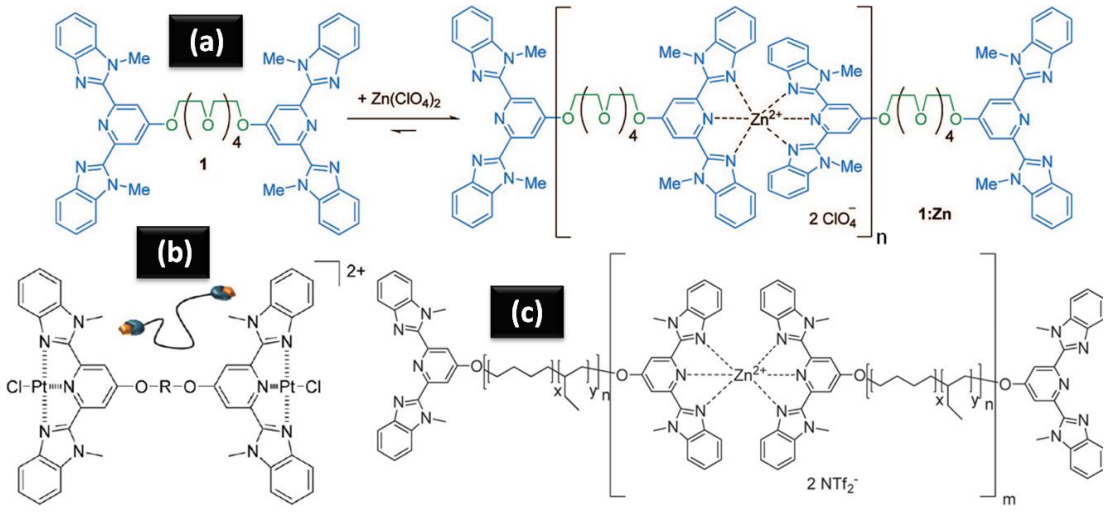

Figure 1.16 Multi-responsive and multi-stimuli metallo-supramolecular polymers prepared by Rowan et al. Figures adapted from ref. 110, 115 and 117.

photo-, and chemo-responsive shape-memory functions,[111,112] coupling[113] and decoupling[114] of optical properties, in situ formation of metal nanoparticle in polymer films,[115] MSP gels having rheological behavior[116] and optically healable polymers[117] (Fig. 1.16).

1.7.2 Side-Chain Metallo-Supramolecular Polymers:

An important property of metal-containing polymers is that they can display interesting optical and electronic characteristics depending on the metal ions. In this

regard the metal ions from the lanthanide series are particularly interesting because of their characteristic intense emissions with distinctive colors depending on the choice of metal. Tew and coworkers[118,119] investigated the optical properties of poly(methyl methacrylates) (PMMA) functionalized with terpyridine groups on the side-chains coordinated with different lanthanides (Eu(III) and Tb(III)). Films prepared by coordination with Eu(III) displayed a characteristic red metal-based emission while those prepared with Tb(III) show green emission. They generated a unique yellow luminescence when these two different metal ions were incorporated into the same molecular backbone at a 1:1 ratio, producing an alloy which generates a selective thermochromism, from yellow to orange/pink, when the film was heated above 50 °C (Fig. 1.17). They also reported a novel white-light emitting terpyridine based MSPs, comprises of two-emitter system, a blue-emitting dysprosium-chelated polymer and a red-emitting ruthenium complex.[120]

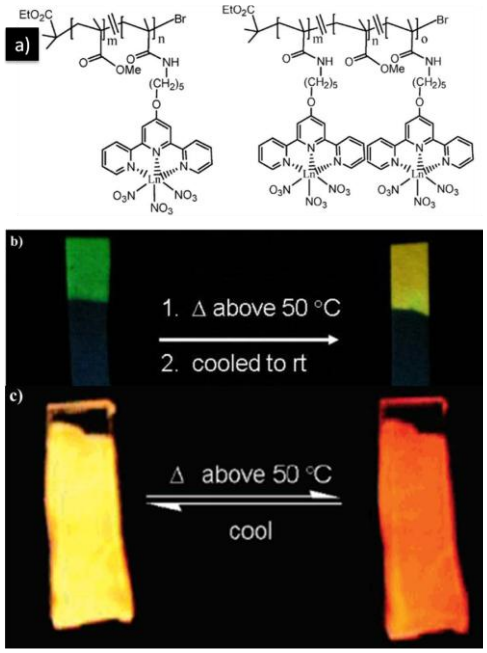

Figure 1.17 a) Structures of PMMA functionalized with either one type of terpyridine:Ln^{3+} complexes in the side-chain (Ln^{3+} = Eu^{3+} or Tb^{3+}) (1.9) or a combination of lanthanides in a 1:1 ratio. b) Images (λ_{ex} = 350 nm) of an irreversible thermo-responsive change in emission by heating two homo polymers to give a new blend and c) new thermo-reversible emission change of the new mixed metal system resulting from quenching of the green Tb^{3+} emission at elevated temperatures. Figures adapted from ref. 118.

Tieke and coworkers prepared several terpyridine based side chain MSPs,[121,122] where they varied the main chain by phenyliminofluorene,[121] polyaniline derivatives.[123] They have also synthesized conjugated copolymer with poly(phenylene-*alt*-fluorene) main chain and 2,6-bis(10-methylbenzimidazolyl)pyridine (bip) ligands attached to the main chain via flexible spacer groups through Pd-catalyzed Suzuki coupling of the 2,7-bispinacolatoboron ester of 9,9-dihexylfluorene and a 1,4-dibromobenzene derivative carrying two ω-bip-substituted alkoxy groups in the 2- and 5-positions.[124] Coupled with Layer-by-layer assembled films from metal ion complexes they have found the reversible ionochromism upon anodic oxidation. They also proposed

the films might be useful as active materials in electrochromic devices, metal ion sensing and for preparation of fluorescent coatings (Fig. 1.18).

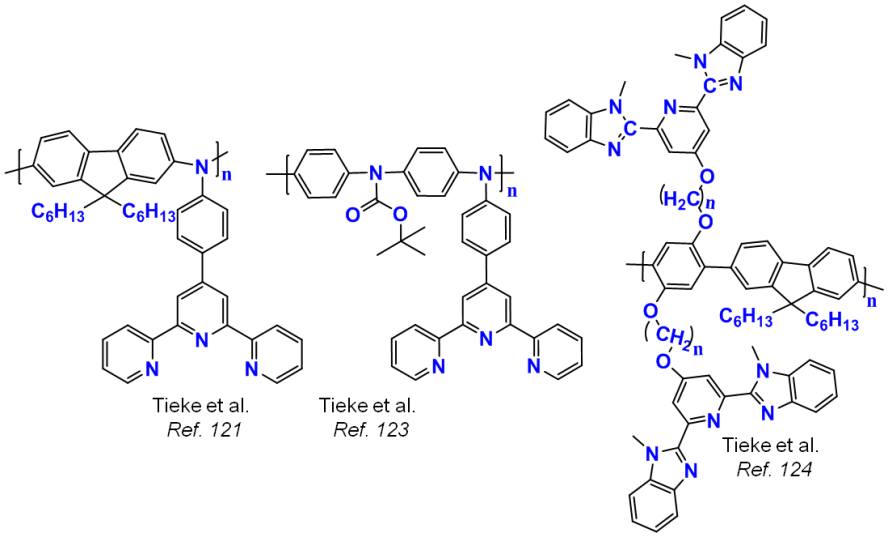

Figure 1.18 Structures of side-chain metallopolymers synthesized by Tieke et al.

1.7.3 Metallo-Supramolecular Polymers - Characterization and Difficulties:

Since the first development of terpyridine by Morgan and Burstall,[125] it has been widely used as building blocks in various MSPs.[126] Terpyridine is known to form kinetically inert bonds with Ru(II), Ni(II), Os(II), and Fe(II) and they form stable MSPs, which can be characterized by standard techniques, including gel permeation chromatography (GPC), viscosity and analytical ultra-centrifugation.[127] Matrix-assisted laser desorption ionization time-of-flight mass spectrometry (MALDI-TOF MS) is not useful since the polymer assemblies tend to fragment during the experiment.[127a] On the other hand terpyridine forms much weaker bonds (low binding constant) with other metal ions such as Zn(II), Cu(II) and lanthanides. As the resulting MSPs exist in equilibrium with free ligand and metal ions, the polymer properties becomes sensitive towards external stimuli like temperature, solvent, concentration and the nature of the counter ions. These types of labile stimuli responsive polymers are not stable during the GPC run. They can be only characterized by solution based techniques like NMR, UV-Vis spectroscopy and viscosity measurements.

1.8 White Light-Emitting Polymer Materials:

White light-emitting devices based on small organic molecules, oligomers or polymers (WOLEDs/WPLEDs) have attracted much attention among both the scientific and the

industrial communities due to their potential applications in areas such as full-colour flat-panel electroluminescent (EL) displays, back-lighting sources for liquid-crystal displays and next-generation solid-state lighting sources (Fig. 1.19).[128] Recently, the WOLEDs attracted particular interests because they have advantages over a fluorescent lamp which contains significant amounts of toxic mercury in the tube and incandescent lighting bulb which converts 90% of consumed power into heat. Indeed several laboratories have achieved power efficiency of WPLEDs exceeding 20 lm W^{-1} which outperforms incandescent light bulbs in efficiency,[129] suggesting WPLEDs can find practical applications as large area lighting sources in the near future.

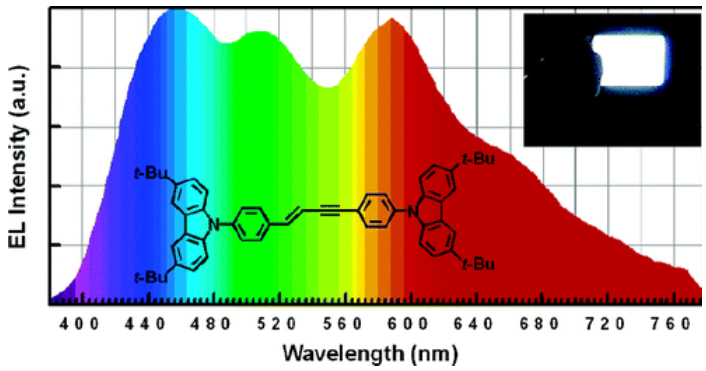

Figure 1.19 A π-conjugated aromatic enynes used for white electroluminescence. Adapted from ref. 128b

In 1931, Commission Internationale d'Eclairage (CIE) set up a set of standard colorimetric system, referred to as CIE 1931, which is the most widely used colorimetric system so far. CIE 1931 regulates that the color coordinates of equal energy point of white light are (0.33, 0.33) (Fig. 1.20). According to optical principles, all the colors can be achieved by mixing the three primary colors (red, green, and blue), so white light can also be obtained in this way. The white light emitting polymer can be generated by many ways some of them are discussed here.

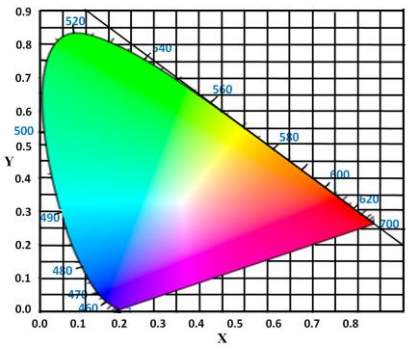

Figure 1.20 The CIE 1931 color space chromaticity diagram.

1.8.1 Small-Molecule-Doped Polymer Type:

In this method the host polymer materials are doped with a little amount of narrow band-gap small light-emitting molecules, and then the incomplete energy transfer can be used to achieve white light emission. The host polymer is generally blue or sky blue light-emitting materials and can be mixed with one, two, or multiple kinds of guest materials,

whose doped contents are about 1000 to 1%. Weight percentage is more often used than mole percentage in lots of reported papers. The thermodynamic compatibility for most of the material systems has not been investigated so far. So if the system of guest and host has no enough thermodynamic stability, there is a potential phase separation, which will leads to decreasing the efficiency and color stability. Since the existence of excimer, the emission spectrum of the material itself will be widened, this provides conditions to prepare PWLED. However, up to now, the thermodynamics and kinetics of excimer formation for conjugated polymer are not very clear and need further investigation. Tsai et al. synthesized a light-emitting polymer through ring-opening metathesis polymerization, which shows excimer based emission, formed due to anthracene chromophore between side chains (Fig. 1.21).[130]

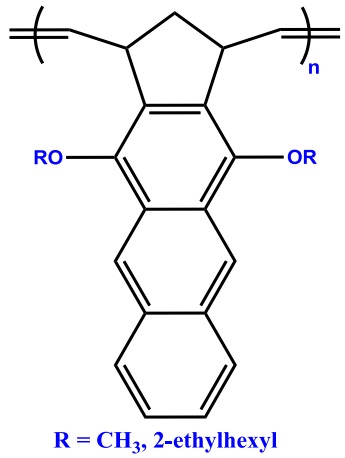

Figure 1.21 Polymer used for excimer based white light emission. Adapted from ref. 130.

1.8.2 Polymer Blend Type:

The principle of fabricating white emission device using polymer blend is similar to that of a small-molecule-doped white emission polymer. The wide-band-gap host materials are also doped with a small amount of guest light-emitting polymers, using incomplete energy transfer to obtain white emission. The amount of doped-chromophore is very small (generally one-thousandth magnitude, mass content). The light color can also be changed by adjusting the primary colors and doping content. Compared with small-molecules-doped polymer, this method is generally considered to possess the advantage against phase separation and thereby improving the device stability.[131]

1.8.3 Fluorescent Molecule-Dispersed Polymer Type: Doping method and polymer blend method in fabricating PWLED are generally discouraged due to phase separation problem, which leads to declined device efficiency and poor reproducibility. One solution is chemically embedding the low-band-gap dye in the conjugated polymer main chain. Stable white emission can be achieved by adjusting the ratio of chromophores and controlling the energy transfer. Additionally, as the doped chromophores disperse at the molecular level, a homogeneous system with high energy transfer efficiency can be obtained. The low-band-gap chromophore can be embedded into the polymer host chain

and also can be suspended in the polymer side chain, during the materials design and synthesis, this approach has great control space (Fig. 1.22).[132] In 2005, Wang et al. for the first time reported the construction of a single polymer displaying white light emission by embedding a red chromophore along the blue chromophore polymer's main chain, and

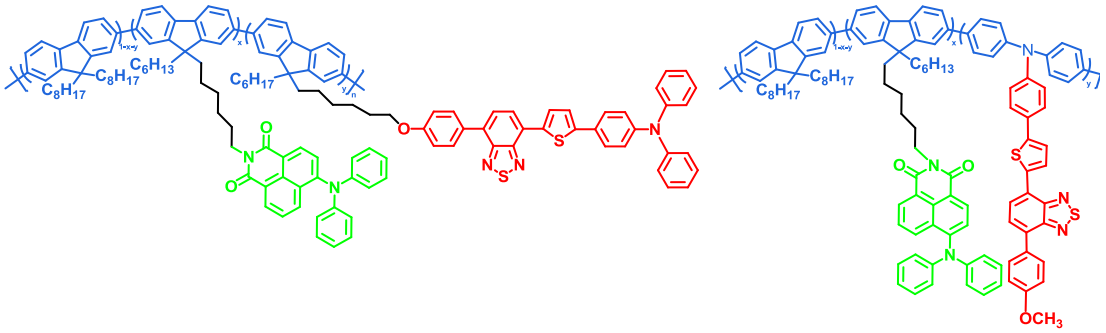

Figure 1.22 Chemical structure of a white emitting polymer prepared by Wang et al. Figure adapted from ref. 132c.

suspending a green chromophore in the polymer's side chain. As a result red, green, and blue chromophores were successfully incorporated in a single polymer chain. Subsequently, by adjusting the ratio of chromophores, they obtained highly efficient PWLED.[133]

1.8.4 Phosphorescent Molecule-Dispersed Polymer: Phosphorescence dye molecule can also be chemically dispersed into the polymer. Because of its high efficiency the doping amount is extremely small, which could effectively avoid phase separation problem. Additionally, the use of triplet and singlet excitons, further improved the efficiency. Cao and coworkers[134] have first introduced the triplet phosphorescent material into the molecule-dispersed (EL) material and developed a new type of single molecule white EL material (Fig 1.23). The host polymer was blue polyfluorene, where the main chain was doped with a little yellow green benzothiazole chromophore. The side chain was grafted with the red triplet iridium complexes. Adjusting the ratio of copolymerizing chromophores gave a pure white EL with a color coordinates (0.32, 0.33) very close to

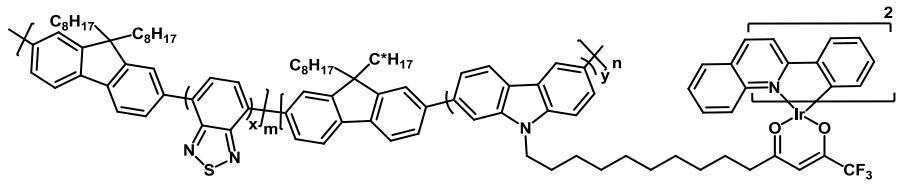

Figure 1.23 Chemical structure of a phosphorescent molecule-dispersed polymer, adapted from ref. 134.

white light. There are many fluorine based polymer system are reported by grafting triplet state Ir based complex onto the side chain,[134,135] or the main chain of the polymer.[136]

1.9 A Brief Overview of Spin Cross-Over Effect:

The spin cross-Over (SCO) phenomenon was first discovered more that 60 years ago by Cambi et al. in 1930s, on the observation of unusual magnetic properties of dithiocarbamato complexes of Fe(III).[137] They interpreted, erroneously, the observation of temperature-dependent moments as arising from equilibria between two magnetic isomers. However after development of ligand field theory (LFT),[138] and the principle of the SCO phenomenon, and the thermal condition to be fulfilled in order to observe it, are now well understood.[139]

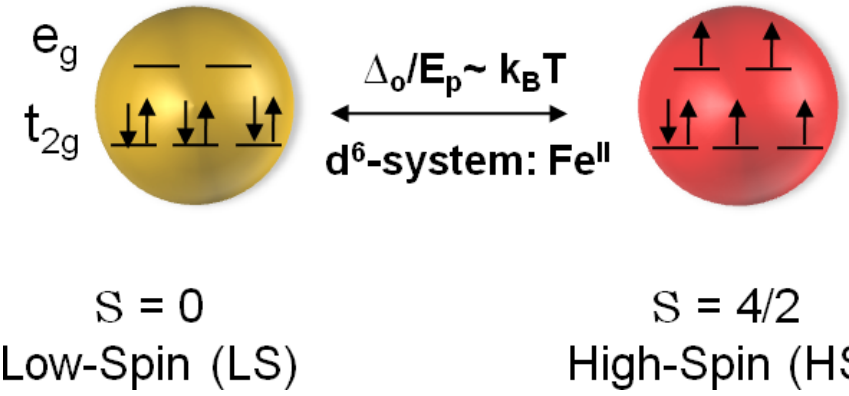

Figure 1.24 Schematic representation of the spin cross-over phenomenon for octahedrally coordinated Fe(II) ions (Δ_O: ligand field splitting parameter; EP: spin pairing energy; k_B: Boltzmann constant; T: temperature).

The SCO phenomenon is only occurred in octahedral complexes of first-row transition metal ions with 4–7 3-D valence electrons. The spin state (LS↔HS) inter-conversion can be achieved by applying external perturbations such as temperature (T), pressure (p) and electromagnetic radiation (hυ). There are no SCO examples known with 4d and 5d transition elements. Because the ligand field strength increases by roughly 50% on going from 3-D to 4d and from 4d to 5d elements, whereas the spin-pairing energy does not change much in this order. Thus, octahedral 4d and 5d complexes show a strong tendency to adopt LS behavior. When all other factor retains unchanged increase of oxidation number increases the ligand field strength about 40–80%, for e.g., the ligand field strength of Fe^{2+} complexes increases by about 40% upon oxidation to the corresponding Fe^{3+} complexes, while the spin-pairing energy does not increase that much.

Thus, one can hardly expect that a SCO complex of Fe(II) will still exhibit SCO behavior after oxidation to the corresponding Fe(III) complex. Tetrahedral SCO complexes of 3-D elements are not known, because the ligand field strength is only about half than that of octahedral complexes,[138b] thus favoring HS behavior. Till now most SCO complexes known are of Fe(II), Fe (III), and Co(II). Only a few SCO complexes of Mn(II), Mn(III), Cr(II), and Co(III) have also been reported.[136,140] The first SCO phenomena of Fe(II) was reported in the literature are $[Fe(phen)_2X_2]$ (where, phen = 1,10-phenanthroline; X = NCS, NCSe), frequently called the "*classical*" Fe(II) SCO complex. This Fe(II) SCO complexes also show difference in the Fe-N bond distances of about 0.2 Å between HS (*S*=2) and LS (*S*=0) states (Fig. 1.24).[141]

The SCO phenomenon is much less frequently observed for Co(II) than for iron(II) complexes. The first spin transition in a six-coordinate cobalt(II) compound was reported by Stoufer et al.[142] The Co(II) six-coordinate compounds undergoes spin transition with the change of electron configuration $t_{2g}^6 eg^1$ (^2E_g; LS) ↔ $t_{2g}^5 eg^2$ ($^4T_{1g}$; HS). Some changes have also observed for four-coordinate and some five coordinate complexes of Co(II). But the phenomenon is believed to be configurational equilibria between the complexes.[143] Ni(II) complexes are known to show spin state equilibria in solution.[140] However, in all these cases, changes of spin states arise from configurational changes such as tetrahedral, HS ↔ square planar, LS.

1.9.1 Effect of Chemical Moieties in SCO: In the early stage of SCO research, it was recognized that SCO behavior can vary considerably with the nature of the coordinated ligands,[139b,144,145] The changes of the chemical composition influence the ligand field strength acting at the central metal ion in several ways: viz. σ-interaction between metal and donor atom, steric hindrance by rotating substituent close to the donor atom influences the distance, r, between the metal and the donor atom and thereby the ligand field strength according to $Dq \approx 1/r^{-5}$ equation;[138]138[b] Hydrogen bonding,[146] π–π stacking of ligands,[147] formation of 1-D, 2-D, and 3-D polymer through weak supramolecular interaction is also known to influence spin transition. As these influences operate in a concerted manner it is almost impossible to make reliable predictions of the effectiveness of the various contributions. Counter anions and trapped solvent molecules also have known to affect the spin crossover behavior.[139b,148] Scientists have also studied the isotope-effect with H/D- and $^{14}N/^{15}N$-labeled SCO compounds to explore hydrogen bonding networks and stepwise spin transitions.[139b,149]

1.9.2 Physical Influences on SCO Behavior: The influence of pressure on SCO behavior is very well known and studied.[150] With the increase of pressure the distance between metal and donor atom decreases resulting HS to the LS state. The low spin state of a SCO compound is generally stabilized and the χT vs T curve tends to be shifted upwards on the temperature scale.[150d]

1.9.2.1 Light-Induced Excited Spin State Trapping (LIESST): It is a method of changing the electronic spin state of a compound by means of irradiation with laser light at low temperatures. The phenomenon was first discovered on a single crystal of the SCO compound $[Fe(ptz)_6](BF_4)_2$ (ptz =1-propyltetrazole), when it was irradiated with green laser light. The green light converts the LS state to a long-lived metastable HS state with a lifetime of hours at cryogenic temperatures.[151] Later it was also found that the metastable HS state can revert back to the LS state by irradiating the crystal with near infrared light.[152] Light-induced SCO and HS↔LS relaxation have been well examined experimentally and theoretically by Hauser.[153] When the green light was irradiated into the polymer embedded single-crystal or polycrystalline $[Fe(ptz)_6](BF_4)_2$ complex, it undergoes transition from $^1A_1$ to $^1T_1$ state, followed by two successive intersystem crossing (ISC) processes $^1T_{1,2} \rightarrow {}^3T_{1,2} \rightarrow {}^5T_{1,2}$ and populate the HS state $^5T_2$. Radiative decay from $^5T_2 \rightarrow {}^1A_1$ is spin and parity forbidden, and due to the considerably larger M-L bond distance in the HS state as compared to the LS state, which builds up an energy barrier between the potential wells of the two states (Fig. 1.25), the lifetime of the metastable HS state can be very long. Recently many light induced phenomena such as *light-induced thermal hysteresis* (LITH),[154] *light-induced optical hysteresis* (LIOH),[155] *hard-X-ray-induced excited spin state trapping* (HAX-IESST),[156] *hard-X-ray-induced thermal hysteresis* (HAXITH),[157] *nuclear de-cay-induced excited spin state trapping* (NIESST),[158] *electron-induced excited spin state trapping* (ELIESST),[159] ligand-*driven light-induced spin change* (LD-LISC),[160]

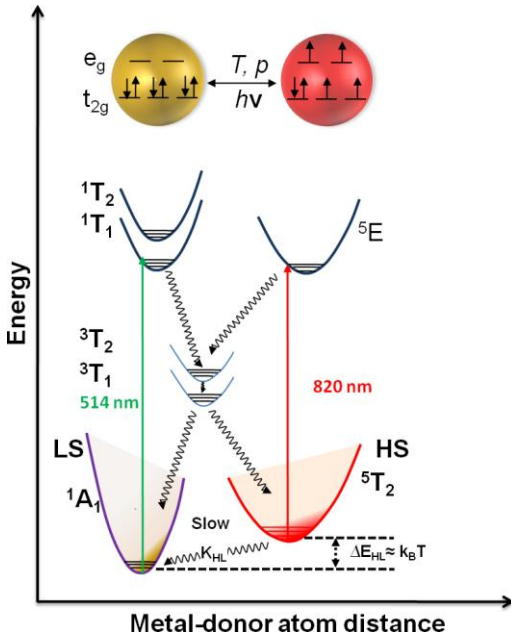

Figure 1.25 Light-induced excited spin state trapping (LIESST).

light-induced cis/trans-isomerization[88] have also been investigated.

In 2011, keeping future molecule based spintronic devices in mind, Ruben and van der Zant et al. have demonstrated the electric field control of the SCO effect, which allows a local, fast, and direct manipulation of single molecular spins, as an important prerequisite for molecular spintronics.[161]

1.9.3 Overview and Future Perspective: Kahn first proposed that spin transition polymers bear the potential for applications in memory devices. Recently in all publications dealing with SCO studies the authors emphasize this aspect.[162] In view of application of SCO, thin films,[163] gels,[164] nanoparticles,[165] cages,[166] micro/nanoporous materials,[167] and multifunctional SCO systems[168] are currently under extensive exploration. To use the spin crossover complexes as multifunctional materials, scientists also have combined the SCO behavior with other physical phenomena such as liquid crystalline properties,[169] electrical conductivity,[170] fluorescence,[171] etc.

1.10 A Brief Overview of Soft Lithographic Techniques:

1.10.1 Micro- and Nanotechnologies Lithography:

Lithography serves a tool to fabricate microelectronics and optoelectronic circuits there by position itself as a central contributor to information technology (IT). An advance in lithography is directly related to the increase in the integration density of silicon chips in modern technology and it is almost in accordance with Moore's Law. The progress in lithographic techniques has lead to an increase in chip yield and a reduction in the chip cost, subsequently steep fall in electronic device price. The past two decades have seen an exorbitant growth in the microelectronics production and associated technologies. Usage of microelectronics impacts on technologies such as communications, computer science, medicine, energy, and more recently, home entertainment and thereby affects our *day-to-day* life. Lithography not only serves in the area of microelectronics but also in the fabrication of sensors, microreactor, combinatorial arrays, microelectromechanical systems (MEMS), microanalytical systems, micro-optical systems, OLEDs and so on.

1.10.2 Conventional Lithography Approaches:

There are two approaches commonly used to fabricate nano/micro structures on various substrates known as "*top-down*" and "*bottom-up*" approaches. The top-down approach essentially ***impose*** a structure or pattern on the substrate being processed e.g., lithography, writing, stamping, etc. On the other hand the bottom up approach uses interactions between molecules or colloidal particles to assemble discrete nanoscale structures in two and three dimensions. Top-down techniques mainly include photolithography and scanning beam lithography (e.g. electron beam and focused ion beam lithography). The limitations of these conventional approaches are their high capital, large proceessing time and operating costs, the difficulty in accessing the facilities necessary to use them motivate the exploration and development of new, or "unconventional nanofabrication techniques.

1.10.3 Photolithography:

It is a process in which UV light is used to transfer a geometric pattern usually called photomask to a light-sensitive chemical "photoresist", on the substrate (Fig. 1.26). In current semiconductor nanofabrication industry photolithography is an extensively used technique and it can pattern 37 nm wide features with 193 nm wavelength light. Photolithography is usually carried out using one of two different ways: contact (or proximity) printing or projection printing.[172] In contact printing the photomask is kept in contact with the resist film. The maximum resolution of contact mode photolithography is typically 0.5-0.8 μm when UV-visible light (360-460 nm) is used and it is primarily determined by diffraction that occurs as the light passes through the gap between the mask and the resist. The drawback of this technique is that the mechanical contact of photomask with the resist film, which can damage fragile structures on the mask or the sample.

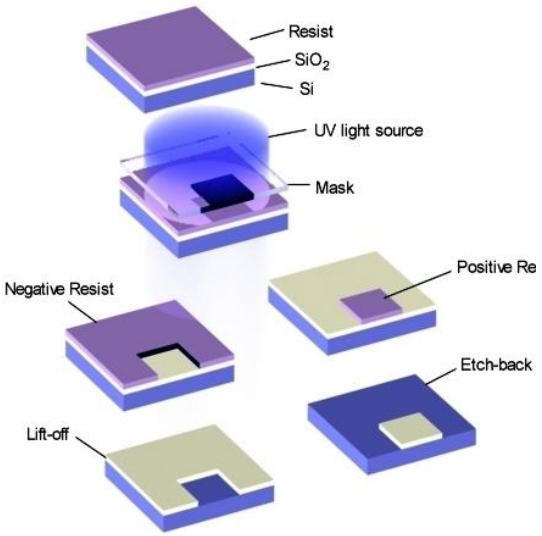

Figure 1.26 Conventional photolithographic technique.

In projection printing, a system of lenses was placed between the mask and the resist film. The features on the resist can be significantly smaller than those on the mask. In recent times all integrated circuits are manufactured by projection photolithography. The theoretical resolution (R) of an optical system for projection printing is limited by Rayleigh diffraction (eq 1.2).[173]

$$\mathbf{R} = \frac{k\lambda}{NA} \qquad \ldots\ldots\ 1.2$$

λ = Wavelength of light

NA = Numerical apperture of the objective

k = A constant that depends on the imaging technology and process control but typically must be 0.7 for adequate production yield.

State-of-the-art photolithographic techniques are capable to reach the limit as small as ~ 250 nm.[174] Photolithography in the regime less than 100 nm include extreme UV (EUV) lithography, soft X-ray lithography, electron-beam writing, focused ion beam (FIB) writing, and proximal-probe lithography.[175]

1.10.4 Soft Lithographic Techniques:

Although these photolithography techniques are capable to generate extremely small features (as small as a few nm), but they are not economical, poorly suited for patterning of nonplanar surfaces, specific chemical functionalities on surfaces cannot be generate by this technique and completely dependent on the photoresists. In order to avoid all these drawbacks a new technique called soft-lithography has come up. The soft-lithographic techniques can be subdivided as i) microcontact printing (μCP),[176] ii) replica molding (REM),[177] iii) microtransfer molding (μTM),[178] iv) micro-molding in capillaries (MIMIC),[179] v) UV-molding, vi) embossing, vii) nanoinprint lithography, viii) solvent-assisted micromolding (SAMIM),[180] ix) microcontact printing, x) nanotransfer printing, xi) microinjection molding,[181] and xii) lithographically controlled wetting.[39a]

All the soft lithographic techniques share the common feature of using a patterned elastomer as the stamp called mold, which is used to generate micropatterns and microstructures. The fabrication of an elastomeric mold is presented in Fig. 1.27 the elastomeric stamp or mold is prepared by cast molding. A prepolymer of the elastomer is poured over a master having relief structure on its surface, and then cured (Fig. 1.27b)

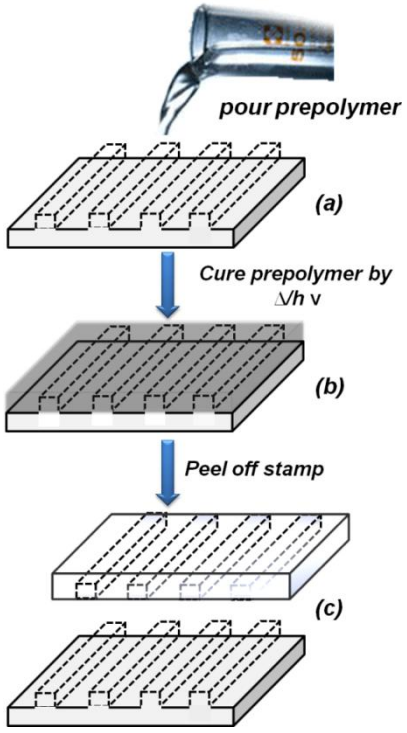

Figure 1.27 The principle of fabrication of polymer stamp or mold for soft lithography.

and peeled off (Fig. 1.27c). The mold replicates the negative features of master, and can be used to fabricate or pattern the next material. The master is, in turn, fabricated using microlithographic techniques such as photolithography, micromachining, e-beam writing, or from available relief structures such as diffraction gratings,[182] TEM grids,[183] polymer beads assembled on solid supports,[184] and relief structures etched in metals or Si.[185]

Soft lithography is not independent of clean room facilities and high-cost equipment in view of master fabrication. The strength of soft-lithography is rather in replication. Once the master is created with the expensive or low-throughput equipment, it can be used more than 50 times. Thus it overcomes the limits of slow throughput compared with scanning beam lithography and makes the soft lithography an attractive alternative in nano scale patterning. Soft lithographic techniques can be divided into major three groups of i) replica molding, ii) UV molding, iii) embossing,and iv) printing, each having sub-groups of techniques.

1.10.4.1 Replica Molding:

Replica molding (RM, REM) transfers the pattern of the master into PDMS. First a photo- or thermally curable prepolymer was poured onto the master. The liquid prepolymer takes the shape of the master and exposure to UV radiation or suitable temperature induces the cross linking, making the polymer solid. Peeling off the mold from the master creates an inverse replica. The process described in Fig. 1.28. The polymer mold is often made of poly(dimethylsiloxane) (PDMS). The soft polymer

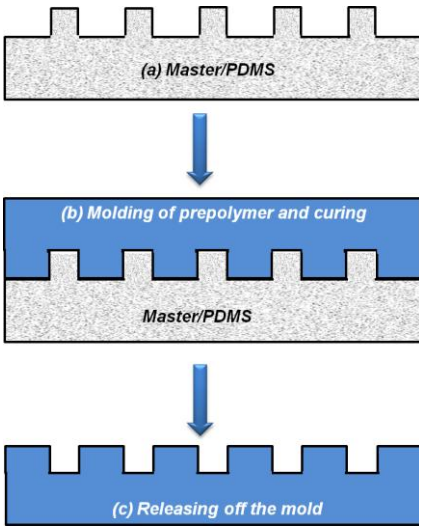

Figure 1.28 Replica molding: casting the prepolymer mixture into a PDMS master and crosslinking it then removing the master, thus fabricating the stamp or mold.

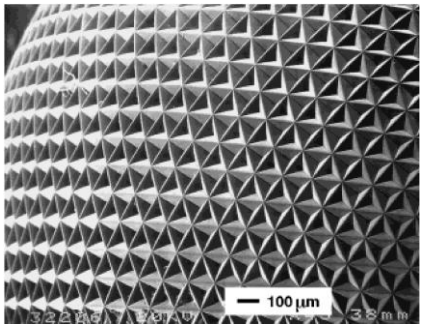

Figure 1.29 A scanning electron micrograph of patterned microstructures on its surface that was formed by replica molding against a stretched PDMS mold, adapted from ref. 186.

mold can be used as a master in the next step, to mold another liquid prepolymer, such as polyurethane (PU)[186]. This is depicted in Fig. 1.28. A microstructure fabricated by replica molding is shown in Fig. 1.29. Replica molding is able to produce numerous molds, replicas, and patterned surfaces from each master. Replica molding has transferred 30-nm lateral features from a diffraction grating.[187] The smallest features replicated using PDMS are ~3-nm wide structures[188] and ~0.5-nm vertical deflections.[189] Replica molding against a rigid mold with an appropriate material (usually a thermoplastic polymer) has been used for the mass-production of a wide range of structured surfaces such as compact disks (CDs),[190] diffraction gratings,[191] holograms,[192] and micro-tools.[193]Three techniques related to RM are microtransfer molding (μTM), micromolding in capillaries (MIMIC) and lithographically controlled wetting (LCW).

1.10.4.1.1 Microtransfer Molding:

In microtransfer molding (μTM), a liquid prepolymer, such as polyurethane (PU) or thermally curable epoxy was poured onto the stamp, making sure that the molded PDMS stamp was wetted by the liquid. The excess prepolymer is scraped away using a piece of flat PDMS. Then the stamp is printed manually onto the desired substrates by applying pressure and heat (Fig. 1.30).

The film of polymer that remains between the surface protrusions is called scum, which is around 100 nm in thickness and can be removed using reactive O_2 ion etching (RIE). μTM is capable of generating both isolated and interconnected microstructures. The most significant advantage of μTM over other μ-lithographic techniques is the ease with which it can fabricate microstructures on nonplanar surfaces, a characteristic that is essential for building three-dimensional microstructures layer-by-layer. Microtransfer molding is able to produce patterned microstructures of a wide variety of polymers (both pristine and doped with fluorescent dyes such as rhodamine 6G) over relatively large areas (~3 cm^2) within a short period of time (~10 min). Zhao et al. have used this technique to fabricate optical waveguides, couplers, and interferometers from organic

polymers.[194] Microtransfer molding is capable of generating both interconnected and isolated microstructures. μTM was recently used by Thibault et al. to fabricate

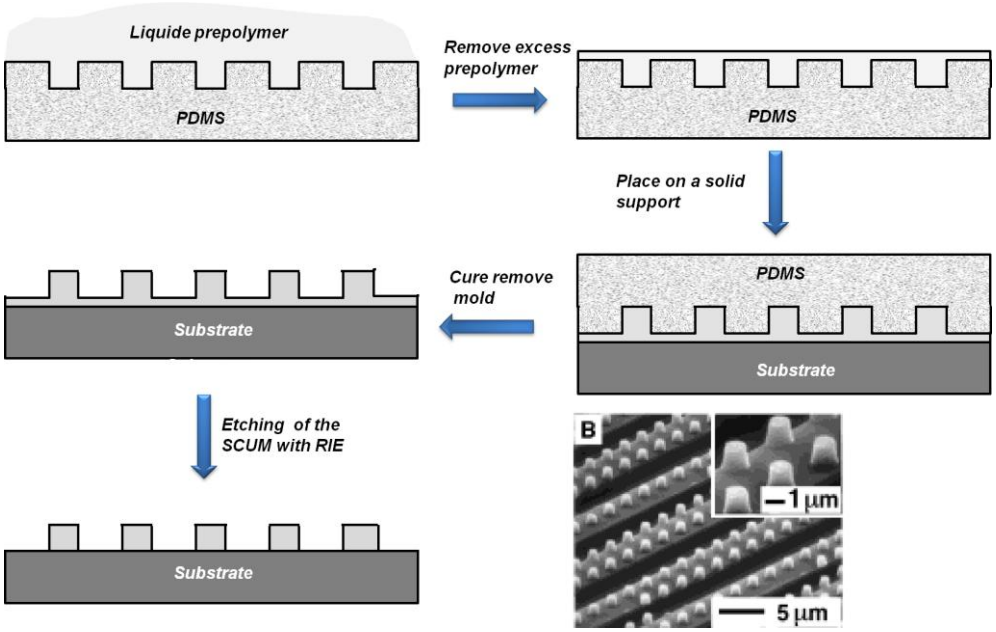

Figure 1.30 Microtransfer molding.

homogeneous micropatterns and nanopatterns of SCO nanoparticles of $[Fe(NH_2trz)](tos)_2$ over a large area. SCO nanoparticles retain their spin crossover properties (with a transition at around room temperature) after the soft lithography step.[195]

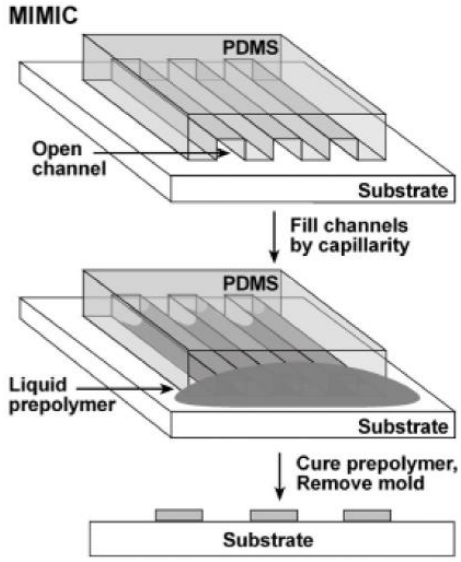

Figure 1.31 Micromolding (MIMIC) in capillaries. Adapted from ref. 179a.

1.10.4.1.2 Micromolding in Capillaries:

During the micromolding in capillaries (MIMIC) technique a soft PDMS master having micro channel structure is used. MIMIC is a simple and versatile soft-lithographic method, introduced by G. Whitesides et al. in 1998. During MIMIC a stamp made of polydimethylsiloxane is placed on a surface to effectively form micro-channels. A low-viscosity prepolymer is then placed at the open ends of the channels, and this liquid instinctively occupies the channels by capillary action. After the complete evaporation of the solvent the stamp is gently

removed and the pattern remains on the surface. The process is shown in Fig. 1.31. The mechanism of this process doesn't allow creating any scum on the substrate and also it is a single step process. Only micro-channels can be fabricated with this technique. The resulting structures are usually thinner than the height of the channels in the PDMS mold but have approximately the same lateral dimensions. Whitesides et al. used MIMIC to fabricate free-standing microstructures of polyurethane.[179,196] Recently Ruben et al. used MIMIC to pattern continuous SCO sub-micrometric stripes of $Fe(phen)_2(NCS)_2$ on a silicon surface.[39a]

1.10.4.1.3 Lithographically Controlled Wetting:

In LCW a PDMS stamp is placed in contact with a liquid film of ink spread on a substrate. The menisci form under the stamp protrusions due to the onset of capillary forces. As the solvent evaporates, the solution remains pinned to the protrusions and the contact line between solution and substrate recedes due to faster solvent evaporation in the region between protrusions (Fig. 1.32). This makes the region between the protrusions free of solution. As the critical concentration is reached, the solute precipitates onto the substrate only below the protrusions, giving rise to a structured thin film that replicates the positive pattern on the stamp (Fig. 1.32). LCW is suitable for a large number of soluble materials and can be, in principle, pushed down to the limit where ST molecules are patterned into ordered arrays, being this process ultimately limited only by coarsening of the individual molecules.

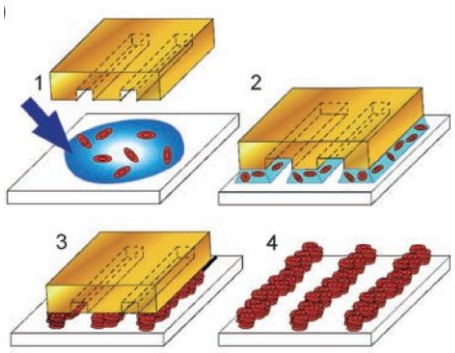

Figure 1.32 Lithographically controlled wetting of SCO compound. Adapted from ref. 39a.

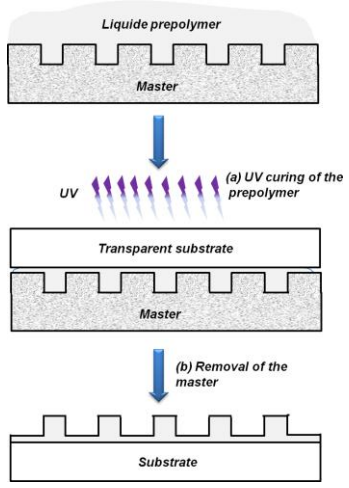

Figure 1.33 Schamatic representation of UV-molding of a UV-curable polymer.

1.10.4.2 UV-Molding:

Ultraviolet-molding (UV-molding) technique is same as the replica molding except hard rigid master and UV radiation is used to crosslink and hardened a UV-curable prepolymer. A simple

schematic diagram of UV-molding is shown in Fig. 1.33. First the prepolymer is poured on top of a master and a UV transparent substrate is placed on top of it and UV radiation is exposed to pass through the substrate. Once it is cured the master is gently taken off and the pattern remains on the transparent substrate.

1.10.4.3 Embossing (Imprinting):

Conventional embossing uses a rigid master (for example, a master made of nickel or SiO_2) to imprint relief structures into a thermoplastic polymer (for example, polycarbonate or PMMA) that has been thermally softened.[197] It is a simple and cost effective process and is the standard for manufacturing replicas of holograms, diffraction gratings, and compact disks (CDs). This technique can also be used for microelectronic circuitry or information storage.[198] Embossing techniques can be divided into two catagories i) nanoimprint lithography (NIL), which uses a rigid master and ii) solvent assisted micro molding (SAMIM), which uses a soft mold as a master.

1.10.4.3.1 Nanoimprint Lithography:

The principle of nanoimprinting is quite simple. The process is first developed by Chou et al.[199] Fig. 1.34 shows a schematic of the originally proposed NIL process. In this process usually a hard rigid master is used to physically deform a solid polymer film that is on a rigid substrate surface. In this process a hard mold that contains nanoscale surface-relief features is pressed into a polymeric material casted on a substrate at a controlled temperature [usually at its glass transition temperature (T_g)] and pressure, thereby creating a thickness contrast in the polymeric material. A thin residual layer of polymeric material is intentionally left underneath the mold protrusions, which acts as a soft cushioning layer that prevents direct impact of the hard mold on the substrate and effectively protects the delicate nanoscale features on the mold surface. The polymer is allowed to deform by filling the voids in the master. Afterwards it is cooled below T_g of the polymer and the master is removed revealing a pattern that is the inverse of the master. The residual layer then removed by an anisotropic O_2 plasma-etching process to complete the pattern. NIL has a tremendous impact over the emerging technologies viz. hybrid plastic electronics,[200] organic electronics and photonics,[201] nanoelectronic devices in Si,[202] and in GaAs,[203] and nonlinear optical polymer nanostructures,[204] high-resolution organic light-emitting diode (OLED) pixels,[205] magnetic devices (e.g., single-domain magnetic structures,[206] high-

density patterned magnetic media and high-capacity disks,[207] and so on.) problem with the lifetime of the master, because the heating and cooling cycles and pressures it experiences, causes ageing.

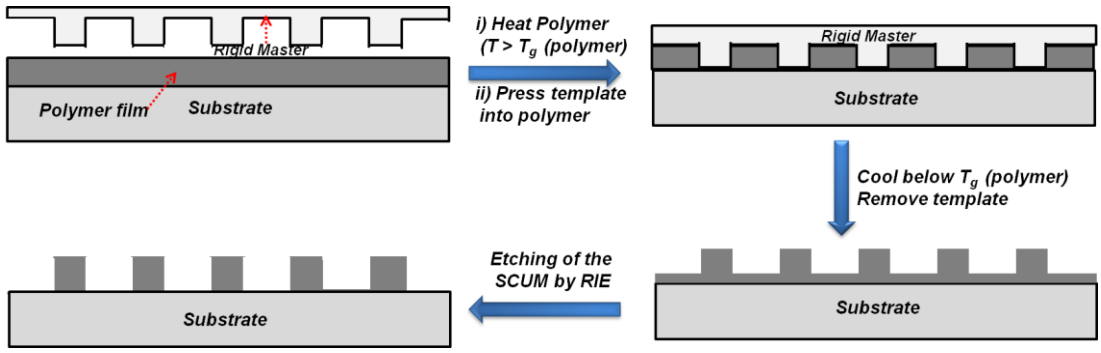

Figure 1.34 Nanoimprint lithography technique.

1.10.4.3.2 Solvent Assisted Micromolding:

Solvent assisted micromolding (SAMIM) has same operational principles with NIL except that SAMIM uses a solvent instead of temperature to "soften" the polymeric material and an elastomeric PDMS mold rather than a rigid one to emboss relief structures into the surface of a substrate to be patterned.[180] In SAMIM process (Fig. 1.35), a PDMS mold is wetted with a good solvent for the polymer to be stamped and brought into contact with the surface of that polymer. The solvent is selected such that it can only

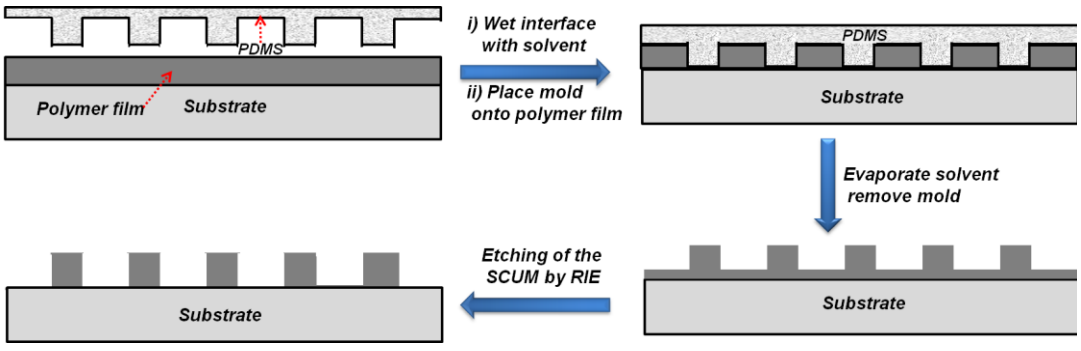

Figure 1.35 Solvent assisted micromolding (SAMIM) process.

dissolve (or "soften") the substrate without affecting/swelling the PDMS mold. After the solvent dissipates and/or evaporates, the mold is removed and a patterned relief structure complementary to that on the surface of the mold remains. A wide variety of organic polymers can be embossed, such as polystyrene, polymethyl metacrylate (PMMA),

poly(vinylchloride), cellulose, acetate, and precursors to conjugated organic polymers.[180,208] SAMIM is capable of replicating complex quasi 3-D relief structures over relatively large areas in a single step. SAMIM is self-cleaning process so dust particles on the surface of the stamp tend to remain in the molded polymer so the mold is cleaned by each cycle. The drawback is, i) some solvents can swell PDMS and as well as the polymer so we have to choose an opposition between the two, ii) a thin layer, typically 10 nm, of polymer is left between the features as in replica molding. This can be removed by O_2 RIE.

1.10.4.4 Printing:

Printing includes material transfer from the mold onto the substrate either physically or chemically. It can be subdivided in following two categories.

1.10.4.4.1 Microcontact Printing:

By micro contact printing (μCP) an existing surface features can be patterned onto a substrate. A simple scheme of microcontact printing is presented in Fig. 1.36. At first the stamp is inked with a material that is to be transferred on the desired substrate. Then the inked stamp was kept by a conformal contact between the protruding features of the stamp and the solid substrate. Only the protruding features of the stamp touches the surface, and the ink is transferred only at these areas. After the material is transferred from the stamp to the substrate, the stamp was gently peeled off creating the desired pattern. The stamp material is usually PDMS. As the PDMS has a highly hydrophobic substrate to increase the hydrophilicity, PDMS stamps are generally oxidised by UV/ozone or by oxygen plasma treatment if a hydrophilic solvent is needed to be used. The first μCP was originally developed by whitesides et al. and used as a method to pattern gold. But later its value in patterning surfaces for other applications

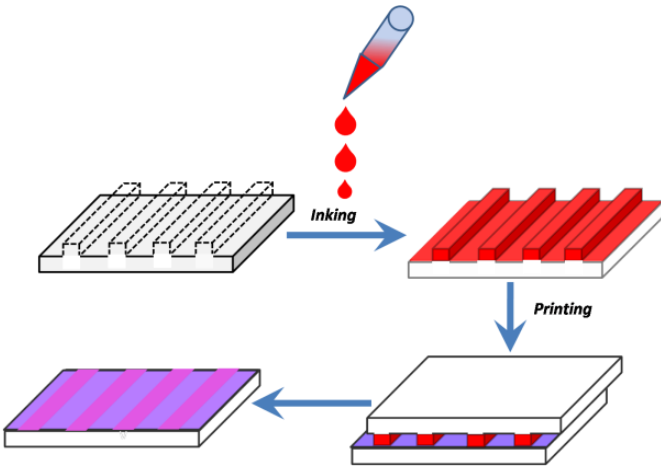

Figure 1.36 The principle of microcontact printing.

quickly became apparent. Since then, μCP has been widely used by researchers in broadly differing fields to pattern water,[209] organic solvents,[210] metals,[176,209a,211] polymers,[212] DNA,[213] proteins,[214] and cells.[215]

Currently its use is versatile in many fields i.e. for the fabrication of organic light emitting diodes[216,217] selectively metalized the polymeric substrate[218], usage of μCP can give easy access to organic electronic devices as well as biological microarrays. Stoddart et al. developed click microcontact printing to selectively perform click chemistry on an azide terminated surface.[219,220] The expediency of micro contact printing is that the same stamp can be used multiple times, and the same master can be used to produce several stamps. To ensure a conformal contact between the substrate and the stamp the material of the stamp needs to be elastomeric.

1.10.4.4.2 Nanotransfer Printing:

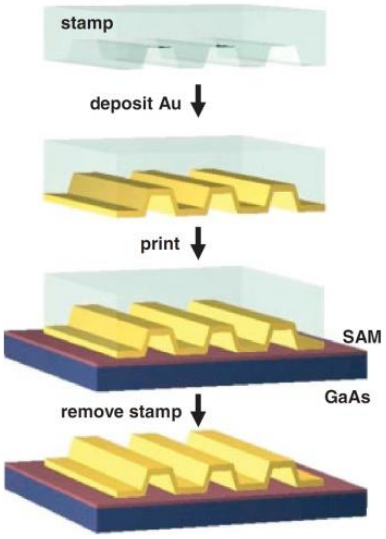

Figure 1.37 The principle of nanotransfer printing. Adapted from ref. 221.

Nanotransfer printing (nTP) is conceptually very similar to microcontact printing (μCP). In both the cases high-resolution stamps are used to generate patterns of their relief structure. nTP technique relies on the principle of surface chemistry. Here chemically modified surfaces act as interfacial "release" or "glue" layers to aid in transfer printing nanostructured metal ink from relief features ("stamp") to a surface of interest. For example, nTP prints gold film onto thiol terminated monolayer. In this approach the material is only deposited in locations where it is needed. nTP is capable of generating complex two or three dimensional structures in single or multiple layers with nanometer resolution. The method is first developed by Rogers et al.[221] and similar approach has been followed by other groups (Fig. 1.37, 1.38).[222] This method is quite practical to fabricate complex structures that would be quite difficult to fabricate in conventional ways for e.g. large stacks of nanochannels can be fabricated in this method (Fig. 1.38) Figure 1.38a shows an optical micrograph of a pattern that illustrates the type of high-resolution printing that is possible by n-TP on a silicon wafer. Unlike only patterning

silicon wafer or gold substrates which are restricted to most of the patterning process, nTP substrates containing surface OH groups. For example, Rogers et al. printed Au patterns onto ~250 μm thick sheets of poly(ethylene terephthalate) by first spin casting and curing a thin film of an organosilsesquioxane on the PET.

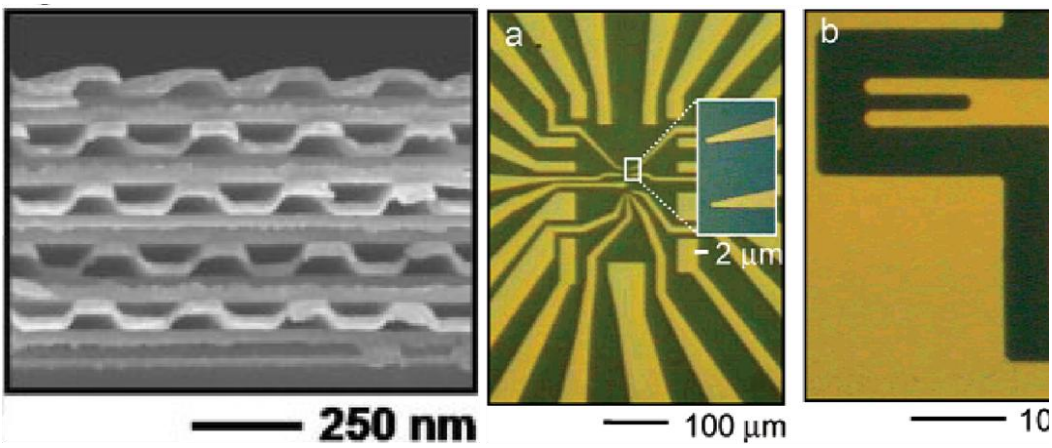

Figure 1.38 SEM and optical microscope images of gold patterns formed by nanotransfer printing. Adapted from 221, 222a.

1.11 Layout of the Thesis:

In this thesis, an attempt has been made to address several functional nano-materials aspects related to BPP chemistry, which include synthesis, processing and device fabrication. Our primary goal has been to synthesize soluble and processable functional monomers and metallo supramolecular polymers based on BPP derivatives and to fabricate nano-assemblies and devices possessing magnetic and photonic properties. Some of the mainly focused aspects include (i) synthesis soluble and processable Zn(II) containing 1-D metallo-supramolecular polymer using tetra-octylated *back-to-back* coupled BPP ligand and exploitation of the polymer in the fabrication of millimeter long fluorescent nano stripes on a glass substrate, (ii) using a magnetically bistable Fe(II) coordinated BPP complex, optically transparent flexible future magnetic memory device comprises of several patterns and arrays has been successfully fabricated, (iii) the self-assembly studies of *back-to-back* coupled BPP ligand shows the formation of blue emitting parallelepipedic nanotubes. Using the surface selective coordination chemistry with red emitting Eu(III) ions a dual emitting (blue+red) nanotubes has been prepared. (iv) BPP based conjugated polymer has been synthesized and used to incorporate metal ions directly to the conjugated polymer back bone containing ligand. Using the multi-colour emission property of the polymer a white light emitting film has also been

developed. (vi) The parallelepipedic nanotubes exhibit optical wave guiding tendency, further more laser ablation has been performed to cut the tubes thereby control the light propagation distance within the organic nano tube.

References

1. Weiss, L. H.; *Meeresunters Kiel* **1908**, *10*, 129.

2. Feynman, R. P. *Eng. Sci.* **1960**, *23*, 22.

3. Faraday, M. *Phil. Trans.* **1857**, 147, 145.

4. (a) Yu, G. H.; Lieber, C. M. *Pure Appl. Chem.* **2010**, *82*, 2295. (b) Lieber, C. M.; Jin, S.; Whang, D. M.; McAlpine, M. C.; Friedman, R. S.; Wu, Y. *Nano Lett.* **2004**, *4*, 915. (c) Yan, H.; Choe, H. S.; Nam, S. W.; Hu, Y. J.; Das, S.; Klemic, J. F.; Ellenbogen, J. C.; Lieber, C. M. *Nature* **2011**, *470*, 240. (d) Lu, W.; Lieber, C. M. *Nat. Mater.* **2007**, *6*, 841. (e) Huang, Y.; Duan, X. F.; Cui, Y.; Lauhon, L. J.; Kim, K. H.; Lieber, C. M. *Science* **2001**, *294*, 1313. (e) Huang, Y.; Duan, X. F.; Wei, Q. Q.; Lieber, C. M. *Science* **2001**, *291*, 630. (f) Kumar, P. *Nanoscale Res. Lett.* **2010**, *5*, 1367.

5.Tao, A. R.; Huang, J. X.; Yang, P. D. *Acc. Chem. Res.* **2008**, *41*, 1662.

6. Tracz, A.; Jeszka, J. K.; Watson, M. D.; Pisula, W.; Müllen, K.; Pakula, T. *J. Am. Chem. Soc.* **2003**, *125*, 1682.

7. Pisula, W.; Menon, A.; Stepputat, M.; Lieberwirth, I.; Kolb, U.; Tracz, A.; Sirringhaus, H.; Pakula, T.; Müllen, K. *Adv. Mater.* **2005**, *17*, 684.

8. Popović, Z.; Busby, M.; Huber, S.; Calzaferri, G.; Cola, L. D. *Angew. Chem. Int. Ed.* **2007**, *46*, 8898.

9. Duzhko, V.; Du, J.; Zorman, C. A.; Singer, K. D. *J. Phys. Chem. C* **2008**, *112*, 12081.

10. Orendorff, C. J.; Hankins, P. L.; Murphy, C. J. *Langmuir*, **2005**, *21*, 2022.

11. Caswell, K. K.; Wilson, J. N.; Bunz, U. H. F.; Murphy, C. J. *J. Am. Chem. Soc.* **2003**, *125*, 13914.

12. Nikoobakht, B.; Wang, Z. L.; El-Sayed, M. A. *J. Phys. Chem. B* **2000**, *104*, 8635.

13. Pierrat, S.; Zins, I.; Breivogel, A.; Sönnichsen, C. *Nano Lett.* **2007**, *7*, 259.

14. Kumar, J.; Wei, X.; Barrow, S.; Funston, A. M.; Thomas, K. G.; Mulvaney, P. *Phys. Chem. Chem. Phys.* **2013**, *15*, 4258.

15. Gogoi, S. K.; Borah, S, M.; Dey, K.; K.; Paul, A.; Chattopadhyay, A. *Langmuir* **2011**, *27*, 12263.

16. Majumdar, G.; Gogoi, S. K.; Paul, A.; Chattopadhyay, A. *Langmuir* **2006**, *22*, 3439.

17. Murugadoss, A.; Chattopadhyay, A. *J. Phys. Chem. C* **2008**, *112*, 11265.

18. Sajanlal, P. R.; Pradeep, T *Adv. Mater.* **2008**, *20*, 980.

19. Shibu, E. S.; Radha, B.; Verma, P. K.; Bhyrappa, P.; Kulkarni, G. U.; Pal, S. K.; Pradeep, T. *ACS Appl. Mater. Interfaces* **2009**, *1*, 2199.

20. Sreeprasad, T. S.; Pradeep, T. *Langmuir* **2011**, *27*, 3381.

21. Talapin, D. V.; Shevchenko, E. V.; Bodnarchuk, M. I.; Ye,X.; Chen, J.; Murray, C. B. *Nature* **2009**, *461*, 964.

22. (a) Ooi, C.; Yellen, B. B. *Langmuir* **2008**, *24*, 8514. (b) Chen, M.; Sun, L.; Bonevich, J. E.; Reich, D. H.; Chien, C. L.; Searson, P. C. *Appl. Phys. Lett.* **2003**, *82*, 3310. (c) Yuan, J. Y.; Gao, H. T.; Schacher, F.; Xu, Y. Y.; Richter, R.; Tremel, W.; Muller, A. H. E. *ACS Nano* **2009**, *3*, 1441. (d) Hangarter, C. M.; Myung, N. V. *Chem. Mater.* **2005**, *17*, 1320. (e) Lalatonne, Y.; Richardi, J.; Pileni, M. P. *Nat. Mater.* **2004**, *3*, 121. (f) Srivastava, A.; Madhavi, S.; Ramanujan, R. *Appl. Phys. A: Mater. Sci. Process.* **2010**, **98**, 821.

23. Wang, B.; Ma, Y. F.; Li, N.; Wu, Y. P.; Li, F. F.; Chen, Y. S. *Adv. Mater.* **2010**, *22*, 3067.

24. (a) Pauzauskie, P. J.; Yang, P. *Mater. Today* **2006**, *9*, 36. (b) Lieber, C. M.; Wang, Z. L. *MRS Bull.* **2007**, *32*, 99. (c) Palmer, L. C.; Stupp, S. I. *Acc. Chem. Res.* **2008**, *41*, 1674. (d) Puigmarti-Luis, J.; Schaffhauser, D.; Burg, B. R.; Dittrich, P. S. *Adv. Mater.* **2010**, *22*, 2255. (e) Smith, P. A.; Nordquist, C. D.; Jackson, T. N.; Mayer, T. S.; Martin, B. R.; Mbindyo, J.; Mallouk, T. E. *Appl. Phys. Lett.* **2000**, *77*, 1399. (f) Tiano, A. L.; Koenigsmann, C.; Santulli, A. C.; Wong, S. S. *Chem. Commun.* **2010**, *46*, 8093. (g) Qiao, Y.; Lin, Y. Y.; Yang, Z. Y.; Chen, H. F.; Zhang, S. F.; Yan, Y.; Huang, J. B. *J. Phys. Chem. B* **2010**, *114*, 11725. (h) Fan, Z. Y.; Ho, J. C.; Jacobson, Z. A.; Yerushalmi, R.; Alley, R. L.; Razavi, H.; Javey, A. *Nano Lett*. **2008**, *8*, 20. (i) Kawasaki, J. K.; Arnold, C. B. *Nano Lett.* **2011**, *11*, 781. (j) Lee, C. H.; Kim, D. R.; Zheng, X. L. *Nano Lett.* **2010**, *10*, 5116. (k) Ryan, K. M.; Mastroianni, A.; Stancil, K. A.; Liu, H. T.; Alivisatos, A. P. *Nano Lett.* **2006**, *6*, 1479. (l) Duan, X. F.; Huang, Y.; Cui, Y.; Wang, J. F.; Lieber, C. M. *Nature* **2001**, *409*, 66. (m) Freer, E. M.; Grachev, O.; Duan, X. F.; Martin, S.; Stumbo, D. P. *Nat. Nanotech.* **2010**, *5*, 525. (n) Li, M. W.; Bhiladvala, R. B.; Morrow, T. J.; Sioss, J. A.; Lew, K. K.; Redwing, J. M.; Keating, C. D.; Mayer, T. S. *Nat. Nanotech.* **2008**, *3*, 88.

25. (a) Gates, B. D. *Nat. Nanotech.* **2010**, *5*, 484. (b) Papadakis, S. J.; Hoffmann, J. A.; Deglau, D.; Chen, A.; Tyagi, P.; Gracias, D. H. *Nanoscale* **2011**, *3*, 1059. (c) Kawasaki, J. K.; Arnold, C. B.; *Nano Lett.* **2011**, *11*, 781. (d) Vestal, C. R.; Zhang, Z. J. *Nano Lett.* **2003**, *3*, 1739.

26. Vijayaraghavan, A.; Blatt, S.; Weissenberger, D.; Oron-Carl, M.; Hennrich, F.; Gerthsen, D.; Hahn, H.; Krupke, R. *Nano Lett.* **2007**, *7*, 1556.

27. (a) Yu, G. H.; Li, X. L.; Lieber, C. M.; Cao, A. Y. *J. Mater. Chem.* **2008**, *18*, 728. (b) Yu, G. H.; Cao, A. Y.; Lieber, C. M. *Nat. Nanotech.* **2007**, *2*, 372.

28. He, D.; Hu, B.; Yao, Q. F.; Wang, K.; Yu, S. H. *ACS Nano*, **2009**, *3*, 3993.

29. (a) Acharya, S.; Hill, J. P.; Ariga, K. *Adv. Mater.* **2009**, *21*, 2959. (b) Cote, L. J.; Kim, F.; Huang, J. X. *J. Am. Chem. Soc.* **2009**, *131*, 1043. (c) Liu, J. W.; Zhu, J. H.; Zhang, C. L.; Liang, H. W.; Yu, S. H. *J.Am. Chem. Soc.* **2010**, *132*, 8945. (d) Guo, Q. J.; Teng, X. W.; Rahman, S.; Yang, H. *J. Am. Chem. Soc.* **2003**, *125*, 630. (e) Whang, D.; Jin, S.; Wu, Y.; Lieber, C. M. *Nano Lett.* **2003**, *3*, 1255. (f) Kim, F.; Kwan, S.; Akana, J.; Yang, P. D. *J. Am. Chem. Soc.* **2001**, *123*, 4360. (g) Mai, L. Q.; Gu, Y. H.; Han, C. H.; Hu, B.; Chen, W.; Zhang, P. C.; Xu, L.; Guo, W. L.; Dai, Y. *Nano Lett.* **2009**, *9*, 826.

30. Bachtold, A.; Hadley, P.; Nakanishi, T.; Dekker, C.; *Science* **2001**, *294*, 1317.

31. Huang,Y.; Duan, X.; Wei, Q.; Lieber, C. M. *Science* **2001**, *291*, 630.

32. Yan, H.; Choe, H. S.; Nam, S. W.; Hu, Y.; Das, S.; Klemic, J. F.; Ellenbogen, J. C.; Lieber, C. M. *Nature* **2011**, *470*, 240.

33. Javey, A.; Nam; Friedman, R. S.; Yan, H.; Lieber, C. M. *Nano Lett.* **2007**, *7*, 773. (b) Fan, Z.; Ho, J. C.; acobson, Z. A.; Yerushalmi, R.; Alley, R. L.; Razavi, H.; Javey, A. *Nano Lett.* **2008**, *8*, 20.

34. Pevzner, A.; Engel, Y.; Elnathan, R.; Ducobni, T.; Ben-Ishai, M.; Reddy, K.; Shpaisman, N.; Tsukernik, A.; Oksman, M.; Patolsky, F. *Nano Lett.* **2010**, *10*, 1202.

35. Xu, F.; Durham, J. W.; Wiley, B. J.; Zhu, Y. *ACS Nano* **2011**, *5*, 1556.

36. Lei, Y.; Wen, L. Y.; Wong, K. M.; Fang, Y. G.; Wu, M. H. *J. Mater. Chem.* **2011**, *21*, 7090.

37. Cavallini, M.; Segura, J. G.; Molina, D. R.; Massi, M.; Albonetti, C.; Rovira, C.; Veciana, J.; Biscarini, F. *Angew. Chem. Int. Ed.* **2005**, *44,* 888. (b) M. Cavallini, M.; Segura, J. G.; Albonetti, C.; Molina, D. R.; Veciana, J.; Biscarini, F. *J. Phys. Chem. B* **2006**, *110*, 11607.

38. Gentili, D.; Maria, F. D.; Liscio, F.; Ferlauto, L.; Leonardi, F.; Maini, L.; Gazzano, M.; Milita, S.; Barbarellab, G.; Cavallini, M. *J. Mater. Chem*. **2012**, *22*, 20852.

39. (a) Cavallini, M.; Bergenti, I.; Milita, S.; Ruani, G.; Salitros, I.; Qu, Z.-R.; Chandrasekar, R. Ruben, M. *Angew. Chem. Int. Ed.* **2008**, *47,* 8596. (b) Cavallini, M.; Bergenti, I.; Milita, S.; Kengne, J. C.; Gentili, D.; Ruani, G.; Salitros, I.; Meded, V.; Ruben, M. *Langmuir* **2011**, 27, 4076.

40. Iijima, S. *Nature* **1991**, *354*, 56.

41. (a) Pan, Z. W.; Dai, Z. R.; Wang, Z. L. Science **2001**, *291*, 1947. (b) Burda, C.; Chen, X. B.; Narayanan, R.; El-Sayed, M. A. *Chem. Rev.* **2005**, *105*, 1025.

42. (a) Greytak, A. B.; Barrelet, C. J.; Li, Y.; Lieber, C. M. *Appl. Phys. Lett*. **2005**, *87*, 151103. (b) Law, M.; Sirbuly, D. J.; Johnson, J. C.; Goldberger, J.; Saykally, R. J.; Yang, P. D. *Science* **2004**, *305*, 1269. (c) Li, Y.; Qian, F.; Xiang, J.; Lieber, C. M. *Mater. Today* **2006**, *9*, 18.

43. Cui, Y.; Wei, Q. Q.; Park, H. K.; Lieber, C. M. *Science* **2001**, *293*, 1289.

44. Qian, F.; Gradecak, S.; Li, Y.; Wen, C. Y.; Lieber, C. M. *Nano Lett.* **2005**, *5*, 2287.

45. Cui, Y.; Zhong, Z. H.; Wang, D. L.; Wang, W. U.; Lieber, C. M. *Nano Lett*. **2003**, *3*, 149.

46. Tian, B.; Zheng, X.; Kempa, T. J.; Fang, Y.; Yu, N.; Yu, G.; Huang. J.; Lieber, C. M. *Nature* **2007**, *449*, 885.

47. (a) Duan, X . F.; Huang, Y.; Cui, Y.; Wang, J. F.; Lieber, C. M. *Nature* **2001**, *409*, 66. (b) Huang, Y.; Duan, X. F.; Cui, Y.; Lauhon, L. J.; Kim, K. H.; Lieber, C. M. *Science* **2001**, *294*, 1313. (c) Gudiksen, M. S.; Lauhon, L. J.; Wang, J.; Smith, D. C.; Lieber, C. M. *Nature* **2002**, *415*, 617. (d) Wang, Z. L.; Song, J. H. *Science* **2006**, *312*, 242.

48. (a) Horowitz, G. *Adv. Mater*. **1998**, *10*, 365. (b) Friend, R. H.; Gymer, R.W.; Holmes, A. B.; Burroughes, J. H.; Marks, R. N.; Taliani, C. D.; Bradley, D.C.; Dos Santos, D. A.; Bredas, J. L.; Logdlund, M.; Salaneck, W. R. *Nature* **1999**, *397*, 121. (c) Sirringhaus, H.; Kawase, T.; Friend, R. H.; Shimoda, T.; Inbasekaran, M.; Wu, W.; Woo, E. P. *Science* **2000**, *290*, 2123. (d) Forrest, S. R. *Nature* **2004**, *428*, 911. (e) Sariciftci, N. S.; Smilowitz, L.; Heeger, A. J.; Wudl, F. *Science*, **1992**, *258*, 1474. (d) Yu, G.; Gao, J.; Hummelen, J. C.; Wudl, F.; Heeger, A. J. *Science* **1995**, *270*, 1789.

49. (a) Liu, H. Q.; Kameoka, J.; Czaplewski, D. A.; Craighead, H. G. *Nano Lett*. **2004**, *4*, 671. (b) Ghadiri, M. R.; Granja, J. R.; Milligan, R. A.; McRee, D. E.; Khazanovich, N. *Nature*, **1993**, *366*, 324. (c) Brunsveld, L.; Folmer, B. J. B.; Meijer, E.W.; Sijbesma, R. P. *Chem. Rev*. **2001**, *101*, 4071. (d) Benedetto, F. D.; Camposeo, A.; Pagliara, S.; Mele, E.; Persano, L.; Stabile, R.; Cingolani, R.; Pisignano, D. *Nat. Nanotech*. **2008**, *3*, 614.

50. Huang, L. M.; Wang, Z. B.; Wang, H. T.; Cheng, X. L.; Mitra, A.; Yan, Y. S. *J. Mater. Chem*. **2002**, *12*, 388.

51. Berdichevsky, Y.; Lo, Y. H. *Adv. Mater*. **2006**, *18*, 122.

52. Yun, M. H.; Myung, N. V.; Vasquez, R. P.; Lee, C. S.; Menke, E.; Penner, R. M. *Nano Lett.* **2004**, *4*, 419.

53. Lu, X.; Wang, C.; Wei, Y. *Small* **2009**, *5*, 2349.

54. (a) Cheng, J. Y.; Ross, C. A.; Smith, H. I.; Thomas, E. L. *Adv. Mater.* **2006**, *18*, 2505. (b) Park, S.; Lim, J. H.; Chung, S. W.; Mirkin, C. A. *Science* **2004**, *303*, 348.

55. (a) Wang, Y.; Zhan, C.; Fu, H. B.; Li, X.; Sheng, X.; Zhao, Y.; Xiao, D. B.; Ma, Y.; Ma, J. S.; Yao, J. N. *Langmuir* **2008**, *24*, 7635. (b) Wang, X.; Zhuang, J.; Peng, Q.; Li, Y. D. *Nature* **2005**, *437*, 121.

56. Peng, A. D.; Xiao, D. B.; Ma, Y.; Yang, W. S.; Yao, J. N. *Adv. Mater.* **2005**, *17*, 2070.

57. (a) Balzer, F.; Bordo, V. G.; Simonsen, A. C.; Rubahn, H. G. *Appl. Phys. Lett*. **2003**, *82*, 10. (b) Balzer, F.; Bordo, V. G.; Simonsen, A. C.; Rubahn, H. G. *Phys. Rev. B: Condens. Matter* **2003**, *67*, 115408.

58. Zhao, Y. S.; Fu, H. B.; Hu, F. Q.; Peng, A. D.; Yang, W. S.; Yao, J. N. *Adv. Mater*. **2008**, *20*, 79.

59. Zhao, Y. S.; Fu, H. B.; Hu, F. Q.; Peng, A. D.; Yang, W. S.; Yao, J. N. *Adv. Mater*. **2008**, *20*, 79.

60. Fu, H. B.; Xiao, D. B.; Yao, J. N.; Yang, G. Q. *Angew. Chem. Int. Ed*. **2003**, *42*, 2883.

61. Zhao, L. Y.; Yang, W. S.; Luo, Y.; Zhai, T. Y.; Zhang, G. J.; Yao, J. N. *Chem. Eur. J*. **2005**, *11*, 3773.

62. (a) Zhao, Y.S.; Fu, H.; Peng, A.; Ma, Y.; Liao, Q.; Yao, J. *Acc. Chem. Res.* **2010**, *43*, 409. (b) Yan, Y.; Zhang, C.; Yao, J.; Zhao, Y.S. *Adv. Mater.* **2013**, *225*, 3627–3638. (c) Yanagi, H.; Morikawa, T. *Appl. Phys. Lett.* **1999**, *75*, 187. (d) Takazawa, K.; Kitahama, Y.; Kimura, Y.; Kido, G. *Nano Lett.* **2005**, *5*, 1293. (e) Balzer, F.; Bordo, V. G.; Simonsen, A. C.; Rubahn, H.-G. *Appl. Phys. Lett.* **2003**, *82*, 10.

63. Zhao, Y. S.; Xu, J. J.; Peng, A. D.; Fu, H. B.; Ma, Y.; Jiang, L.; Yao, J. N. *Angew. Chem. Int. Ed.* **2008**, *47*, 7301.

64. Chandrasekhar, N.; Mohiddon, Md. A.; Chandrasekar, R. *Adv. Optical Mater.* **2013**, *1*, 305.

65. Zhao, Y. S.; Peng, A. D.; Fu, H. B.; Ma, Y.; Yao, J. N. *Adv. Mater*. **2008**, *20*, 1661.

66. Zhao, Y. S.; Fu, H. B.; Hu, F. Q.; Peng, A. D.; Yao, J. N. *Adv. Mater*. **2007**, *19*, 3554.

67. Zhao, Y. S.; Fu, H. B.; Hu, F. Q.; Peng, A. D.; Yang, W. S.; Yao, J. N. *Adv. Mater*. **2008**, *20*, 79.

68. Zhang, C.; Zhao, Y. S.; Yao, J. N. *New J. Chem*. **2011**, *35*, 973.

69. Zhao, Y. S.; Di, C. A.; Yang, W. S.; Yu, G.; Liu, Y. Q.; Yao, J. N. *Adv. Funct. Mater*. **2006**, *16*, 1985.

70. Cui, Q. H.; Jiang, L.; Zhang, C.; Zhao, Y. S.; Hu, W.; Yao, J. N. *Adv. Mater*. **2012**, *24*, 2332.

71. Zheng, J. Y.; Zhang, C.; Zhao, Y. S.; Yao, J. N. *Phys. Chem. Chem. Phys* **2010**, *12*, 12935.

72. (a) Solanki, N. K.; Leech, M. A.; Mcinnes, E. J. L.; Zhao, J. P.; Mabbs, F. E.; Feeder, N.; Howard, J. A. K.; Davies, J. E.; Rawsona, J. M.; Halcrow, M. A. *J. Chem. Soc. Dalton Trans.* **2001**, 2083. (b) Holland, J. M.; Kilner, C. A.; Thornton-Pett, M.; Halcrow, M. A. *Polyhedron* **2001**, *20,* 2829.

73. Brunet, E.; Juanes, O.; Sedano, R.; Rodríguez-Ubis, J. C. *Org. Lett.* **2002**, *4*, 213.

74. Holland, J. M.; McAllister, J. A.; Lu, Z.; Kilner, C. A.; Thornton-Petta, M.; Halcrow, M. A. *Chem. Commun*. **2001**, 577.

75. Chryssou, K.; Stergiopoulos, T.; Falaras, P. *Polyhedron* **2002**, *21,* 2773.

76. Kurtarana, R.; Arıcı, C.; Emregül, K. C.; Ülküb, D.; Atakol, O.; Taştekin, M. *Z. Anorg. Allg. Chem.* **2003**, *629*, 1617.

77. Elhaïk, J.; Pask, C. M.; Kilner, C. A. Halcrow, M. A. *Tetrahedron* **2007**, *67*, 291.

78. Rajadurai, C.; Qu, Z.; Fuhr, O.; Gopalan, B.; Kruk, R.; Ghafari, M.; Ruben, M. *Dalton Trans.* **2007**, 3531.

79. Nihei, M.; Han, L.; Oshio, H. *J. Am. Chem. Soc.* **2007**, *129*, 5312.

80. Nihei, M.; Maeshima, T.; Kose, Y.; Oshio, H. *Polyhedron* **2007**, *26*, 1993.

81. Chandrasekar, R.; Schramm, F.; Fuhr, O.; Ruben, M. *Eur. J. Inorg. Chem.* **2008**, 2649.

82. (a) Kadjane, P.; Starck, M.; Camerel, F.; Hill, D.; Hildebrandt, N.; Ziessel, R.; Charbonnière, L. J. *Inorg. Chem.* **2009**, *48*, 4601. (b) Mato-Iglesias, M.; Rodríguez-Blas, T.; Platas-Iglesias, C.; Starck, M.; Kadjane, P.; Ziessel, R.; Charbonnière, L. *Inorg. Chem.* **2009**, *48*, 4601.

83. Pritchard, R.; Lazar, H.; Barrett, S. A.; Kilner, C. A.; Asthana, S.; Carbonera, C.; Létard, J-F.; Halcrow, M. A. *Dalton Trans*. **2009**, 6656.

84. Chandrasekhar, N.; Chandrasekar, R. *Chem. Commun.* **2010**, *46*, 2915.

85. Zhu, X. J.; Holliday, B. J. *Macromol. Rapid Commun.* **2010**, *31*, 904.

86. Stanley, J. M.; Zhu, X.; Yang, X.; Holliday, B. J. *Inorg. Chem.* **2010**, *49*, 2035.

87. Ye, Z.; Wang, G.; Chen, J.; Fu, X.; Zhang, W.; Yuan, J. *Biosensors and Bioelectronics* **2010**, *26*, 1043.

88. Hasegawa, Y.; Takahashi, K.; Kume, S.; Nishihara, H. *Chem. Commun.* **2011**, *47*, 6846.

89. Nihei, M.; Takahashi, N.; Nishikawab, H.; Oshio, H. *Dalton Trans*. **2011**, *40*, 2154.

90. González-Prieto, R.; Fleury, B.; Schramm, F.; Zoppellaro, G.; Chandrasekar, R.; Fuhr, O.; Lebedkin, S.; Kappesa, M.; Ruben, M. *Dalton Trans*. **2011**, *40*, 7564.

91. Hui, P.; Arif, K. Md.; Chandrasekar, R. *Org. Biomol. Chem*. **2012**, *10*, 2439.

92. (a) Starck, M.; Ziessel, R. *Dalton Trans*. **2012**, *41*, 13298. (b) Ziessel, R.; Sutter, A.; Starck, M. *Tet. Lett.* **2012**, *53*, 3717.

93. (a) ten Brinke, G.; Ruokolainen, J.; Ikkala, O. *Adv. Polym. Sci*., **2007**, *207*, 113.

(b) Serpe, M. J.; Craig, S. L. *Langmuir* **2007**, *23*, 1626.

94. Lehn, J. M. *Chem. Soc. Rev.* **2007**, *36*, 151.

95. (a) Armstrong, G.; Buggy, M. *J. Mater. Sci.*, **2005**, *40*, 547. (b) Aida, T.; Meijer, E. W.; Stupp, S. I. *Science* **2012**, *335*, 813.

96. Burattini, S.; Colquhoun, H. M.; Fox, J. D.; Friedmann, D.; Greenland, B. W.; Harris, P. J. F.; Hayes, W.; Mackay, M. E.; Rowan, S. J. *Chem. Commun.* **2009**, 6717.

97. (a) Whittell, G. R.; Hager, M. D.; Schubert, U. S.; Manners, I. *Nat. Mater.* **2011**, *10*, 176. (b) McKenzie, B. M.; Rowan, S. J. *Molecular Recognition and Polymers*, ed. Rotello, V. M.; Thayumanavan, S. John Wiley and Sons, Hoboken, NJ, **2008**, ch. 7, pp. 157. (c) Whittell, G. R.; Manners, I. *Adv. Mater.* **2007**, *19*, 3439.

98. Chiper, M.; Hoogenboom, R.; Schubert, U. S. *Macromol. Rapid Commun.* **2009**, *30*, 565.

99. (a) Pollino, J. M.; Weck, M. *Chem. Soc. Rev.* **2005**, *34*, 193. (b) Hammond, M. R.; Andreopoulou, A. K.; Pefkianakis, E.; Kallitsis, J. K.; Mezzenga, R. *Chem. Mater.* **2009**, *21*, 2169.

100. Weng, W.; Beck, J. B.; Jamieson, A. M.; Rowan, S. J. *J. Am. Chem. Soc*. **2006**, *128*, 11663.

101. Sievers, T. K.; Vergin, A.; Möhwald, H.; Kurth, D. G. *Langmuir* **2007**, *23*, 12179.

102. (a) Hoogenboom, R.; Schubert, U. S. *Chem. Soc. Rev.* **2006**, *35*, 622. (b) Payne, S. J.; Fiore, G. L.; Fraser, C. L.; Demas, J. N. *Anal. Chem.* **2010**, *82*, 917.

103. (a) Astruc, D.; Chardac, F. *Chem. Rev.* **2001**, *101*, 2991. (b) Astruc, D.; Boisselier, E.; Ornelas, C. *Chem. Rev.* **2010**, *110*, 1857.

104. (a) Meudtner, R. M.; Ostermeier, M.; Goddard, R.; Limberg, C.; Hecht, S. *Chem. Eur. J.* **2007**, *13*, 9834. (b) Meudtner, R. M.; Hecht, S. *Macromol. Rapid Commun*, **2008**, *29*, 347.

105. Lahn, B.; Rehahn, M. *Macromol. Symp.* **2001**, *163*, 157.

106. (a) Schmatloch, S.; van den Berg, A. M. J.; Alexeev, A. S.; Hofmeier, H.; Schubert, U. S. *Macromolecules* **2003**, *36*, 9943. (b) Schmatloch, S.; Gonzalez, M.F.; Schubert, U.S. *Macromol. Rapid Commun.* **2002**, *23*, 957. (c) Schubert, U.S.; Hien, O.; Eschbaumer, C. *Macromol. Rapid Commun.* **2000**, *21*,

1156. (d) Hofmeier, H.; Schmatloch, S.; Wouters, D.; Schubert, U.S. *Macromol. Chem. Phys.* **2003**, *204*, 2197. (e) Schmatloch, S.; Schubert, U. S. *Macromol. Symp.* **2003**, *199*, 483.

107. (a) Vermonden, T.; van Steenbergen, M. J.; Bessling, N. A. M.; Marcelis, A. T. M.; Hennink, W. E.; Sudhölter, E. J. R.; Cohen Stuart, M. A. *J. Am. Chem. Soc.* **2004**, *126*, 15802. (b) Vermonden, T.; van der Gucht, J.; de Waard, P.; Marcelis, A. T. M.; Bessling, N. A. M.; Sudhölter, E. J. R.; Fleer, G. J.; Cohen Stuart, M. A. *Macromolecules* **2003**, *36*, 7035.

108. Holliday, B. J.; Stanford, T. B.; Swager, T. M. *Chem. Mater.* **2006**, *18*, 5649.

109. Gasnier, A.; Royal, G.; Terech, P. *Langmuir* **2009**, *25*, 8751.

110. (a) Beck, J. B.; Rowan, S. J. *J. Am. Chem. Soc.* **2003**, *125*, 13922. (b) Weng, W.; Beck, J. B.; Jamieson, A. M.; Rowan, S. J. *J. Am. Chem. Soc*. **2006**, *128*, 11663. (c) Weng, W.; Li, Z.; Jamieson, A. M.; Rowan, S. J. *Macromolecules* **2009**, *42*, 236.

111. Kumpfer, J. R.; Rowan, S. J. *J. Am. Chem. Soc.* **2011**, *133*, 12866.

112. (a) Sivakova, S.; Bohnsack, D. A.; Mackay, M. E.; Suwanmala, P.; Rowan, S. J. *J. Am. Chem. Soc.* **2005**, *127*, 18202. (b) Fox, J. D.; Rowan, S. J. *Macromolecules* **2009**, *42*, 6823.

113. (a) Knapton, D.; Rowan, S. J. Weder, C. *Macromolecules* **2006**, *39*, 651. (b) Parameswar, K. I.; Beck, J. B.; Weder, C.; Rowan, S. J. *Chem. Commun.* **2005**, 319.

114. (a) Burnworth, M.; Mendez, J. D.; Schroeter, M.; Rowan, S. J.; Weder, C. *Macromolecules* **2008**, *41*, 2157. (b) Beck, J. B.; Kokil, A.; Ray, D.; Rowan, S. J.; Weder, C. *Macromolecules* **2002**, *35*, 590.

115. Lee, S. W.; Kumpfer, J. R.; Lin, P. A.; Li, G.; Gao, X. P. A.; Rowan, S. J.; Sankaran, R. M. *Macromolecules* **2012**, 45, 8201.

116. (a) Kumpfer, J. R.; Wie, J. J.; Swanson, J. P.; Beyer, F. L.; Mackay, M. l. E.; Rowan, S. J. *Macromolecules* **2012**, *45*, 473. (b) Zhao, Y.; Beck, J. B.; Rowan, S. J. Jamieson, A. M. *Macromolecules* **2004**, *37*, 3529.

117. (a) Fiore, G. L.; Rowan, S. J. Weder, C. *Chem. Soc. Rev.* DOI: 10.1039/c3cs35471g. (b) Burnworth, M.; Tang, L.; Kumpfer, J. R.; Duncan, A. J.; Beyer, F. L.; Fiore, G. L.; Rowan, S. J.; Weder, C. *Nature* **2011**, *472*, 334.

118. Shunmugam, R.; Tew, G. N. *J. Am. Chem. Soc.* **2005**, *127*, 13567.

119. Shunmugam, R.; Tew, G.N. *Macromol. Rapid Commun.* **2008**, *29*, 1355.

120. Shunmugam, R.; Tew, G. N. *Polym. Adv. Technol.* **2008**, DOI: 10.1002/pat.1115.

121. Maier, A.; Rabindranath, A. R.; Tieke, B. *Chem. Mater.* **2009**, *21*, 3668.

122. Maier, A.; Cheng, K.; Savych, J.; Tieke, B.; *ACS Appl. Mater. Interfaces* **2011**, *3*, 2710.

123. Maier, A.; Tieke, B. *J. Phys. Chem. B* **2012**, *116*, 925.

124. Welterlich, I.; Tieke, B. *Macromolecules* **2011**, *44*, 4194.

125. (a) Morgan, S.G.; Burstall, F.H. *J. Chem. Soc.* **1931**, 20. (b) Morgan, S.G.; Burstall, F.H. *J. Chem. Soc.* **1937**, 1649.

126. (a) Schubert, U.S.; Eschbaumer, C. *Angew. Chem. Int. Ed.* **2002**, *41*, 2892. (b) Chiper, M.; Hoogenboom, R.; Schubert, U.S. *Macromol. Rapid. Commun.* **2009**, *30*, 565. (c) Kurth, D.G.; Higuchi, M. *Soft Matter* **2006**, *2*, 915. (d) Friese, V.A.; Kurth, D.G. *Coord. Chem. Rev.* **2008**, *252*, 199.

127. (a) Merer, M.A.R.; Lohmerjer, B.G.G.; Schubert, U. S. *Macromol. Rapid Commun.* **2003**, *24*, 852. (b) Chiper, M.; Meier, M. A. R.; Wouters, D.; Hoeppener, S.; Fustin, C.; Gohy, J. Schubert, U. S. *Macromolecules* **2008**, *41*, 2771. (c) Chiper, M.; Meier, M. A. R.; Kranenburg, J. M.; Schbert, U. S.

Macromol. Chem. Phys. **2007**, *208*, 679. (d) Raşa, M.; Lohmeijer, B. G. G.; Hofmeier, H.; Thijs, H. M. L.; Schubert, D.; Schubert, U. S.; Tziatzios, C. *Macromol. Chem. Phys.* **2006**, *207*, 2029.

128. (a) D'Andrade, B. W.; Forrest, S. R. *Adv. Mater*. **2004**, *16*, 1585. (b) Liu, Y.; Nishiura, M.; Wang, Y.; Hou, Z. *J. Am. Chem. Soc.* **2006**, *128*, 5592.

129. Huang, F.; Shih, P.-I.; Shu, C.-F.; Chi, Y.; Jen, A. K.-Y. *Adv. Mater*. **2009**, *21*, 361.

130. Tsai, M. L.; Liu, C. Y.; Hsu, M. A.; Chow, T. J. *Appl. Phys. Lett.* **2003**, *82*, 550.

131. (a) Shih, P. I.; Tseng, Y. H.; Wu, F. I.; Dixit, A. K.; Shu, C. F. *Adv. Funct. Mater.* **2006**, *16*, 1582. (b) Granstrom, M.; Inganas, O.; *Appl. Phys. Lett.* **1996**, *68*, 147. (c) Shim, H. K.; Kang, I. N.; Jang, M. S.; Zyung, T.; Jung, S. D. *Macromolecules* **1997**, *30*, 7749. (c) Xin, Y.; Wen, G. A.; Zeng, W. J.; Zhao, L.; Zhu, X. R.; Fan, Q. L.; Feng, J. C.; Wang, L. H.; Wei, W.; Peng, B.; Cao, Y.; Huang, W. *Macromolecules* **2005**, *38*, 6755.

132. (a) Tu, G. L.; Mei, C. Y.; Zhou, Q. G.; Cheng, Y. X.; Geng, Y. H.; Wang, L. X.; Ma, D. G.; Jing, X. B.; Wang, F. S. *Adv. Funct. Mater.* **2006**, *16*, 101. (b) Liu, J.; Zhou, Q. G.; Cheng, Y. X.; Geng, Y. H.; Wang, L. X.; Ma, D. G.; Jing, X. B.; Wang, F. S. *Adv. Funct. Mater.* **2006** , *16*, 957. (c) Liu, J.; Xie, Z. Y.; Cheng, Y. X.; Geng, Y. H.; Wang, L. X.; Jing, X. B.; Wang, F. S. *Adv. Mater.* **2007**, *19*, 531. (d) Guo, X.; Qin, C. J.; Cheng, Y. X.; Xie, Z. Y.; Geng, Y. H.; Jing, X. B.; Wang, F. S.; Wang, L. X. *Adv. Mater.* **2009**, *21*, 3682. (e) Park, M. J.; Lee, J.; Park, J. H.; Lee, S. K.; Lee, J. I.; Chu, H. Y.; Hwang, D. H.; Shim, H. K. *Macromolecules* **2008**, *41*, 3063 .

133. Liu, J.; Zhou, Q. G.; Cheng, Y. X.; Geng, Y. H.; Wang, L. X.; Ma, D. G.; Jing, X. B.; Wang, F. S. *Adv. Mater.* **2005**, *17*, 2974.

134. Jiang, J. X.; Xu, Y. H.; Yang, W.; Guan, R.; Liu, Z. Q.; Zhen, H. Y.; Cao, Y. *Adv. Mater.* **2006**, *18*, 1769.

135. Xu, Y. H.; Guan, R.; Jiang, J. X.; Yang, W.; Zhen, H. Y.; Peng, J. B.; Cao, Y. *J. Polym. Sci. Polym. Chem.* **2008**, *46*, 453.

136. (a) Zhen, H. Y.; Xu, W.; King, W.; Chen, Q. L.; Xu, Y. H.; Jiang, J. X.; Peng, J. B.; Cao, Y.; *Macromol. Rapid. Comm.* **2006**, *27*, 2095. (b) Park, M. J.; Kwak, J.; Lee, J.; Jung, I. H.; Kong, H.; Lee, C.; Hwang, D. H.; Shim,H. K. *Macromolecules* **2010**, *43*, 1379.

137. Cambi, L.; Szegö, L. *Ber. Dtsch. Chem. Ges. (A and B Series)* **1931**, *64*, 2591. (b) Cambi, L.; Szegö, L. *Dtsch. Chem. Ges. (A and B Series)* **1933**, *66*, 656. (c) Cambi, L.; Malatesta, L. *Ber. Dtsch. Chem. Ges. (A and BSeries)* **1937**, *70*, 2067.

138. (a) Ballhausen, C. J. *Introduction to Ligand Field Theory*, McGraw-Hill, New York, **1962**. (b) Schläfer,H. L.; Gliemann, G. *Einführung in die Ligandenfeldtheorie*, Akademische Verlagsgesellschaft, Frankfurt/Main,**1967**.

139. (a) Hauser, A. *Top. Curr. Chem.* **2004**, *233*, 49 (Eds.: P. Gütlich, H. A. Goodwin). (b) Gütlich, P.; Hauser, A.; Spiering, H. *Angew. Chem.* **1994**, *106*, 2109; *Angew. Chem. Int. Ed. Engl.* **1994**, *33*, 2024.

140. Garcia, Y.; Gütlich, P. *Top. Curr. Chem.* **2004**, *234*, 49 (Eds.: P. Gütlich, H. A. Goodwin).

141. Chandrasekhar, N.; Chandrasekar, R. *Dalton Trans.* **2010**, 39, 9872.

142. Stoufer, R. C.; Busch, D. H.; Hadley, W. B. *J. Am. Chem. Soc.* **1961**, *83*, 3732.

143. Sacconi, L. *Coord. Chem. Rev.* **1972**, *8*, 351.

144. König, E. *Coord. Chem. Rev.* **1968**, *3*, 471.

145. Goodwin, H. A. *Coord. Chem. Rev.* **1976**, *18*, 293.

146. Rajadurai, C.; Schramm, F.; Brink, S.; Fuhr, O.; Ghafari, M.; Kruk. R.; Ruben, M. *Inorg. Chem.*, **2006**, *45*, 10019.

147. González-Prieto, R.; Fleury, B.; Schramm, F.; Zoppellaro, G.; Chandrasekar, R.; Fuhr, O.; Lebedkin, S.; Kappes, M.; Ruben, M. *Dalton Trans.* **2011**,*40*, 7564.

148. Hauser, A. *Chem. Phys. Lett.* **1986**, *124*, 543. b) Hauser, A. *Coord. Chem. Rev.* **1991**, *111*, 275.

149. Bousseksou, A.; Tommasi, L.; Lemercier, G.; Varret, F.; Tuchagues, J. P. *Chem. Phys. Lett.* **1995**, *243*, 493.

150. (a) Drickamer, H. G.; Frank, C. W. *Electronic Transitions and the High Pressure Chemistry and Physics of Solids*, Wiley, New York, **1973**. (b) Drickamer, H. *Angew. Chem.* **1974**, *86*, 61; *Angew. Chem. Int. Ed. Engl.* **1974**, *13*, 39. (c) Bousseksou, A.; Molnar, G.; Matouzenko, G. *Eur. J. Inorg. Chem.* **2004**, 4353. (d) Ksenofontov, V.; Gaspar, A. B.; Gütlich, P. *Top. Curr. Chem.* **2004**, *235*, 23 (Eds.: P. Gütlich, H. A. Goodwin). (e) Real, J. A.; Gaspar, A. B.; Munoz, M. C. *Dalton Trans.* **2005**, 2062.

151. a) Decurtins, S.; Gütlich, P.; Köhler, C. P.; Spiering, H.; Hauser, A. *Chem. Phys. Lett.* **1984**, *105*, 1. b) Decurtins, S.; Gütlich, P.; Hasselbach, K. M.; Hauser, A.; Spiering, H. *Inorg. Chem.* **1985**, *24*, 2174.

152. a) Hauser, A. *Chem. Phys. Lett.* **1986**, *124*, 543; b) Hauser, A. *Coord. Chem. Rev.* **1991**, *111*, 275.

153. Hauser, A. *Top. Curr. Chem.* **2004**, *234*, 155 (Eds.: P. Gütlich, H. A. Goodwin).

154. Renz, F.; Spiering, H.; Goodwin, H. A.; Gütlich, P. *Hyperfine Interact.* **2000**, *126*, 155.

155. Varret, F.; Boukheddaden, K.; Codjovi, E.; Enachescu, C.; Linares, J. *Top. Curr. Chem.* **2004**, *234*, 199 (Eds.: P. Gütlich, H. A. Goodwin).

156. Vanko, G.; Renz, F.; Molnar, G.; Neisius, T.; Karpati, S. *Angew. Chem.* **2007**, *119*, 5400; *Angew. Chem. Int. Ed.* **2007**, *46*, 5306.

157. Renz, F.; Vanko, G.; Homenya, P.; Saadat, R.; Nemeth, Z.; Huotari, S. *Eur. J. Inorg. Chem.* **2012**, 2653.

158. Gütlich, P. *Top. Curr. Chem.* **2004**, *234*, 231 (Eds.: Gütlich, P.; Goodwin, H. A.).

159. Gopakumar, T. G.; Matino, F.; Naggert, H.; Bannwarth, A.; Tuczek, F.; Berndt, R. *Angew. Chem.* **2012**, *124*, 6367.; *Angew. Chem. Int. Ed.* **2012**, *51*, 6262.

160. Boillot, M. L.; Zarembowitch, J.; Sour, A. *Top. Curr. Chem.* **2004**, *234*, 261 (Eds.: Gütlich, P.; Goodwin, H. A.).

161. Meded, V.; Bagrets, A.; Fink, K.; Chandrasekar, R.; Ruben, M.; Evers, F.; Bernand-Mantel, A.; Seldenthuis, J. S.; Beukman, A.; van der Zant, H. S. *J. Physical Review B* **2011**, *83*, 245415.

162. Kahn, O.; Martinez, C. J. *Science* **1998**, *279*, 44.

163. (a) Cobo, S.; Molnar, G.; Real, J. A.; Bousseksou, A. *Angew. Chem.* **2006**, *118*, 5918; *Angew. Chem. Int. Ed.* **2006**, *45*, 5786. (b) Bodenthin, Y.; Pietsch, U.; Möhwald, H.; Kurth, D. G. *J. Am. Chem. Soc.* **2005**, *127*, 3110. (c) Rubio, M.; Hernandez, R.; Nogales, A.; Roig, A.; Lopez, D. *Eur. Polym. J.* **2011**, *47*, 52.

164. (a) Roubeau, O.; Colin, A.; Schmitt, W.; Clerac, R. *Angew.Chem.* **2004**, *116*, 3345; *Angew. Chem. Int. Ed.* **2004**, *43*, 3283. (b) Matsukizono, H.; Kuroiwa, K.; Kimizuka, N. *J. Am. Chem. Soc.* **2008**, *130*, 5622. d) Rubio, M.; Lopez, D. *Eur. Polym. J.* **2009**, *45*, 3339. e) Grondin, P.; Roubeau, O.; Castro, M.; Saadaoui, H.; Colin, A.; Clerac, R. *Langmuir* **2010**, *26*, 5184.

165. a) Thibault, C.; Molnar, G.; Salmon, L.; Bousseksou, A.; Vieu, C. *Langmuir* **2010**, *26*, 1557. b) Cavallini, M.; Bergenti, I.; Milita, S.; Kengne, J. C.; Gentili, D.; Ruani, G.; Salitros, I.; Meded, V.; Ruben, M. *Langmuir* **2011**, *27*, 4076. c) Faulmann, C.; Chahine, J.; Malfant, I.; de Caro, D.; Cormary, B.; Valade, L. *Dalton Trans.* **2011**, *40*, 2480. d) Martinez, V.; Boldog, I.; Gaspar, A. B.; Ksenofontov, V.; Bhattacharjee, A.; Gutlich, P.; Real, J. A. *Chem. Mater.* **2010**, *22*, 4271. e) Galan-Mascaros, J. R.; Coronado, E.; Forment-Aliaga, A.; Monrabal-Capilla, M.; Pinilla-Cienfuegos, E.; Ceolin, M. *Inorg. Chem.* **2010**, *49*, 5706. f) Boldog, I.; Gaspar,

A. B.; Martinez, V.; Pardo-Ibanez, P.; Ksenofontov, V.; Bhattacharjee, A.; Gutlich, P.; Real, J. A. *Angew. Chem.* **2008**, *120*, 6533; *Angew. Chem. Int. Ed.* **2008**, *47*, 6433.

166. Hayami, S.; Hashiguchi, K.; Juhasz, G.; Ohba, M.; Okawa, H.; Maeda, Y.; Kato, K.; Osaka, K.; Takata, M.; Inoue, K. *Inorg. Chem.* **2004**, *43*, 4124.

167. a) Murray, K. S.; Kepert, C. J. *Top. Curr. Chem.* **2004**, *233*, 195 (Eds.: Gütlich, P.; Goodwin, H. A.). b) Horike, S.; . Shimomura, S.; Kitagawa, S. *Nat. Chem.* **2009**, *1*, 695.

168. Gaspar, A. B.; Ksenofontov, V.; Seredyuk, M.; Gütlich, P. *Coord. Chem. Rev.* **2005**, *249*, 2661.

169. (a) Hayami, S.; Danjobara, K.; Inoue, K.; Ogawa, Y.; Matsumoto, N.; Maeda, Y. *Adv. Mater.* **2004**, *16*, 869. b) Hayami, S.; Motokawa, N.; Shuto, A.; Masuhara, N.; Someya, T.; Ogawa, Y.; Inoue, K.; Maeda, Y.; *Inorg. Chem.* **2007**, *46*, 1789. c) Hayami, S.; Moriyama, R.; Shuto, A.; Maeda, Y.; Ohta, K.; Inoue, K.; *Inorg. Chem.* **2007**, *46*, 7692.

170. (a) Nihei, M.; Sekine, Y.; Suganami, N.; Nakazawa, K.; Nakao, A.; Nakao, H.; Murakami, Y.; Oshio, H. *J. Am. Chem. Soc.* **2011**, *133*, 3592. (b) Mahfoud, T.; Molnar, G.; Cobo, S.; Salmon, L.; Thibault, C.; Vieu, C.; Demont, P.; Bousseksou, A. *Appl. Phys. Lett.* **2011**, 99. c) Dorbes, S.; Valade, L.; Real, J. A.; Faulmann, C. *Chem. Commun.* **2005**, 69.

171. Salmon, L.; Molnar, G.; Zitouni, D.; Quintero, C.; Bergaud, C.; Micheau, J. C.; Bousseksou, A. *J. Mater. Chem.* **2010**, *20*, 5499.

172. Moreau, W. M. *Semiconductor Lithography: Principles and Materials*; Plenum: New York, **1988**.

173. *Handbook of Microlithogrpahy, Micromachining and Microfabrication*; Choudhury, P., Ed.; SPIE Optical Engineering Press: Bellingham, WA, **1997**.

174. (a) Rai-Choudhury, P ed. **1997**. *Handbook of Microlithography, Micromachining, and Microfabrication.* Bellingham,WA: SPIE Opt. Engineer. Press. Vol. 1, (b) Levenson, MD. **1995**. *Solid State Technol.* February:57-66.

175. (a) Pease RFW. **1992**. *J. Vac. Sci. Technol. B 10*, 278–85. (b) Cerrina, F.; Marrian, C. **1996**. *Mater. Res.Soc. Bull.* XXI, No. 12, 56–62.

176. Kumar, A.; Whitesides. G. M. *Appl. Phys. Lett.* **1993**, *63*, 2002.

177. Xia, Y.; Kim, E.; Zhao, X-M.; Rogers, J. A.; Prentiss, M.; Whitesides, G. M. *Science* **1996**, *273*, 347.

178. Zhao, X-M.; Xia, Y.; Whitesides, G. M. *Adv. Mater.* **1996**, *8*, 837.

179. (a) *Annu. Rev. Mater. Res.* **2004**, *34,* 339. (b) Kim, E.; Xia, Y.; Whitesides, G. M. *Nature* **1995**, *376*, 581.

180. Kim, E.; Xia, Y.; Zhao, X-M.; Whitesides, G. M. *Adv. Mater.* **1997**, *9*, 651.

181. (a) Masuda, H.; Fukuda, K.; *Science* **1995**, *268*, 1446. (b) Hoyer, P. *Adv. Mater.***1996**, *8*, 857. (c) Huber, T. E.; Luo, L. *Appl. Phys. Lett.* **1997**, *70*, 2502.

182. Xia, Y.; Tien, J.; Qin, D.; Whitesides, G. M. *Langmuir* **1996**, *12*, 4033.

183. Kumar, A.; Whitesides, G. M. *Appl. Phys. Lett.***1993**, *63*, 2002.

184. Xia, Y.; Tien, J.; Qin, D.; Whitesides, G. M. *Langmuir* **1996**. *12*, 4033.

185. (a) Xia, Y.; Tien, J.; Qin, D.; Whitesides, G. M. *Langmuir* **1996**, *12*, 4033. (b) Wilbur, J. L.; Kim. E.; Xia, Y.; Whitesides, G. M. *Adv. Mater.* **1995**, *7*, 649.

186. Xia, Y.; Rogers, J. A.; Paul, K. E.; Whitesides, G. M. *Chem. Rev.* **1999**, *99,* 1823.

187. (a) Xia, Y.; Kim, E.; Zhao, X.-M.; Rogers, J. A.; Prentiss, M.; Whitesides, G. M. *Science* **1996**, *273*, 347.

(b) Xia, Y.; McClelland, J. J.; Gupta, R.; Qin, D.; Zhao, X. M.; Sohn, L. L.; Celotta, R. J.; Whitesides, G. M. *Adv. Mater.* **1997**, *9*, 147.

188. Hua, F.; Sun, Y.; Gaur, A.; Meitl, M.; Bilhaut, L.; Rotkina, L.; Wang, J. F.; Geil, P.; Shim, M.; Rogers, J. A.; Shim, A. *Nano Lett.* **2004**, *4*, 2467.

189. Xu, Q.; Mayers, B.; Lahav, M.; Vezenov, D. V.; Whitesides, G. M. *J. Am. Chem. Soc.* **2005**, *127*, 854.

190. (a) Terris, B. D.; Mamin, H. J.; Best, M. E.; Logan, J. A.; Rugar, D. *Appl. Phys. Lett.* **1996**. *69*, 4262.

191. Hutley, M. C. *Diffraction Gratings.*New York: Academic, **1982**.

192. Nakano, M.; Nishida, N.; *Appl. Opt.* **1979**, *18*, 3073.

193. Kiewit, D. A. *Rev. Sci. Instrum.* **1973**, *44*, 1741.

194. (a) Zhao, X-M.; Smith, S. P.; Waldman, S. J.; Whitesides, G. M.; Prentiss, M. *Appl. Phys. Lett.* **1997**, *71*, 1017. (b) Zhao, X-M.; Xia, Y.; Whitesides, G. M. *Adv. Mater.* **1996**. *8*, 837.

195. Thibault, C.; Molnar, G.; Salmon, L.; Bousseksou. A.; Vieu, C. *Langmuir*, **2010**, *26*, 1557.

196. Xia, Y.; Kim , E.; Whitesides, G. M. *Chem. Mater.* **1996**. *8*, 1558.

197. Emmelius, M.; Pawlowski, G.; Vollmann, H. W. *Angew. Chem. Int. Ed.* **1989**, *28*, 1445.

198. Chou, S. Y.; Krauss, P. R.; Renstrom, P. J. *Science* **1996**, *272*, 85. (b) Chou, S. Y.; Krauss, P. R.; Renstrom, P. J. *Appl. Phys. Lett.* **1995**, *67*, 3114.

199. (a) Chou, S. Y.; Krauss, P. R.; Renstrom, P. J. *Appl. Phys. Lett.* **1995**, *67,* 3114. (b) Chou, S. Y.; Krauss, P. R.; Renstrom, P. J. *Science* **1996**, *272*, 85.

200. McAlpine, M. C.; Friedman, R. S.; Lieber, D. M. *Nano Lett.* **2003**, *3*, 443.

201. Cedeno, C. C.; Seekamp, J.; Kam, A. P.; Hoffmann, T.; Zankovych, S.; Torres, C. M. S.; Menozzi, C.; Cavallini, M.; Murgia, M.; Ruani, G.; Biscarini, F.; Behl, M.; Zentel, R.; Ahopelto, J. *Microelectron. Eng.* **2002**, *61*, 25. (b) Li, D.; Guo, L. J.; *Appl. Phys. Lett.* **2006**, *88*, 513.

202. Guo, L. J.; Krauss, P. R.; Chou, S. Y. *Appl. Phys. Lett.* **1997**, *71*, 1881. (b) Zhang, W.; Chou, S. Y. *Appl. Phys. Lett.* **2003**, *83*, 1632.

203. Macintyre, D. S.; Chen, Y.; Gourlay, D.; Boyd, E.; Moran, D.; Cao, X.; Elgaid, K.; Stanley, C. R.; Thayne, I.; Thoms, S. *J. Vac. Sci. Technol. B* **2003**, *21*, 2783.

204. Guo, L. J.; Cheng, X.; Chao, C. Y. *J. Mod. Opt.* **2002**, *49*, 663.

205. Cheng, X.; Hong, Y. T.; Kanicki, J.; Guo, L. J. *J. Vac. Sci. Technol. B* **2002**, *20*, 2877. (b) Kao, P. C.; Chu, S. Y.; Chen, T. Y.; Zhan, C. Y.; Hong, F. C.; Chang, C. Y.; Hsu, L. C.; Liao, W. C.; Hon, M. H. *IEEE Trans. Electron Devices* **2005**, *52*, 1722.

206. Chou, S. Y. *Proc. IEEE* **1997**, *85*, 652. (b) Wu, W.; Cui, B.; Sun, X. Y.; Zhang, W.; Zhuang, L.; Kong, L. S.; Chou, S. Y. *J. Vac. Sci. Technol. B* **1998**, *16*, 3825.

207. (a) Martin, J. I.; Nogues, J.; Liu, K.; Vicent, J. L.; Schuller, I. K. *J. Magn. Magn. Mater.* **2003**, *256*, 449. (b) Glinsner, T.; Hangweier, P.; Luesebrink, H.; Dorsey, P.; Homola, A.; Wachenschwanz, D. *Solid State Technol.* **2005**, *48*, 51. (c) McClelland, G. M.; Hart, M. W.; Rettner, C. T.; Best, M. E.; Carter, K. R.; Terris, B. D. *Appl. Phys. Lett.* **2002**, *81*, 1483.

208. Rogers, J. A.; Bao, Z.; Dhar, L. *Appl. Phys. Lett.* **1998**, *73*, 294.

209. (a) Kumar, A.; Biebuyck, H. A.; Whitesides, G. M. *Langmuir* **1994**, *10*, 1498. (b) Wilbur, J. L.; Kumar, A.; Biebuyck, H. A.; Kim, E.; Whitesides, G. M. *Nanotechnology* **1996**, *7*, 452.

210. Biebuyck, H. A.; Whitesides, G. M. *Langmuir* **1994**, *10*, 2790.

211. (a) Wilbur, J. L.; Kumar, A.; Kim, E.; Whitesides, G. M. *Adv. Mater*. **1994**, *6*, 600. (b) Loo, Y. L.; Willett, R. L.; Baldwin, K. W.; Rogers, J. A. *Appl. Phys. Lett.* **2002**, *81*, 562.

212. (a) Ghosh, P.; Lackowski, W. M.; Crooks, R. M. *Macromolecules* **2001**, *34*, 1230. (b) Arrington, D.; Curry, M.; Street, S. C. *Langmuir* **2002**, *18*, 7788.

213. (a) Lange, S. A.; Benes, V.; Kern, D. P.; Horber, J. K. H.; Bernard, A. *Anal. Chem*. **2004**, *76*, 1641. (b) Thibault, C.; Berre, V. L.; Casimirius, S.; Trevisiol, E.; Francois, J.; Vieu, C. *J. Nanobiotechnol.* **2005**, *3*, 7.

214. (a) James, C. D.; Davis, R. C.; Kam, L.; Craighead, H. G.; Isaacson, M.; Turner, J. N.; Shain, W. *Langmuir* **1998**, *14*, 741. (b) Bernard, A.; Delamarche, E.; Schmid, H.; Michel, B.; Bosshard, H. R.; Biebuyck, H. *Langmuir* **1998**, *14*, 2225.

215. (a) Mrksich, M.; Dike, L. E.; Tien, J.; Ingber, D. E.; Whitesides, G. M. *Exp. Cell Res.* **1997**, *235*, 305. (b) Singhvi, R.; Kumar, A.; Lopez, G. P.; Stephanopoulos, G. N.; Wang, D. I. C.; Whitesides, G. M.; Ingber, D. E. *Science* **1994**, *264*, 696.

216. Kim, T -H.; Cho, K-S.; Lee, E. K.; Lee, S. J.; Chae, J.; Kim, J. W.; Kim, D. Hwan.; K, J-Y.; Amaratunga, G.; Lee, S. Y.; Choi, B. Y.; Kuk, Y.; Kim, J. M. Kim, K. *Nature Photonics*, **2011**, *5*, 176.

217. Granlund, T.; Nyberg,T.; Roman, L. S.; Svensson, M.; Inganäs, O. *Adv. Mater.* **2000**, *12*, 269.

218. Miller, M. S.; Filiatrault, H. L.; Davidson, G. J. E.; Luo, M.; Carmichael, T. B. *J. Am. Chem. Soc.* **2010**, *132*, 765.

219. Gassensmith, J. J.; Erne, P. M.; Paxton, W. F. ; Frasconi, M.; Donakowski, M. D.; Stoddart, J. F. *Adv. Mater.* **2013**, *25*, 223.

220. Gassensmith, J. J.; Erne, P. M.; Paxton, W. F. ; Valente, C.; Stoddart, J. F. *Langmuir*, **2011**, *27*, 1341.

221. Jeon, S.; Menard, E.; Park, J-U.; Maria, J.; Meitl, M.; Zaumseil, J.; Rogers, J. A. *Adv. Mater.* **2004**, *16,* 1369.

222. (a) Loo, Y-L.; Willett, R. L.; Baldwin, K. W.; Rogers, J. A. *J. Am. Chem. Soc.* **2002**, *124*, 7654. (b) Childs, W. R.; Nuzzo, R. G.; *J. Am. Chem. Soc.* **2002**, *124*, 13583.

2

Micro-Patterning of Metallo-Supramolecular Polymers: Syntheses of Back-to-back Coupled Octylated 2,6-Bis(pyrazol-1-yl)pyridines Ligands and Their Solution Processable 1-D Zn(II) Coordination Polymers

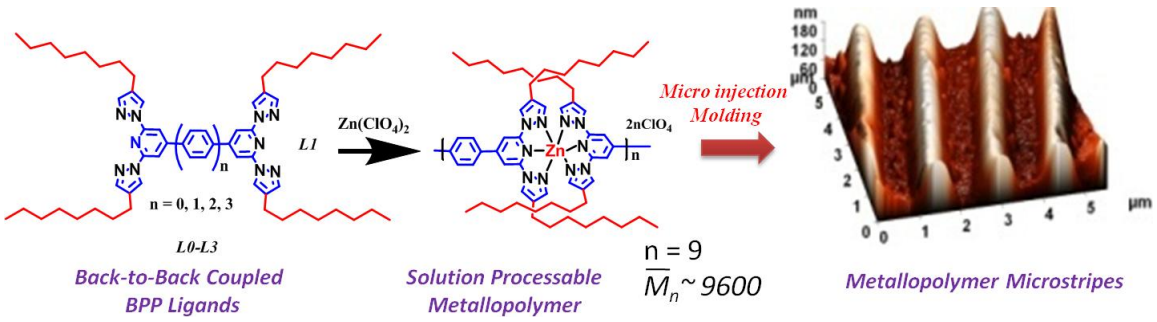

*This chapter is adapted from:

i) S. Basak, P. Hui, R. Chandrasekar* *Synthesis*, **2009,** *23*, 4042.
ii) S. Basak, P. Hui, S. Boodida and R. Chandrasekar*
J. Org. Chem. **2012,** *77*, 3620.

2.1 Abstract

*This chapter presents a ten-step synthetic route for the preparation of a series of new back-to-back coupled 2,6-bis(pyrazol-1-yl)pyridine (BPP) ligands (**L0**-**L3**) decorated with tetra-octyl chains. Ligand **L1** self-assemble with Zn^{2+} ion forming a highly soluble metallo-supramolecular polymer $[\mathbf{L1}\cdot Zn(ClO_4)_2]_n$ with a number average molecular weight ($\overline{M_n}$) ~ 9600 g/mol. To demonstrate the processability of $[\mathbf{L1}\cdot Zn(ClO_4)_2]_n$ by following a "top-down" approach periodic one dimensional fluorescent micro-stripes were fabricated on a glass substrate.*

2.2 Introduction

The design and synthesis of heterocyclic tridentate ligand molecules have attracted significant attention in recent years due to their imperative role they play in biology, medicine, chemistry, materials science, nano science and technology.[1-9,13] Particularly, the challenge lies in the synthesis of novel heterocyclic ditopic ligand molecules which can form metallo-supramolecular polymers (MSPs) having good solubility and high molecular weight. To obtain better solution processability for practical device applications, mostly MSPs were synthesized by using appropriate combination of ligands, counter ions and organic polymeric units into the main or side chain of the polymers. Typically, modified benzimidazole[2], terpyridine[3-6] and bistriazolylpyridine[7,8] type ligands were exploited for this purpose.

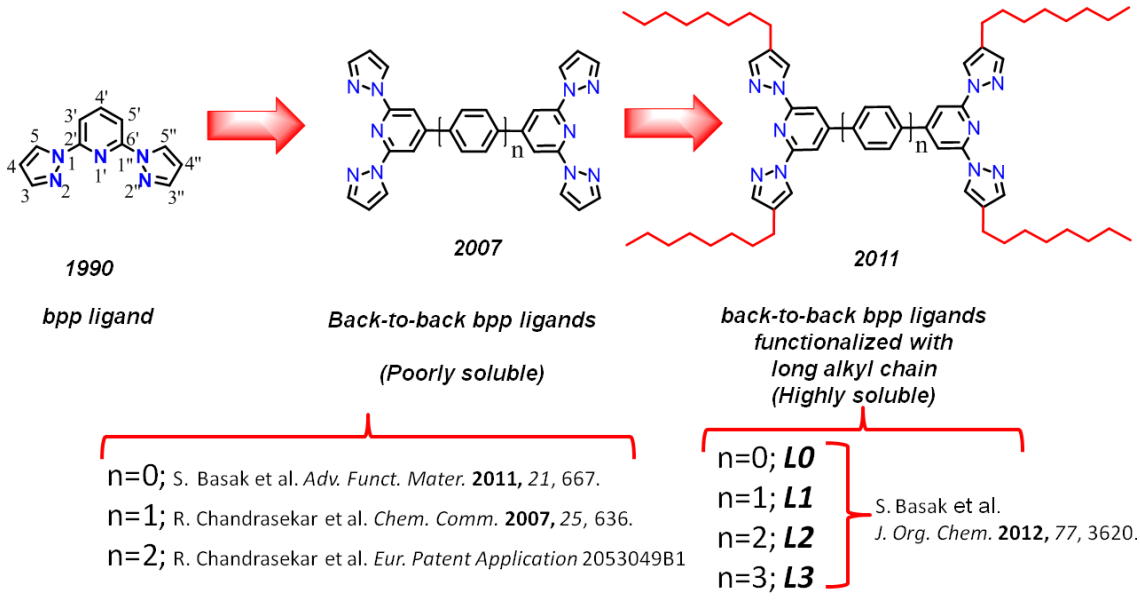

A recent addition to the club of functional MSPs is derived from *back-to-back* coupled 2,6-bis(pyrazolyl)pyridine (bpp)[9,10] molecule. *Back-to-back* coupled BPP forms magnetically bistable spin crossover 1-D MSP with iron(II) ions having spin cross-over temperature $T_{1/2}$ ~ 323 K.[9a] But unfortunately the obtained low molecular weight (*m/z* = 1518.5, n = 5) MSP is not processable for any device fabrication due to its poor solubility in most of the organic solvents. In this context, the design and synthesis of alkylated ditopic BPP ligands for the preparation of solution processable MSPs is necessary for a straightforward device fabrication. In this chapter, our novel synthetic methodology to access a series of π-conjugated *back-to-back* coupled octylated BPP ligands ***L0-L3*** connected by different aromatic spacers [no bridging unit (***L0***), with phenyl (***L1***), with biphenyl (***L2***) and with terphenyl (***L3***) bridging units, respectively]will be presented. Additionally to demonstrate the use of these highly soluble ligands, a well soluble 1-D MSP [***L1***•$Zn(ClO_4)_2]_n$ having molecular weight ($\overline{M_n}$) ~ 9,600 g/mol from ***L1*** and Zn^{2+} ion was prepared. By following a top-down approach, by utilizing the good solubility of [***L1***•$Zn(ClO_4)_2]_n$ in many organic solvents, several millimeters long of micro-strips of width in the range of 600-700 nm was fabricated by using a *micro-inject molding technique*. The MSP micro-strip pattern was characterized by using field emission scanning electron microscopy (FESEM), atomic force microscopy (AFM) and Raman imaging/spectroscopy.

2.3 Results and Discussion

2.3.1 Synthesis of Octylated Ditopic Ligands:

For the synthesis of ***L0-L3*** molecules, a novel ten-step synthetic protocol from the low-priced citrazinic acid was developed (Scheme 2.2). Citrazinic acid was transformed into 2,6-dichloroisonicotinicacidmethyl ester **2** as per our reported procedure.[10,11] Compound **2** upon reaction with potassium metal in diglyme leads to the formation of mono and bis pyrazolyl acid **3** and **4**. The white colour crude mixture (**3** and **4**) was not isolable by columnn chromatography, so it was converted to its mono and diethyl esters **5** and **6,** respectively. The mixture of mono and diethyl ester was seperated over column chromatography using 92:8 hexane/EtOAc mixture. Compound **6** was subsequently converted into **7** as per our previous reported procedure.[10] Attachment of 1-octyne to the 4 and 4″-carbons of the pyrazole unit in

bpp of **7** was successfully carried out under Sonogashira cross coupling (Scheme 2.1)

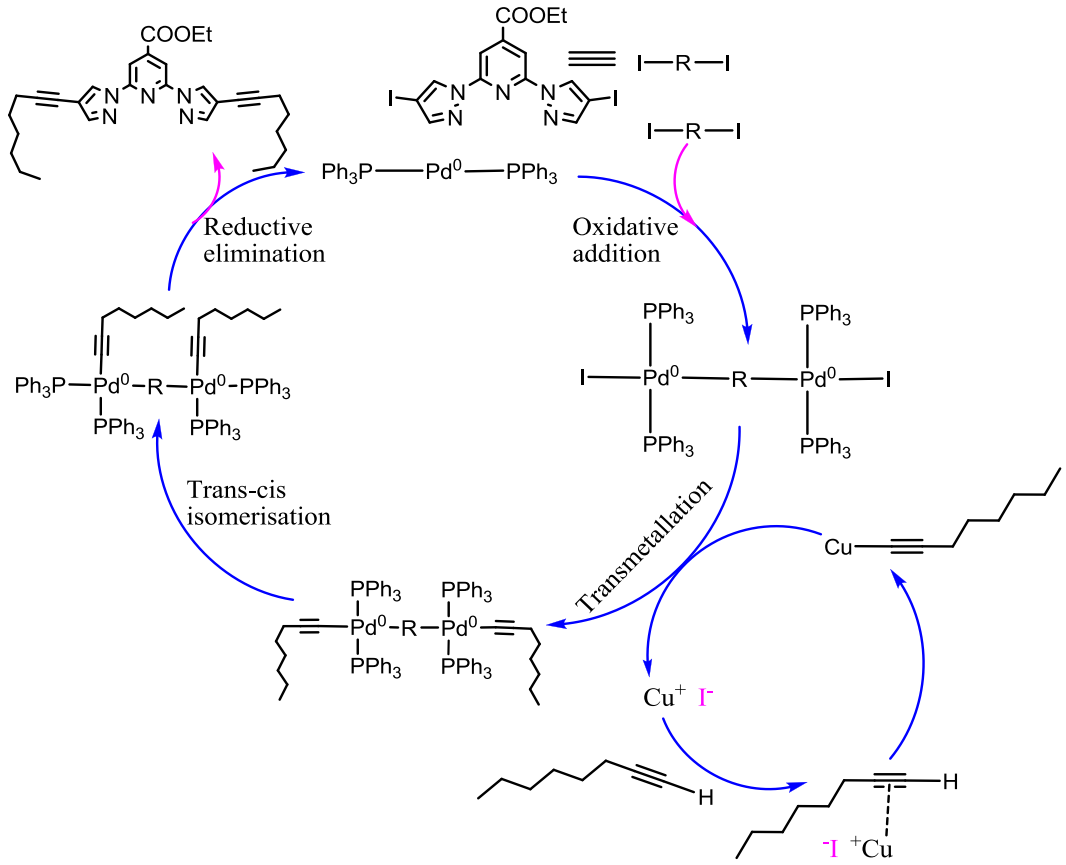

Scheme 2.1 Mechanism of Sonogashira-Hagihara Coupling.

conditions to get **8** in 82% yield (scheme 2.2). The alkyne groups in **8** was reduced using Pd/C, under H_2 atmosphere to get highly souble 2,6-dioctyl precursor **9** in a very good 99% yield. The saponification reaction quantitatively converted compound **9** into its carboxylic acid derivative **10** in 98% yield. Furthermore sequential conversion of the carboxylic acid **10** into acyl azide followed by a thermal Curtius rearrangement and succeeding hydrolysis of the trifluoroacetamide provided the amino derivative **11** in 78% yield. From this compound **11**, a key intermediate dioctylated 4-iodo bpp derivative **12** was synthesized in a modest 34% yield by using isoamylnitrite in presence of KI and I_2. Treatment of compound **12** with bispinacalato diboron under Suzuki cross-coupling condition formed a directly *back-to-back* coupled dioctylated bpp ***L0*** in a decent 72% yield. Similarly, Suzuki cross-coupling reactions of compound **12** with 1,4-phenyldiboronicacid, 4,4′-biphenyldiboronicacid and 4,4″-triphenyldiboronicacid provided the other target molecules ***L1***, ***L2*** and ***L3***, respectively in *ca*. 70-90% yield. Earlier, an alternative unsuccessful route towards ***L0-L3*** was undertaken (scheme 2.3). In this route, saponification of **8** yielded 90% of **13**, which upon subsequent Curtius rearrangement converted the alkyne bonds to carb-

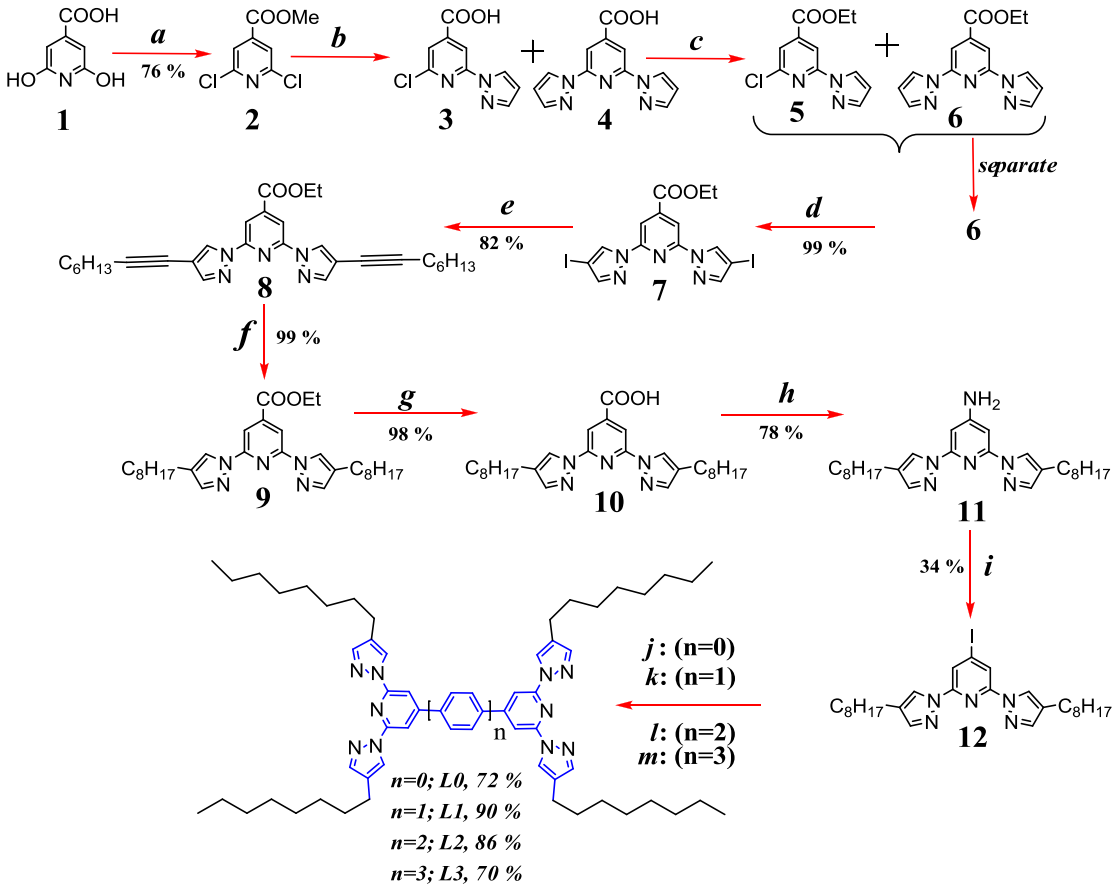

Scheme 2.2 Reagents and conditions: (a) $POCl_3$, Me_4NCl, 130 °C; CH_3OH; (b) K metal, pyrazole, diglyme, 130 °C; (c) EtOH, H_2SO_4; (d) $I_2/HIO_3/H^+$/80 °C; (e) 1-octyne, CuI, 5% $Pd(PPh_3)_2Cl_2$, PPh_3, Dioxane/TEA; (f) Pd/C, H_2; (g) LiOH/THF/HCl; (h) oxalyl chloride ($C_2O_2Cl_2$)/NaN_3 /TFA/K_2CO_3; (i) I_2/KI/Isoamylnitrite/DCM/ 60 °C; (j-m) Suzuki Conditions: Na_2CO_3/1,4-dioxane/3d/70 °C; (j) Bispinacolatodiborane; (k) 1,4-phenyldiboronicacid; (l) 4,4′-biphenyldiboronic acid (**18**); (m) 4,4″-

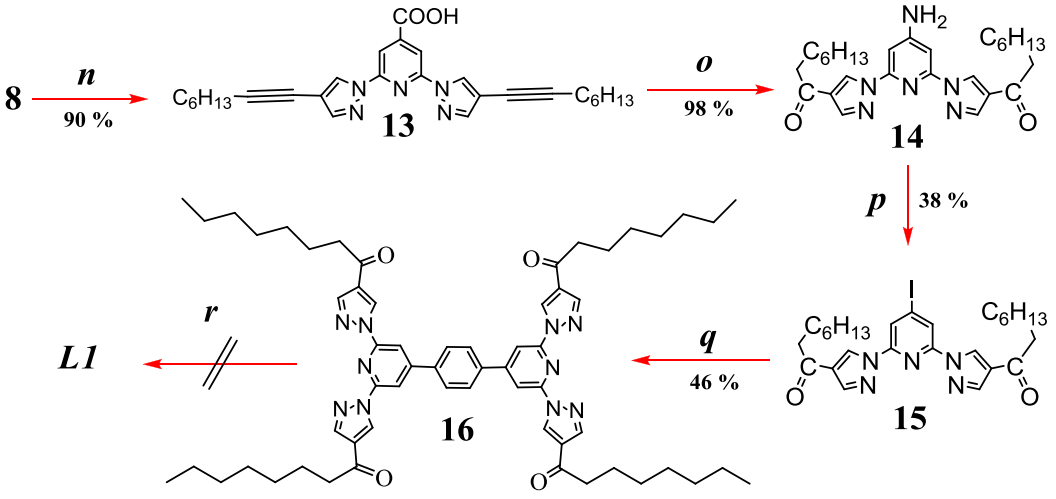

Scheme 2.3 Reagents and conditions: (n) LiOH/THF/HCl(2N); (o) $C_2O_2Cl_2$ /NaN_3 /TFA/K_2CO_3; (p) I_2/KI/Isoamylnitrite/DCM/ 60 °C; (q) 1,4-phenylenebisboronic acid/1,4-dioxane/Na_2CO_3/3 d/70 °C; (r) NH_2-NH_2/KOH/diethyleneglycol/180 °C/2 d.

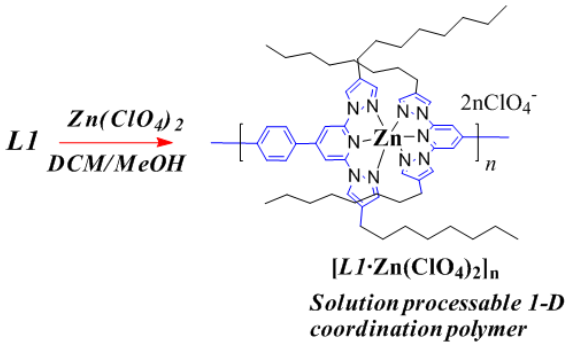

Scheme 2.4 Synthesis of solution processable coordination polymer [***L1***•$Zn(ClO_4)_2$]$_n$

-onyl group to give **14** due to the use of strong trifluoroacetic acid.[12] Transformation of the amino group in **14** to iodo compound **15** is effective. Later under Suzuki coupling condition **15** gave a back-to-back coupled ligand **16** with four octyl chains containing carbonyl groups. Unfortunately, reduction of the carbonyl groups in **16** to synthesis ***L1*** was unsuccessful under wolf-Kishner reduction condition.

2.3.2 Optical Properties of Ligands (L0-L3):

The UV–Vis absorption studies of ***L0***–***L3*** in dichloromethane (DCM) displayed absorption maxima (λ_{max}) at 334, 292, 313 and 321 nm, respectively (Fig. 2.1). All ligands ***L0***–***L3*** in DCM showed a violet fluorescence with emission maxima λ_{max} at 457, 394, 388 and 401 nm, respectively. The quantum yields (Φ_f) of ***L0***–***L3*** are in the following order: 0.78, 0.22 0.60 and 0.62, respectively (Table 2.1). In the solid state (powder, crystalline) ligands ***L1***–***L3*** displayed a violet fluorescence upon irradiation with 365 nm UV light. Here it is interesting to note that in spite of increasing conjugation length in the ***L1-L3*** the fluorescence maxima is decreased compared to ***L0*** this can be explained from crystal structure of ***L1*** and ***L6*** (analogues to ***L0***). In ***L0*** the two pyridine

TABLE 2.1 Photo physical properties of ***L1–L3*** in dichloromethane.

Compound	λ_{abs} [nm] (ε) [M^{-1} cm^{-1}]	$\lambda_{emission}$ [nm]	Φ_f[a]
L0	255 (48777) ; 290 (33771) ; 334 (17923)	457	0.779
L1	228 (16187) ; 258 (26700) ; 292 (32173)	394	0.217
L2	229 (22444) ; 259 (32753) ; 313 (41933)	388	0.60
L3	229 (34435) ; 259 (41350) ; 321(61204)	401	0.62

a) quininesulfate as reference (Q_{ref} = 0.577)

rings are nearly planer to each other with torsion angle 1.4°. But in the ***L1*** the two pyridine rings are not planer to the middle phenyl moiety and have torsion angle 26.75-27.28°, which leads to the breaking of conjugation and the blue shift of fluorescence maxima in ***L1-L3*** (Fig. A1).

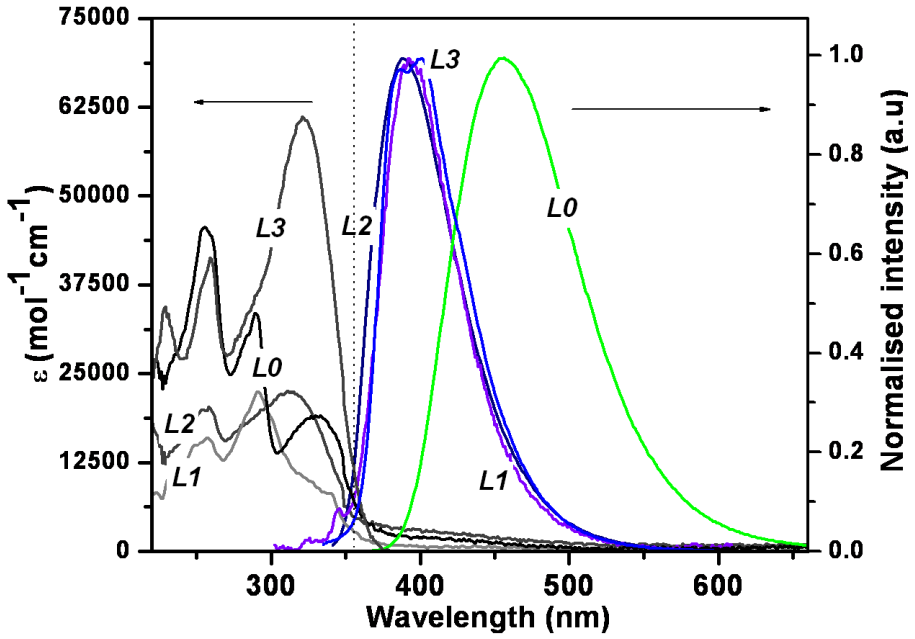

Figure 2.1 UV-Vis absorbance and emission properties of ***L0-L3*** in DCM.

2.3.3 Optical Properties of Metallo-Supramolecular Polymer:

In order to prepare a highly soluble 1D metallo-supramolecular polymer, ***L1*** was reacted with $Zn(ClO_4)_2$ (1:1 ratio) to get a coordination polymer $[\boldsymbol{L1}\cdot Zn(ClO_4)_2]_n$. Complexation of the metal ion to the ligand was followed by UV-Vis, fluorescent and NMR spectroscopy titration studies. In UV-Vis studies, upon addition of Zn(II) ion to ligand ***L1*** (1:1 ratio) the intensity of the ligand absorption band at 292 nm decreased sharply with broadening of the band (Fig. 2.2) due to the formation of a linear chain of six coordinated Zn(II) complex.[14] Furthermore the steady-state fluorescence spectra showed a sharp decrease in the fluorescence intensity accompanied by a 14 nm bathochromic shift of the free ligand (***L1***) fluorescent signal upon reaching the 1:1 stoichiometry of ***L1*** and Zn^{2+}, with no change in the intensity upon further addition of metal ion (Fig. 2.2). The plot of extinction and the Zn/***L1*** ratio showed a linear decrease and a sharp endpoint at a metal/ligand ratio of 1:1, indicating the formation of a 1:1 $[\boldsymbol{L1}\cdot Zn(ClO_4)_2]_n$ complex.

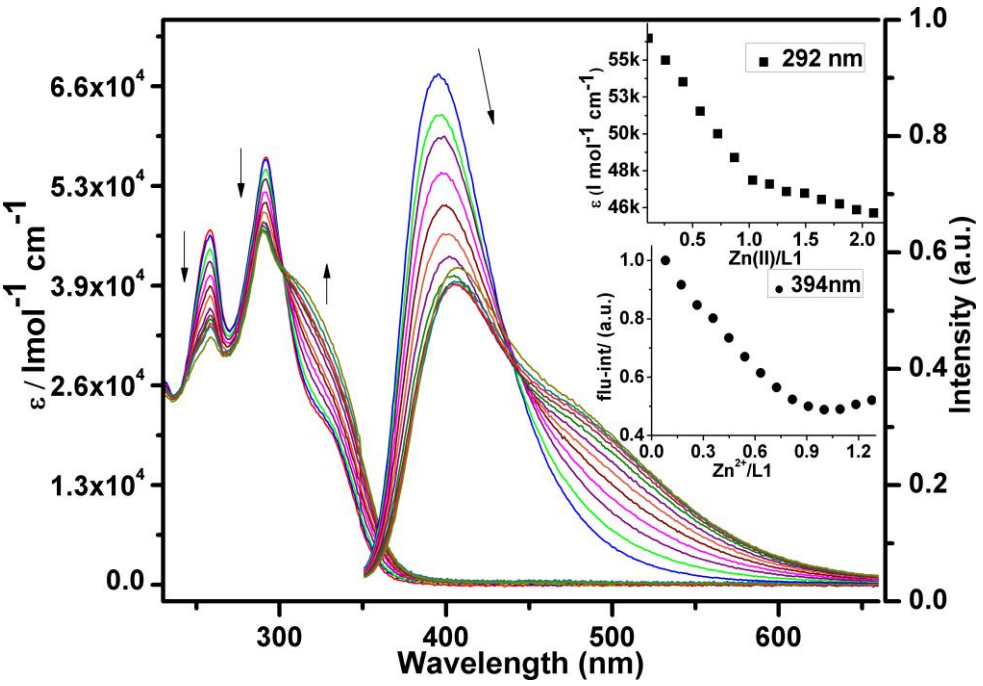

Figure 2.2 UV-Vis and fluorescence titration spectra of ligand ***L1*** with $Zn(ClO_4)_2$ in dichloromethane at 25 ˚C; the top inset shows the plot of molar extinction coefficient of 292 nm band as a function Zn(II) ion to ***L1*** ratio; the bottom inset shows the plot of change in the fluorescence intensity at 394 nm, as a function of Zn(II) ion to ***L1*** ratio. Arrows indicate the spectral changes with increasing amounts of Zn(II) ions.

2.3.4 Fluorescence Anisotropy Titration:

Fluoroscent anisotropy measurement has been widely used for studying the change in length of a fluorophore during a titration experiment. In biology biochemistry, people often used Fluorescence anisotropy measurements to detect binding events between fluorescence-labeled ligands and biomacromolecules.

The process involves (*a*) the excitation of the fluorophore with vertically polarized light which leads to the preferential excitation of fluorophores, whose excitation transition dipoles are collinear with the polarization direction of the excitation light i.e. a photoselection must occur between the randomly oriented molecules. (*b*) The emitted light will also be polarized vertically if three prerequisites are given: (i) the molecules are fixed in their position within the duration of their fluorescence lifetime without rotational or translational diffusion or flow effects, (ii) other depolarization processes like energy transfer are absent and (iii) the transition dipole moments for absorption and emission are collinear. The relevant quantity for the fluorescence depolarization is the anisotropy r.

Anisotropy measurements are done by exciting the sample with vertically

polarized light and detecting the fluorescence intensities with the emission polarizer in both vertical and horizontal alignment, and r is then calculated using the equation:

$$\boldsymbol{r = \frac{I_{VV} - I_{VH}}{I_{VV} + 2I_{VH}}} \qquad \ldots\ldots \textit{2.1}$$

The terms I_{VV} and I_{VH} represent the fluorescence intensities at vertical (V) or horizontal (H) orientation of the excitation (first subscript) and the emission (second subscript) polarizer with respect to the excitation/emission plane. The anisotropy can range between +0.4 and -0.2 with 0 indicating totally depolarized emission. The Perrin equation connects the anisotropy with external parameters:

$$\boldsymbol{\frac{r_o}{r} = 1 + \frac{\tau}{\theta} = 1 + 6D_R\tau} \qquad \ldots\ldots \textit{2.2}$$

$$\boldsymbol{\theta = \frac{n \cdot V}{RT}} \qquad \ldots\ldots \textit{2.3}$$

In this equation, r_0 represents the limiting anisotropy in the absence of diffusion effects, which can be determined at low temperatures in highly viscous solution, τ is the fluorescence lifetime of the fluorophore and D_R is the rotational diffusion coefficient. The term θ is the rotational correlation time, which depends on the molecular volume V, the viscosity η of the solvent and the temperature T. If the correlation time is significantly higher than the fluorescence lifetime ($\theta >> \tau$), then the anisotropy r will be equal to r_0, since no movement of the excited fluorophore is possible. In the inverse case, when $\theta << \tau$ the anisotropy will be zero and the fluorescence will be totally depolarized. It has to be noted that the above mentioned equations only hold for spherical chromophores. The (oblate or prolate) shape of fluorophores can be judged from time dependent anisotropy measurements, which resolve the contributions of various individual correlation times. That gives information about the change in size and shape of the molecular species upon addition of Zn^{2+} ions into a DCM solution of ***L1*** due to the formation of coordination polymers and fragmentation of polymer to oligomers upon addition of excess Zn^{2+} ions. (Fig. 2.3) shows a plot of the fluorescence anisotropy (r), of ***L1*** against the Zn^{2+}/***L1*** ratio. The molecule was excited at 341 nm, and the fluorescence was detected at 391 nm to ensure the maximum possible anisotropy value. The titration was performed in a

dichloromethane-methanol mixture. For the monomer ***L1*** an anisotropy value of r 0.011 was observed which increased nearly linearly to a maximum of r, 0.021 at a 1:1 ratio of Zn^{2+}/***L1***. These results are in accordance with the formation of coordination polymer since the slower rotational diffusion of polymer lead to higher anisotropy because of its enlarged size. As expected, the anisotropy decreases again upon exceeding the 1:1 stoichiometry due to the fragmentation of the polymer into oligomeric units. The value saturates at r 0.019, indicating that these fragments are a bit smaller than the polymer but still larger than the monomer unit. which is also evident from ^{1}H- NMR titration.

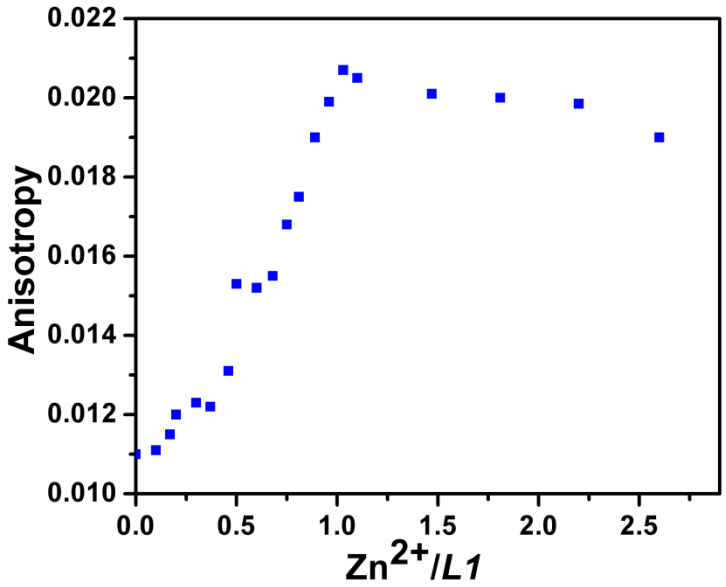

Figure 2.3 Fluorescence anisotropy titration of ligand ***L1*** (3 mL of 4.56 × 10^{-6} M) with zinc perchlorate (2.52 × 10^{-4} M) in dichloromethane, λ_{ex} = 341 nm, λ_{em} = 391 nm, at 25 °C.

2.3.5 Estimation of Molecular Weight by ^{1}H-NMR End Group Analysis:

^{1}H-NMR spectrum of complex [***L1***•$Zn(ClO_4)_2]_n$ showed a substantial downfield shifting and broadening of the peaks for pyrazole and pyridine ring protons compared to ***L1*** due to complex [***L1***•$Zn(ClO_4)_2]_n$ formation. Furthermore, the spectrum of [***L1***•$Zn(ClO_4)_2]_n$ showed a clearly distinguishable three new low intensity peaks (8.74, 8.17 and 8.0 ppm) corresponding to pyridine and pyrazole protons of the metal free end group of the polymer chain. As expected the bridging phenyl peak of the ligand not shifted much even after metal coordination (Fig. 2.5 and 2.6). The integration ratio of the end group signal to the polymer [***L1***•$Zn(ClO_4)_2]_n$ signal is 1:8, respectively (Fig. 2.4). From the end group analysis the estimated molecular weight ($\overline{M_n}$) of the polymer [***L1***·$Zn(ClO_4)_2]_n$ is ca. 9600 g/mol.

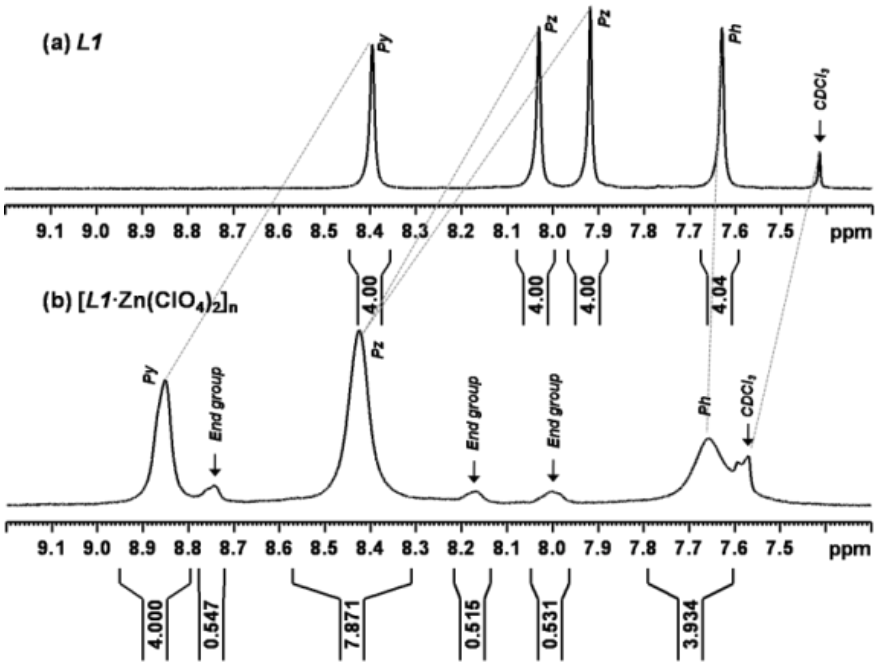

Figure 2.4 ^{1}H NMR (400 MHz, $CDCl_3$-d_1:CD_3OD-d_4 (3:2)) spectra of (a) ***L1*** and (b) polymer $[\textbf{\textit{L1}}\cdot Zn(ClO_4)_2]_n$.

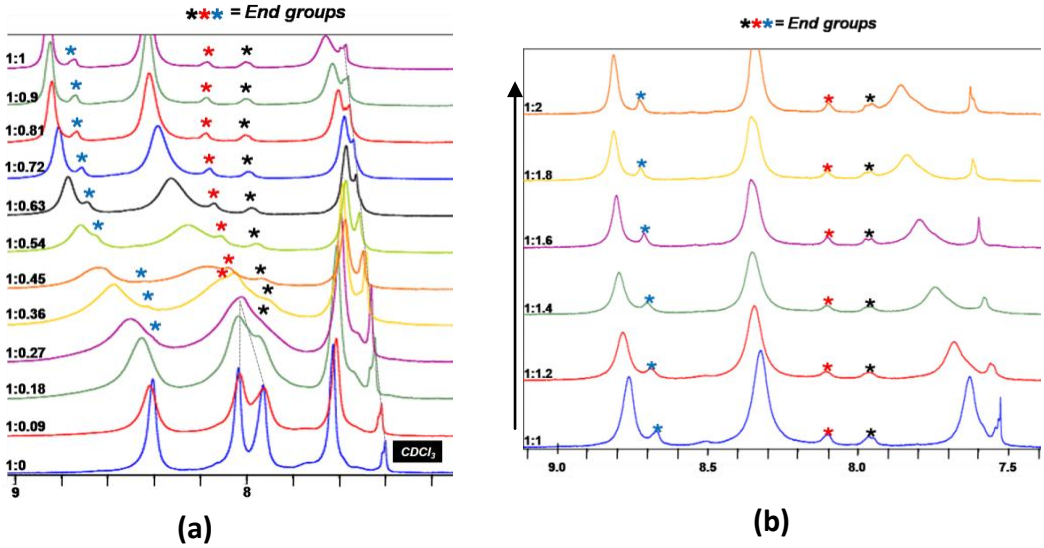

Figure 2.5 (a) ^{1}H NMR spectra at different ligand/metal ion ratios for the ditopic ligand ***L1*** and zinc per chlorate in $CDCl_3$-CD_3OD (3:2 of ***L1***) from free ***L1*** (below spectrum) to polymer $[\textbf{\textit{L1}}\cdot Zn(ClO_4)_2]_n$ (upper, 1:1). (*) corresponds to the evolution of end group protons. (b) ^{1}H NMR spectra at different ligand/metal ion ratios for the complex of ***L1*** and zinc per chlorate in $CDCl_3$-CD_3OD (3:2) from 1:1 complex polymer (***L1***/Zn(II)) (below spectrum) to 1:2 complex polymer (***L1***/Zn(II)).

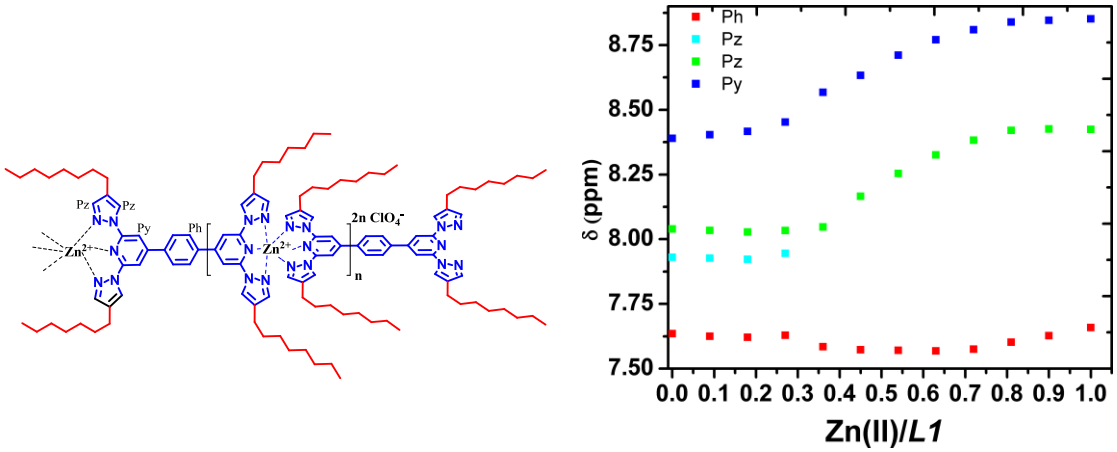

Figure 2.6 Plot of chemical shift (δ) of aromatic hydrogen atoms vs. the equivalent of Zn(II) added to ***L1*** solution in $CDCl_3$-CD_3OD at 298 K [Ph, Pz and Py indicate the proton on Phenyl ring, pyrazole moiety and pyridine moiety respectively of ***L1***.

2.3.6 Determination of viscosity (η) of metallo supramolecular polymer:

Viscosity is a measure of the resistance to flow due to internal friction when one layer of fluid is caused to move in relationship to another layer.[b]

Since now we have demonstrated the formation of 1:1 coordination polymer by UV, photoluminescent, fluoroscent anisotropy measurement and ^{1}H titration experiments, investigation of the viscosity change during the metallo supramolecular polymer formation was carried out. According to Mark Houwink Sakurada equation,

$$[\eta] = KM_v^a \qquad \ldots\ldots \; 2.9$$

In this equation the intrinsic viscosity [η] is related with the polymer molecular weight (M_v). where "K" and "a" are experimentally determined polymer and environmentally specific constants. There values for the present supramolecular polymer are not known; however, one can draw some conclusions based on the

b

Huggins equation:	$[\eta] = \lim_{c \to 0} \eta_{red}$	…… 2.4
Inherent Viscosity (η_{inh}):	$\eta_{inh} = \frac{\eta_{rel}}{c}$	…… 2.5
Reduced Viscosity (η_{red}):	$\eta_{red} = \frac{\eta_{rel} - 1}{c}$	…… 2.6
Specific Viscosity (η_{sp}):	$\eta_{rel} - 1$	…… 2.7
Relative Viscosity (η_{rel}):	$\eta_{rel} = \frac{\eta}{\eta_o}$	…… 2.8

comparison of the reduced viscosity values, which in turn related with the specific viscosity (η_{sp}) by Huggins equation, $[\eta] = \lim_{c \to 0} \eta_{red}$. All viscosity studies were carried out using a Ubbelohde microdilution viscometer supplied by Cannon.

The formation of metallo-supramolecular polymers having 1:1 metal to ligand concentration is evident from the viscosity data. The viscosity measurement for a series of solutions was carried out at different $Zn(ClO_4)_2$:***L1*** ratios keeping the total solute concentration constant (2.4 mg/mL). The obtained reduced viscosity data showed a steady increase of the reduced viscosity up to a Zn(II):***L1*** ratio of 1. Beyond

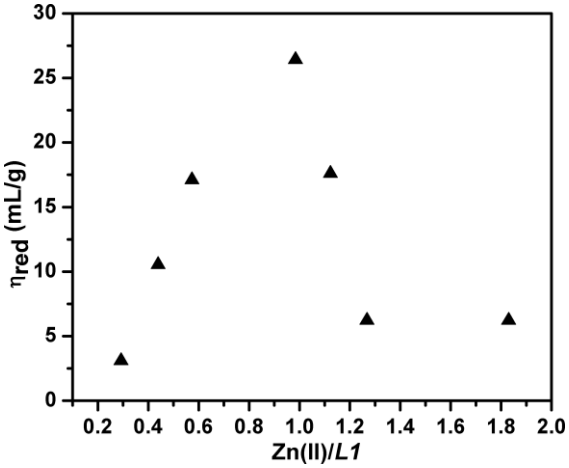

Figure 2.7 Reduced viscosities of a series of ($CHCl_3$:MeOH; 3:2) solutions containing Zn(II)/***L1*** at different ratio. The total solute concentration was kept constant at 2.4 mg/ mL.

this point a decrease in the reduced viscosity was observed, due to the possible breakdown of the polymer chain at higher Zn(II):***L1*** ratio (Fig. 2.7).[4a]

2.3.7 Thermal Properties:

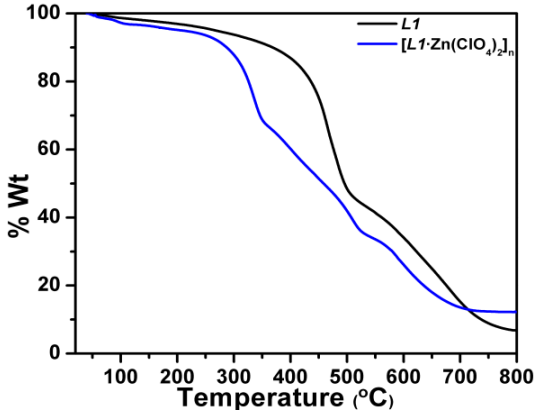

Figure 2.8 Thermogravimetric analysis plot of ***L1*** and [***L1***·$Zn(ClO_4)_2$]$_n$.

The thermal properties of the [***L1***·$Zn(ClO_4)_2$]$_n$ polymer and ***L1*** were performed on a TGA unit under N_2 at awith heating rate of 10^{o}C/min. TGA data of neat ***L1*** was obtained under nitrogen atmosphere demonstrate the beginning of significant weight loss at 407 °C, consequent to the thermal degradation of the polymer side chains. The Zn(II) metallopolymer shows a decrease of weight loss at 286 °C which was assumed due to the thermal degradation of the

perchlorate counter-ions.

Taking advantage of the good solubility of MSP [***L1***·$Zn(ClO_4)_2$]$_n$ in most of the organic solvents, by following a "top-down approach" fabrication of a periodic micro-stripes composed of [***L1***·$Zn(ClO_4)_2$]$_n$ was envisioned using micro-injection molding in capillaries (MIMIC) technique.[9e] At first elastomeric stamp was fabricated by replica molding of polydimethylsiloxane (PDMS) on a commercially available compact disk (CD) (Expt.Section. 2.5).

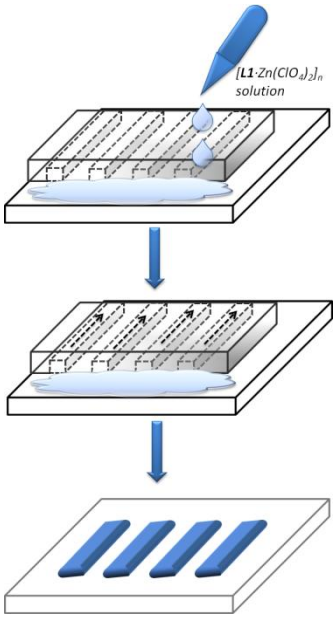

Figure 2.9 Schematic representation of micro injection molding technique.

The PDMS stamp was placed on a clean SiO_2 substrate. A 60 μL of dichloromethane solution containing MSP [***L1***·$Zn(ClO_4)_2$]$_n$ (2 mg of [***L1***·$Zn(ClO_4)_2$]$_n$ in 1 mL DCM) was dropped at one edge of the stamp so that the micro channels can be filled with solute by spontaneous capillary action (Fig. 2.9). After 30 min the PDMS mold was carefully peeled off to get periodic micro-strips of several micron length composed of coordination polymer [***L1***·$Zn(ClO_4)_2$]$_n$ on glass substrate. FESEM investigation of the sample revealed the formation of several millimeter long periodic micro-strips which are well separated by empty channels

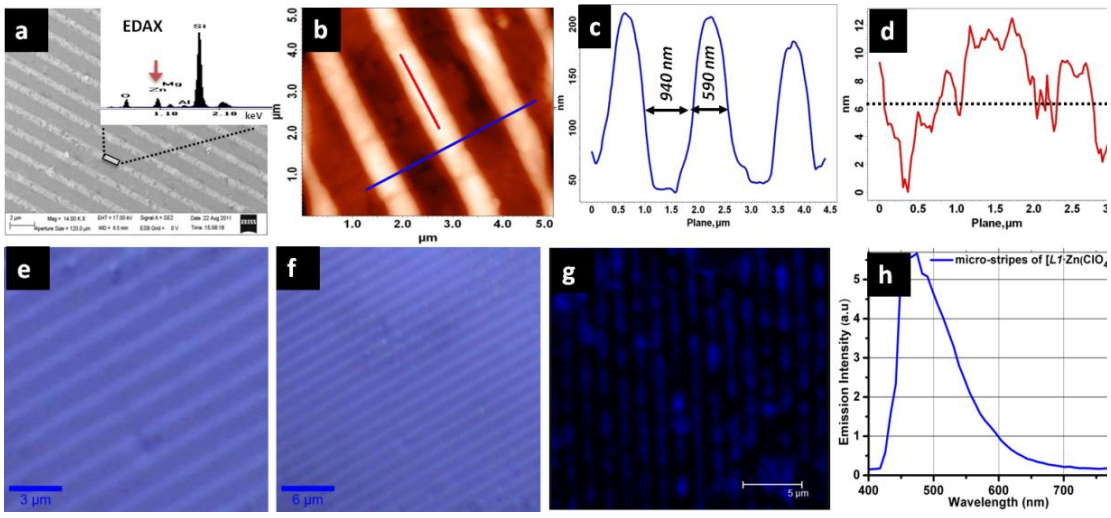

Figure 2.10 (a) FESEM image of micro-stripes of MSP [***L1***·$Zn(ClO_4)_2$]$_n$ formed on silica substrate (scale bar is 2 μm). Inset shows the EDAX spectra of Zn containing micro-stripes. (b) AFM topography image. (c) AFM height, width and channel profiles of stripes shown in (b) as blue line. (d) Roughness profile of the micro-stripes shown in (b) as brown line. (e) and f) Confocal microscope images of micro-stripes of [***L1***·$Zn(ClO_4)_2$]$_n$. (g) Stripes under illumination with UV (356/365) laser. (h) Corresponding spectra of the blue stripes.

(Fig. 2.10a). AFM topography measurement of the same sample showed that the micro-stripes width × height × roughness profiles are *ca.* 590 nm × 200 nm × ~ 6 nm, respectively with an uniform periodicity over larger area (Fig. 2.10 b-d). The empty channel width between the two adjacent micro-strips is ca. 940 nm. Raman

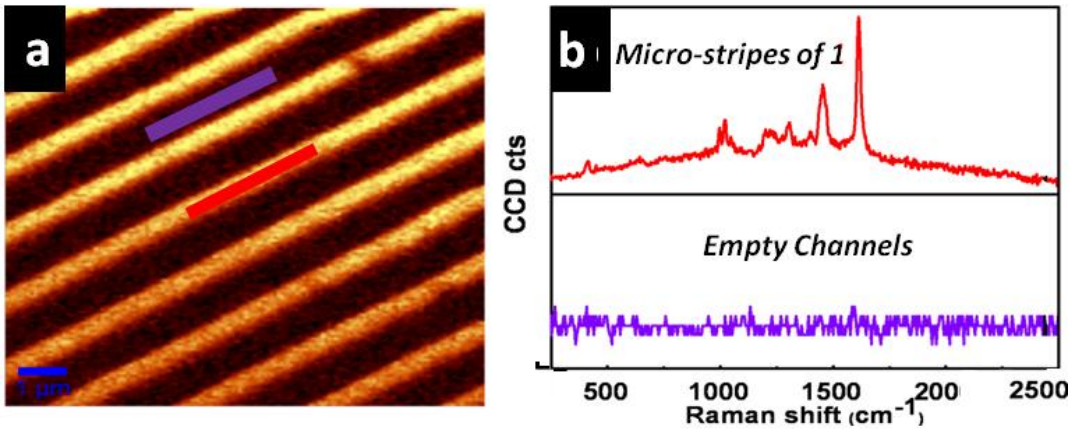

Figure 2.11 (a) Raman image of the micro-stripes (Scale bar is 1 μm). (b) Raman spectra of micro-stripes and empty channels shown in (a) as red and blue lines, respectively.

imaging/spectrocopy (633 nm laser) further confirmed that the micro-stripes indeed composed of $[\boldsymbol{L1}\cdot Zn(ClO_4)_2]_n$ having uniform periodicity by exhibiting clear Raman shifts at 1613, 1454, 1398, 1307, 1201, 1020, 998 and 412 cm^{-1}. (Fig. 2.11a and b; red bar and lines) corresponding to bulk of $[\boldsymbol{L1}\cdot Zn(ClO_4)_2]_n$ (Fig. A2 a) and no Raman shift from the empty channels (Fig. 2.11a and b; blue bar and lines).

2.4 Conclusions

In this chapter-2 we presented an efficient ten-step synthetic protocol to synthesize a series of novel *back-to-back* coupled tetraoctylated-BPP molecules ***L0–L3***. The preparation of solution processable metallo-supramolecular coordination polymer from a representative ligand (***L1***) and its use in the fabrication of ordered 1D micro-stripes using micro-injection molding technique was demonstrated. This general methodology can be applied to prepare soluble functional coordination polymers with diverse metal centers and their corresponding nano/micro structures. Using the similar methodology, the fabrication of a thermally switchable spin transition logic pattern sandwiched between an optically transperent polymer film will be disgussed in the following *chapter 3*.

2.5 Experimental Section

Preparation of PDMS Replica Mold of a Compact Disc (CD):

At first 50 mL PDMS base was taken into a graduated plastic measuring cylinder. Then 5 mL of catalyst (curing agent) was injected into the PDMS. The viscous

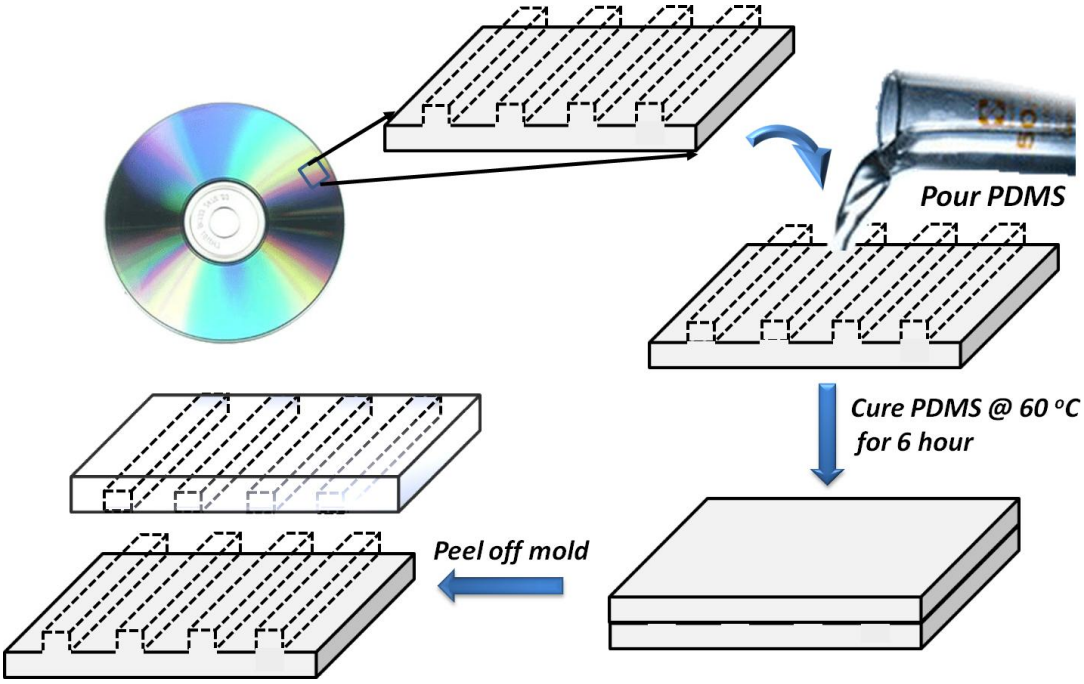

Scheme 2.5 Prepataion of PDMS mold from a commercially available compact disk.

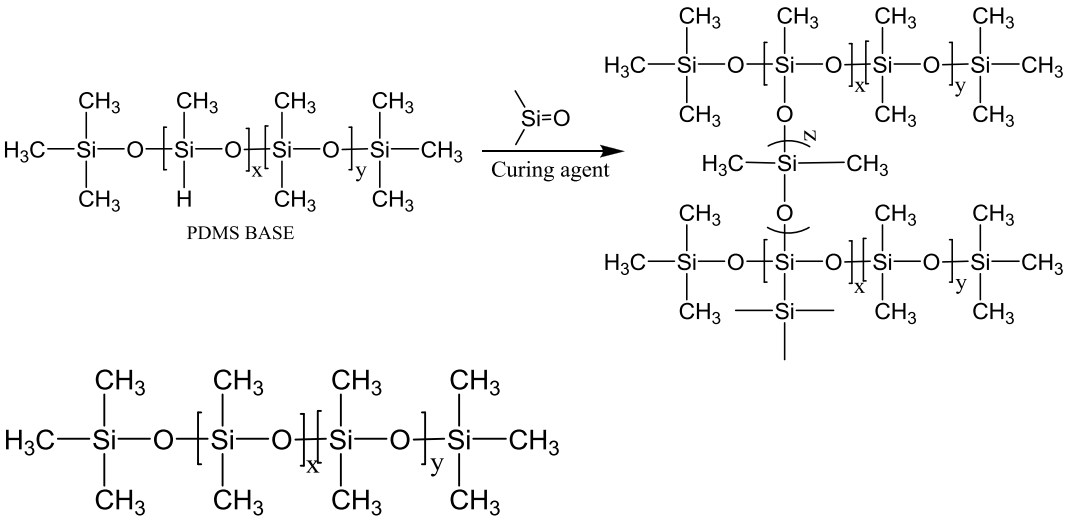

Figure 2.12 Chemical structure of PDMS used for the stamp preparation.

solution was vigorously stirred for 2 minutes using a clean disposable plastic rod. The mixture was de-gassed by placing it in the vacuum oven for 50-60 minutes to removed air bubbles from the mixture. Afterwards the mixture was poured onto a commercially available compact disk (CD). Because of the high surface tension of the PDMS mold it holds on the top of the master. Afterwards the mold was heated in a oven at 60 ^{o}C for 6 hour. After curing, the PDMS was carefully removed from the master and was used accordingly.

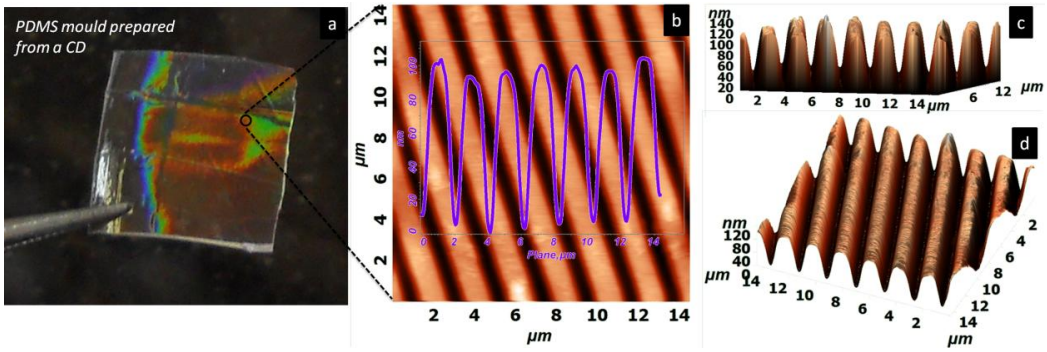

Figure 2.13 (a) A PDMS mold prepared from a CD. (b) AFM topography image of the mold and the corresponding profile. (c) & (d) 3-D side and top view of the mold.

2,2',6,6'-tetrakis(4-octyl-1H-pyrazol-1-yl)-4,4'-bipyridine (*L0*): In a 100 mL flask DMSO (20 mL), compound **12** (100 mg, 0.178 mmol), bispinacolatodiborane (49 mg, 0.192 mmol), K_2CO_3 (80.48 mg, 0.582 mmol) and $Pd(PPh_3)_4$ (14.0 mg, 7 mol %) were taken. The flask containing the mixture was stirred at 80 °C under N_2 atmosphere for 18 h until the starting material **12** was completely disappeared as monitored by TLC (eluent: EtOAc:Hexane; 5:95 ratio; R_f ~ 0.2). After cooling the reaction mixture to room temperature the solid was removed by filtration followed by washing with $CHCl_3$. The filtrate was then washed with deionised water (50 mL each) for five times. The organic layer was dried over Na_2SO_4 and the concentrated organic fraction was subsequently purified by column chromatography (eluent: EtOAc:Hexane; 5:95 ratio) on silica gel to get an analytically pure white color powder of ***L0***. Yield 55 mg (72%). mp 52-54 °C. ^{1}H NMR (400 MHz, $CDCl_3$-d_1, 298 K) δ: 8.37 (s, 4H), 8.17 (s, 4H), 7.62 (s, 4H), 2.59-2.56 (t, 8H), 1.66-1.63 (m, 8H), 1.37-1.26 (m, 40H), 0.91-0.88 (q, 12H). ^{13}C NMR

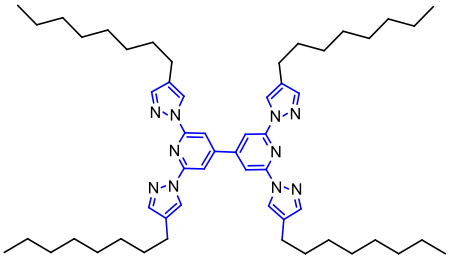

(100 MHz, $CDCl_3$-d_1, 298 K) δ**:** 151.0, 142.8, 124.9, 124.7, 108.5, 106.6, 31.9, 30.7, 29.4, 29.34, 29.3, 24.3, 22.7, 14.1. FTIR (KBr disc; ν in cm^{-1}): 2926, 2854, 1732, 1606, 1556, 1464, 1394, 1261, 1221, 1097, 1016, 970, 949, 862, 802, 725, 659, 611, 524. ESI MS: *m/z* calcd 868.66, found 891.63 [M^+ + Na]. Anal. Calcd for $C_{54}H_{80}N_{10}$: C, 74.61; H, 9.28; N, 16.11. Found: C, 74.48; H, 9.21; N, 16.25.

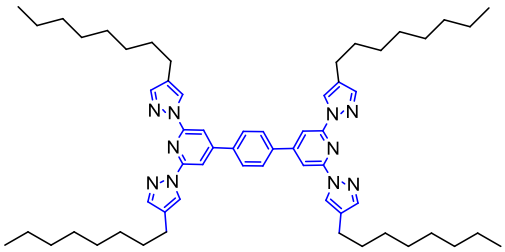

1,4-bis(2,6-bis(4-octyl-1H-pyrazol-1-yl)pyridin-4-yl)benzene (*L1*): Compound **12** (60 mg, 0.106 mmol), 1,4-phenyldiboronic acid (8.85 mg, 0.053 mmol) and $Pd(PPh_3)_4$ (6.17 mg, 5 mol %) were suspended in a N_2 gas bubbled solution of dioxane (20 mL) and 2M Na_2CO_3 (5 mL). The mixture was heated to 80 °C for 3 d under nitrogen atmosphere. The mixture of solvents was removed in vacuo and the remaining brown residue was treated with water and extracted with CH_2Cl_2 solvent. The separated organic layer was dried over Na_2SO_4 and the solvent was removed by evaporation. The solid residue was washed with MeOH (3 × 5 mL) to remove colored impurities and to get a white flake like compound ***L1***. Yield 45 mg (90%). mp 105-107 °C. ^{1}H NMR (400 MHz, $CDCl_3$-d_1, 298K) δ: 8.39 (s, 4H), 8.08 (s, 4H), 7.94 (s, 4H), 7.64 (s, 4H), 2.60-2.56 (t, 8H), 1.67-1.61 (t, 8H), 1.37-1.26 (m, 40H), 0.89-0.88 (t, 12H). ^{13}C NMR (100 MHz, $CDCl_3$-d_1, 298 K) δ**:** 152.8, 150.8, 142.6, 138.7, 127.8, 125.0, 124.5, 106.3, 31.9, 30.8, 29.4, 29.3, 24.3, 22.7, 14.1. FTIR (KBr disc; ν in cm^{-1}): 3115, 2926, 2852, 1701, 1608, 1558, 1541, 1458, 1394, 1261, 1195, 1016, 954, 798. ESI-MS: *m/z* calcd 944.69, found 967.66 [M^+ + Na]. Anal. Calcd for $C_{60}H_{84}N_{10}$: C, 76.23; H, 8.96; N, 14.82. Found: C, 76.12; H, 8.91; N, 14.75.

L2 and ***L3*** were prepared as per the above mentioned procedure for ***L1***, using the corresponding diboronic acids **18** and **21**, respectively. Yield and spectral data are given below.

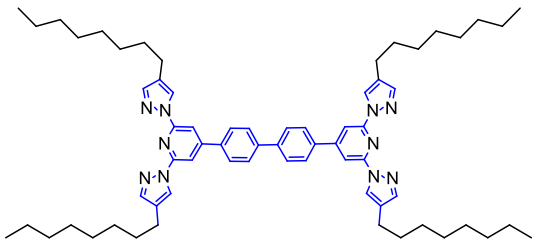

For ***L2*****:** Compound **12** (90 mg, 0.16 mmol), 4,4′-biphenyldiboronic acid (19.3 mg, 0.080 mmol) and $Pd(PPh_3)_4$ (9.26 mg, 5 mol %) Yield 70 mg (86%). mp 158-159 °C. ^{1}H NMR (400 MHz, $CDCl_3$-d_1, 298 K) δ: 8.39 (s,

4H), 8.11 (s, 4H), 7.95-7.93 (d, 4H), 7.81-7.79 (d, 4H),7.64 (s, 4H) 2.61-2.57 (t, 8H), 1.67-1.64 (t, 8H), 1.37-1.26 (m, 40H), 0.89-0.88 (t, 12H). ^{13}C NMR (100 MHz, $CDCl_3$-d_1, 298 K) δ**:** 153.2, 150.8, 142.6, 141.43, 137.0, 127.8, 127.7, 125.0, 124.4, 106.3, 31.9, 30.8, 29.4, 29.32, 29.27, 24.3, 22.7, 14.1. FTIR (KBr disc; ν in cm^{-1}): 2924, 2851, 1612, 1576, 1549, 1462, 1395, 1262, 1198, 1098, 1019, 804. ESI MS: *m/z* calcd 1020.72, found 1043.68 [M^+ + Na]. Anal. Calcd for $C_{66}H_{88}N_{10}$: C, 77.60; H, 8.68; N, 13.71. Found: C, 77.85; H, 8.61; N, 13.61.

For ***L3*****:** Compound **12** (100 mg, 0.17 mmol), 4,4″-triphenyldiboronic acid (28.3 mg, 0.089 mmol) and $Pd(PPh_3)_4$ (10.2 mg, 5 mol %), Yield 68.4 mg (70%). mp 177-178 °C. ^{1}H NMR

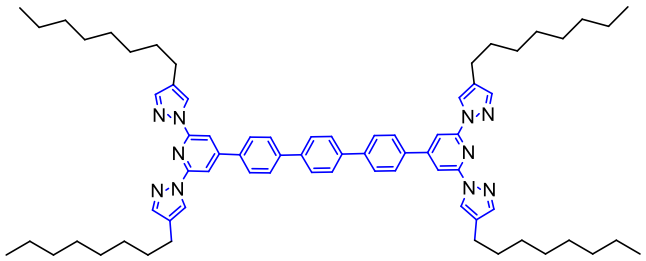

(400 MHz, $CDCl_3$-d_1, 298K) δ: 8.41 (s, 4H), 8.12 (s, 4H), 7.79-7.93 (d, 4H), 7.81-7.78 (d, 8H), 7.65-7.64 (d, 4H),) 2.62-2.58 (t, 8H), 1.73-1.65 (t, 8H), 1.42-1.27 (m, 40H), 0.93-0.90 (t, 12H) ppm. ^{13}C NMR (100 MHz, $CDCl_3$-d_1, 298 K) δ: 153.3, 150.8, 142.5, 139.6, 137.9, 136.6, 127.7, 127.6, 127.5, 125.1, 124.4, 106.23, 31.9, 30.8, 29.4, 29.34, 29.31, 24.3, 22.7, 14.1. FTIR (KBr disc; ν in cm^{-1}): 3437, 3354, 3242, 2957, 2920, 2851, 2521, 1798, 1659, 1576, 1481, 1393, 1323, 1190, 984, 920, 872, 808, 714, 633.

Preparation of metallosupramolecular polymer [*L1*·Zn $(ClO_4)_2$]$_n$: To a solution of ***L1*** (17.3 mg, 0.0183 mmol) in 20 mL of $CHCl_3$, 10 mL of MeOH solution of $Zn(ClO_4)_2$·$6H_2O$ (6.81 mg, 0.0182 mmol) was added and the solution was stirred for 30 min at room temperature. The obtained solution was concentrated in vacuo and the yellowish-white polymer was precipitated by adding excess of hexane. Yield 18.0 mg. ^{1}H NMR (400 MHz, $CDCl_3$-d_1:CD_3OD-d_4 (3:2), 298 K) δ : 8.85 (s, 8H),

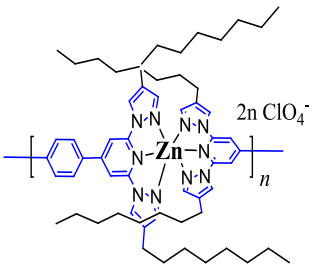

8.74 (s, 1H, end group), 8.42 (s, 16H), 8.17 (s, 1H, end group), 8.0 (s, 1H, end group), 7.66 (s, 8H), 2.59 (s, 16H), 1.67 (s, 16H), 1.28 (m, 80H), 0.87 (m, 24H). FTIR (KBr disc; ν in cm^{-1}): 3111, 2923, 2853, 1658, 1619, 1564, 1495, 1465, 1396, 1262, 1091(perchlorate Cl-O), 1012, 990, 970, 955, 930, 864, 831, 813, 795, 722, 622, 602. Raman (633 nm; ν in cm^{-1}): 1613, 1454, 1398, 1307, 1201, 1020, 998 and 412 cm^{-1}.

Compound **2**[11] was synthesized according to literature procedure.

Synthesis of 3 and 4: In a clean and dry 250 mL two-neck flask, small pieces of K metal flakes (2.02 g, 2.14 mmol) were dispersed completely in diglyme (100 mL) by vigorous stirring under N_2 atmosphere and left stirring for one hour. To this pyrazole (3.53 g, 2.14 mmol) was added slowly to minimize the violent reaction that occurred due to the formation of potassium salt of pyrazole. The mixture was stirred for about 30 minutes at 60 ºC until all the K was reacted to pyrazole to afford a white turbid solution. 2,6-dichloro-isonicotinic acid methyl ester **2** (5 g, 24.26 mmol) was added into this reaction mixture and heated at 110 ºC for 3 days under nitrogen gas. The mixture was poured into water and the white precipitate that formed was filtered and dried to isolate 6.9 g of mixture of compound of **3** and **4**. These products were used for the next step without purification.

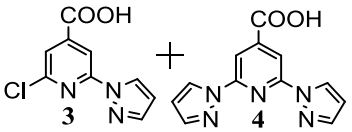

Synthesis of 5 and 6 and separation of 6: The mixture of **3** and **4** (3.9 g) was dissolved in ethanol (70 ml) and added conc. H_2SO_4 (1.5 ml). The mixture was heated to reflux for 4 hours. Then excess EtOH was evaporated in vacuum to get an oily liquid, to this 100 mL water was added to remove H_2SO_4 and extracted with $CHCl_3$ (3 × 50 mL). The organic fraction were washed with brine, dried over $MgSO_4$ and concentrated under reduced pressure yielding colorless oil which hardened upon standing. The mixture of mono (**5**) and di pyrazolyl (**6**) ester were separated by column chromatography using 92:2 Hexane/EtOAc (Yield for **6**: 1.8 g; and for **5**: 1 g).

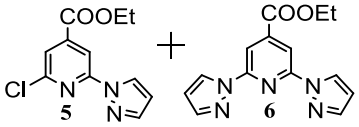

Ethyl 2-chloro-6-(1H-pyrazol-1-yl)isonicotinate (5): ^{1}H-NMR (400 MHz, $CDCl_3$-d_1, 298 K) δ: 8.53 (s, 1H), 8.41 (s, 1H), 7.77 (s, 1H), 7.73 (s, 1H) 6.49 (s, 1H), 4.47-4.20 (q, 2H, ^3J = 8 Hz, -CH_2), 1.45-1.42 (t, 3H, ^3J = 7.2 Hz, -CH_3) ppm. ^{13}C-NMR (100 MHz, $CDCl_3$-d_1, 298K) δ: 163.4, 151.9, 150.4, 143.1, 143.08, 127.7, 120.8, 110.4, 108.6, 62.4, 14.2 ppm.

Ethyl 2,6-di(1H-pyrazol-1-yl)isonicotinate (**6**): ^{1}H-NMR (400 MHz, $CDCl_3$-d_1, 298 K) δ: 8.51-8.50 (d, 2H, ^3J = 2.8 Hz), 8.33 (s, 2H), 7.76 (s, 2H),), 6.48 (m, 2H), 4.46-4.40 (q, 2H, ^3J = 8 Hz, -CH_2), 1.48-1.40 (t, 3H, ^3J = 7.2 Hz, -CH_3) ppm. ^{13}C-NMR (100MHz, $CDCl_3$-d_1, 298K) δ: 163.9, 150.7, 143.5, 142.8, 127.2, 109.1, 108.4, 64.2, 14.2 ppm.

LCMS analysis *m/z* = 284.00. calculated = 283.29. FT-IR (KBr)**:** ν in cm^{-1} = 3129, 1721, 1616, 1574, 1524, 1462, 1399, 1285, 1242, 1208, 1142, 1094, 1053, 949, 916, 887, 787,770, 648, 608, 490 Elemental analysis: $C_{14}H_{13}N_5O_2$: found C 59.18 H 4.67 N 24.85, required C 59.36, H 4.63, N 24.72%.

Ethyl 2,6-bis(4-iodo-1H-pyrazol-1-yl)isonicotinate (7): Ethyl 2′,6′-bis(pyrazol-1,1″-yl)isonicotinate **6** (1.12 g, 3.95 mmol) was suspended in a round bottomed flask with acetic acid (5 mL), H_2SO_4 (30% in water, 1.0 mL). Separately, a deep violet water solution (10 mL containing HIO_3 (0.278 g, 1.58 mmol), I_2 (0.806 g, 3.17 mmol) and two drops of concentrated H_2SO_4 was slowly added into the solution of **6** and heated up to 130°C. The solution was left under this condition for 4 hour and subsequently an aqueous solution of $Na_2S_2O_3$ was added just in enough amounts to destroy the excess iodine. Afterwards the mixture was quenched with aqueous $NaHCO_3$ solutions until (pH ~ 7–8) was reached. The solution mixture was extracted with $CHCl_3$ (3 × 100 mL) and the chloroform fraction was dried over $MgSO_4$, evaporated on rotary evaporator to get white precipitate. The white precipitate was recrystallized from $CHCl_3$ as white needles to get analytically pure **7.** Yield = 2.1 g (>99%). ^{1}H-NMR (400 MHz, $CDCl_3$-d_1, 298 K) δ: 8.58 (s, 2H), 8.34 (s, 2H), 7.77 (s, 2H), 4.43 - 4.49 (q, 2H, ^3J = 7.2 Hz, $-CH_2$), 1.42 - 1.46 (t, ^3J = 7.2 Hz, 3H) ppm. ^{13}C-NMR (100 MHz, $CDCl_3$-d_1, 298 K) δ**:** 163.6, 149.8, 147.6, 144.0, 131.1, 109.3, 62.4, 60.9, 14.3 ppm. LCMS analysis**:** *m/z* = 535.0 calculated = 535.90. FT-IR (KBr)**:** ν in cm^{-1} = 3102, 2922, 2855, 1786, 1725, 1618, 1576, 1458, 1179, 1046, 941, 766, 600. Elemental analysis: found C 31.36, H 2.11, N 13.15. $C_{14}H_{12}I_2N_5O_2$ (535.08), required C 31.43, H 2.07, N 13.09

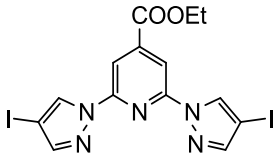

Ethyl-2,6-bis(4-(oct-1-ynyl)-1*H*-pyrazole-1-yl)isonicotinate (8): A Schlenk tube was charged with ethyl-2′,6′-bis(4,4″-iodo-pyrazol-1,1″-yl)isonicotinate **7** (2.6 g, 4.86 mmol) together with $Pd(PPh_3)_2Cl_2$ (170 mg, 0.242 mmol), triphenylphosphine (200 mg, 0.762 mmol) and CuI (200 mg, 1.05 mmol) as additional catalyst. Freshly distilled anhydrous triethylamine (20 mL) and 1,4-dioxane (10 mL) were added to it. The Schlenk tube was carefully degassed by several freeze and thaw cycles. 1-octyne (2.15 mL, (*d* = 0.746 g/mL), 14.5 mmol) was added under argon atmosphere by syringe, and

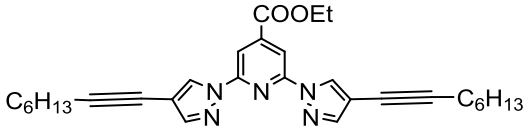

the resulting mixture was heated to 80 °C for 48 h. It was then cooled to room temperature and left for stirring for a one additional hour. The mixture was filtered and washed through filter paper and washed with 1,4-dioxane, the filtrate was evaporated in vacuo to get a dark brown solid which was column chromatographed on silica (100-200 mesh) using (8 : 92) EtOAc/Hexane to isolate **8** as a white solid. Yield 2.0 g (82%). mp 86-87 ^{o}C. ^{1}H NMR (400 MHz, $CDCl_3$, 298 K) δ: 8.56 (s, 2H), 8.34 (s, 2H), 7.78 (s, 2H), 4.48-4.43 (q, 2H), 2.43-2.39 (t, 4H), 1.65-1.58 (p, 3H), 1.5-1.4 (p, 8H), 1.34-1.25 (m, 8H), 0.94-0.91 (t, 6H) ppm. ^{13}C NMR (100 MHz, $CDCl_3$-d_1, 298 K) δ: 163.8, 150.2, 145.0, 143.7, 129.1, 109.4, 107.0, 93.1, 70.4, 62.3, 31.4, 28.7, 28.6, 22.6, 19.5, 14.3, 14.1 ppm. FTIR (KBr disc; ν in cm^{-1}): 3113, 2928, 2856, 1730, 1618, 1574, 1469, 1390, 1348, 1305, 1234, 1099, 1030, 964, 895, 864, 819, 790, 769, 733, 655, 617, 507. LC-MS *m/z* calcd 499.29, found 500.50. Anal. Calcd for $C_{30}H_{37}N_5O_2$: C, 72.12; H, 7.46; N, 14.02. Found: C, 72.36; H, 7.41; N, 14.15.

Ethyl 2,6-bis(4-octyl-1H-pyrazol-1-yl)isonicotinate (9): To a degassed solution of **8** (0.619 g, 1.23 mmol) in EtOAc (200 mL) was added 10% Pd/C (0.350 g, 0.3 mmol), the mixture was stirred under H_2 bladder and monitored by TLC. After 4 days the mixture was filtered through a celite plug to remove activated Pd/C. Afterwards the plug was washed with 100 mL of EtOAc and the collected fraction was concentrated in vaccuo to afford **9** as yellowish gummy oil. Yield 0.618 g (99%). ^{1}H NMR (400 MHz, $CDCl_3$-d_1, 298 K) δ: 8.30 (s, 2H), 8.28 (s, 2H), 7.6 (s, 2H), 4.46-4.42 (q, 2H), 2.56-2.53 (t, 4H), 1.64-1.62 (t, 4H), 1.36-1.24 (m, 23H), 0.89-0.88 (t, 6H). ^{13}C NMR (100 MHz, $CDCl_3$-d_1, 298 K) δ: 164.1, 150.8, 143.3, 142.9, 124.9, 124.8, 108.2, 62.0, 31.9, 30.7, 29.7, 29.4, 29.30, 24.26, 22.7, 14.25, 14.1 ppm. FTIR (KBr disc; ν in cm^{-1}): 2924, 2853, 1612, 1576, 1547, 1464, 1392, 1261, 1099, 1016, 804. LCMS analysis: *m/z* calcd 507.71, found 508.65. Anal. Calcd for $C_{30}H_{45}N_5O_2$: C, 70.97; H, 8.93; N, 13.79. Found: C, 70.79; H, 8.86; N, 13.65.

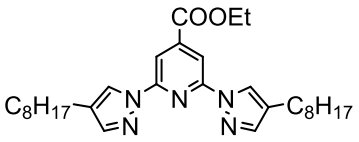

2,6-bis(4-(oct-1-ynyl)-1H-pyrazol-1-yl)isonicotinic acid (10): Compound **9** (0.619 g, 1.23 mmol) was dissolved in 25 mL of THF. An aqueous LiOH (0.2 g, 8.33 mmol, 7 equiv in 75 ml of water) added to the THF solution. After an hour, the THF was removed in vacuo and the solution was cooled in an ice bath. To this 27 mL of 2 M HCl was then slowly added. After an hour the white solid product **10** was isolated by filtration followed by drying in air (0.5 g, >98%). mp 124-126 ^{o}C. ^{1}H NMR (400 MHz, $CDCl_3$-d_1, 298 K) δ:

8.46 (s, 2H), 8.36 (s, 2H), 7.72 (s, 2H), 4.8-4.6 (broad, OH), 2.60-2.56 (t, 4H), 1.69-1.63 (t, 4H), 1.38-1.24 (m, 20H), 0.92-0.89 (t, 6H). ^{13}C NMR (100 MHz, $CDCl_3$-d_1, 298 K) δ: 165.8, 150.6, 143.5, 142.9, 125.3, 124.9, 109.0, 31.9, 30.6, 29.4, 29.3, 24.3, 22.7, 14.1 ppm. FTIR (KBr disc; ν in cm^{-1}): 3427 (broad-COOH), 3113, 2926, 2854, 1707, 1618, 1574, 1460, 1392, 1261, 1192, 1060, 964, 802, 721, 673, 611, 408. LCMS analysis: *m/z* calcd 479.65, found 478.40.

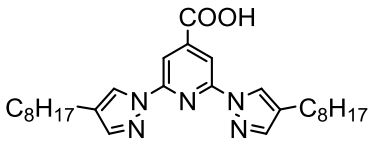

2,6-bis(4-octyl-1H-pyrazol-1-yl)pyridin-4-amine (11): Compound **10** (0.4 g, 0.83 mmol, 1 equiv) was dissolved in a mixture of 3 : 1 CH_2Cl_2: THF (50 mL). To this oxalyl chloride (0.09 mL, 1.017 mmol and 1.22 equiv) was slowly added and stirred at room temperature. After 4 h, the solvent was removed in vacuo and the resultant residue was dissolved in dry acetone (10 mL). This acetone mixture was added to a solution of NaN_3 (0.234 g, 3.60 mmol, 4.32 equiv) in H_2O (20 mL). The solution was immediately extracted with Et_2O (3 × 20 mL). The combined organic fraction was dried with $MgSO_4$, and concentrated to yield a white solid. The solid was redissolved in 50 mL of dry benzene; trifluoroacetic acid was added (0.09 mL, 1.25 mmol, 1.50 equiv) and the solution was heated to reflux for 16 h. After cooling, the benzene was removed in vacuo and the residue was redissolved in CH_3OH (50 mL). Solid K_2CO_3 was added (0.250 g, 1.80 mmol and 2.17 equiv) to it and the mixture vigorously stirred for 8 h. After removing 95% of the CH_3OH in vacuo, 70 mL of H_2O was added to it, and the mixture was cooled in an ice bath for 2 h. The resulting precipitate was isolated by filtration followed by drying in air. (0.307 mg, 78%). mp 104-105 ^{o}C. ^{1}H NMR (400 MHz, $CDCl_3$-d_1, 298 K) δ: 8.29 (s, 2H), 7.53 (s, 2H), 7.03 (s, 2H), 4.51 (s, 2H), 2.55-2.51 (t, 4H), 1.65-1.61 (m, 4H), 1.34-1.26 (m, 20H), 0.90-0.87 (q, 6H) ppm. ^{13}C NMR (100 MHz, $CDCl_3$-d_1, 298 K) δ: 156.8, 151.2, 141.9, 125.0, 123.8, 94.1, 31.9, 30.8, 29.4, 29.3, 29.28, 24.3, 22.7, 14.1 ppm. FTIR (KBr disc; ν in cm^{-1}): 3437, 3354, 3238, 2920, 2851, 1655, 1575, 1479, 1394, 1190, 983, 920, 871, 808, 713, 632, 459. LCMS analysis: *m/z* calcd 450.34, found 451.55. Anal. Calcd for $C_{27}H_{42}N_6$: C, 71.96; H, 9.39; N, 18.65. Found: C, 72.13; H, 9.31; N, 18.56.

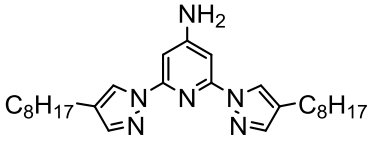

4-iodo-2,6-bis(4-octyl-1H-pyrazol-1-yl)pyridine (12): Compound **11** (0.5 g, 1.108 mmol), iodine (0.562 g, 2.217 mmol) and KI (0.552 g, 3.325 mmol) were suspended in a degassed solutions of dichloromethane/isoamyl nitrite (2 : 1, 30 mL). The mixture was

heated with stirring for 12 h under N_2 atmosphere. After cooling, the mixture was poured into a saturated aqueous solution of $Na_2S_2O_3$ (100 mL) and extracted with dichloromethane (3 × 30 mL). The collected orange organic layers were dried over Na_2SO_4 and the solvent was evaporated in vacuo. The crude orange product was purified by column chromatography on silica using a mixture of n-Hexane : CH_2Cl_2 (3 : 2) to afford a white color product **12** (210 mg, 34%). mp 75-77 ^oC. ^1H NMR (400 MHz, $CDCl_3$-d_1, 298 K) δ: 8.25 (s, 2H), 8.15 (s, 2H), 7.57 (s, 2H), 2.54-2.50 (t, 4H), 1.65-1.58 (m, 4H), 1.33-1.27 (m, 20H), 0.89-0.86 (q, 6H) ppm. ^{13}C NMR (100 MHz, $CDCl_3$-d_1, 298 K) δ: 149.8, 143.0, 124.9, 124.8, 117.5, 108.5, 31.9, 30.7, 29.4, 29.3, 24.2, 22.7, 14.1 ppm. FTIR (KBr disc; ν in cm^{-1}): 3103, 2926, 2851, 1734, 1585, 1568, 1454, 1392, 1263, 1190, 1157, 1053, 1018, 960, 866, 839, 802, 760, 706, 646, 609, 540. LCMS analysis: *m/z* calcd 562.0, found 561.23. Anal. Calcd for $C_{27}H_{40}IN_5$: C, 57.75; H, 7.18; N, 12.47. Found: C, 57.68; H, 7.25; N, 12.36.

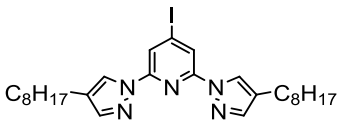

2,6-bis(4-(oct-1-ynyl)-1H-pyrazol-1-yl)isonicotinic acid (13): Compound **8** (0.6 g, 1.18 mmol) was dissolved in 25 mL of THF and 75 mL of aqueous LiOH (0.2 g, 8.33 mmol, 7 equiv) was added to it. After an hour, the THF was removed in vacuo and the solution was cooled in an ice bath. Subsequently 2 M HCl (27 mL) was slowly added to it. After 1 h the white solid was isolated by filtration and air dried to get compound **13** (0.5 g, 90 %).^1H NMR (400 MHz, $CDCl_3$-d_1, 298 K) δ: 8.55 (s, 2H), 8.40 (s, 2H), 7.81 (s, 2H), 2.42 (s, 4H), 1.62 (s, 4H), 1.46 (s, 4H), 1.27 (s, 8H), 0.93 (s, 6H). ^{13}C NMR (100 MHz, $CDCl_3$-d_1, 298 K) δ: 166.9, 150.2, 145.1 143.0, 129.2, 109.8, 107.2, 93.2, 70.3, 31.4, 28.7, 22.6, 19.5, 14.1 ppm. FTIR (KBr disc; ν in cm^{-1}): 2924, 2853, 1701, 1618, 1572, 1460, 1348, 1306, 1258, 1182, 1030, 962, 891, 816, 795, 773, 703, 665, 534. Anal. Calcd for $C_{28}H_{33}N_5O_2$: C, 71.31; H, 7.05; N, 14.85. Found: C, 71.19; H, 7.12; N, 14.68.

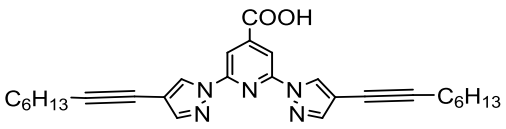

1,1'-(1,1'-(4-aminopyridine-2,6-diyl)bis(1H-pyrazole-4,1-diyl))dioctan-1-one (14): Compound **13** (0.4g, 0.83 mmol, 1 equiv) was dissolved in a mixture of 3:1 CH_2Cl_2: THF (50 mL). To thisoxalyl chloride (0.09 mL, 1.017 mmol, 1.22 equiv) was then slowly added at room temperature. After 4 h, the solvent was removed in vacuo and the residue was dissolved in dry

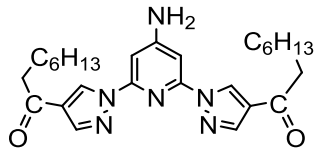

acetone (10 mL). This was added to a solution of NaN_3 (0.234 g, 3.60 mmol, 4.32 equiv) in H_2O (20 mL). The solution was immediately extracted with Et_2O (3 × 20 mL). The organic fractions were combined, dried with $MgSO_4$, and concentrated to give a white solid. The solid was redissolved in 50 mL of dry benzene; trifluoroacetic acid was added (0.09 mL, 1.25 mmol, 1.50 equiv) to it, and the solution was heated to reflux for 16 h. After cooling, the benzene was removed in vacuo and the resultant residue was dissolved in CH_3OH (50 mL). To this K_2CO_3 was added (0.250 g, 1.80 mmol and 2.17 equiv) and the mixture vigorously stirred. After for 8 h, 95 vol % of the CH_3OH was removed on a rotary evaporator and 70 mL of H_2O was added and the mixture was cooled in an ice bath for 2 h. The resulting white precipitate (**14**) was isolated by filtration. (0.37 mg, 98%). ^{1}H NMR (400 MHz, $CDCl_3$-d_1, 298K) δ: 8.95 (s, 2H), 8.08 (s, 2H), 7.18 (s, 2H), 4.84 (s, 2H), 2.86 (s, 4H), 1.75-1.73 (m, 4H), 1.29-1.25 (m, 15H), 0.87 (s, 6H) ppm. ^{13}C NMR (100 MHz, $CDCl_3$-d_1, 298K) δ: 195.2, 157.3, 150.5, 142.0, 129.1, 125.1, 96.3, 40.7, 31.7, 29.6, 29.3, 29.2, 24.3, 22.6, 14.1 ppm. FTIR (KBr disc; ν in cm^{-1}): 3466, 3434, 3364, 3229, 3113, 2926, 2855, 1670, 1632, 1547, 1487, 1410, 1186, 982, 943, 941, 835, 788, 723, 642, 540. LCMS analysis: *m/z* calcd 478.31, found 479.65 (positive mode). Anal. Calcd for $C_{27}H_{38}N_6O_2$: C, 67.75; H, 8.00; N, 17.56. Found: C, 67.86; H, 8.09; N, 17.45.

1,1'-(1,1'-(4-iodopyridine-2,6-diyl)bis(1H-pyrazole-4,1-diyl))dioctan-1-one(15): 1,1'-(1,1'-(4-aminopyridine-2,6-diyl)bis(1H-pyrazole-4,1-diyl))dioctan-1-one (**14**) (0.5 g, 1.04 mmol), iodine (0.562 g, 2.217 mmol) and KI (0.552 g, 3.325 mmol) were suspended in a degassed mixture of dichloromethane/isoamyl nitrite (2 : 1, 30 mL) and heated with stirring for 12 h. After cooling, the mixture was poured into a saturated aqueous solution of $Na_2S_2O_3$ (100 mL) and extracted with dichloromethane (3 × 30 mL). The collected orange organic layer was dried over Na_2SO_4 and the solvent was evaporated in vacuo. The crude orange product was purified by column chromatography on silica using a mixture of n-Hexane: CH_2Cl_2 (3 : 2) to afford a white product of **15** (230 mg, 38%). mp 154-155 ^{o}C. ^{1}H NMR (400 MHz, $CDCl_3$-d_1, 298 K) δ/ppm: 8.95 (s, 2H), 8.35 (s, 2H), 8.13 (s, 2H), 2.88-2.85 (t, 4H), 1.77-1.71 (t, 4H), 1.39-1.35 (m, 12H), 0.87-0.86 (t, 6H). ^{13}C NMR (400 MHz, $CDCl_3$-d_1, 298 K) δ/ppm: 194.9, 149.2, 142.8, 129.1, 125.9, 120.4, 109.5, 40.9, 31.7, 29.3, 29.2, 24.2, 22.6, 14.1. FT-IR (KBr) ν in cm$^{-1:}$ 3111, 2926, 2851, 1663, 1595, 1549, 1456, 1414, 1269, 1190, 1130, 962, 851, 793, 768, 663,

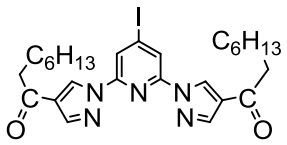

623, 540. HR-MS: *m/z* calcd 589.1914, found 590.1993 $[M + H]^+$. Anal. Calcd for $C_{27}H_{36}IN_5O_2$: C, 55.01; H, 6.16; N, 11.88; Found: C, 55.16; H, 6.21; N, 11.68.

1,1',1'',1'''-(1,1',1'',1'''-(4,4'-(1,4-phenylene)bis(pyridine-6,4,2-triyl))tetrakis(1H-pyrazole-4,1-diyl))tetraoctan-1-one (16): Compound **15** (76 mg, 0.131 mmol), 1, 4-phenyldiboronic acid (10.8 mg, 0.655 mmol) and $Pd(PPh_3)_4$ (7.9 mg, 0.0068 mmol, 5 mol %) were suspended in a degassed mixed solution of 1,4-dioxane (20 mL) and 2 M Na_2CO_3 (5 mL) and heated to 80 °C for 3 d under nitrogen atmosphere. The mixtures of solvents were removed in vacuo and the remaining residue was treated with water and extracted with CH_2Cl_2 solvent. The separated organic layer was dried over Na_2SO_4 and the solvent was removed by evaporation. The resultant solid residue was washed with MeOH (3 × 5 mL) to get white color compound **16**. Yield 30 mg (46%). mp 282-283 °C. ^{1}H NMR (400 MHz, $CDCl_3$-d_1, 298K) δ: 9.08 (s, 4H), 8.26-8.20 (d, 8H), 7.97 (s, 4H), 2.92 (s, 8H), 1.80 (s, 8H), 1.40-1.26 (m, 32H), 0.91 (t, 12H) ppm. ^{13}C NMR (100 MHz, $CDCl_3$-d_1, 298K) δ: 195.0, 153.6, 150.2, 142.5, 138.4, 129.1, 128.2, 125.7, 109.0, 40.9, 31.7, 29.3, 29.2, 24.2, 22.6, 14.1 ppm. FTIR (KBr disc; ν in cm^{-1}): 2926, 2853, 1674, 1615, 1545, 1472, 1408, 1202, 1150, 959, 831, 795, 664. HR-MS: *m/z* calcd 1000.6051, found 1001.6030 $[M + H]^+$. Anal. Calcd for $C_{60}H_{76}N_{10}O_4$: C, 71.97; H, 7.65; N, 13.99. Found: C, 71.76; H, 7.61; N, 13.85.

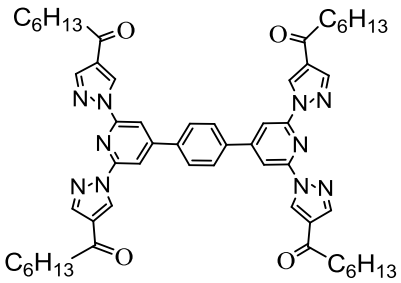

Preparation of boronic acid having phenyl spacer:

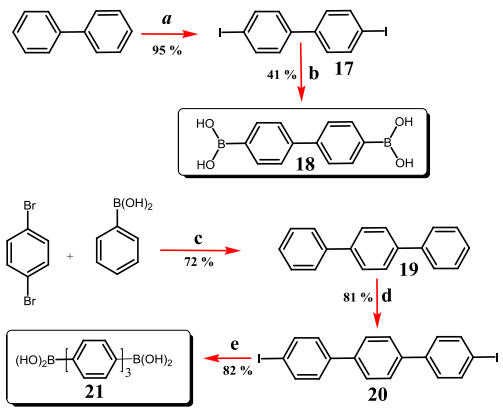

Scheme 2.6 Reagents and conditions: (a) $I_2/HIO_3/H^+$/80 °C; (b) n-BuLi/$B(OMe)_3$/ -78 °C; (c) 1,4-dioxane/Na_2CO_3/3 d/ 70 °C; (d) $I_2/HIO_3/H^+$/80 °C; (e) n-BuLi/$B(OMe)_3$/ -78 °C.

4,4'-diiodobiphenyl (17): Compound **17** was synthesized according to the reported literature procedure[15] in 95% yield. ^{1}H NMR (400 MHz, DMSO-d6, 298K) δ**:** 7.82-7.80 (d, 4H), 7.47-7.45 (d, 4H). ^{13}C NMR (100 MHz, DMSO-d6, 298 K) δ**:** 139.0, 138.2, 129.2, 94.8 ppm. LCMS analysis: calcd *m/z* calcd 406.0, found 405.65. Anal. Calcd for $C_{12}H_8I_2$: C, 35.50; H, 1.99. Found: C, 35.41; H, 1.92. FTIR (KBr disc; ν in cm^{-1}):3059, 2926, 2857, 1647, 1578, 1470, 1379, 1126, 1065, 993, 802, 459.

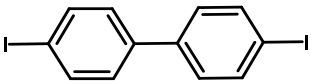

***p*-diphenyldiboronic acid (18):** At -78 °C n-butyl lithium (15.12 mL, 1.6 M in hexane) was added drop wise to a solution of 4,4'-diiodobiphenyl **17** (2.0 g; 4.92 mmol) in dry THF (20 mL). The resultant yellowish suspension was then stirred for an additional 1 h at -78 ^{o}C. Tri-methyl borate (4.0 mL; 35.8 mmol) was added within 15 min at 30 ^{o}C. The resultant pale yellowish solution was stirred for 15h at room temperature. The reaction mixture was acidified with 2 M HCl (50 mL) to get an insoluble white precipitate of **18**. Yield 0.50 g (41%). ^{1}H NMR (400 MHz, DMSO-d_6, 298 K) δ**:** 8.09 (s, 4H), 7.89-7.87 (d, 4H), 7.67-7.65 (d, 4H). ^{13}C NMR (100 MHz, DMSO-d_6, 298 K) δ**:** 142.0, 135.3, 133.8 (low intensity due to quadruple resonance between ^{11}B and ^{13}C nucleus), 126.1 ppm. FTIR (KBr disc; ν in cm^{-1}): 3370 (broad, -OH), 1607, 1555, 1535, 1379, 1341, 1155, 1092, 1022, 999, 814, 737, 627.

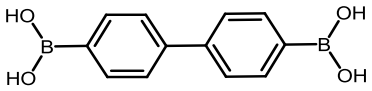

***p*-terphenyl (19):** p-dibromo benzene (2 g, 8.47 mmol), phenyl boronic acid (2.27 g, 18.64 mmol) and $Pd(PPh_3)_4$ (0.489 g, 0.423 mmol) were discharged in a degassed 1,4-dioxane (20 mL) and 5 mL of 2 M Na_2CO_3 was added to this mixture. Then the reaction mixture was heated at 70 ^{o}C for 3 days under inert atmosphere. The progress of the reaction was monitored by TLC. After the disappearance of starting material, the reaction mixture cooled to room temperature and dried on vacuo. Then the residue was treated with water and extracted with DCM. The organic layer was collected and dried over sodium sulphate. The solvent dried on vacuo and the resultant solid residue was washed with pet-ether to remove colored impurities and to get compound **18** in pure form. Yield 1.4 g (72%). ^{1}H NMR (400 MHz, $CDCl_3$-d_1, 298 K) δ**:** 7.7 (s, 4H), 7.67-7.65 (d, 4H), 7.5-7.46 (t, 4H), 7.4-7.36 (t, 2H) ppm. LCMS analysis calcd: *m/z* 230.30, found 231.1. Anal. Calcd for $C_{18}H_{14}$: C, 93.87; H, 6.13 Found: C,

93.76; H, 6.21. FTIR (KBr disc; ν in cm^{-1}): 2926, 1734, 1651, 1618, 1559, 1541, 1472, 1234, 1182, 1107, 1024, 837, 746, 687, 540, 457.

Diiodo-terphenyl (20): Compound **20** was synthesized according to the literature procedure.[15] Yield (81%). ^{1}H NMR (400 MHz, $CDCl_3$-d_1, 298 K) δ**:** 7.84-7.82 (d, 4H), 7.76 (s, 4H), 7.55-7.53 (d, 4H). Elemental analysis: calcd for $C_{18}H_{12}I_2$: C, 44.84; H, 2.51. Found: C, 44.75; H, 2.58. FTIR (KBr disc; ν in cm^{-1}): 2917, 1559, 1456, 1393, 802, 461.

***p*-terphenyldiboronic acid (21):** At -78 °C n-butyl lithium (6 mL; 1.6 M in hexane) was added drop wise to a solution of diiodo-*p*-terphenyl **20** (1.0 g; 2.07 mmol) in dry THF (20 mL). The resultant yellowish suspension was then stirred for an additional hour at -78 ^{o}C. The solution was slowly warmed up to -30 ^{o}C and tri-methyl borate (1.5 mL; 12.42 mmol) was added drop-wise within 15 min. The resultant pale yellowish solution was stirred for 15 h at room temperature. The reaction mixture was acidified with 2 M HCl (50 mL) and the insoluble precipitate was filtered and air dried to get **21** as a white solid. Yield 0.55 g (82%). ^{1}H NMR (400 MHz, DMSO-d_6, 298 K) δ: 8.07 (s, 4H), 7.90-7.88 (d, 4H), 7.79 (s, 4H), 7.71-7.69 (d, 4H). ^{13}C NMR (100 MHz, DMSO-d_6, 298 K) δ: 141.4, 139.7, 135.3, 134.8 (low intensity due to quadruple resonance between ^{11}B and ^{13}C nucleus), 127.7, 126.0 ppm. FTIR (KBr disc; ν in cm^{-1}): 3370 (broad, -OH), 1607, 1555, 1535, 1379, 1341, 1155, 1092, 1022, 999, 814, 737, 627.

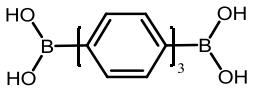

References

1. (a) Lehn, J.-M. *Supramolecular Chemistry,* VCH, Weinheim, **1995**. (b) Schubert, U. S.; Hofmeier, H.; Newkome, G. R., *Modern TerpyridineChemsitry*; Wiley-VCH: Weinheim, **2006**, *69*. (c) Constable, E. C.; Ward, M. D. *J. Chem. Soc., Dalton Trans.* **1990**, 1405. (d) Collin, J. P.; Lainé, P.; Launay, J.-P.; Sauvage, J.-P.; Sour, A. *J. Chem.Soc., Chem. Commun.* **1993**, 434. (e) Chelucci, G; Thummel, R. P. *Chem. Rev.* **2002**, *102*, 3129. (f) Constable, E. C. *Chem. Soc. Rev.* **2007**, *36*, 246. (g) Whittell, G. R.; Hager, M. D.; Schubert, U. S.; Manners, I. *Nat. Mater.* **2011**, *10*, 176.

2. (a) Burnworth, M.; Tang, L.; Kumpfer, J. R.; Duncan, A. J.; Beyer, F. L.; Fiore, G. L.; Rowan, S. J.; Weder, C. *Nature* **2011**, *472*, 334. (b) Iyer, P. K.; Beck, J. B.; Weder, C.; Rowan, S. J. *Chem. Commun.* **2005**, *319*.

3. (a) Mas-Balleste, R. Gomez-Herrero, J. Zamora, F. Chem. Soc. Rev. 2010, 39, 4220. (b) Kelch, S. Rehahn, M. *Macromolecules* **1998**, *31*, 4102.

4. (a) Dobrawa, R.; Lysetska, M.; Ballester, P.; Grune, M.; Würthner, F. *Macromolecules* **2005**, *38*, 1315. (b) Stepanenko, V. Stocker, M. Muller, P. Buchner, M. Wurthner, F. *J. Mater. Chem.* **2009**, *19*, 6816. (c) Bernhard, S.; Goldsmith, J. I.; Takada, K.; Abruňa, H. D. *Inorg. Chem.* **2003**, *42,* 4389. (d) Yu, S. -C.; Kwok, C.

-C.; Chan, W. -K.; Che, C. -M. *Adv. Mater.* **2003**, *15*, 1643. (e) Kadjane, P.; Starck, M.; Camerel, F.; Hill, D.; Hildebrandt, N.; Ziessel, R. Charbonnière, L. J. *Inorg. Chem*. **2009**, *48*, 4601.

5. (a) Schwarz, G.; Bodenthin, Y.; Geue, T.; Koetz, J.; Kurth, D. G. *Macromolecules*. **2010**, *43*, 494. (b) Miyashitaa, N.; Kurth, D. G. *J. Mater. Chem.* **2008**, *18*, 2636.

6. (a) Mugemana, C.; Guillet, P.; Hoeppener, S.; Schubert, U. S.; Fustin, C. A.; Gohy, J. F. *Chem. Commun*. **2010**, *46*, 1296. (b) Hager, M. D.; Greil, P.; Leyens, C.; Zwaag, S. V. D.; Schubert, U. S. *Adv. Mater.* **2010**, *22*, 5424. (c) Ruben, M.; Landa, A.; Lörtscher, E.; Riel, H.; Mayor, M.; Görls, H.; Weber, H. B.; Arnold, A.; Evers, F. *Small* **2008**, *4*, 2229.

7. (a) Li, Y.; Huffmana, J. C.; Flood, A. H. *Chem. Commun*. **2007**, 2692. (b) Meudtner, R. M.; Ostermeier, M.; Goddard, R.; Limberg, C.; Hecht, S. *Chem. Eur. J.* **2007**, *13*, 9834. (c) Li, Y.; Flood, A. H. *Angew. Chem. Int. Ed.* **2008**, *47*, 2649. (d) Meudtner, R. M.; Hecht, S. *Angew. Chem. Int. Ed.* **2008**, *47*, 4926. (e) Juwarker, H.; Lenhardt, J. M.; Pham, D. M.; Craig, S. L. *Angew. Chem. Int. Ed.* **2008**, *47*, 3740.

8. (a) Chandrasekhar, N.; Chandrasekar, R. *J. Org. Chem.* **2010**, *75*, 4852. (b) Chandrasekhar, N.; Chandrasekar, R. *Angew. Chem. Int. Ed*. **2012**, *51*, 3556.

9. (a) Rajadurai, C.; Fuhr, O.; Kruk, R.; Ghafari, M.; Hahn, H.; Ruben, M. *Chem. Commun*. **2007**, 2636. (b) Chandrasekar, R.; Schramm, F.; Fuhr, O.; Ruben, M. *Eur. J. Inorg. Chem.* **2008**, *17*, 2649. (c) Chandrasekhar, N.; Chandrasekar, R. *Chem. Commun.* **2010**, *46*, 2915. (d) Basak, S.; Chandrasekar. R. *Adv. Funct. Mater.* **2010**, *21*, 667. (e) Cavallini, M.; Bergenti, I.; Milita, S.; Ruani, G.; Salitros, I.; Qu, Z.-R.; Chandrasekar, R.; Ruben, M. *Angew. Chem. Int. Ed*. **2008**, *47*, 8596. (f) Zoppellaro, G.; Enkelmann, V.; Geies, A.; Baumgarten, M. *Org. Lett.* **2004**, *6*, 4929.

10. Basak, S.; Hui, P.; Chandrasekar, R. *Synthesis,* **2009**, *23*, 4042.

11. Mello, J. V.; Finney, N. S. *Org. Lett.* **2001**, *3*, 4263.

12. Noyce, D. S.; Schiavelli, M. D. *J. Am. Chem. Soc*. **1968**, *90*, 1020.

13. Kim, E.; Xia, Y.; Whitesides, G. M. *Nature* **1995**, *376*, 581.

14. Solanki, N. K.; Leech, M. A.; McInnes, E. J. L.; Mabbs, F. E.; Howard, J. A. K.; Kilner, C. A.; Rawson, J. M.; Halcrow. M. A. *J. Chem. Soc., Dalton Trans.* **2002**, 1295.

15. Schlickum, U.; Decker, R.; Klappenberger, F.; Zoppellaro, G.; Klyatskaya, S.; Auwärter, W.; Neppl, S.; Kern, K.; Brune, H.; Ruben, M.; Barth, J. V. *J. Am. Chem. Soc*. **2008**, *130*, 11778.

Appendix

A1. Crystal Structure of Ligands *L1* and *L5:*

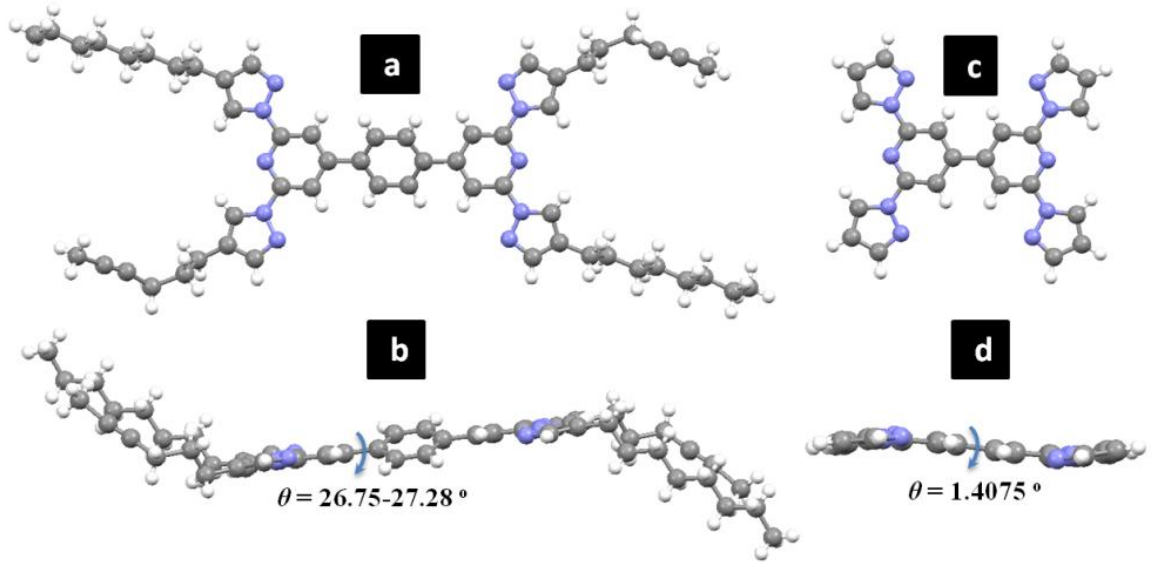

Figure A1 : ORTEP plot (50% probability); (a) and (b) Top and side view of ***L1*** respectively; (c) and (d) top and side view of ***L5***.

A2. Raman Spectra of Ligands and $[L1 \cdot Zn(ClO_4)_2]_n$:

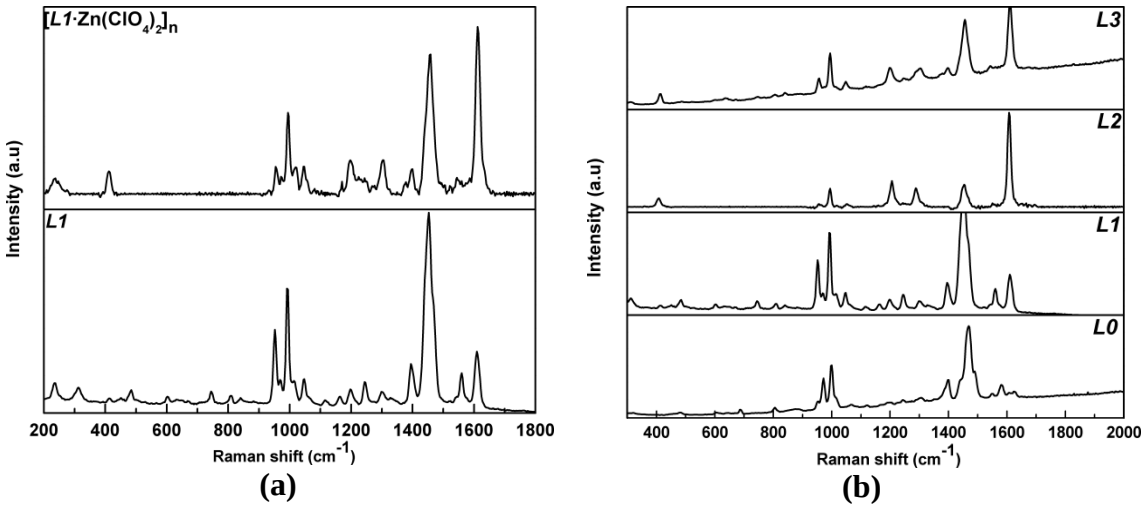

Figure A2 : (a) Bulk Raman spectra of ***L1*** and $[L1 \cdot Zn(ClO_4)_2]_n$. (b) Bulk Raman spectra of all ligands.

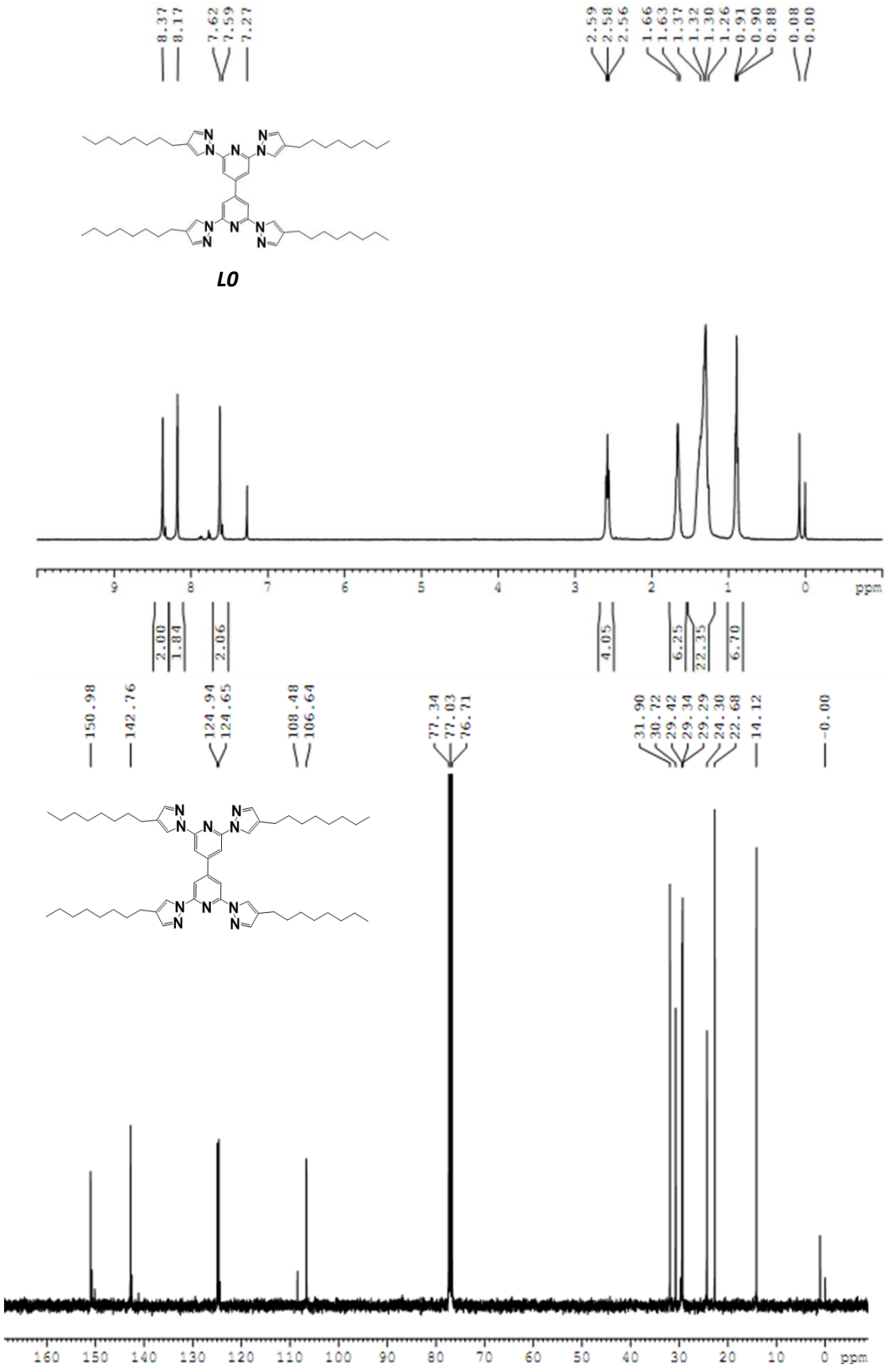
8.37
8.17
7.62
7.59
7.27
2.59
2.58
2.56
1.66
1.63
1.37
1.32
1.30
1.26
0.91
0.90
0.88
0.08
0.00
ppm
2.00
1.84
2.06
4.05
6.25
22.35
6.70
150.98
142.76
124.94
124.65
108.48
106.64
77.34
77.03
76.71
31.90
30.72
29.42
29.34
29.29
24.30
22.68
14.12
-0.00
ppm

L0

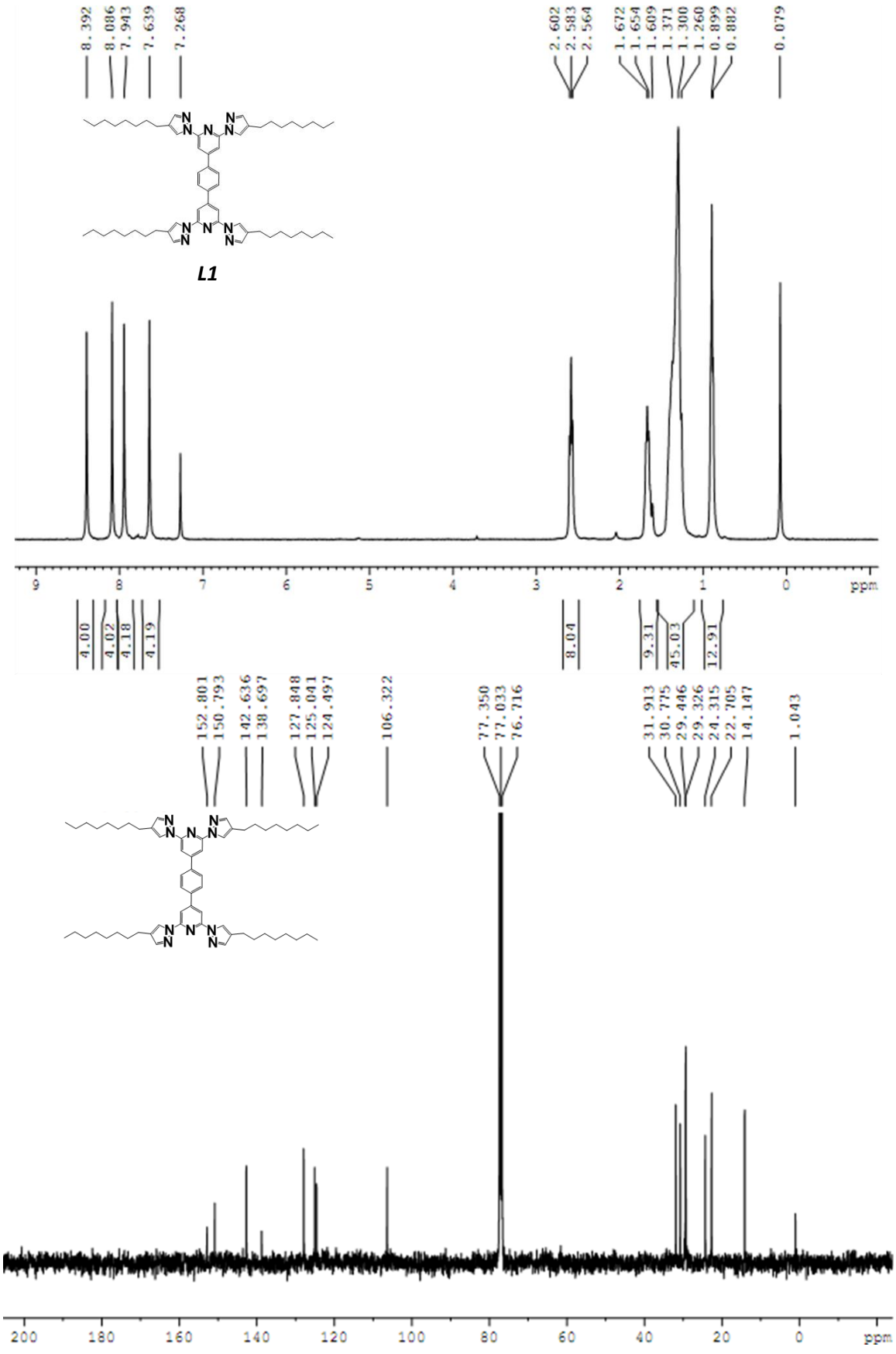
8.392
8.086
7.943
7.639
7.268
2.602
2.583
2.564
1.672
1.654
1.609
1.371
1.300
1.260
0.899
0.882
0.079
L1
ppm
4.00
4.02
4.18
4.19
8.04
9.31
45.03
12.91
152.801
150.793
142.636
138.697
127.848
125.041
124.497
106.322
77.350
77.033
76.716
31.913
30.775
29.446
29.326
24.315
22.705
14.147
1.043
ppm

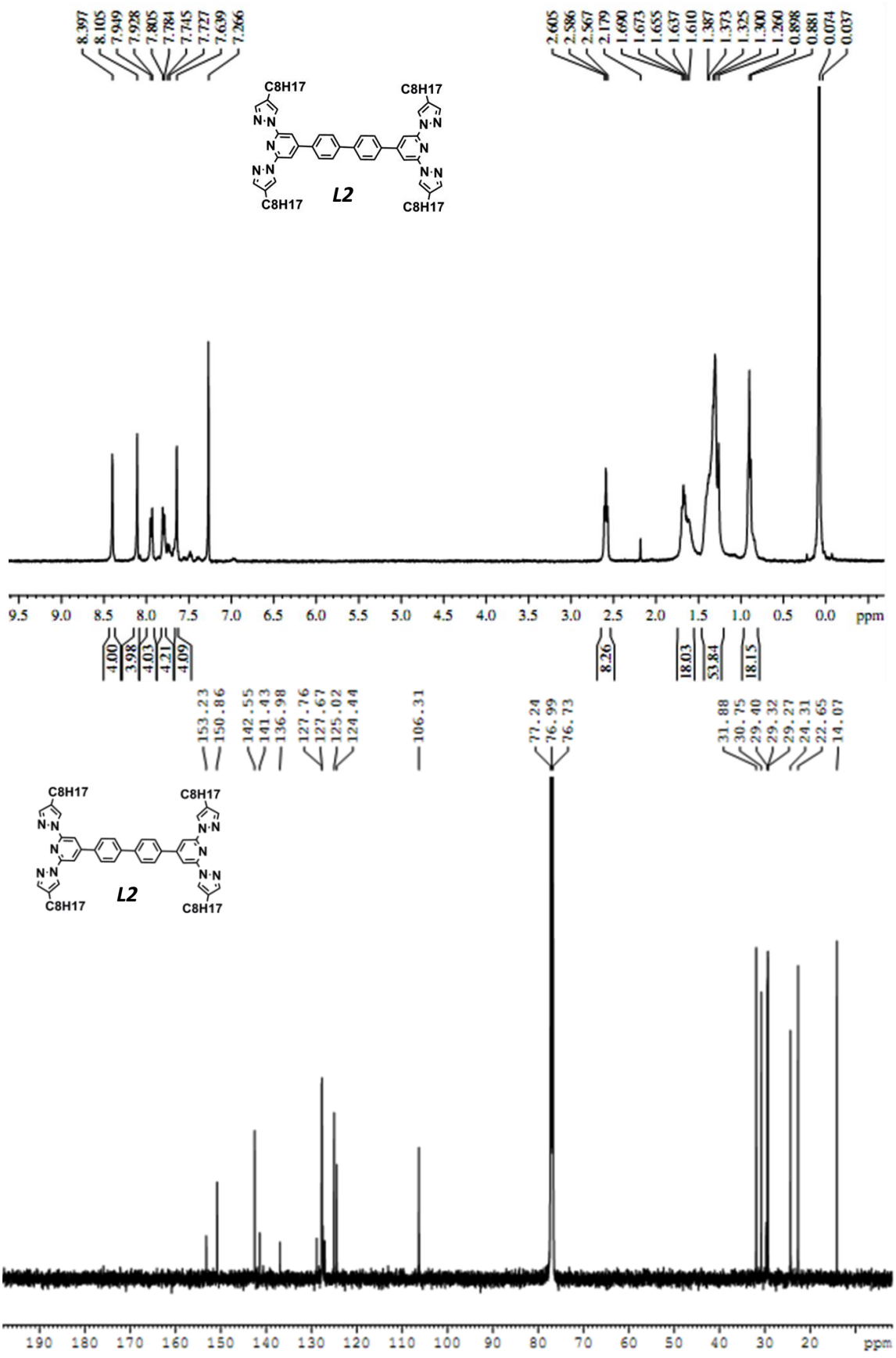
8.397
8.105
7.949
7.928
7.805
7.784
7.745
7.727
7.639
7.266
2.605
2.586
2.567
2.179
1.690
1.673
1.655
1.637
1.610
1.387
1.373
1.325
1.300
1.260
0.898
0.881
0.074
0.037
C8H17
L2
9.5 9.0 8.5 8.0 7.5 7.0 6.5 6.0 5.5 5.0 4.5 4.0 3.5 3.0 2.5 2.0 1.5 1.0 0.5 0.0 ppm
4.00
3.98
4.03
4.21
4.09
8.26
18.03
53.84
18.15
153.23
150.86
142.55
141.43
136.98
127.76
127.67
125.02
124.44
106.31
77.24
76.99
76.73
31.88
30.75
29.40
29.32
29.27
24.31
22.65
14.07
190 180 170 160 150 140 130 120 110 100 90 80 70 60 50 40 30 20 ppm

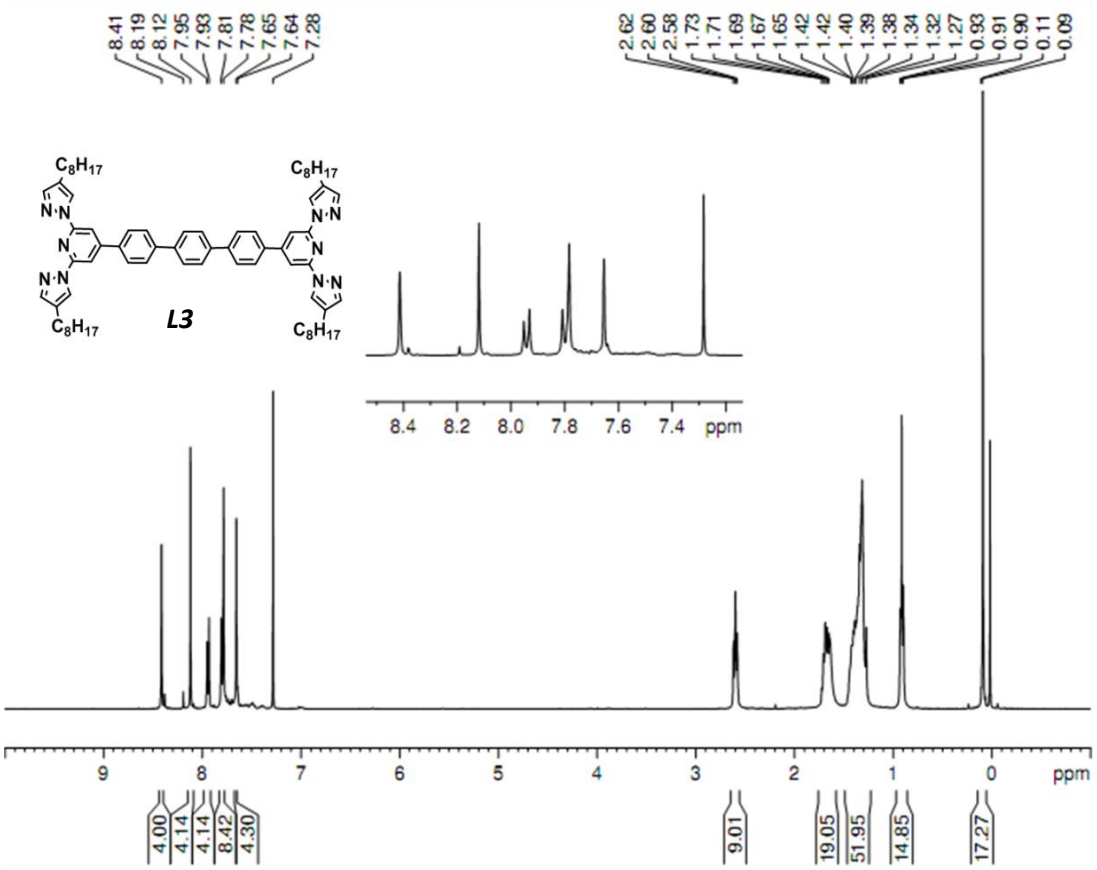
8.41
8.19
8.12
7.95
7.93
7.81
7.78
7.65
7.64
7.28
2.62
2.60
2.58
1.73
1.71
1.69
1.67
1.65
1.42
1.42
1.40
1.39
1.38
1.34
1.32
1.27
0.93
0.91
0.90
0.11
0.09
L3
8.4 8.2 8.0 7.8 7.6 7.4 ppm
9 8 7 6 5 4 3 2 1 0 ppm
4.00
4.14
4.14
8.42
4.30
9.01
19.05
51.95
14.85
17.27

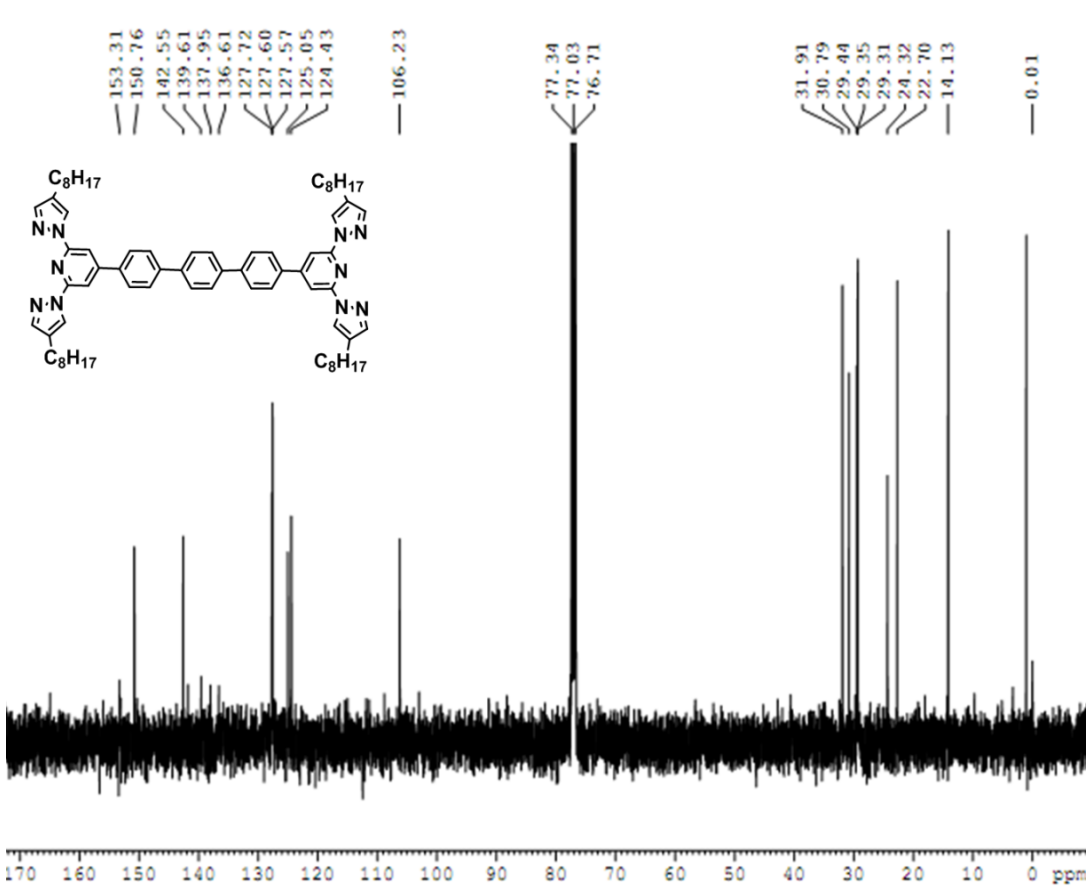
153.31
150.76
142.55
139.61
137.95
136.61
127.72
127.60
127.57
125.05
124.43
106.23
77.34
77.03
76.71
31.91
30.79
29.44
29.35
29.31
24.32
22.70
14.13
0.01
170 160 150 140 130 120 110 100 90 80 70 60 50 40 30 20 10 0 ppm

3

Flexible and Optically Transparent Polymer Embedded Nano/Micro Scale Spin Cross-Over Fe(II) Complex Patterns/Arrays

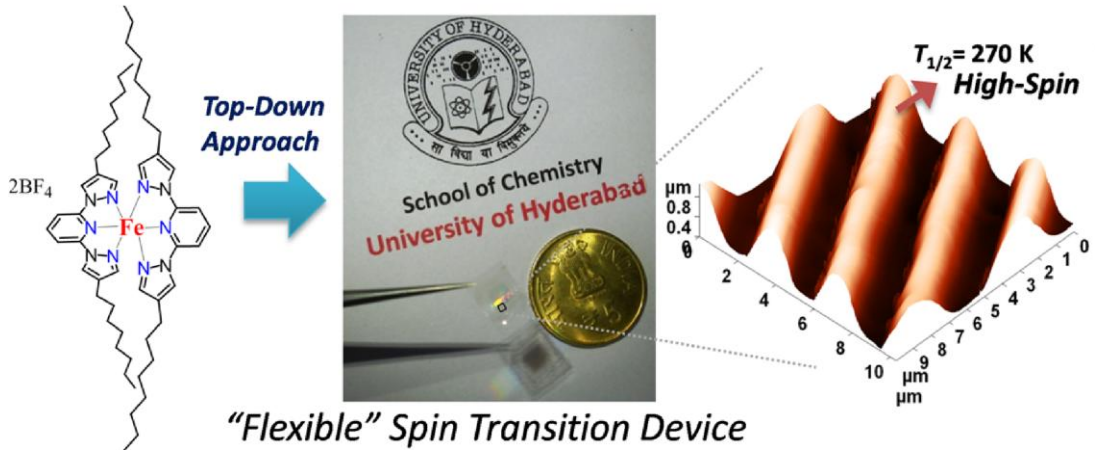

*This chapter is adapted from:

S. Basak, P. Hui, R. Chandrasekar*
Chem. Mater. **2013,** *25*, 3408.

3.1 Abstract

*A novel spin-crossover (SCO) $[Fe^{II}(\mathbf{L4})_2](BF_4)_2$ complex (**C2**) was prepared, where **L4** is 4,4''-dioctylated 2',6'-bispyrazolylpyridine. Complex **C2** shows reversible temperature dependent SCO behaviour with a $T_{1/2}$ centred around 270 K together with a ~2 K wide hysteresis loop. Exploiting the high solubility and hence superior processability of SCO complex **C2**, nano/micro scale arrays and square patterns were fabricated on a glass substrate. Additionally, for the first time, for possible flexible technological applications, the SCO arrays (area 2 × 2 mm^2) were successfully embedded within an optically transparent thin polystyrene film and studied using Raman spectroscopy/imaging technique. Variable temperature Raman spectroscopy studies further confirmed the SCO behaviour of complex **C2**.*

3.2 Introduction

SCO or spin transition compounds, are an efficient spin-state switchable (high-spin; HS ↔ low-spin; LS) bistable inorganic materials proposed for several technological applications such as in molecular memory devices, sensors, and displays.[1-3] Many octahedral Fe(II) complexes are known to show reversible SCO between two different spin states (HS; *S*=2; paramagnetic ↔ LS; *S*=0; diamagnetic) with respect to external stimulus such as pressure,[3] temperature,[3,4] magnetic field,[5a] electric field[1d] and light irradiation.[5b] Among the other applications, one of the uses of these SCO compounds is possible exploitation as logical structures (0 or 1) for information storage.[1c] For potential technological applications, fabrication of diverse nano/micro scale SCO domains having various dimensions and shapes are an essential step.

Great amount of efforts have been taken towards the development of novel procedures to fabricate thin deposits, films and patterned nanostructures composed of SCO compounds preserving the magnetic bistability. The first fabrication of ST thin films was reported by Kahn et al. using Langmuir–Blodgett (LB) techniques[6] and then later developed by many other groups.[7] Patterning of spin crossover compounds was carried out previously by electron beam lithography,[8,9] polymeric masks[10] and also by soft lithographic techniques[11a] such as micro molding in capillaries[11b] and micro transfer molding.[10a] Earlier, Cavallini and Ruben et al. have reported the fabrication of one dimensional (1D) ST micro arrays using PDMS (polydimethylsiloxane) stamps on a glass

substrate.[12] Recently, we have fabricated 1D micro arrays composed of highly soluble $Zn^{(II)}$ coordination polymers prepared from a *back-to-back* coupled tetraoctylated-2,6-bispyrazolylpyridine ligand and $Zn^{(II)}$ ions (discussed in *chapter 2*).[13] Till now all of the existing SCO based nano/micro molding was performed on non-flexible solid substrate. To improve the existing *stiff* SCO patterns/array technology into the next stage *flexible smart devices*, it is necessary to organize (implant) these nano/micro SCO patterns with in an optically transparent polymer substrate.

In this chapter, we present a new synthetic protocol for the preparation of novel 4,4″-dioctylated 2,6-bispyrazolylpyridine (Oct-BPP) ligand ***L4*** and its SCO complex $[Fe^{II}(\boldsymbol{L4})_2](BF_4)_2$ (***C2***). We also present the utilization of model compound ***C2*** to pattern nano/micro scale i) 1D wedge stripes, ii) 1D rectangular stripes and iii) 0D square pillars using LCW (lithographically controlled wetting) technique. Additionally by keeping the *flexible* device fabrication in mind, for the first time, linear SCO arrays were successfully implanted within an optically transparent polymer film. All fabricated nano/micro SCO structures were thoroughly characterized by scanning electron microscopy (SEM), transmission electron microscopy (TEM), atomic force microscopy (AFM), optical microscopy and confocal Raman imaging techniques. The SCO property of the bulk materials was studied by using variable temperature magnetic susceptibility and Raman spectroscopy.

3.3. EXPERIMENTAL SECTION

3.3.1 Synthesis:

Compounds **23** and **24** were prepared according to literature procedure.[14,15a]

2,6-bis(4-(oct-1-ynyl)-1H-pyrazol-1-yl)pyridine (25): A Schlenk flask was charged with 2,6-bis(4-iodo-1H-pyrazol-1-yl)pyridine **24** (500 mg, 1.07 mmol) together with $Pd(PPh_3)_2Cl_2$ (37.89 mg, 0.053 mmol), triphenylphosphene (50 mg, 0.19 mmol) and CuI (200 mg, 0.262 mmol). Freshly distilled anhydrous triethylamine (Et_3N, 20 mL) and 1,4-dioxane (10 mL) were added to it. The flask was carefully degassed by freeze-and-thaw cycles several times. 1-octyne (0.5 mL; d = 0.746 g/mL, 3.24 mmol) was injected into the flask under argon atmosphere and the resulting mixture was heated to 80 °C for 48 h. It was then cooled to room temperature and left for stirring for an additional 1 hour. The mixture was filtered through filter paper and washed with tetrahydrofuran (THF) and the

filtrate was evaporated to get a dark brown solid which was column chromatographed on silica (100-200 mesh) using initially (60:40) DCM/Hexane and finally (80:20) DCM/Hexane to get white solid of **25**. Yield 350 mg (76%). mp 86-87 ^{o}C. ^{1}H NMR (400 MHz, $CDCl_3$) δ: 8.6 (s, 2H), 7.92-7.90 (t, 1H), 7.82-7.81 (d, 2H), 7.74 (s, 2H), 2.43-2.39 (t, 4H), 1.66-1.58 (m, 4H), 1.48-1.45 (m, 4H), 1.34 (s, 8H), 0.93-0.90 (m, 6H) ppm. ^{13}C NMR (100 MHz, $CDCl_3$) δ: 149.5, 144.6, 141.5, 129.0, 109.6, 106.6, 92.7, 70.6, 31.4, 28.7, 28.6, 22.6, 19.5, 14.1 ppm. FTIR (KBr disc; ν in cm^{-1}): 3146 *(-C≡C-)*, 2926, 2848, 2361, 1599, 1464, 1026, 953, 800, 656. Raman Shift (powder, RT, λ_{ex} = *633 line of* He-Ne laser): 954, 997, 1076, 1260, 1405, 1442, 1487, 1569, 1588, 2241*(-C≡C-)* cm^{-1}. LC-MS *m/z* calcd 427.27, found 428.10. ESI-MS: *m/z* calcd 427.27, found 428.2714 [M^{+}+H]. Anal. Calcd for $C_{27}H_{33}N_5$: C, 75.84; H, 7.78; N, 16.38%. Found: C, 75.92; H, 7.85; N, 16.27%.

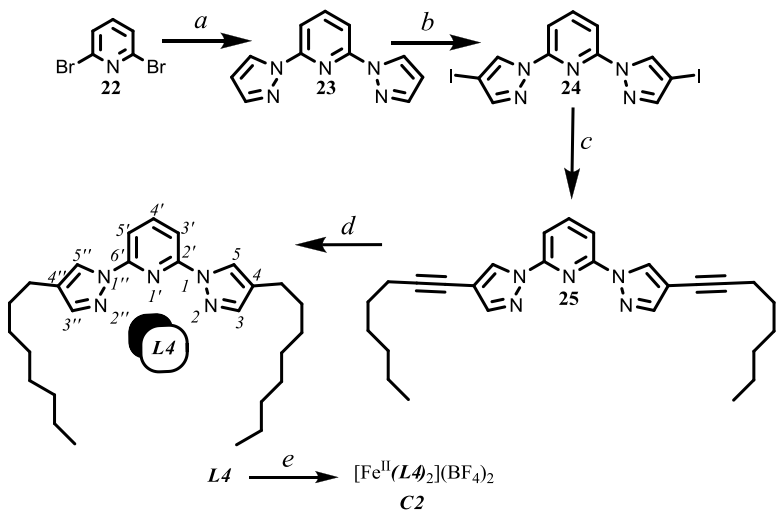

Scheme 3.1 Reagents and conditions: (a) K/Diglyme, 5 days; (b) I_2/HIO_3; (c) 1-octyne, CuI, $Pd(PPh_3)_2Cl_2$, PPh_3, dioxane/TEA; (d) Pd/C, H_2, 1 h; (e) DCM/MeOH , $Fe(BF_4)_2{\cdot}6H_2O$.

2,6-bis(4-octyl-1H-pyrazol-1-yl)pyridine (*L4*): To a degassed solution of **25** (0.3 g, 00.7 mmol) in EtOAc (60 mL) was added 10% Pd/C (0.073 g, 0.07 mmol), the mixture was stirred under H_2 atmosphere (at ambient pressure) and monitored by TLC. After 1 hour the mixture was filtered through a celite plug to remove activated Pd/C and subsequently washed with 100 mL of EtOAc. The collected fractions were combined and concentrated in vacuum to get compound ***L4*** as viscous oil. Yield 0.302 g (>99%) ^{1}H NMR (400 MHz, $CDCl_3$) δ: 8.33 (s, 2H), 7.90-7.86 (t, 1H), 7.77-7.75 (d, 2H), 7.59 (s, 2H), 2.58-2.54 (t, 4H), 1.67-1.64 (m, 4H), 1.36-1.29 (m, 20H), 0.89-0.87 (m, 6H) ppm. ^{13}C NMR (100 MHz, $CDCl_3$) δ: 150.1, 142.5, 141.1, 124.8, 124.4, 108.5, 31.9, 30.8, 29.7, 29.4, 29.3, 24.3, 22.7, 14.1 ppm. FTIR (KBr disc; ν in cm^{-1}): 2958, 2918, 2848, 1604, 1585, 1475, 1390, 970, 800, 648, 607, 536, 480, 467. Raman Shift (powder, RT, λ_{ex} = *633 line of* He-Ne laser): 954, 997, 1397, 1439, 1469, 1591, 1609 cm^{-1}. LCMS analysis: *m/z* calcd

435.34, found = 436.25 (positive mode). ESIMS: *m/z* calcd 435.34, found 436.3403 [M^+ + H]. Anal. Calcd for $C_{27}H_{41}N_5$: C, 74.44; H, 9.49; N, 16.08%. Found: C, 74.28; H, 9.41; N, 16.21%.

$[Fe^{II}(L4)_2](BF_4)_2$ (*C2*): A 100 mL flask was charged with ***L4*** (80 mg, 0.183 mmol) and 10 mL DCM was added to it. A solution of $Fe(BF_4)_2 \cdot 6H_2O$ (31 mg, 0.091 mmol) in MeOH (10 mL) was added to the above solution. The mixture was heated to reflux for 12 h under N_2 atmosphere. After cooling, the solvent was evaporated on a rotary evaporator. The resultant residue was washed with diisopropyl ether (20 mL × 1) and dried in vacuum to get a yellow powder of ***C2***. Yield 74 mg (73%). Anal. Calcd for $C_{54}H_{82}B_2F_8FeN_{10}$: C, 58.92; H, 7.51; N, 12.72%. Found: C, 58.83; H, 7.61; N, 12.52%. FTIR (KBr disc; ν in cm^{-1}): 3118, 2958, 2927, 2856, 1620, 1572, 1491, 1400, 1321, 1103 *(broad, B-F)*, 1014, 991, 796, 725, 625. M.p.: ~80 °C.

3.3.2 Method for pattering. Micro patterning of ***C2*** was carried out by drop casting 20 μL acetonitrile solution of ***C2*** (2 mg/mL) on a glass substrate. Before use, the substrate was cleaned by sonication using electronic-grade water (Milli-Q-pure quality), acetone (Aldrich chromatography quality) and 2-propanol (Aldrich spectroscopic-grade quality) for 2 min each. Before micro patterning, an acetonitrile (Aldrich, ≥ 99% purity) solution of ***C2*** was filtered through a Whatman filter paper.

3.3.3 Stamps for lithograph:[12,13] Elastomeric PDMS (Sylgard 184 Down Corning) stamps were prepared by replica molding of a series of structured masters. The curing process was carried out for 6 h at 60 ^oC. Once cured, the replica (Fig. 3.1) was carefully peeled off from the master and used as such for nano/micro patterning techniques. Test gratings TGQ1, TGZ3 and TGG1 were purchased from NT-MDT and used as masters.

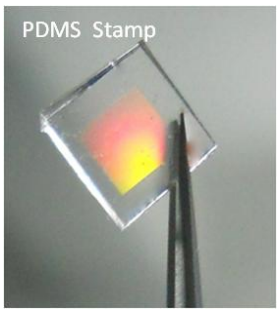

Figure 3.1 A PDMS stamp.

3.3.4 Confocal Raman micro spectroscopy studies: Raman spectra of the samples were recorded on a WI-Tec confocal Raman spectrometer equipped with a Peltier-cooled CCD detector. Using a 600 grooves/mm grating BLZ = 500 nm, the integration time was typically 2.0000 s. Ten accumulations was performed for acquiring a single spectrum. For imaging the integration time was typically 2.000 s, keeping in mind that the x or y resolution is ~ 250 nm for a 100X objective having NA 0.95, four points per line and four line per image was taken for imaging of a 1μm × 1μm area. A He-Ne 633 nm laser was

used as an excitation source for the Raman scattering. All measurements were done at ambient conditions.

3.4 RESULT AND DISCUSSION

3.4.1 Synthesis:

Ligand ***L4*** was synthesized from a commercially available 2,6-dibromopyridine in four steps in good yields (Scheme 3.1). Conversion of 2,6-dibromopyridine into 2,6-bispyrazolylpyridine **23** was carried out as per the reported procedure.[14] Compound **23** was successfully converted to its diiodinated derivative **24** as per our earlier procedure in 74% yield.[15,16] Transformation of compound **24** into **25** was achieved via Sonogashira coupling reaction conditions by using 1-octyne in Et_3N/THF solvents using $Pd(PPh_3)_2Cl_2$ catalyst in 78% yield. The alkynes groups in **25** was reduced using Pd/C under H_2 atmosphere to obtain highly soluble 2,6-dioctylated bispyrazolylpyridine ***L4*** in a quantitative 99% yield. The reduction of compound **25** was confirmed by disappearance of -*C*≡*C*- peak in ^{13}C NMR at 92.7 and 70.6 ppm and appears below 40 ppm i.e. aliphatic region. The progress of the reaction can also be confirmed by Raman spectroscopic measurement. The -*C*≡*C*- Raman shift which appears at 2241 cm^{-1}, disappears for ***L4*** (Fig. A2). An yellowish mononuclear iron(II) complex $[Fe^{II}(\boldsymbol{L4})_2](BF_4)_2$ (***C2***), was synthesized from ***L4*** by using the respective Fe(II) salt in 2:1 DCM/MeOH solvent mixture. Attempts to crystallize the complex ***C2*** in various solvents were unsuccessful as it formed single crystals not suitable for X-ray diffraction.

3.4.2 UV-Vis Spectroscopy Studies:

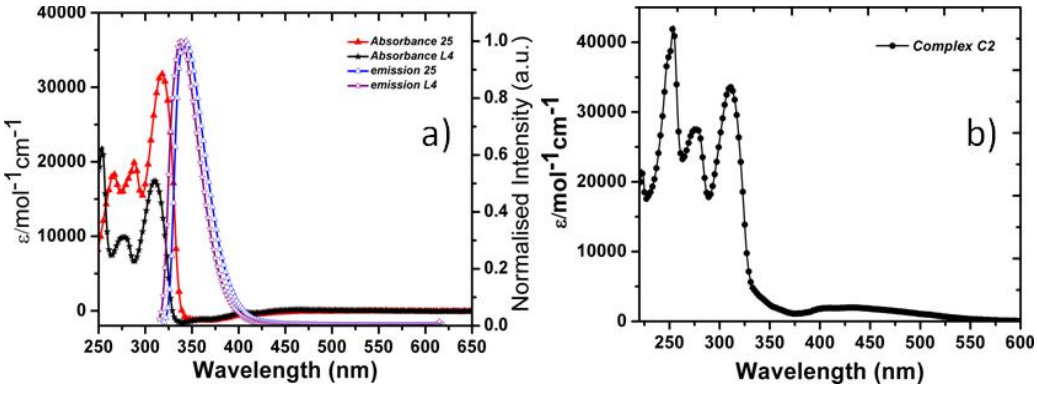

Figure 3.2 (a) Absorption and emission spectra of ligand ***L4*** and compound **25** recorded at RT. (b) Absorption spectra of complex ***C2*** in DCM recorded at RT.

Compounds **25** and ***L4*** in dichloromethane (DCM) displayed absorption/emission maxima (λ_{max}) centered at 318/343 and 310/337nm, respectively. Whereas the UV−Vis absorption studies of ~10^{-5} M DCM solution of complex ***C2*** showed an absorption maximum (λ_{max}) at 314 nm, (Fig. 3.2 b) which is 4 nm red shifted compared to ligand ***L4***. The broad band in Fig. 3.2b at around 400-500 region can be assigned to metal to ligand charge transfer.[17]

3.4.3 Magnetic Susceptibility Studies:

The temperature dependent magnetic susceptibility of complex ***C2*** showed a reversible SCO behavior at multiple heating and cooling cycles (Fig. 3.3). The heating mode measurement was performed only up to 340 K to avoid sample melting. At 340 K the product of the molar magnetic susceptibility and temperature (χT) is 3.56 emu K mol^{-1}, which is almost close to an expected value for a HS iron(II) ion (S = 2). Upon cooling the χT value decreased sharply and reached a minimum value of 1.03 emu K mol^{-1} down to ~ 210 K indicating operating SCO behavior. The calculated $T_{1/2}$ value of this regime is 270 K, which remained nearly constant for three heating and cooling cycles. Interestingly, the SCO curve was accompanied by a hysteresis loop ($\Delta T_{1/2}$). In the first measurement cycle the $\Delta T_{1/2}$ was about 5 K, which reduced to 2 K at the end of the third cycle, indicating the evaporation of trapped solvent/moisture from the microcrystalline powder sample. Below, 210 K the χT value decreased in a sluggish manner and reached 0.34 emu K mol^{-1} at 16 K. Upon subsequent cooling the χT value dropped down abruptly to the minimum value of 0.07 emu K mol^{-1} at 2 K because of zero-field splitting of the remaining HS molecules. Calculation of the number fraction (f) involved in the SCO event showed that ca. 70% of the molecules undertake rather sharp SCO in the temperature range of 340 K-210 K and the remaining fractions show very

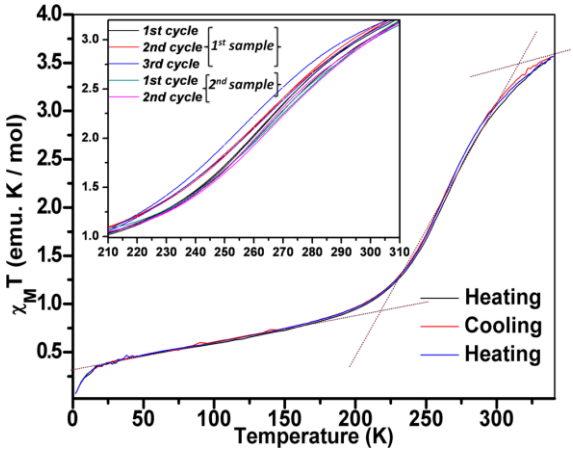

Figure 3.3 The χT *vs* T plot for the complex ***C2*** in the temperature range of 2–340 K in the heating, cooling and heating mode cycles with an applied DC magnetic field of 0.5 T. Inset shows the multiple cycle measurements of samples obtained from two different batches.

sluggish SCO below 210 K down to 16 K. The lowest value of about 0.34 emu K mol^{-1} in the sluggish plateau indicates the presence of paramagnetic impurities in the sample. EPR measurement of the sample down to 4 K confirmed the presence of HS state Fe(III) impurities by displaying characteristic peaks (Fig. A3).

3.4.4 Raman Spectroscopy Studies:

Furthermore in Fe–N_6 type SCO compounds; the difference in the average Fe–N bond distances between HS and LS states is ~ 0.2 Å. This is due to the population of the anti-bonding e_g* orbitals in the HS state. Hence Raman spectroscopy at variable temperature is a very sensitive technique to probe the Raman active vibration modes associated with HS↔LS state structural transformation in Fe(II) complexes. Confocal Raman spectroscopy investigations of complex ***C2*** at 77 K (HS 14%; LS 86 %), 298 K (HS 88%; LS 12%) and 323 K (99% ~ HS) were performed to monitor the SCO event. In comparison to the Raman spectrum at 348 K, the low temperature spectrum showed two new prominent peaks at 899 cm^{-1} and 1127 cm^{-1}. Additionally, the intensity of the peaks at 1021 cm^{-1} and 1398 cm^{-1} gradually increased in the LS state. This observation supports the operating SCO phenomenon in ***C2***. The other major vibration bands at 964 cm^{-1}, 998 cm^{-1}, 1021 cm^{-1}, 1398 cm^{-1}, 1441 cm^{-1}, 1445 cm^{-1}, 1590 cm^{-1} and 1610 cm^{-1} correspond to complex ***C2*** in both spin states (Fig. 3.4).

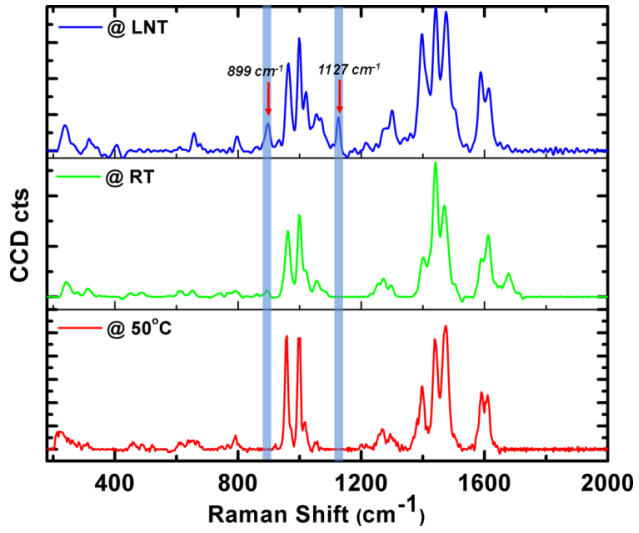

Figure 3.4 Variable temperature Raman spectra of complex ***C2***. Raman signals at 77 K, 298 K and 323 K.

3.4.5 Micro/Nano Fabrication

The octahedral SCO complex ***C2*** was highly soluble in common solvents because of the presence of four octyl chains per Fe(II) complex molecule. Taking advantage of its solubility, lithographic patterning of SCO compound ***C2*** into several geometrical shapes embedded within an optically transparent flexible polymer film was envisaged. Hence,

several new PDMS stamps consists of i) 1D wedge stripes, ii) 1D rectangular stripes and iii) 0D square pillars from several commercially available AFM test gratings, were prepared (Fig. 3.5 and 3.6).

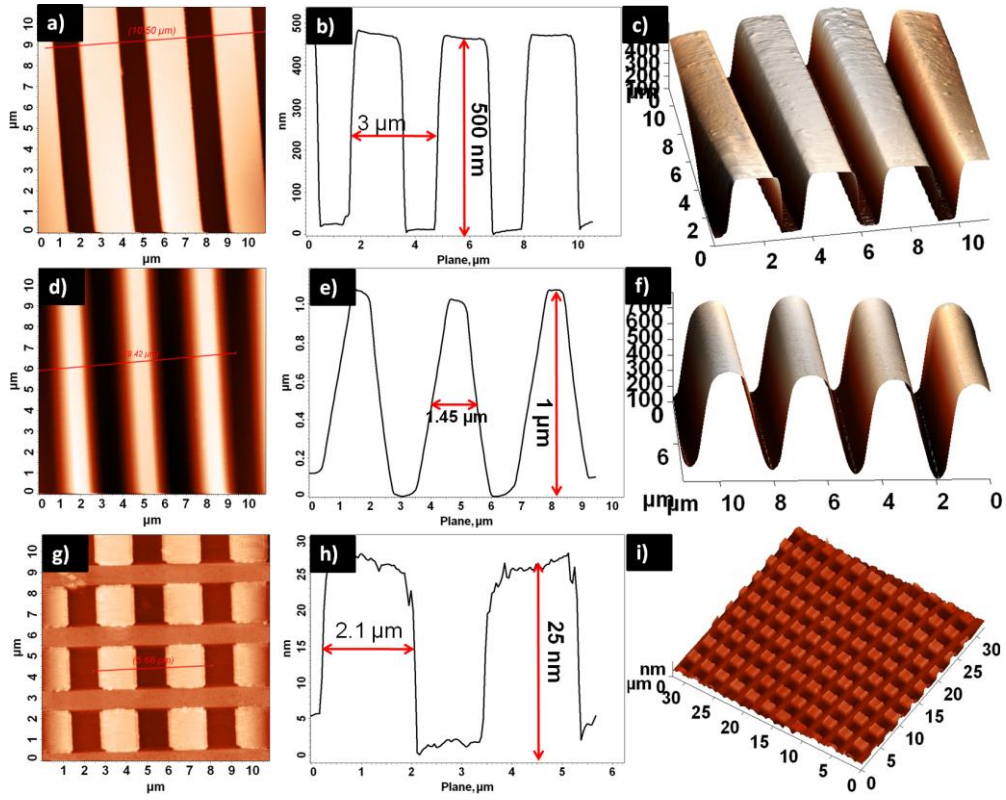

Figure 3.5 Non contact mode AFM images, height profile and 3D image of (a, b and c) Rectangular pattern, (d, e and f) Triangle pattern, and (g, h and i) Square pattern of molds.

For nano/micro fabrication, at first LCW technique on glass slide was adopted. A 20 μL acetonitrile solution of complex ***C2*** was placed on a clean glass slide. After that the PDMS stamp was gently placed on the solution meniscus and the stamp was pressed with a weight of ~ 10 g. This pressure allowed the solution to stay within the micro channels

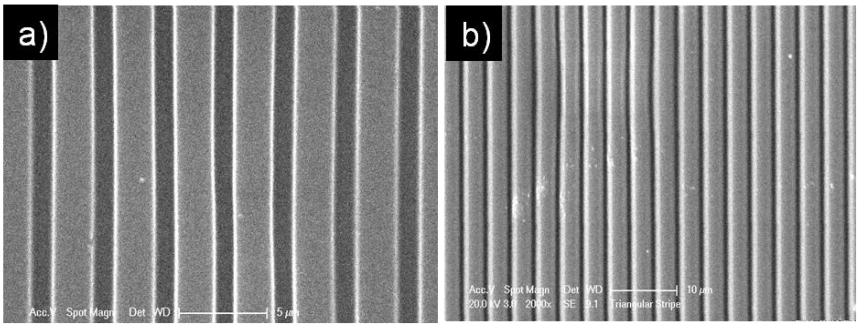

Figure 3.6 SEM images of (a) Rectangular pattern, (b) Triangle pattern of mold.

of the stamp. As the solvent evaporates, the solute precipitates onto the substrate only

below the micro channels, giving rise to a structured pattern that replicates the negative features of the stamp. The confocal microscope (Fig. 3.7a) and SEM image (Fig. 3.7b) of

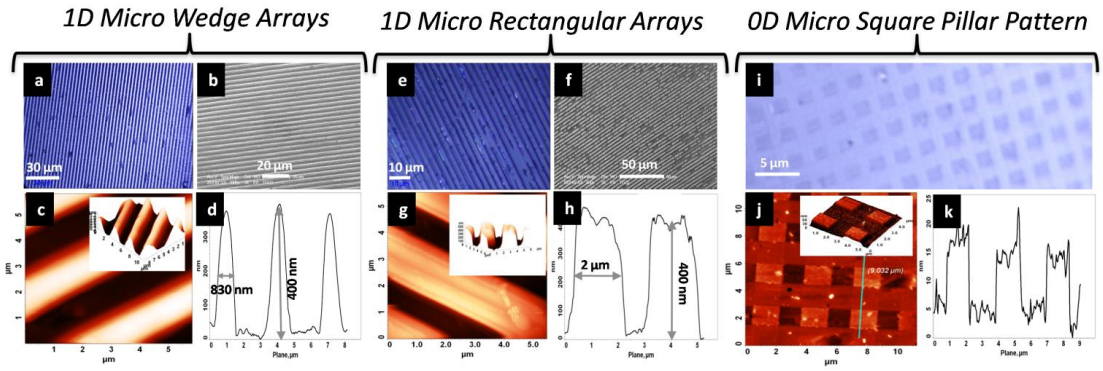

Figure 3.7 a,e,i) Optical images of wedge stripes, rectangular stripes, and square pillars, respectively. b,f) SEM images of wedge and rectangular stripes. c,g,j) AFM 3D images of wedge stripes, rectangular stripes, and square pillars, respectively. d, h, k) AFM topographic profile (height and width) of the patterns shown in c,g,j respectively.

the 1D wedge stripes showed that the length of a SCO stripe is extended up to several hundred micrometers with the height within the submicron domain. The AFM profile measurements of the wedge stripes showed that the height, FWHM (full width at half maxima) and period/channel parameters were 400 nm, 830 nm and 3 μm, respectively (Fig. 3.7c, d).

The triangular edge angle of a stripe was about 70°. Investigation of the rectangular stripes by confocal microscopy and SEM studies revealed the formation of periodic micro stripes of several millimeters long which are well separated by empty

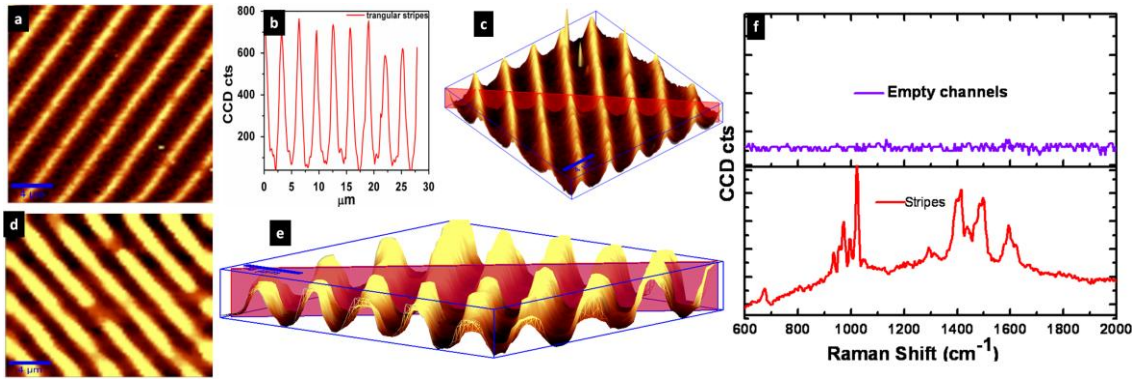

Figure 3.8 Micro-Raman image of wedge and rectangular patterns: a) Raman image of a wedge pattern. b) Raman intensity profile along the red line in c. c) Raman 3D image profile. d) Raman image of rectangular pattern. e) Raman 3D profile. f) Raman signal from the empty channel (violet line), Raman signal along the stripes (red line).

channels (Fig. 3.7e, f). AFM topography measurement of the same sample showed that

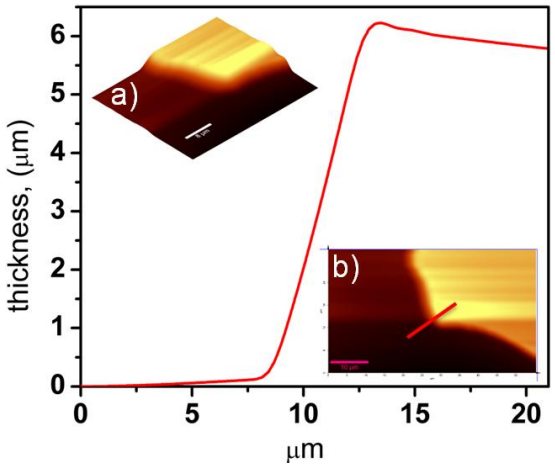

Figure 3.9 Measurement of the thickness of polystyrene film before embedding SCO rectangular pattern. The inset (a) shows a 3D profile of the film and (b) shows topographic image of ultrathin film. The thickness was measured along the red line.

the rectangular micro stripes width × height × roughness (along the stripe) profiles were about 2 μm × ~ 400 nm × ~ 7 nm, respectively, with a uniform periodicity (Fig. 3.7g, h). The empty channel width between the two adjacent micro stripes was about 1.5 μm. Similarly, arrays of 0D micro square pillars were fabricated, which might be useful as logical structures with photonic properties, if the synergy between the two properties is established. The optical microscope evidently displayed the presence of 0D micro square pillar arrays covering wide surface area (Fig. 3.7i). AFM measurements revealed the formation of nearly perfect squares with the height (H) and width (W) profiles of 25 nm × 1.5 μm, respectively (Fig. 3.7j, k). Here, the height of each square is 27 times smaller than the height of 1D arrays. The top surface area of each square is just 2.25 μm^2. Confocal Raman spectroscopy (laser: He-Ne 633 nm) studies evidently confirmed the chemical composition of all arrays by displaying characteristic peaks corresponding to complex ***C2*** $[Fe^{II}(\boldsymbol{L4})_2](BF_4)_2$. Furthermore the empty channel/areas showed no Raman signals indicating the precision and quality of the patterns (Fig. 3.8).

3.4.6 Fabrication of Flexible SCO Device:

Finally to fabricate a flexible, compact and easy to handle nano/micro scale transparent SCO device, as a model, we intended to embed these micro stripes within a transparent polymer film. In this context, we found polystyrene (PS) quite attractive, since it is easy to handle and dissolves in most of the organic solvent except acetonitrile. The solubility of the polymer plays an important role because the polymer should not dissolve in the solvent which is used for the preparation of SCO nano/micro patterns. For fabrication, at first a solution of PS in toluene was prepared by dissolving 125 mg of PS in 2 mL of toluene. Then a thin layer of PS was fabricated on a clean and smooth glass substrate of dimension (1.2 cm × 1.5 cm) by drop casting of 100 μL of the polymer solut-

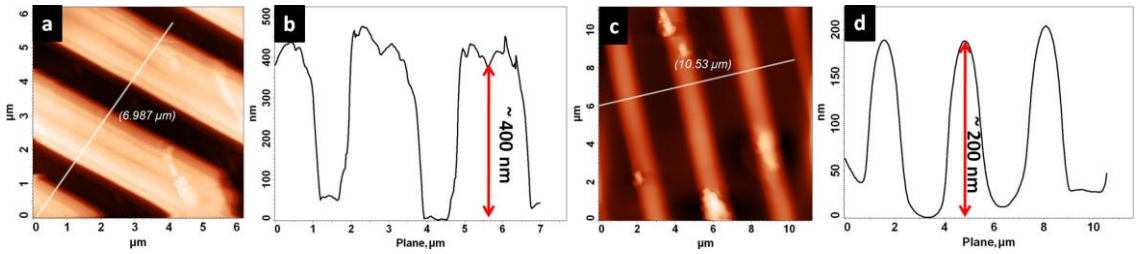

Figure 3.10 (a) Rectangular SCO pattern formed on top of a polystyrene film. (b) Corresponding profile along the white line shows the height of the pattern is around 400 nm. (c) Topographic image of embedded pattern i.e. after forming a top layer of polystyrene on the pattern. (d) Corresponding profile along the white line in Fig. (c) shows the pattern height is around 200 nm.

-ion. Upon evaporation of the solvent, a free standing thin film of thickness around 5-6 μm was obtained (Fig. 3.9). The thickness of a sample film was determined by scratching the film with a scalpel and then measuring the lateral profile by AFM. Subsequently, a 1D rectangular stripe composed of SCO complex ***C2*** was fabricated on the top of the PS layer. The formation of the rectangular stripes was easily observed by confocal optical microscope. Finally, the SCO pattern was concealed by carefully spin coating a PS solution without destroying the lower PS layer. The photograph of flexible SCO device of area 2 × 2 mm^2 embedded within an optically transparent polymer film is shown in (Fig. 3.12).

For TEM measurement the SCO device was fabricated on a copper-coated TEM grid and the top and bottom PS layers were formed by spin coating of a toluene solution of PS at 1000 rpm for 10s. The total entrenched polystyrene layer thickness is around 6.2 μm. The bottom layer thickness is ~ 5-6 μm and top layer thickness is ~ 200 nm as measured from AFM (Fig. 3.10). However it is possible to change the polymer layer thickness by changing the concentration of PS solution and spin coating speed. TEM

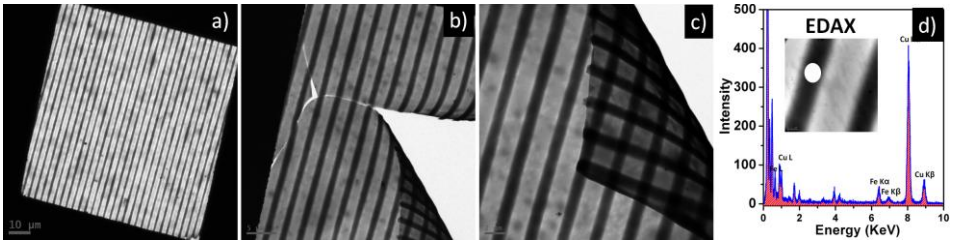

Figure 3.11 a) SCO complex (***C2***) embedded PS film formed on TEM grid (scale bar is 10 μm). b and c) A folded film displaying its flexibility. d) EDAX performed on the SCO stripes is marked in white circle displaying Fe signals for K_α, K_β and L lines at 6.4, 6.9 and 0.65 KeV, respectively.

investigation of the flexible polymer embedded SCO thin film clearly showed a light and

dark areas from the polymer and SCO pattern, respectively (Fig. 3.11a-c). Additionally, the energy dispersive X-ray analysis (EDAX) evidently confirmed the presence of Fe in the dark SCO patterns, by exhibiting characteristic Fe signals (Fig. 3.11d). Raman spectroscopy/imaging of the embedded film showed collective signals from PS and complex ***C2***. Imaging of Raman signal (at 958 cm^{-1} corresponds to complex ***C2***) established the presence of rectangular stripe at regular intervals within the polymer matrix (see red color, Fig. 3.12a, b). Imaging of the PS signal (1037 cm^{-1}) is shown in blue in color, which confirmed the distribution of polymer in the entire area of the film (Fig. 3.12c, d). The combination of the two images (Fig. 3.12b and Fig. 3.12d) is shown in (Fig. 3.12f). Here, the blue area indicates the presence of PS and the pink lines (red + blue color code mixing) correspond to complex ***C2*** stripes as well as PS.

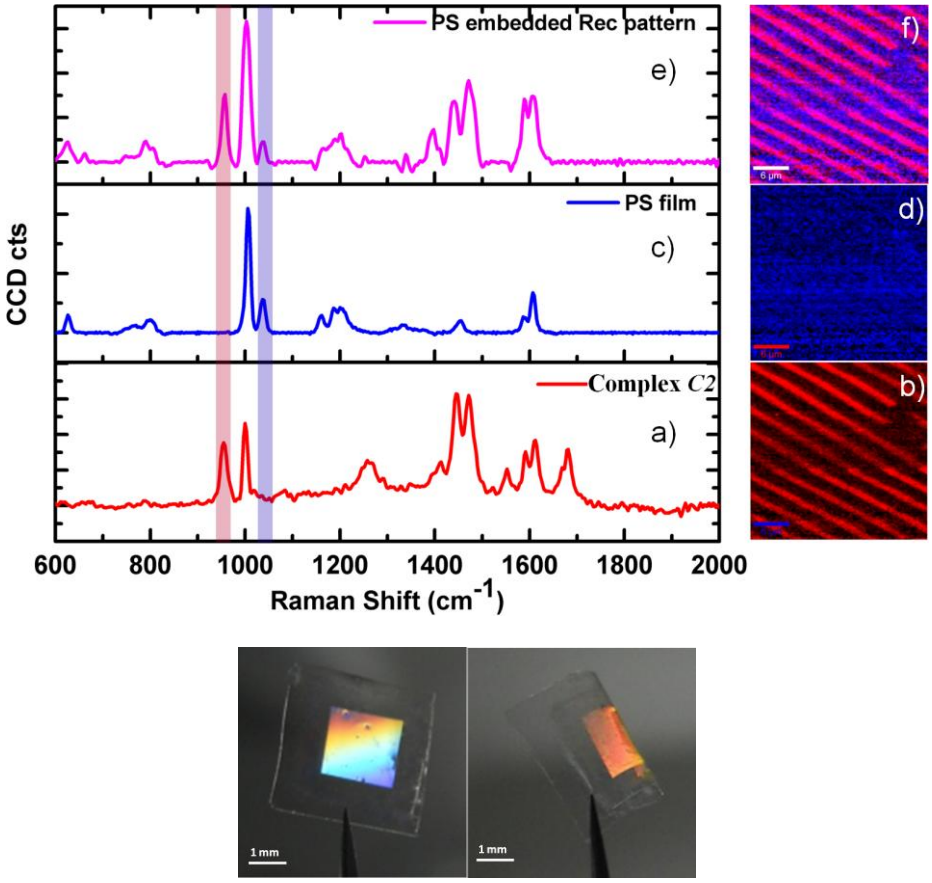

Figure 3.12 Raman spectroscopy/images of a flexible SCO complex ***C2*** embedded PS film. a) Raman spectrum of complex ***C2***. b) Imaging of the SCO device embedded PS film using complex ***C2*** peaks. c) Raman spectrum of bulk PS film. d) Imaging of the SCO device embedded PS film using PS peaks. e) Raman spectrum of SCO complex ***C2*** embedded film. f) Combined image of (b) and (d). The bottom photographs show the flexibility of the SCO device embedded within the optically transparent polymer film.

3.5 Conclusions

A highly soluble Fe(II) SCO compound with the $T_{1/2}$ of 270 K was prepared from a novel 4,4″-dioctylated 2,6-bispyrazolylpyridine ligand. Various nano/microscale geometric patterns composed of the Fe(II) SCO complex was successfully fabricated. Keeping in mind that the SCO pattern can act as future memory based devices, one of the patterns was embedded within an optically transparent and flexible polymer. The embedded film was well characterized to support their fabrication as well as functional behaviour. The presented technology is very simple, unprecedented and promising for potential future development in the SCO-based memory storage devices.

References

1. (a) Garcia, V.; Bibes, M. *Nature*, **2012**, *483*, 279. (b) Bousseksou, A.; Molnár, G.; Salmon, L.; Nicolazzi, W.; *Chem. Soc. Rev.* **2011**, *40*, 3313. (c) Kahn, O.; Martinez, C. J. *Science* **1998**, *279*, 44. (d) Bousseksou, A.; Molnar, G.; Demont, P.; Menegotto, J. *J. Mater. Chem.* **2003**, *13*, 2069. (e) Meded, V.; Bagrets, A.; Fink, K.; Chandrasekar, R.; Ruben, M.; Ever, F. *Phys. Rev. B.* **2011**, *83*, 245415. (f) Halcrow, M. A. *Chem. Soc. Rev.* **2011**, *40*, 4119. (g) Halcrow, M. A. *Coord. Chem. Rev.* **2009**, *253*, 2493. (h) Halcrow, M. A., Ed.; Spin Crossover Materials: Properties and Application; Wiley-Blackwell: Oxford, U.K., 2013. (i) Olguín, J.; Brooker, S. *Coord. Chem. Rev.* **2011**, *255*, 203. (j) Wagner, S.; Kisslinger, F.; Ballmann, S.; Schramm, F.; Chandrasekar, R.; Bodenstein, T.; Fuhr, O.; Secker, D.; Fink, K.; Ruben, M.; Weber, H. B. *Nat. Nanotech.* **2013,** *8*, 575.

2. (a) Bonhommeau, S.; Guillon, T.; Daku, L. M. L.; Demont, P.; Costa, J. S.; Letard, J. F.; Molnar, G.; Bousseksou, A. *Angew. Chem. Int. Ed.* **2006**, *45*, 1625.

3. (a) Letard, J. F.; Guionneau, P.; Goux-Capes, L. Towards Spin Crossover Applications. In *Spin Crossover in Transition Metal Compounds III*; Gütlich, P., Goodwin, H. A., Eds.; Topics in Current Chemistry; Springer: Berlin, **2004**; Vol. 233; 221. (b) Pritchard, R.; Kilner, C. A.; Halcrow, M. A. *Chem. Commun.* **2007**, 577. (c) Bousseksou, A.; Boukheddaden, K.; Goiran, M.; Tuchagues, J. P.; Varret, F. *Top. Curr. Chem.* **2004**, *235*, 65. (d) Real, J. A.; Gaspara, A. B.; Mûnozb, M, C. *Dalton Trans.* **2005**, 2062. (e) Bhattacharjee, A.; Roy, M.; Ksenofontov, V.; Kitchen, J. A.; Brooker, S.; Gütlich, P. *Eur. J. Inorg. Chem.* **2013**, 843. (f) Levchenko, G.; Bukin, G. V.; Terekhov, S. A.; Gaspar, A. B.; Martínez, V.; Muñoz, M. C.; Real, J. A. *J. Phys. Chem. B* **2011**, *115*, 8176.

4. (a) Salitros, I.; Pavlik, J.; Boca, R.; Fuhr, O.; Chandrasekar R.; Ruben, M. *Cryst. Eng. Comm,* **2010**, *12*, 2361. (b) Rajadurai, C.; Schramm, F.; Brink, S.; Fuhr, O.; Kruk, R.; Ghafari, M.; Ruben, M. *Inorg. Chem.* **2006**, *45*, 10019. (c) Rajadurai, C.; Fuhr, O.; Kruk, R.; Ghafari, M.; Hahn, H.; Ruben, M. *Chem. Commun.* **2007**, 2636. (d) Rajadurai, C.; Qu, Z.; Fuhr, O.; Gopalan, B.; Kruk, R.; Ghafari, M.; Ruben, M. *Dalton Trans*. **2007**, 3531. (e) Chandrasekar, R.; Schramm, F.; Fuhr, O.; Ruben, M.; *Eur. J. Inorg. Chem.* **2008**, 2649. (f) Chandrasekhar, N.; Chandrasekar, R. *Dalton Trans.* **2010**, *39*, 9872. (g) Gonzallez-Prieto, R.; Fleury, B.; Schramm, F.; Zoppellaro, G.; Chandrasekar, R.; Fuhr, O.; Lebedkin, S.; Kappes, M.; Ruben, M. *Dalton Trans.* **2011**, *40*, 7564.

5. (a) Yu, Z.; Liu, K.; Tao, J. Q.; Zhong, Z. J.; You, X. Z.; Siu, G. G. *App. Phys. Lett.* **1999**, *74*, 4029. b) Hauser, A. *Top. Curr. Chem.* **2004**, *234*, 155.

6. (a) Armand, F.; Badoux, C.; Bonville, P.; Ruaudelteixier, A.; Kahn, O. *Langmuir* **1995**, *11*, 3467. (b) Guo, Q.; Teng, X.; Rahman, S.; Yang, H. *J. Am. Chem. Soc.* **2003**, *125*, 630.

7. (a) Soyer, H.; Dupart, E.; Gomez-Garcia, C. J.; Mingotaud, C.; Delhaes, P. *Adv. Mater.* **1999**, *11*, 382. (b) Soyer, H.; Mingotaud, C.; Boillot, M. L.; Delhaes, P. *Langmuir* **1998**, *14*, 5890. (c) Cobo, S.; Molnar, G.; Real, J. A.; Bousseksou, A. *Angew. Chem. Int. Ed.* **2006**, *45*, 5786.

8. Molnar, G.; Cobo, S.; Real, J. A.; Carcenac, F.; Daran, E.; Vien, C.; Bousseksou, A. *Adv. Mater.* **2007**, *19*, 2163.

9. Agusti, G.; Cobo, S.; Gaspar, A. B.; Molnar, G.; Moussa, N. O.; Szilagyi, P. A.; Palfi, V.; Vieu, C.; Munoz, M. C.; Real, J. A.; Bousseksou, A. *Chem. Mater.* **2008**, *20*, 6721.

10. (a) Thibault, C.; Molnar, G.; Salmon, L.; Bousseksou, A.; Vieu, C. *Langmuir* **2010**, *26*, 1557. (b) Kaehr, B.; Shear, J. B. *J. Am. Chem. Soc.* **2007**, *129*, 1904.

11. (a) Quintero, C. M.; Guralskiy, I.; Salmon, L.; Molnár, G.; Bergaud, C.; Bousseksou, A. *J. Mater. Chem.* **2012**, *22*, 3745. (b) Xia, Y. N.; Whitesides, G. M. *Annu. Rev. Mater. Sci,* **1998**, *28*, 153.

12. (a) Cavallini, M.; Bergenti, I.; Milita, S.; Ruani, G.; Salitros, I.; Qu, Z. R.; Chandrasekar, R.; Ruben, M. *Angew. Chem. Int. Ed.* **2008**, *47*, 8596. (b) Cavallini, M.; Bergenti, I.; Milita, S.; Kengne, J. C.; Gentili, D.; Ruani, G.; Salitros, I.; Meded, V.; Ruben, M. *Langmuir* **2011**, *27*, 4076.

13. Basak, S.; Hui, P.; Boodida S.; Chandrasekar, R. *J. Org. Chem.* **2012**, *77*, 3620.

14. Jameson, D. L.; Goldsby, K. A. *J. Org. Chem.* **1990**, *55*, 4992.

15. (a) Zoppellaro, G.; Baumgarten, M. *Eur. J. Org. Chem.* **2005**, 2888. b) Basak, S.; Hui, P.; Chandrasekar, R. *Synthesis* **2009**, *23*, 4042.

16. (a) Hui, P.; Chandrasekar, R. *Chem Plus Chem* **2012**, *12*, 1051. (b) Basak, S.; Narayana, YSLV.; Baumgarten, M.; Muellen, K.; Chandrasekar, R. *Macromolecules* **2013**, *46*, 362. (c) Narayana, YSLV.; Basak, S.; Baumgarten, M.; Muellen, K.; Chandrasekar, R. *Adv. Funct. Mater.* **2013**, DOI: 10.1002/adfm.201301476.

17. Hauser, A. *Topics in Current Chemistry* **2004**, *234*, 155.

Appendix

FTIR Spectra:

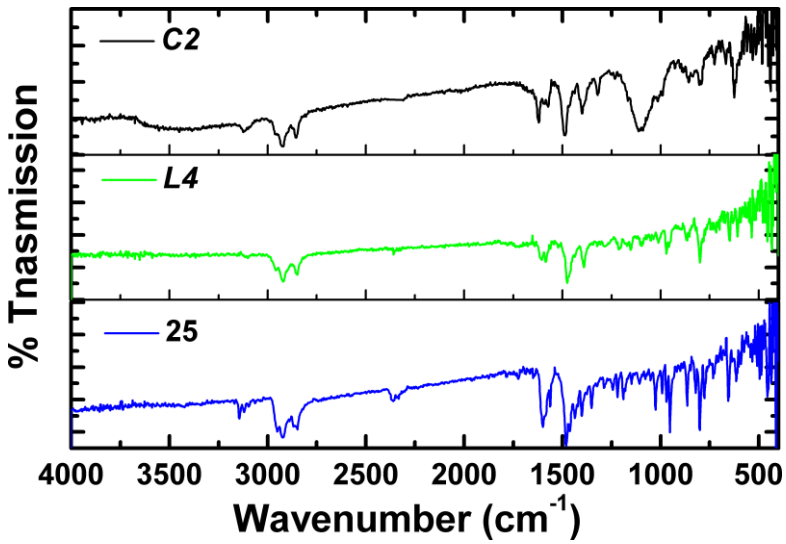

Figure A1. FTIR spectra of complexes and ligands.

NOTE (Fig. A1.): *Compound **25**: 3146 cm^{-1} (−C≡C−), 1599, 1464, 2361 cm^{-1}(aromatic −C=C−). Compound **L4**: 1475, 1585, 1390 cm^{-1} (aromatic −C=C−). Complex **C2**: 1103 cm^{-1} (broad, B-F), 1572, 1491, 1400 cm^{-1} (aromatic −C=C−).*

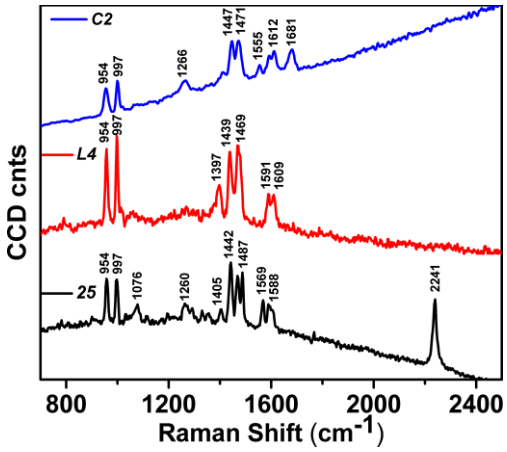

Figure A2. Confocal Raman micro spectroscopic data of powder sample complex ***C2*** and ligands. Excitation wavelength λ_{ex} = 633 nm (He-Ne Laser).

NOTE (Fig. A2.): *Confocal Raman micro spectroscopy investigation of bulk powder of complex **C2** and ligands have shown clear evidence for the formation of complex from ligand **L4**. The peaks 1266, 1555 and 1681cm^{-1} in complex **C2** are newly appeared and 1397 cm^{-1} peak is disappeared. The doubled peaks of ligand **L4** at 1591 and 1609 cm^{-1} are shifted to 1585 and 1612 cm^{-1} in complex **C2**. The −C≡C− stretching frequency is showing at 2241 cm^{-1}in compound **25**. This is disappearing at ligand **L4**. There are new peaks at 1076 and 1260 cm^{-1} in compound **25**. The 1405 cm^{-1} peak intensity increased and shifted in ligand **L4** than **25**.*

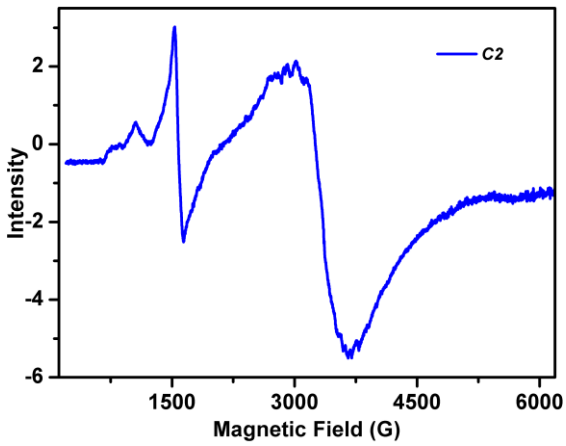

Figure A3. Liquid He temperature ESR measurement of $Fe^{(II)}(\boldsymbol{L4})_2](BF_4)_2$. Parameters: frequency 9.388755 GHz, and 100 kHz modulation frequency, 0.3 Gauss modulation amplitude, 21 msec time constant, 42 sec sweep time, 0.998 mW microwave power, 105 gain, 1 scan.

NOTE (Fig. A3.): *The ESR measurement of the powder sample of complex **C2** at 4 K shows signal due to $Fe^{(III)}$ impurities.*

4

Multi Colour Hybrid Organic/Inorganic Nanotubes: One-Pot Fabrication of Tricolour (Blue-Red-Purple) Displaying Parallelepipedic Organic Nanotubes Coordinated with $Eu^{III}(tta)_3$

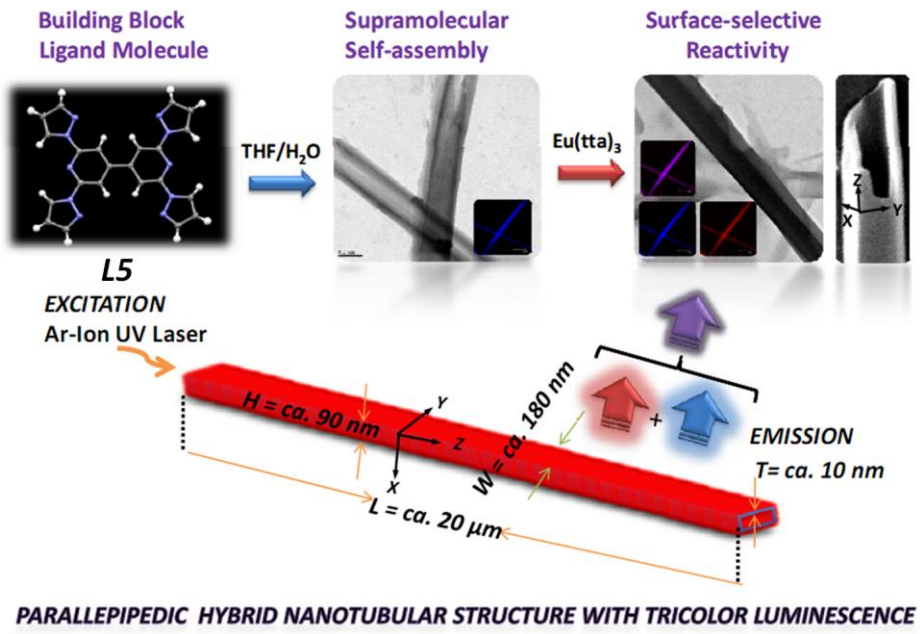

*This chapter is adapted from:

S. Basak, R. Chandrasekar*
Adv. Funct. Mater. **2011,** *21*, 667.

4.1 Abstract

This chapter focuses on an innovative one-pot fabrication of organic/inorganic hybrid parallelepipedic tubes with rectangular cavities displaying multicolor luminescence. Firstly, using a novel back-to-back coupled 2,6-di(1H-pyrazol-1-yl)pyridine ligand, several-micrometer-long (ca. 50 µm) blue-emitting parallelepipedic organic nanotubes with rectangular cavities were fabricated in THF/water via solvent-assisted supramolecular (H-bonding and π – π stacking) self-assembly. Secondly, in the same pot, the ligand molecules available on the rough (~ 50 nm roughness) surface of the nanotubes were reacted with $Eu(tta)_3$ molecules at the solid/liquid interface to form a layer of red-emitting Eu(III) complex coating on the inner and outer surface of the tubes. The resultant organic / inorganic hybrid parallelepipedic nanotubes fabricated using this novel bottom-up one-pot technique display tricolor (blue–red–purple) under UV light, i.e., blue and red dual emission from the organic ligand and the Eu(III) complex, respectively and a purple color due to the mixing of two colors. This simple technique signifies an innovative and important method in the development of multiluminescent organic/inorganic hybrid nanotubes adopting bottom-up nanotechnology.

4.2 Introduction

Luminescent organic nanotubes are of great importance as a building block in future miniaturized devices.[1,11a] With the rapid advancement of nano-electronics, one-dimensional luminescent nanotubular structures have attracted particular interest because of their unique, photonic (particularly wave guiding) and opto-electronic properties as a result of two-dimensional (2D) optical confinement effect.[1] Till now most of the known luminescent nanotubular structures are of pure organic in nature and display only single color PL. Nanofabrication of multicolor emitting hybrid nanotubular materials from two different soft matters (organic/inorganic) is an unexplored and sophisticated research area of nanoscience and technology. A successful groundwork in this area could lead to new hybrid nanotubular luminogens capable of performing a sensing, photonic, biological or transport function. However, the controlled and selective fabrication of hybrid nanotubes with multicolor emission requires a rational design and step-wise preparation strategy at the nanoscale, if they have to be successfully integrated into miniaturized functional devices.

Controlling and understanding the growth[2] of an organic soft matter into a shape-defined nanotubular configuration (cylindrical, hexagonal,[3] rectangular,[4] and parallelepipedic[8f]) is itself a challenging area. Till now, most of the organic nano/submicro tubes fabricated from the self-assembly of disc-like molecules,[5] dendrimers,[6] amphiphiles,[7] small organic molecules,[8] peptides,[9] and polymers[10] are all of single-component in nature and the shape control at the nanoscale had been achieved by using crystallization, template synthesis, vaporization and amphiphilic assembly techniques. It has been recently recognized that, apart from supramolecular interactions[3-11] (Van der Waals interaction, hydrogen bond, coordination bond, and π-π stack), the solubility of molecular building blocks in organic solvents and their concentration also play a crucial role in controlling the shape, size and texture of the organic nanostructures.[8,11a] To fabricate multifunctional organic/inorganic hybrid nanotubular structures, the use of small organic ligand molecules as nanobricks is a logical approach, since it provides easy structural tunability and diversity, which are important to control their solubility as well as their molecular function at the nanoscale. Additionally the ligand molecules available on the surface of the shape-defined nano tubes can also be effectively utilized to perform coordination chemistry with different metal ions (surface modification) at the solid-liquid interface. This methodology may form core-shell type organic/inorganic nanotubes with multi-functional properties. Based on this idea, we have fabricated a tricolor displaying parallelepipedic organic/inorganic nano structure via step-wise self-assembly approach from ligand ***L5***.

In this chapter, we report our one-pot and two-step nanofabrication approach (Scheme 4.1): i) fabrication of several micron (*ca.* 50 μm) long blue emitting primary organic rectangular nanotubular structures with well-defined rectangular cavities (parallelepipedic nano tubes) from ligand molecule ***L5*** in THF/H_2O solvents, ii) reaction of red-emitting Eu(III) complexes (***C3***) with ***L5*** available on the surface of the blue emitting and iii) generation of a spectacular tricolor (blue-red-purple) from organic/inorganic hybrid parallelepipedic nanostructures upon UV excitation. We also present the preparation of a directly back-to-back coupled 2,6-di-pyrazol-1-yl pyridine ***L5*** and its Eu(III) complex ***C3***. Single crystal X-ray structure of ***L5***, comprehensive characterization of the organic and hybrid parallelepipedic nanostructures using electron microscopy (FESEM/SEM/TEM), atomic force microscopy (AFM) and confocal Raman

micro spectroscopy and examination of luminescence properties of the hybrid nanostructures using confocal fluorescence microscopy also have been presented.

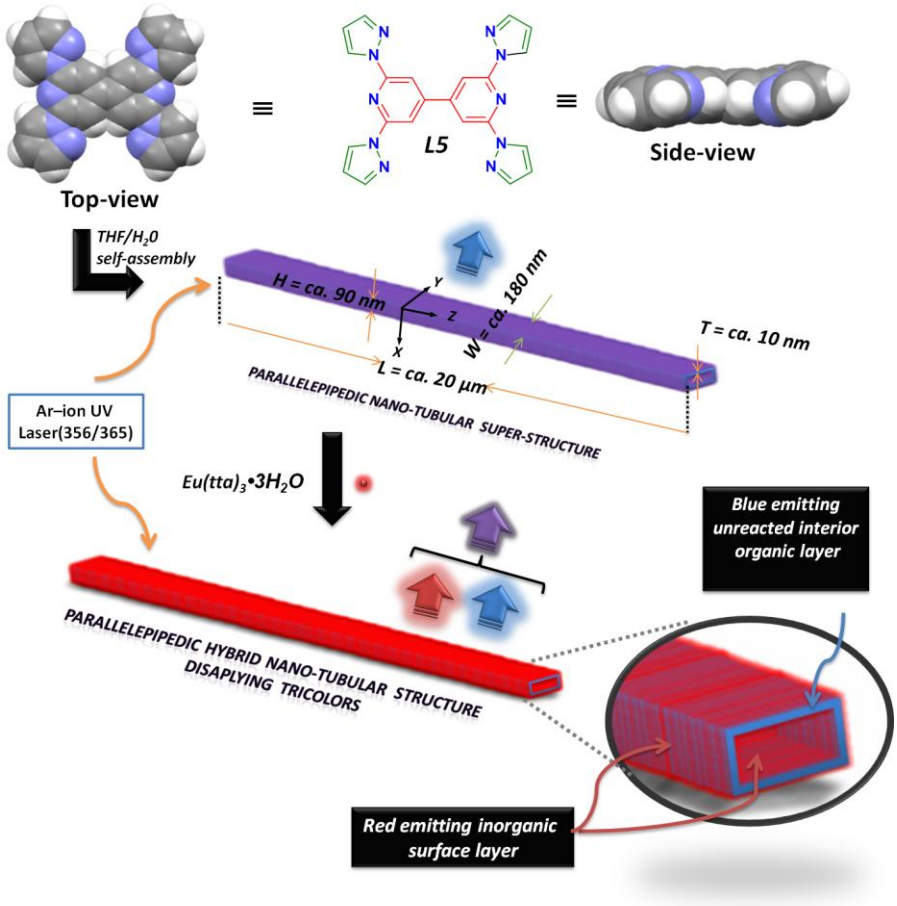

Scheme 4.1 Schematic elucidation of the formation of a dual (blue + red = purple) emitting Eu(III) coated parallepipedic nanotubular structure in THF/water *via* supramolecular self-assembly.

4.3 Results and Discussion

4.3.1 Synthesis:

Synthesis of Ditopic Ligand (L5):

The building block ligand ***L5*** was synthesized from 4-iodo-2,6-di(1H-pyrazol-1-yl)pyridine[9a,c-e] under Suzuki reaction conditions using $Pd(PPh_3)_4$ catalyst (7 mol%) in a good yield (72%) as white powder. The THF solution of ***L5*** showed fluorescence maximum at 390 nm (Φ_f = 0.16) for the excitation (λ_{ex}) performed at 331 nm (Fig. 4.1).

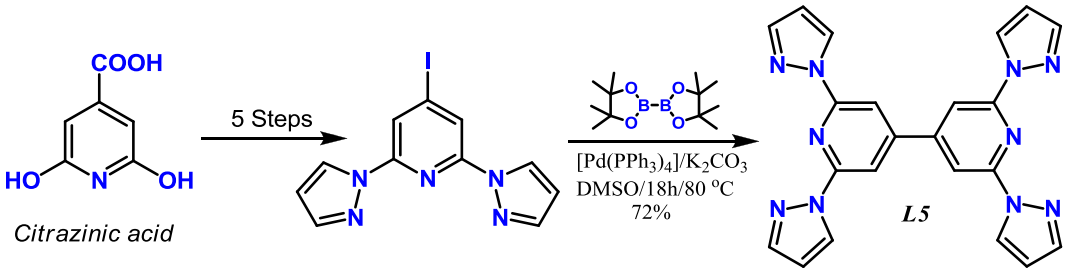

Scheme 4.2 Synthesis of 2,2′,6,6′-tetra(1H-pyrazol-1-yl)-4,4′-bipyridine ***L5***. *Reaction conditions:* (a) Bis(pinacolato)diboron, $[Pd(PPh_3)_4]$ / K_2CO_3 / DMSO /18 h/ 80 °C.

Synthesis of 4-iodo-2,6-di-pyrazol-1-ylpyridine: This compound was synthesized as per our reported procedure.[11e,f]

Synthesis of 2,2′,6,6′-tetra(1H-pyrazol-1-yl)-4,4′-bipyridine *L5*: In a 100 mL flask containing DMSO (30 ml), 4-iodo-2,6-di-pyrazol-1-yl pyridine (200 mg, 0.593 mmol), bis(pinacolato)diboron (150 mg, 0.593 mmol), K_2CO_3 (245 mg, 1.77 mmol) and $Pd(PPh_3)_4$ (47 mg, 7 mol %) were taken. The solution was stirred at 80 °C under N_2 atmosphere until the starting material was disappeared as monitored by TLC (EtOAc:Hexane; 5:95). The catalyst was removed by filtration and the residue was washed with $CHCl_3$. The filtrate was cooled to room temperature and then washed with

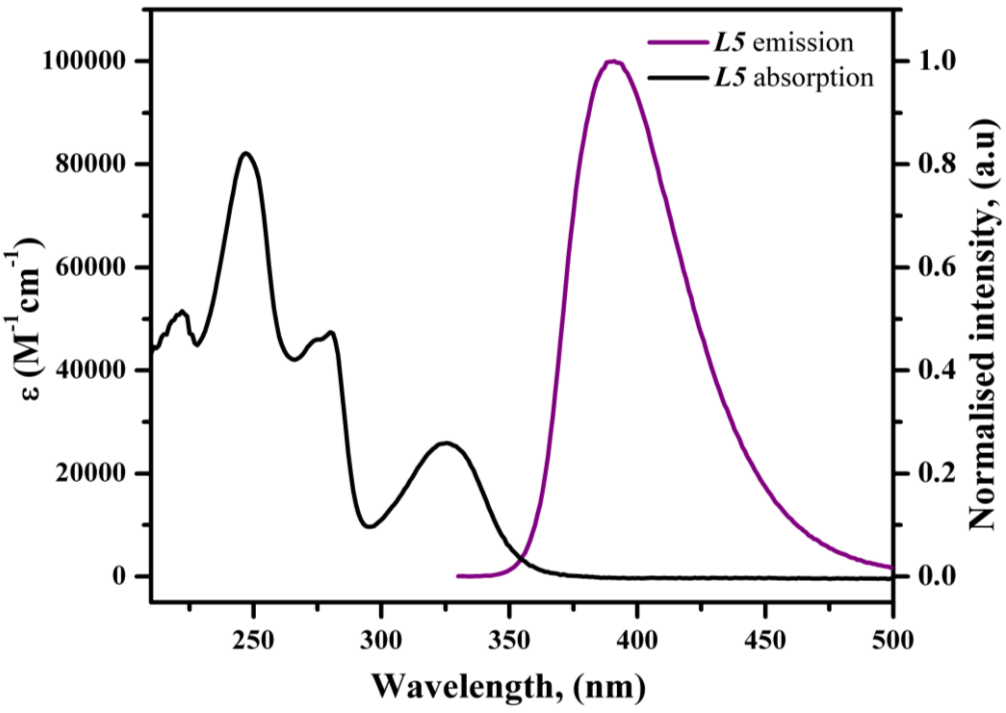

Figure 4.1: UV-Vis absorption and emission spectra of compound ***L5*** in THF solvent.

deionised water (50 mL) for 5 times. The organic layer was separated and dried over Na_2SO_4, filtered, concentrated and purified by column chromatography on activated silica gel to afford a pure white color powder of ***L5***. Yield 90 mg (72 %). ^{1}H NMR (400 MHz, $CDCl_3$, 25 °C) δ/ppm: 8.6 (d, 4H, *J* = 2.4 Hz), 8.26 (s, 4H), 7.8 (s, 4H), 6.53 (d, 4H, *J* = 1.2 Hz). ^{13}C NMR (100 MHz, $CDCl_3$, 25 °C) δ/ppm: 150.9, 150.8, 142.7, 127.3, 108.3, 107.5. LCMS analysis m/z: experimental value: 420.35, calculated value: 420.43. FT-IR (KBr) υ in cm^{-1} = 2957, 2924, 2854, 1711, 1614, 1553, 1462, 1395, 1221, 1186, 1080, 1034, 959, 853, 752, 660, 606. Elemental analysis: experimental value: C 63.02, H 3.95, N 33.03; calculated value: C 62.85, H 3.84, N 33.32.

Preparation of [(Eu(tta)$_3$)$_2$(*L5*)] complex *C3*: Ligand (***L5***) (50 mg, 0.119 mmol) and Europium(III) thenoyltrifluoroacetonate trihydrate (207 mg, 0.238 mmol) were dissolved in 25 mL toluene. The reaction mixture was refluxed for 12 h at 110 °C. The solvent toluene was removed under vacuum leaving a brown solid as the crude product. FT-IR (KBr) υ in cm^{-1}: 3470, 3129, 2965, 2924, 2857, 1721, 1611, 1535, 1462, 1412, 1354, 1304, 1182, 1136, 1036, 972, 934, 856, 791, 640, 604, 577. Micro Raman υ in cm^{-1} (pellet): 1637, 1524, 1456, 1416, 1355, 1309, 1241, 1085, 1062, 1010, 934, 750, 686, 643. Elemental analysis: experimental value: C 40.98, H 1.97, N 6.83; calculated value: C 41.12, H 2.05, N 6.75. Melting point: decomposes over 80 °C.

4.3.2 Solid State Structure of L5:

Single crystals suitable for X-ray analysis and nano level studies were obtained from toluene via slow solvent evaporation. Examination of the single crystal X-ray structure of ***L5*** (*P*-1 space group) showed a unique structural features for hierarchical supramolecular self-assembly (Fig. 4.2).[12] The molecule is near planar [C(8)-C(9)-C(9)-C(10) torsion angle = 1.49°] and the N_{py}•••N_{py} distance between the two pyridine rings is ca. 0.71 nm. The solid state structure showed both intermolecular H bonding and π-π stacking which is responsible for supramolecular self-assembly. Each pyrazole ring nitrogen (N1) participates in a head-to-tail intermolecular H bonding interaction with the pyrazole ring proton (H6) of the neighboring molecule [N(1)•••H(6)$_{Pz}$ = 2.699 Å] forming a 1D chain-like structure (Fig. 4.2D). Each 1-D chain is closely packed and forms a pseudo sheet-like structure. These sheet-like structures form 3-D multi-layered supramolecular aggregates via intermolecular π-π stacking (*d* = 3.342 Å) interactions of the pyridine rings (Fig. 4.2C).

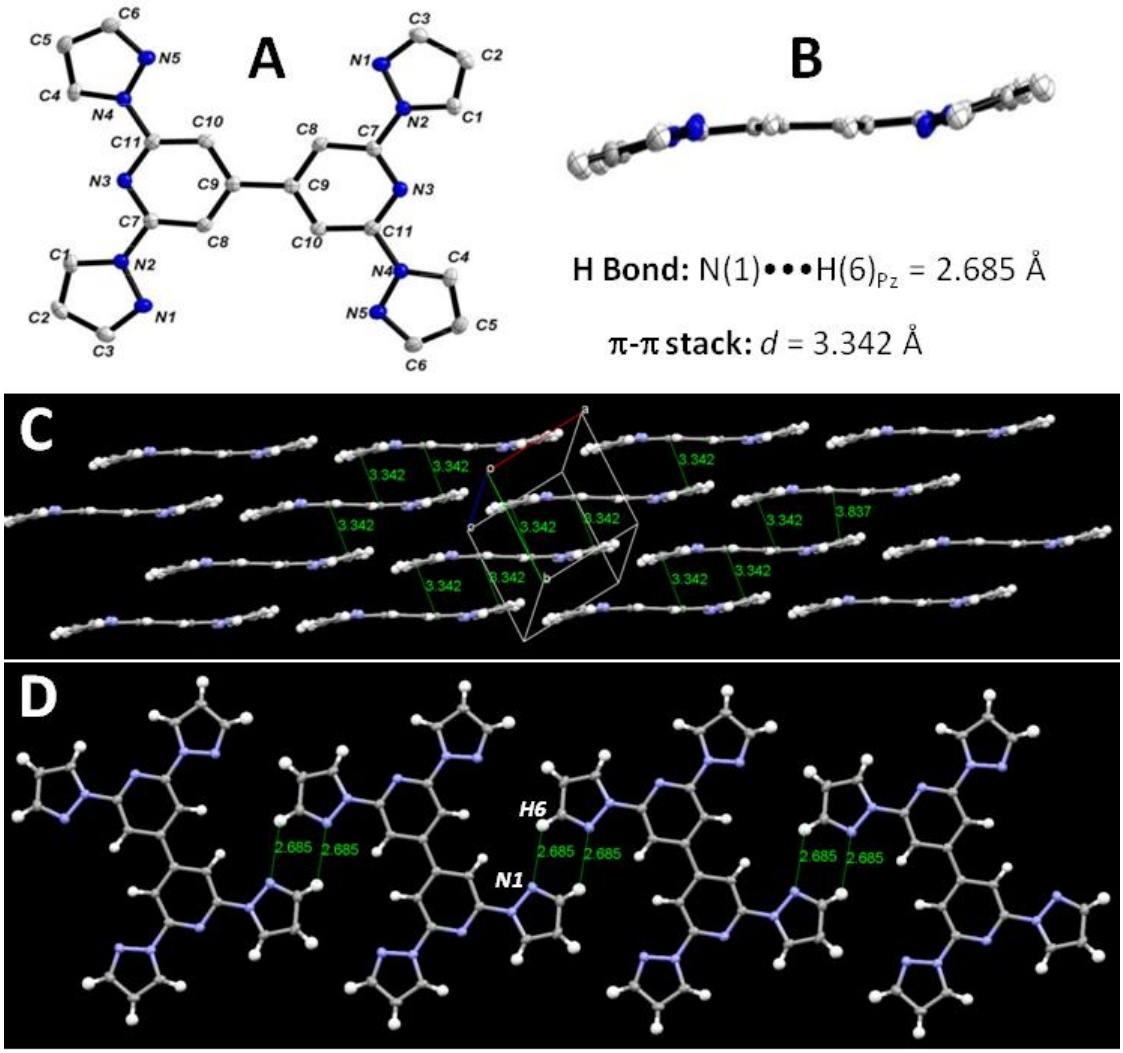

Figure 4.2: A) ORTEP plot (50 % probability) of a building block molecule ***L5*** (Front-view). B) side-view of ***L5***. In both A and B the H-atoms are omitted for clarity. C) Intermolecular π-π stacking (*d* = 3.342 Å) interaction of the pyridine rings forming 3-D multi-layered supramolecular aggregates. D) Formation of a 1-D chain-like structure through intermolecular hydrogen bonding interaction of pyrazole ring proton and pyrazole nitrogen. In both A and B hydrogen atoms are omitted for clarity.

4.3.3 Fabrication of Parallelepipedic Nano-Tubes:

Reprecipitation method first developed by Nakanishi and co-workers,[13] is a very simple and convenient route to fabricate organic nanostructures. Because of its ease of implementation over the other method Viz. CVD, template synthesis, laser ablation etc., this method is widely used to prepare nanostructures.[14,15-22] It is a solvent-exchange process; the target compound is dissolved in a good solvent, and micro quantities of the solute are injected rapidly into excess of a second liquid, which while miscible with the

first liquid, acts as a nonsolvent or poor solvent for the compound of interest. The immense discrepancy between the solubilities of the target compound in the good and poor solvents and the good compatibility of the two solvents are essential for this method. The good solvent disperses, and the sudden change in the surroundings of the molecules causes aggregation leading to the formation of nano/microparticles dispersed homogeneously in the poor solvent (Scheme 4.3).

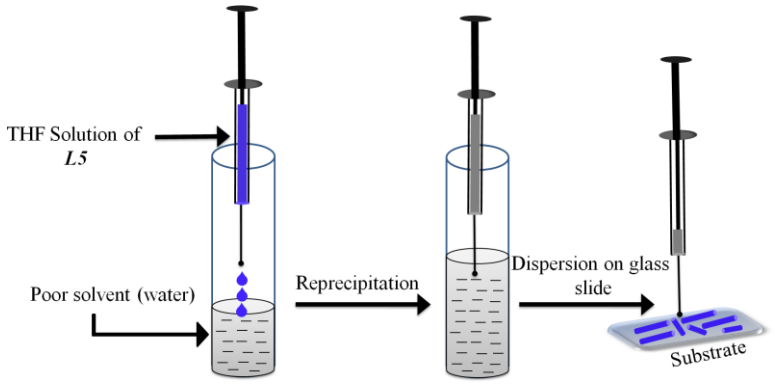

Scheme 4.3 Schematic representation of reprecipitation method.

Reprecipitation method may be divided roughly into four stages: (i) injection of the stock solution into stirred poor solvent leads to formation of droplets, (ii) good solvent elutes from liquid droplets; sudden change in the micro-environment of the molecules induce the formation of clusters, (iii) thermal collision between these clusters causes nucleation leading to (iv) crystal growth. Nakanishi and coworkers have reported the growth dynamics of a single perylene nanocrystal prepared through reprecipitation technique in water, by in situ and ex situ single particle fluorescence measurements.[15] Recent investigations also suggest the importance of unstable clusters in the growth process.[16] As the reprecipitation method follows heterogeneous nucleation so the factors which affect the Gibbs free energy parameter also affect the nanostructures. So we can control over the morphology and size of the particles produced. Some of these parameters are the concentration of the injected solution,[17] temperature of the poor solvent,[18] use of microwaves[13b] or ultrasounds,[19] and the aging period for the colloid.[20] In some cases, additives can also be introduced into water before the addition of the solution of the target compound to control the reprecipitation process. Often small molecules, such as surfactants, that gets inserted into the crystal network and interferes with crystal growth.[21] Fery-Forgues and co-workers used macromolecules in the medium and investigated their effect on the size and shape evolution of the particles.[22]

4.3.3.1 Preparation of Organic Nanotubes:

The parallelepipedic nanotubes were fabricated by reprecipitation method. In this method 2 mg of compound ***L5*** was taken in a test tube and 2 ml THF was added to dissolve. Then 1 mL Millipore water was rapidly injected to the above solution and the test tube was left for four hours without disturbance to grow the nanotubes. Afterwards two drops of this solution was slowly evaporated on a clean glass substrate at room

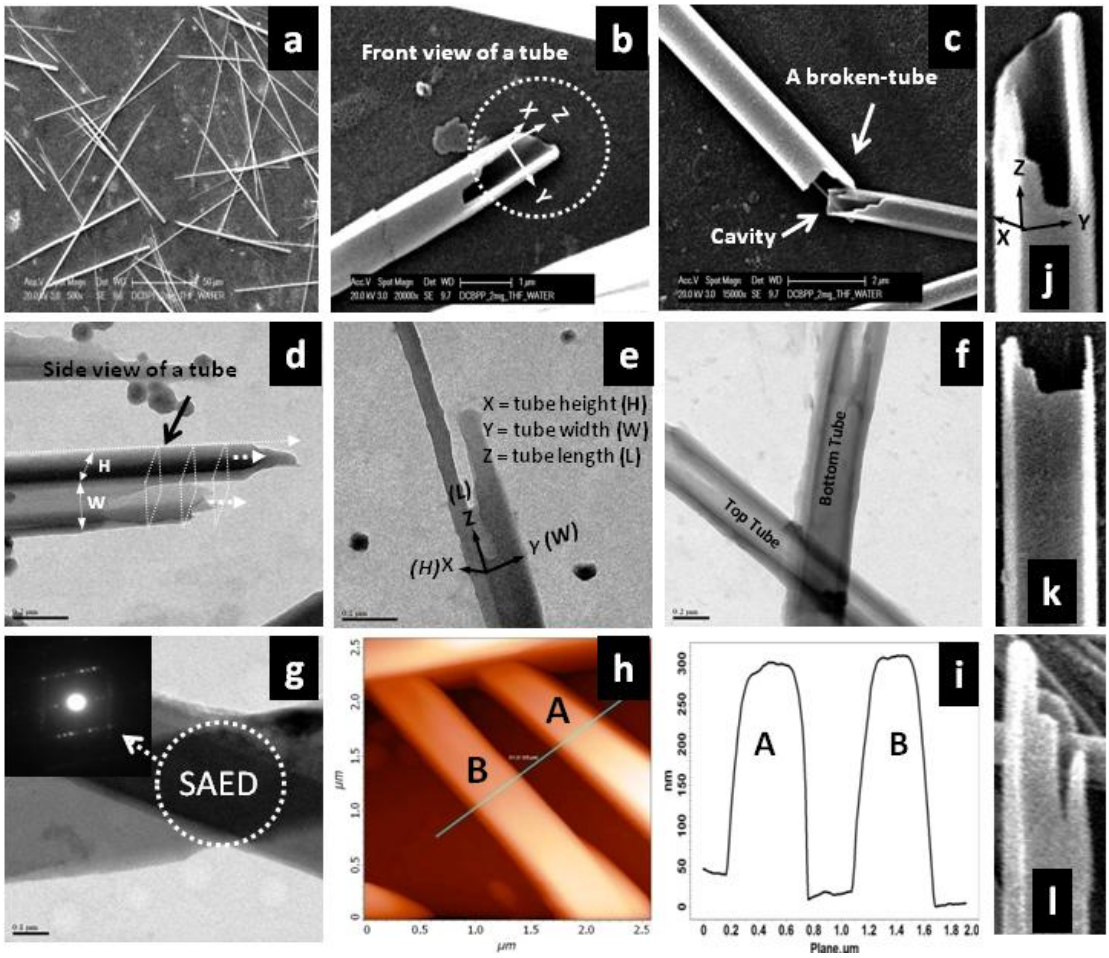

Figure 4.3 SEM micrographs of parallelepipedic nanostructures obtained from ***L5***: a) nearly mono dispersed rectangular tubes (scale bar is 50 μm), b) front-view of a tube exhibiting a rectangular open-ended cavity, White dotted circle: X, Y, Z coordinate labels mark the rectangular cross-section of the tube (scale bar is 1 μm), c) a broken tube displaying the hollow cavity (scale bar is 2 μm). Bright-field TEM micrographs: d and e) parallelepipedic nanotubular structure with irregular open-ended features. White double headed arrows: width (W) and height (H) are shown (scale bar is 200 nm). f and g) a tube sitting on top of another tube demonstrating the crystalline nature of the tubes. Inset of g): Selected-area electron diffraction (SAED) pattern displaying twinned diffraction pattern originating from the four faces of the two tubes (scale bar is 200 nm), h): semi-contact mode AFM image of the parallelepipedic nanotubular structure. i) height and length profile of selected tubes shown in fig. h; j) front-view of the tubes, k) back-view of a tube, and l) side-view of a tube.

temperature or directly deposited on a carbon coated TEM grid for the further investigation.

4.3.4 Characterization of Parallelepipedic Nano-Tubes:

The scanning electron microscopy (SEM) investigation of the sample revealed the formation of *ca.* 50 μm long parallelepipedic nanotubular structures with rectangular open-ended features (Fig. 4.3a-c). The presence of elongated hollow structures along the axis of the tubes is evident from a broken tube (Fig. 4.3c). A closure looks at the open-ended feature of each tube clearly showed the front-view (Fig. 4.3j), back-view (Fig. 4.3k) and side-view (Fig. 4.3l) of the tubes. Furthermore the bright-field transmission electron microscopy (TEM) images of nanostructures obtained from ***L5*** evidently supported the formation of parallelepipedic nanotubular structure with rectangular cavity by providing a 3D perspective view of the nanotubes (Fig. 4.3d-g). The selected area electron diffraction (SAED) pattern revealed a twinned diffraction pattern originating from the front and back faces of the nanotubes confirming the crystalline nature of the tubes (Fig. 4.3g and inset). In order to determine an accurate width (W) and height (H) profile of the nanotubes, semi-contact-mode AFM was performed (Fig. 4.3h and i). A typical H × W profiles of two parallelepipedic nanotubes is 275 nm × 400 nm. The H × W distribution pattern for thirty nanotubular structures that was acquired using AFM revealed that the aspect ratio (H/W) varies from 0.29–0.8. In this distribution range the majority of the tubes have aspect ratios below 0.51 (Fig. 4.4).

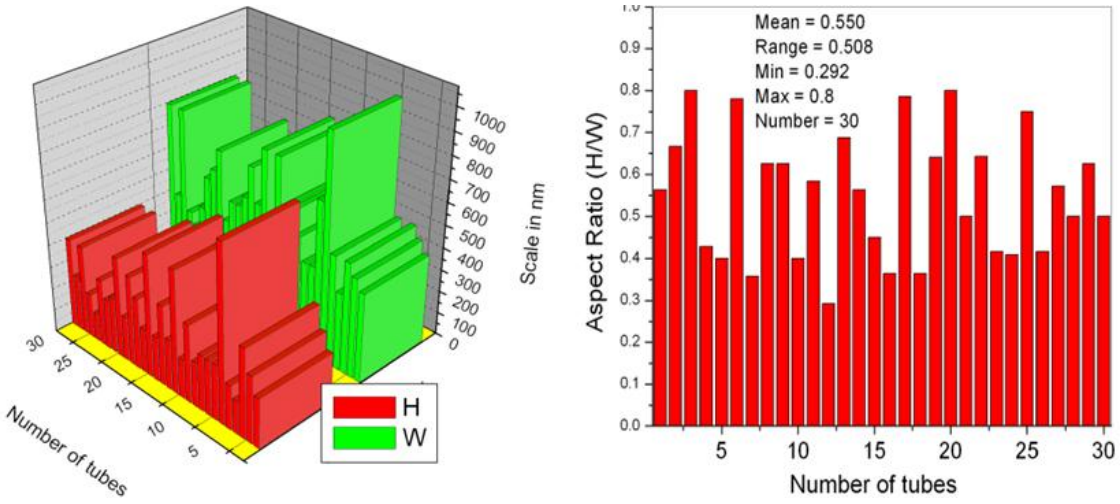

Figure 4.4 AFM height and width profiles of several ligand nanotubes obtained from ***L5***.

4.3.5 Formation Mechanism of the Parallelepipedic Nano-Tubes:

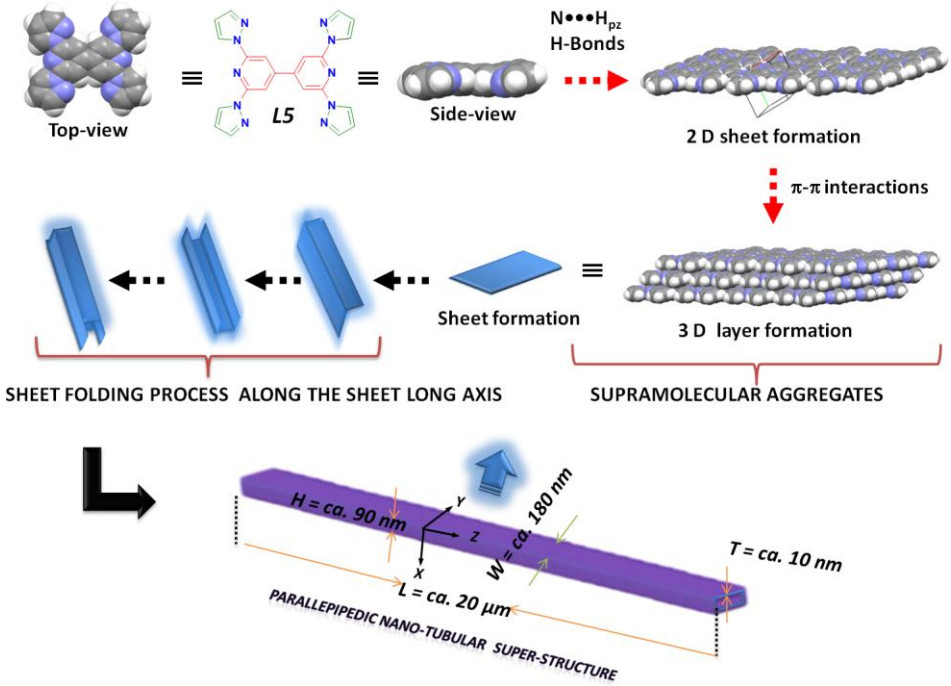

Scheme 4.4 Schematic elucidation of the possible formation mechanism of parallelepipedic nanotubular structures in THF/water via supramolecular self-assembly.

The formation of parallelepipedic nanotubes can be explained by using two possible mechanisms. In the first mechanism it starts from the supramolecular aggregates of ***L5***, (Scheme 4.4, and Fig. A3): i) forming sheet-like structures of micron dimension through supramolecular interactions (H-bond and π-π stack), folding of the sheets along the sheet axis forming a rectangular curled structures, and finally seaming of the curled sheets to form rectangular tubes. The main driving force behind the sheet folding and

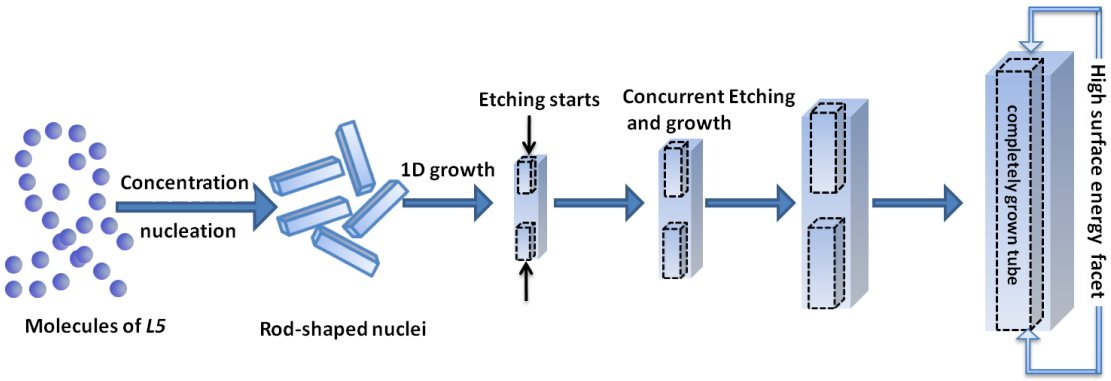

Scheme 4.5 Schematic elucidation of the etching mechanism responsible for the formation of parallelepipedic nanotubes in THF/water via nucleation, formation of rod like structure and concurrent etching/growth process.

curling process is probably due to the minimization of surface energy. Once the low surface energy tubular morphology has formed further growth proceeds only along the tube axis (concentration dependent) with the dimension of the width and height remain constant. The growth of the tube along the tube axis (Z-axis) is steered by the rapid growth of tube walls (X, Z plane) along the Z-axis (Fig. 4.3d-e). But this mechanism can't explain the 90^{o} folding of the sheets and formation of rectangular tubes.

In the second mechanism, upon injection of the solution of organic molecules (***L5***) in a good solvent (THF) into a poor solvent (water), the sudden change in the environment of the ***L5*** molecules induces molecular isolation from THF and precipitation in water to form seed crystals. The initial growth process primarily occurs through intermolecular hydrogen bonding and π-π interaction. In the subsequent growth process the molecules of ***L5*** quickly concentrate and nucleate into rod-like structures. The inadequate solubility of ***L5*** in water together with the strong intermolecular interactions forces the ***L5*** molecules to pack orderly to form a rod-like structure. The solvent etching of the rod started at the high surface energy facets of the crystal lattice immediately after its formation. Etching through solvent THF starts at the high energy facet of the rod, continues towards the interior along the length axis, and thus gradually converts the solid nanorods into hollow nano tubular structures. The tube formation process is similar to the "dissolution" process proposed by Sun et al. to explain the formation of hematite nanotubes, in which the tips of the spindle-like nanorods dissolved to form hollow nanotubes (scheme 4.5).[23] In ZnO nanodisks, a high density of defects at the growth facet

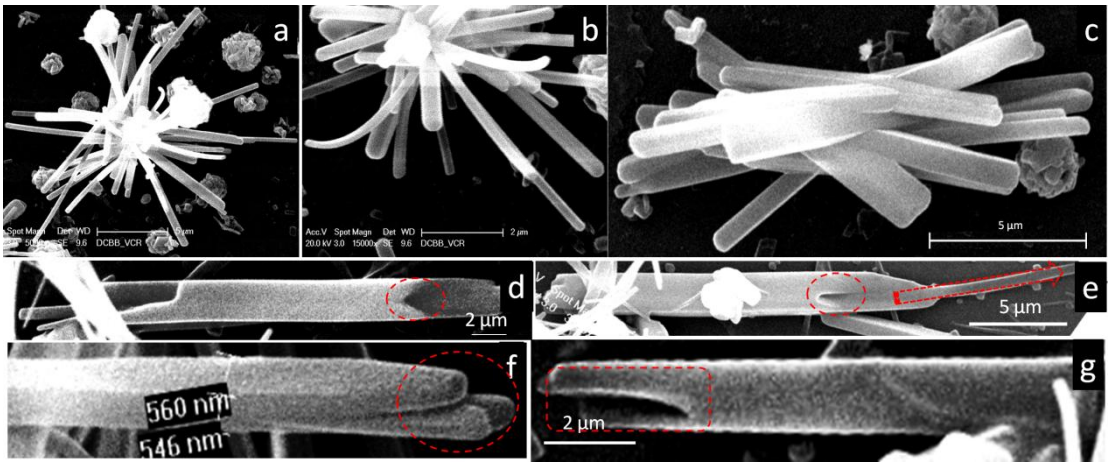

Figure 4.5 Growth of both rods and tubes during the sublimation of ***L5***: (a) growth of multiple rods; (b,c) closer view of rod ends; (d-g) several rods with tube like open end features (see red circles).

of the rectangular nanorods induced a high etching rate at the facet and resulted in the formation of tubular structures.[24] Probably the longitudinal growth of a rod and etching of its core by THF solvent is a simultaneous process. Hence we were unable to isolate rod structure from the binary solvent mixture (Scheme 4.5).

In order to confirm the role of solvent in the tube formation, ***L5*** molecules were sublimed onto a glass slide. Interestingly a mixture of rod and tubular structures were formed on the glass surface (Fig. 4.5). The dimension of the rods and the tubes matches with the tubes grown by reprecipitation method. This sublimation study confirms that the tubular structure growth is not mediated by the solvent etching. It is the preferential growth of the low energy walls of the tube and the high energy core contribute to the tube formation (Scheme 4.6).

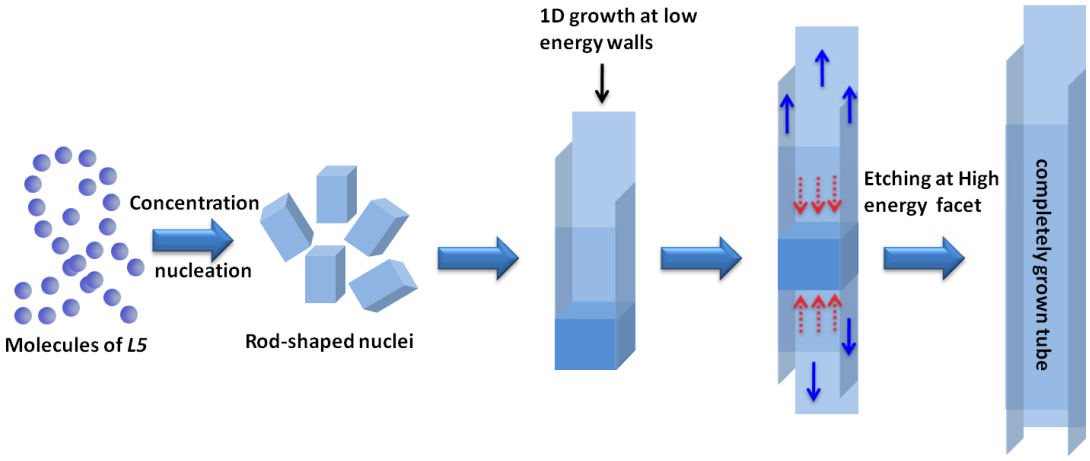

Scheme 4.6 Schematic elucidation of the low energy wall growth mechanism involved in the evolution of parallelepipedic nanotubes in THF/water. a) nucleation, b) formation of rod like structure, c) rapid growth of the low energy wall and concurrent etching/growth process.

4.3.6 Eu(III) Coordination Chemistry on the Surface of the Parallelepipedic Nano-Tubes:

Since the parallelepipedic nanostructures exhibited blue emission upon exciation with UV light, by utilizing the metal coordination ability of the building block ligand molecules ***L5*** exposed/available on the tube rough surface, synthesis of a thin layer of red-light emitting Eu(III) coordination complexes[9b,25] on the inner and outer surface of the tubes was envisaged. The ditopic molecule retains its coordination ability in the tubular form, since the rapid self-assembly process leaves lots of surface defects on the tubes, which is clearly evident from the surface roughness of the tube. The tapping mode AFM

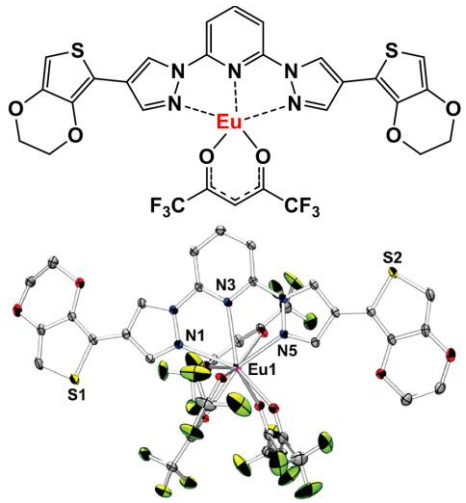

Figure 4.6 ORTEP diagram of an Eu(III) complex showing the labeling scheme of selected atoms at a 30% probability level. Hydrogen atoms are omitted for clarity. Adapted from ref. 25b.

studies showed the tubes roughness is around ~25-30 nm (Fig. A2). We anticipated that the surface selective coordination chemistry at the solid-liquid interface on the surface of the ligand nanotubes may form an inorganic/organic hybrid nanotubular structure which could display tricolors upon excitation with UV light i.e., a sensitized[26] red emission from the inner and outer surface of the tube (from the hypersensitive transitions $^5D_0 \rightarrow {}^7F_J$ (J = 0-4) of the Eu(III) ion), blue emission from the rest of the organic ligand part of the tube (from the unreacted middle layer) and purple color due to the mixing of blue and red colors. Firstly, the shape-defined parallelepipedic nanotubues were grown in a mixture of THF/water solvents as mentioned before.

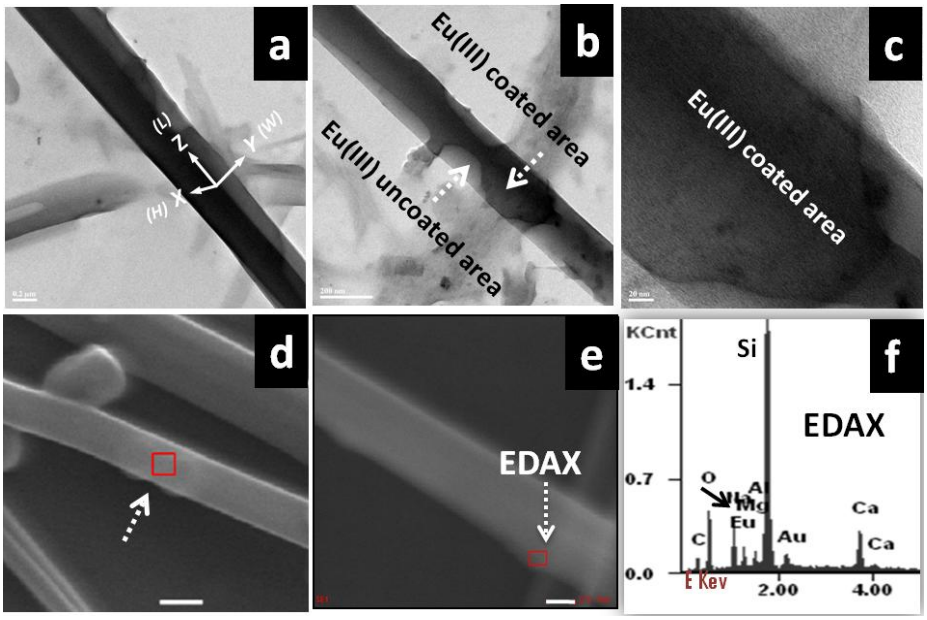

Figure 4.7 Formation of a [(Eu(tta)$_3$)$_2$***L5***] complex ***C3*** coating on the surface of the parallelepipedic nanotubular structure of ***L5*** in THF/water *via* self-assembly. TEM images: a) a tube coated with complex ***C3*** displaying dark contrast. b and c) a partially reacted tube surface with Eu(III) ions. The dark (coated) and light contrast (uncoated) areas are clearly marked. d) a fully Eu(III) coated area. e) FESEM image: EDAX data collected in a selected area are shown as red rectangles. Scale bar is 100 nm. f) EDAX analysis of the selected area shown in e confirming the presence of Eu ions on the tubes (the actual KCnt of Si is *ca.* 3.3, which is not shown fully for the sake of picture clarity).

Secondly, by injecting a THF solution of $Eu(tta)_3 \cdot (H_2O)_3$ (tta: thenoyltrifluoroacetonate) (0.065 mg/0.02 mL; ***L5*** mol%) to the solution containing the tubes obtained from ligand ***L5***, followed by gentle shaking, a layer of $[(Eu(tta)_3)_2(\boldsymbol{L5})]$ coordination complex ***C3*** was formed on the surface of the nanotubes. Here, each 2,6-bispyrazolylpyridine moiety present in ligand ***L5*** acts as a tridentate ligand and expels the water molecules out of the first coordination sphere of the $Eu(tta)_3 \cdot (H_2O)_3$ complex[25b,c] forming a binuclear complex ***C3*** with a distorted tricapped trigonal prismatic geometry around the Eu(III) ion (for example: Fig 4.6). Once all the exposed ligand molecules available on the tube rough surface have reacted (sub-stochiometric binding)[2h] further reaction is not possible thereby forming a thin layer of inorganic complex ***C3*** on the ligand nanostructure. The coating of the complex ***C3*** on the tube surfaces is probably stabilized by the non-covalent binding forces between the complex molecules and unreacted ligand molecules present in the lattice of the tube. Investigation of the TEM-bright field images obtained from the resultant organic/inorganic nanostructures showed a clear dark contrast for the areas coated with complex ***C3*** and light contrast for the unreacted or less reacted part of nanotubes (Fig. 4.7a-c). This observation clearly supported the growth of complex ***C3*** on the tube surface. Furthermore, the FESEM investigation of the Eu(III) coated tubes

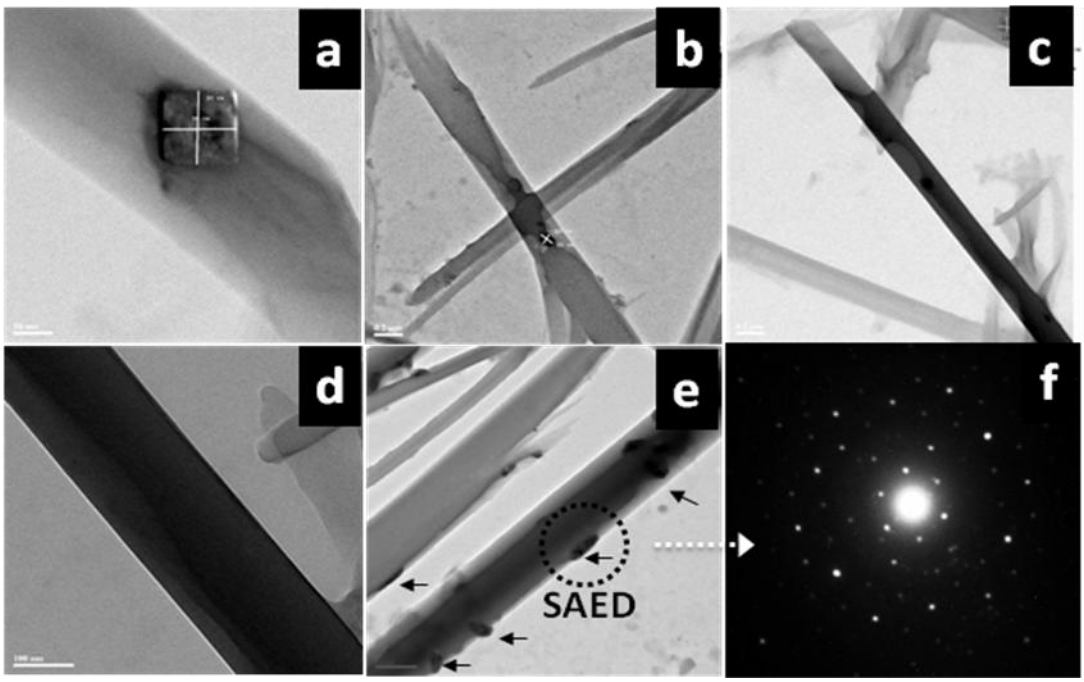

Figure 4.8 TEM Studies: (a) formation of an $Eu(tta)_3$ crystal; (b) etching of tube by $Eu(tta)_3$; (c) a completely coated tube by $Eu(tta)_3$; (d) uneven tube edges due to complextion; (e) formation of $Eu(tta)_3$ crystal on the tube edges; (f) corresponding SAED pattern of the marked crystal.

exhibited clear distinctive areas on the tube surfaces and edges (Fig. 4.7d and e) due to

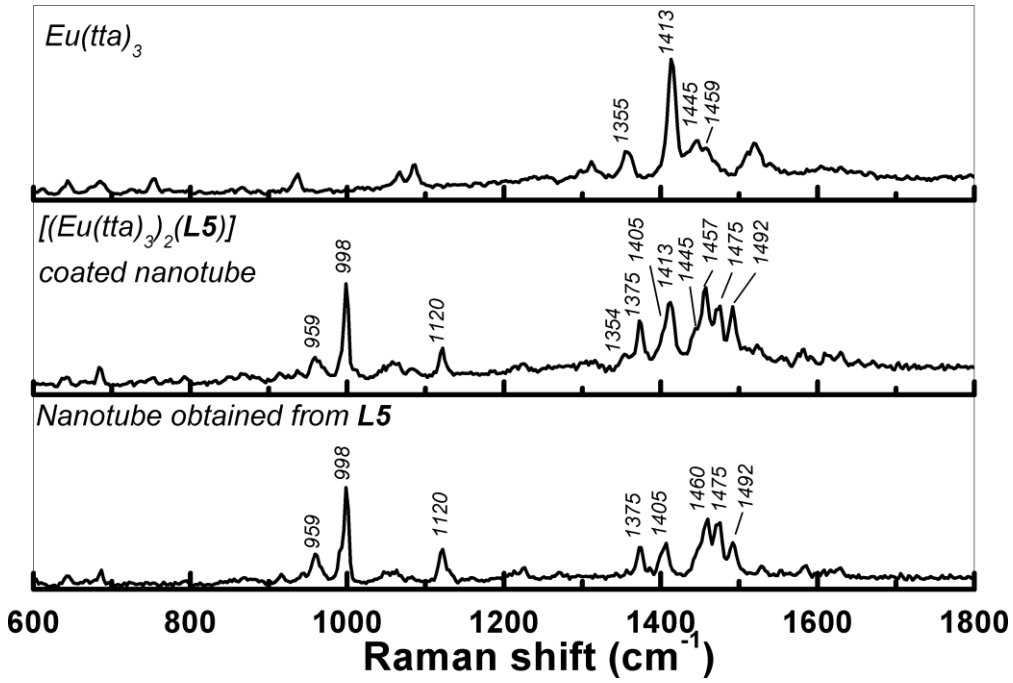

Figure 4.9 Confocal Raman micro spectroscopic data of parallelepipedic nanotubular structure coated with [(Eu(tta)$_3$)$_2$(***L5***)] complex ***C3***. Excitation wavelength λ_{ex} = 633 nm (HeNe Laser).

the growth of complex ***C3***. Energy dispersive X-ray analysis (EDAX) performed on this areas formed on the tube surfaces clearly confirmed the presence of Eu(III) ions (Fig. 4.7f).

Interestingly, addition more than 30% of Eu(tta)$_3$·3H$_2$O leads to formation of the nano/micro crystal growth on the tube surface. The cavity acts as a nanocontainer for growth of Eu(tta)$_3$ crystal. The formation of Eu(tta)$_3$·3H$_2$O crystal also confirmed by

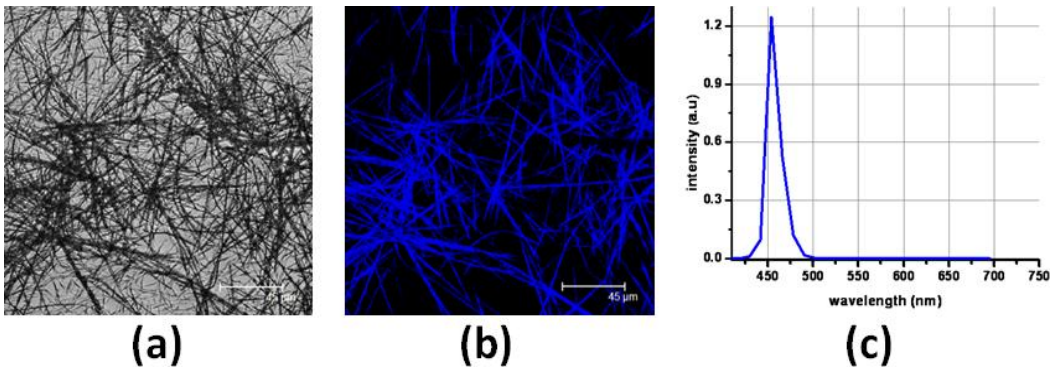

Figure 4.10 Confocal Fluorescence microscopy images of rectangular nanotubes obtained from ***L5***; nanotubes a) before excitation b) after excitation and c) its solid state emission spectrum (λ_{ex} = 356/365 nm).

SAED pattern (Fig. 4.8e and f), which is matching with the bulk $Eu(tta)_3 \cdot 3H_2O$ crystal (Fig. A1).

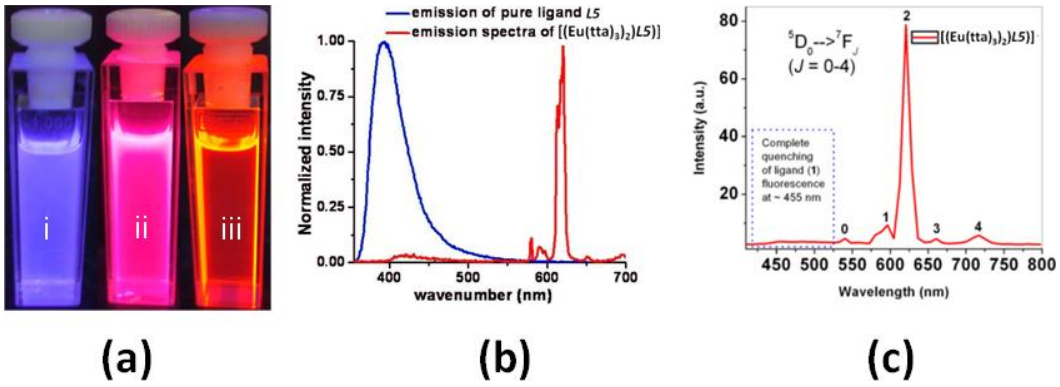

Figure 4.11 (a) (left) THF-H_2O solution of rectangular tube obtained from ligand (***L5***); (middle) $[Eu(tta)_3]_2$(***L5***) coated tube (0.1 mL mother solution of $Eu(tta)_3 \cdot 3H_2O$ added); (right) 3.73 X 10^{-6} M $Eu(tta)_3 \cdot 3H_2O$ solution. (b) Solution state emission spectra (c ~ 10^{-5} M) of ligand (***L5***) and complex $[Eu(tta)_3]_2$(***L5***) in toluene (excited at 331 nm). (c) Solid state confocal emission spectra of the powder sample of stochiometric $[(Eu(tta)_3)_2$ (***L5***)] complex ***C3*** displaying Eu(III) centred red emission and complete quenching of the ligand ***L5*** blue emission.

Additionally, confocal Raman micro spectroscopy investigation of the tubes self-assembled from ***L5*** and the tubes coated with ***C3*** have shown clear evidence for the formation a layer of complex ***C3*** on the tube surface by exhibiting characteristics Raman shifts (Fig. 4.9). Particularly, the signal intensities of the tube middle (organic) layer is higher than the intensities originated from the complex ***C3*** (inorganic) layer due to the surface selective reactivity and the resultant complex layer formation in and around the tube by leaving the majority of ***L5*** from middle part of the tube unreacted. In order to determine dual color emission from the Eu(III) coated nanotubes scanning confocal fluorescence microscopy measurement was performed. The topography of the tubes (XYT-mode) and the corresponding emission (XYλ- mode; the λ step width is 10 nm) properties were recorded. The topographic structural data were directly coupled with the spectroscopic properties of the specimen. For the excitation Ar+ (UV 356/365) laser light was used. The pure organic rectangular tubes obtained from ***L5*** have exhibited a blue emission at 455 nm (Fig. 4.10). Remarkably, from the tubes coated with complex ***C3***, blue (λ_{em} = 455 nm) and red (λ_{em} ~ 540-720 nm region) color dual emissions were detected at the blue and red channels of the photo multiplier tube due to the coating of a thin layer of red-emissive Eu(III) complexes ***C3*** on the surfaces of the blue emissive nanotubular super-structure (Fig. 4.11b, c). The wavelengths of the observed red emission

peaks and their intensities are matching with the bulk sample [$(Eu(tta)_3)_2$(***L5***)] of ***C3*** (Fig. 4.11) supporting the formation of the same at the tube surface (Fig. 4.11).

Additionally, the inclusive reactivity of the $Eu(tta)_3$ on the ligand nanotubular surfaces was clearly evident from the confocal fluorescence microscopic image shown in (Fig. 4.12 b, c). As a result of the merging of these blue and red colors the hybrid tubes also displayed an additive purple color (Fig. 4.12d) even under normal UV light excitation there by displaying three colors i.e., blue-red-purple. The signal intensity of the Eu(III) centered emission was lower than the ligand molecule emission due to the presence of a thin layer complex ***C3*** molecules on the ligand nanotubular surface leaving majority of the interior ligand molecules of the tubes unreacted. Interestingly, the intensity of the Eu(III) centered emission [$^5D_0 \rightarrow {}^7F_J$ (J = 0-4)] increases progressively upon increasing the amount of $Eu(tta)_3{\cdot}(H_2O)_3$ due to the increase of the reactivity of $Eu(tta)_3$ to the most of the accessible ligand molecules available on the ligand tube surfaces (Fig. 4.13).

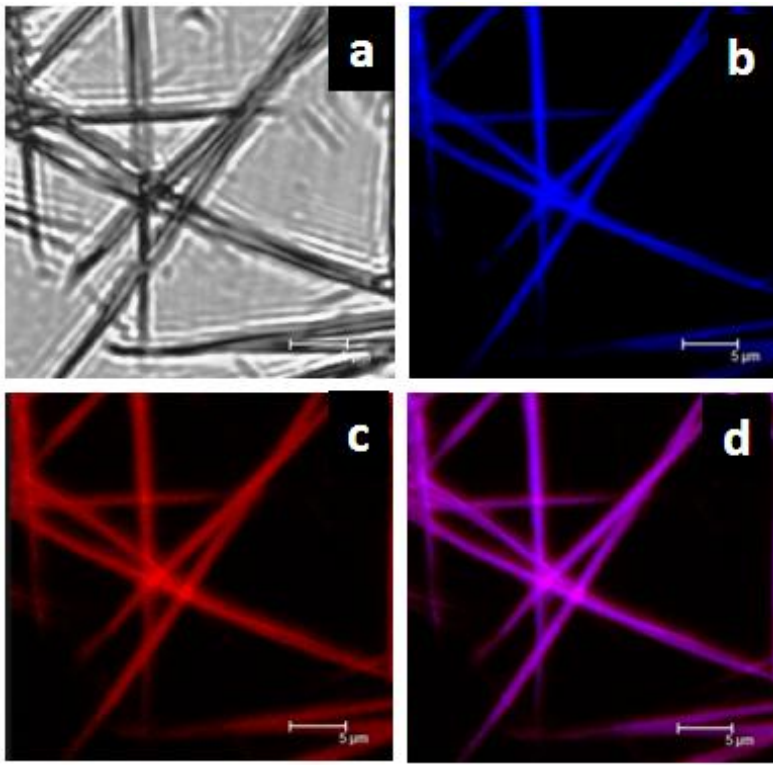

Figure 4.12 Confocal fluorescence microscopic images of parallepipedic nanotubular structures coated with a layer of complex ***C3*****.** a) before excitation, b) blue emission from the ligand part of the tubes (middle of the walls), c) red emission from the Eu(III) ion of the complex ***C3*** formed on the surface of the tubes, and d) overlay of the two images b) and c) displays purple color from the organic/inorganic hybrid tubes due to the mixing of the colors.

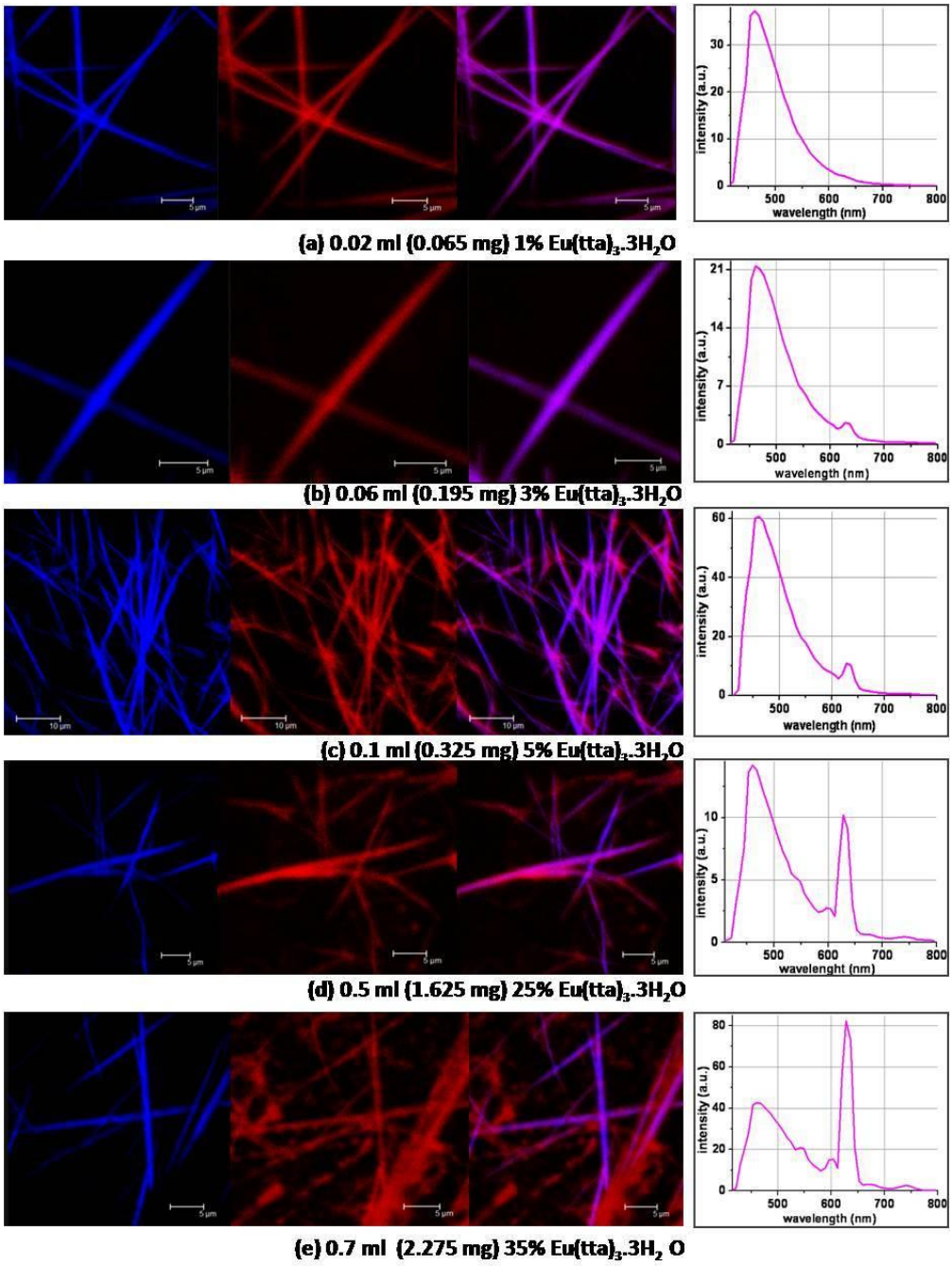

Figure 4.13 Confocal Fluorescence microscopy images and the corresponding spectra of $Eu(tta)_3$ coated organic nanotubes displaying increase in the Eu(III) centred red emission upon increasing $Eu(tta)_3$ concentration. Left Column Images: Blue emission; Middle Column Images: Red emission and Right Column Images: Purple color due to the mixing of red and blue.

4.3.7 Probing the Energy Transfer in Complex C3:

The involvement of any energy transfer process between the coordinated Eu(III) center and ligand ***L5*** in the $[(Eu(tta)_3)_2(\boldsymbol{L5})]$ complex was examined. There is a significant amount of overlap between the ligand emission spectra and the complex absorption spectra (Fig. 4.14). Excitation of the complex at 342 nm (corresponding to the

absorption maximum of the complex) showed a collective luminescence bands of pristine ligand together with features corresponding to $Eu(tta)_3$ emission[$^5D_0 \rightarrow {}^7F_J$; see visible J = 2 transition at 611 nm] (Fig. 4.15 b and c). Interestingly the ligand emission almost

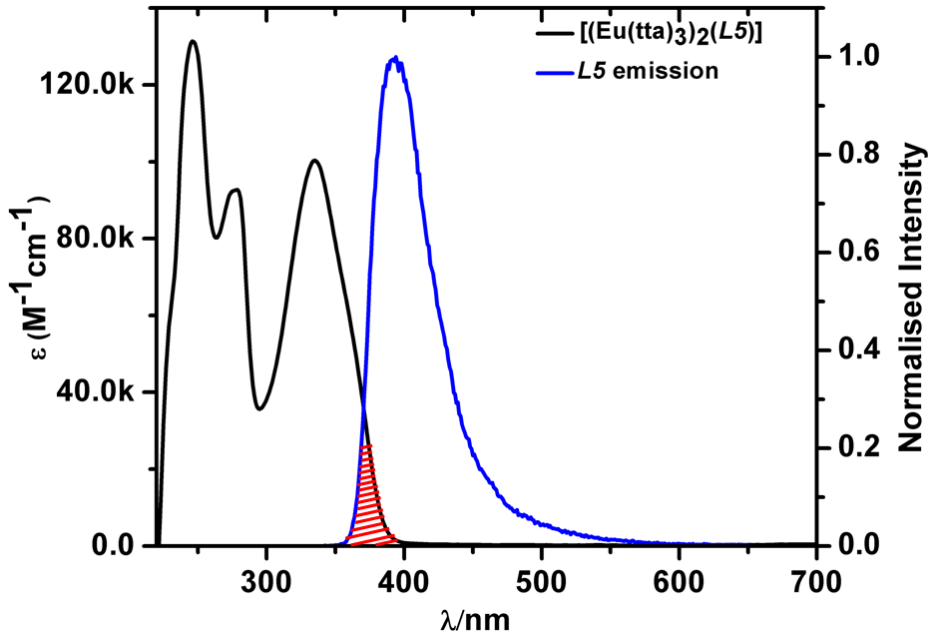

Fig. 4.14 Absorption spectra of complex [$(Eu(tta)_3)_2$(***L5***)] (——); Emission spectra of ***L5*** (——). Overlap region shown in red colour.

quenched due to possible energy transfer from the ligand to Eu(III) centre. This result confirmed the coordination of $Eu(tta)_3$ with ***L5*** and the formation of [$(Eu(tta)_3)_2$(***L5***)] complex ***(C3)***. Additionally, the excitation spectrum of [$(Eu(tta)_3)_2$(***L5***)] complex monitored at λ_{em} of 611 nm (J = 2 transition) resulted in a profile with three maxima at 269, 291 and 361 nm, assignable to the absorption of ***C3*** complex (Figure 4.15e). Thus indicating an energy transfer from the ligand backbone to Eu(III) center.[27]

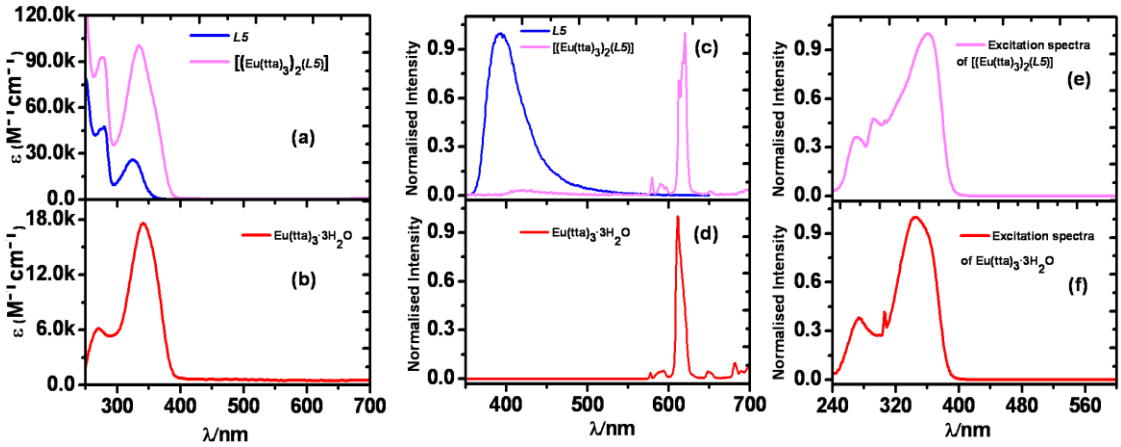

Figure 4.15 (a) absorption: *L5* (——) and [$(Eu(tta)_3)_2$(***L5***)] (——). (c) Emission: [$(Eu(tta)_3)_2$(***L5***)], λ_{exc} = 353 nm(——); *L5* (——), λ_{exc} = 353 nm; (e) Excitation: [$(Eu(tta)_3)_2$(***L5***)], λ_{em} = 613 nm (——).(b) absorption, (d) emission (λ_{exc} = 353 nm) and (f) excitation (λ_{em} = 613 nm) spectra of $Eu(tta)_3 \cdot 3H_2O$ (——).

Conclusions

In conclusion, we demonstrated an efficient one-pot technique for the fabrication of organic/inorganic hybrid parallelepipedic nanotubular structures displaying dual color luminescence by employing step-wise solvent assisted self-assembly techniques. Firstly, the parallelepipedic nano tubular-structures were grown from a novel blue emitting π-conjugated ligand molecule ***L5*** in THF/water. Secondly, for the first time a controlled surface selective coordination chemistry was performed on the ligand nanotubes by using $Eu(tta)_3$ to form a thin layer of red emitting $[(Eu(tta)_3)_2(\boldsymbol{L5})]$ complex ***C3***. Upon UV excitation the resultant organic/inorganic hybrid parallelepipedic nanostructures display a blue emission from the unreacted ligand (***L5***) part of the nanotubes, a Eu(III) centered red emission from the complex (***C3***) layer and the mixing of these two colors exhibit purple color (***L5****(blue)*+***C3****(red)* = purple emissions). The presented one-pot bottom-up nanotechnology technique to prepare tricolor displaying parallelepipedic nanotubes signifies an innovative step towards achieving multi-luminescent tubular photonic structures down to nanoscale. The detailed study on the optical wave guiding behavior of these nanotubes will be described in *Chapter 6*.

References

1. For a comprehensive overview on luminescent organic nanotubes: (a) Hu, J.; Odom, T. W.; Lieber, C. M. *Acc. Chem. Res*. **1999**, *32*, 435. (b) Zhao, Y. S.; Fu, H.; Peng, A.; Ma, Y.; Liao, Q.; Yao, J. *Acc. Chem. Res*. **2010**, *43*, 409. (c) Zhao, Y. S.; Xu, J.; Peng, A.; Fu, H.; Ma, Y.; Jiang, L.; Yao. J. *Angew. Chem., Int. Ed.* **2008**, *47*, 7301. (d) Liao, Q.; Fu, H.; Yao, J. *Adv. Mater.* **2009**, *21*, 4153. (e) Zhao, Y. S.; Peng, A.; Fu, H.; Ma, Y.; Yao, J. *Adv. Mater.* **2008**, *20*, 1661. (f) Zhao, L.; Yang, W.; Ma, Y.; Yao, J.; Li, Y.; Liu, H. *Chem. Commun.* **2003**, 2442.

2. For comprehensive overview about the role of supramolecular interaction for the formation of nanostructures: (a) Medforth, C. J.; Wang, Z.; Martin, K. E.; Song, Y.; Jacobsen, J. L.; Shelnutt, J. A. *Chem. Commun.* **2009**, 7261. (b) Schnur, J. M. *Science* **1993**, *262*, 1669. (c) Harada, A.; Li, J. Kamachi, M. *Nature*, **1993**, *364*, 516. (d) Shimizu, T.; *J. Polym. Sci. Part A: Polym. Chem.* **2008**, *46*, 2601. (e) Ajayaghosh, A.; Praveen, V. K. *Acc. Chem. Res.* **2007**, *40*, 644. (f) Nakanishi, T. *Chem. Commum.* **2010**, *46*, 3425. (g) Kimizuka, N.; Kawasaki, T.; Hirata, K.; Kunitake, T. *J. Am. Chem. Soc.* **1995**, *117*, 6360. (h) Mann, S. *Nat. Mater.* **2009**, *8*, 781. (i) Zubarev, E. R.; Sone, E. D.; Stupp, S. I. *Chem. Eur. J*. **2006**, *12*, 7313. (j) Iwamura, R.; Hoeben, F. J. M.; Masuda, M.; Scenning, A. P. H. J.; Meijer, E. W.; Shimizu, T. *J. Am. Chem. Soc.* **2006**, *128*, 13298. (k) Whitesides, G. M.; Grzybowski, B. *Science*, **2002**, *295*, 5564

3. (a) Seley, D. B.; Nath, M.; Parkinson, B. A. *J. Mater. Chem.* **2009**, *19*, 1532. (b) Wang, F.; Liu, X. *Chem. Soc. Rev.* **2009**, *38*, 976. (c) Vasileiadis, T.; Dracopoulos, V.; Kollia, M.; Yannopoulos, S. *Sci. Rep.* **2013**, *3*, 1.

4. (a) Hu, J.; Chen, Z.; Jiang, H.; Sun, Y.; Bandoc, Y.; Golbergc, D. *J. Mater. Chem*. **2009**, *19*, 3063. (b) Liu, J.; Xue, D. *J. Mater. Chem*. **2011**, *21*, 223.

5. (a) Ghadiri, M. R.; Granja, J. R.; Milligan, R. A.; McRee, D. E.; Khazanovich, N. *Nature,* **1993**, *366*, 324. (b) Hong, B. H.; Lee, J. Y.; Lee, C. W.; Kim, J. C.; Bae, S. C.; Kim, K. S. *J. Am. Chem. Soc.* **2001**, *123*, 10748. (c) Samori, P.; Francke, V.; Müllen, K.; Rabe, J. P. *Chem. Eur. J.* **1999**, *5*, 2312.

6. Yamaguchi, T.; Ishii, N.; Tashiro, K.; Aida, T. *J. Am. Chem. Soc.* **2003**, *125*, 13934.

7. John, G.; Masuda, M.; Okada, Y.; Yase, K.; Shimizu, T. *Adv. Mater.* **2001**, *13*, 715.

8. a) Zhao, Y. S.; Yang, W.; Xiao, D.; Sheng, X.; Yang, X.; Shuai, Z.; Luo, Y.; Yao, J. *Chem. Mater*. **2005**, *17*, 6430. b) Xu, Y. X.; Zhao, X.; Jiang, X. K.; Li, Z. T. *Chem. Commun.* **2009**, 4212. (c) Diaz, N.; Simon, F. X.; Schmutz, M.; Rawiso, M.; Decher, G.; Jestin, J.; Mésini, P. J. *Angew. Chem. Int. Ed*. **2005**, *44*, 3260. (d) Yoon, S. M.; Hwang, I. C.; Kim, K. S.; Choi, H. C. *Angew. Chem. Int. Ed*. **2009**, *48*, 2506. (e) Pantos, G. D.; Pengo, P.; Sanders, J. K. M. *Angew. Chem. Int. Ed*. **2007**, *46*, 2238. (f) Seo, M.; Kim, J. H.; Seo, G.; Shin, C. H.; Kim, S. Y. *Chem. Eur. J.* **2009**, *15*, 612. (g) Seo, M.; Seo, G.; Kim, S. Y. *Angew. Chem. Int. Ed*. **2006**, *45*, 6306. (h) Wu, D.; Zhi, L.; Bodwell, G. J.; Cui, G.; Tsao, N.; Müllen, K. *Angew. Chem. Int. Ed*. **2007**, *46*, 5417.

9. (a) Yan, X.; He, Q.; Wang, K.; Duan, L.; Cui, Y.; Li, J. *Angew. Chem. Int. Ed*. **2007**, *46*, 2431. (b) Leclair, S.; Baillargeon, P.; Skouta, R.; Gauthier, D.; Zhao, Y.; Dory, Y. L. *Angew. Chem. Int. Ed*. **2004**, *43*, 349.

10. Savariar, E. N.; Krishnamoorthy, K.; Thayumanavan, S. *Nat. Nanotech.* **2008**, *3*, 112.

11. (a) Chandrasekhar, N.; Chandrasekar, R. *J. Org. Chem.* **2010**, *75*, 4852. (b) Chandrasekhar, N.; Chandrasekar, R. *Chem. Commun.* **2010**, *46*, 2915. (c) Basak, S.; Hui. P.; Chandrasekar, R. *Synthesis* **2009**, *23*, 4042. (d) Rajadurai, C.; Fuhr, O.; Kruk, R.; Ghafari, M.; Hahn, H.; Ruben, M. *Chem. Commun.* **2007**, 2636. (e) Rajadurai, C.; Schramm, F.; Brink, S.; Fuhr, O.; Kruk, R.; Ghafari, M.; Ruben, M. *Inorg. Chem*. **2006**, *45*, 10019. (f) Rajadurai, C.; Ruben, M. *European Patent Application*, EP 2053049B1.

12. Crystal data for **1:** C_{22} H_{16} N_{10}; Triclinic; Space group *P*-1; F.W. = 420.45; a = 6.2631(12)Å; b = 7.4007(14)Å; c = 10.739(2)Å; α = 96.262(3)°; β = 101.807(3)°; γ = 95.236(3)°; V (Å^3) = 481.01(16); Index ranges = -7<=h<=7, -9<=k<=9, -13<=l<=13; Theta range for data collection (°) = 1.96 to 25.85; Z = 1; D_{obsd} (g/cm^3) = 1.451; Reflection Collected = 4981; μ (mm^{-1}) = 0.095; R(reflections) = 0.0531(1567); $R(Fo)$ = 0.0670; $R_w(F)$ = 0.1231; GOF on F^2 = 1.134; T = 100(2) K.

13. (a) Kasai, H.; Nalwa, H. S.; Oikawa, H.; Okada, S.; Matsuda, H.; Minami, N.; Kakuta, A.; Ono, K.; Mukoh, A.; Nakanishi, H. *Jpn. J. Appl. Phys.* **1992**, *31*, L1132. (b) Baba, K.; Kasai, H.; Okada, S.; Oikawa, H.; Nakanishi, H. *Opt. Mater.* **2002**, *21*, 591. (c) Nalwa, H. S.; Kasai, H.; Kamatani, H.; Okada, S.; Oikawa, H.; Matsuda, H.; Kakuta, A.; Mukoh, A.; Nakanishi, H. *Adv. Mater.* **1993**, *5*, 758. (c) Kasai, H.; Oikawa, H.; Nakanishi, H. *Organic Mesoscopic Chemistry* (Eds: H. Masuhara, F. C. Schryver), Blackwell Science, Oxford **1999**, pp. 145–170.

14. Zhao, Y. S.; Fu, H.; Peng, A.; Ma, Y.; Xiao, D.; Yao. J. *Adv. Mater.* **2008**, *20*, 2859.

15. Tachikawa, T.; Chung, H.; Masuhara, A.; Kasai, H.; Oikawa, H.; Nakanishi, H.; Fujitsuka, M.; Majima, T. *J. Am. Chem. Soc.* **2006**, *128*, 15944.

16. Keuren, E. V.; Bone, A.; Ma, C. *Langmuir* **2008**, *24*, 6079.

17. Tian, Z.; Chen, Y.; Yang, W.; Yao, J.; Zhu, L.; Shuai, Z. *Angew. Chem. Int. Ed.* **2004**, *43*, 4060.

18. Zhang, X.; Zhang, X.; Zou, K.; Lee, C.; Lee, S. *J. Am. Chem. Soc.* **2007**, *129*, 3527.

19. (a) Al-Kaysi, R. O.; Müller, A. M.; Ahn, T.; Lee, S.; Bardeen, C. J. *Langmuir* **2005**, *21*, 7990. (b) Bučar, D.; MacGillivray, L. R. *J. Am. Chem. Soc.* **2007**, *129*, 32.

20. Li, S.; He, L.; Xiong, F.; Li, Y.; Yang, G. *J. Phys. Chem. B* **2004**, *108*, 10887.

21. Hu, J.; Guo, Y.; Liang, H.; Wan, L.; Jiang, L. *J. Am. Chem. Soc.* **2005**, *127*, 17090.

22. (a) Bertorelle, F.; Lavabre, D.; Fery-Forgues, S. *J. Am. Chem. Soc.* **2003**, *125*, 6244. (b) Bîrlă, L.; Bertorelle, F.; Rodrigues, F.; Badré, S.; Pansu, R.; Fery-Forgues, S. *Langmuir* **2006**, *22*, 6256.

23. Jia, C. J.; Sun, L. D.; Yan, Z. G.; You, L. P.; Luo, F.; Han, X. D.; Pang, Y. C.; Zhang, Z.; Yan, C. H. *Angew. Chem.* **2005**, *117*, 4402; *Angew. Chem. Int. Ed.* **2005**, *44*, 4328.

24. Li, F.; Ding, Y.; Gao, P. X.; Xin, X. Q.; Wang, Z. L. *Angew. Chem.* **2004**, *116*, 5350; *Angew. Chem. Int. Ed.* **2004**, *43*, 5238.

25. (a) Bunzli, J. -C. G.; Piguet, C. *Chem. Soc. Rev*. **2005**, *34*, 1048. (b) Stanley, J. M.; Zhu, X.; Yang, X.; Holliday, B. J. *Inorg. Chem.* **2010**, *49*, 2035. (c) Kadjane, P.; Starck, M.; Camerel, F.; Hill, D.; Hildebrandt, N.; Ziessel, R.; Charbonnière, L. J. *Inorg. Chem*. **2009**, *48*, 4601.

26. Weissman, S. I. *J. Chem. Phys*. **1942**, *10*, 214.

27. (a) Pal, R. R.; Higuchi, M.; Kurth, D. G. *Org. Lett.* **2009**, *11*, 3562. (b) Binnemans, K.; Lenaerts, P.; Driesen, K.; Gorller-Walrand, C. *J. Mater. Chem.* **2004**, *14*, 191. (c) Li, J.; Song, F.; Wang, L.; Jiao, J.; Cheng, Y.; Zhu, C. *Macromol. Rapid Commun.* **2012**, *33*, 1268. (d) McGehee, M. D.; Bergstedt, T.; Zhang, C.; Saab, A. P.; O'Regan, M. B.; Bazan, G. C.; Srdanov, V. I.; Heeger, A. J. *Adv. Mater.* **1999**, *11*, 1349.

Appendix

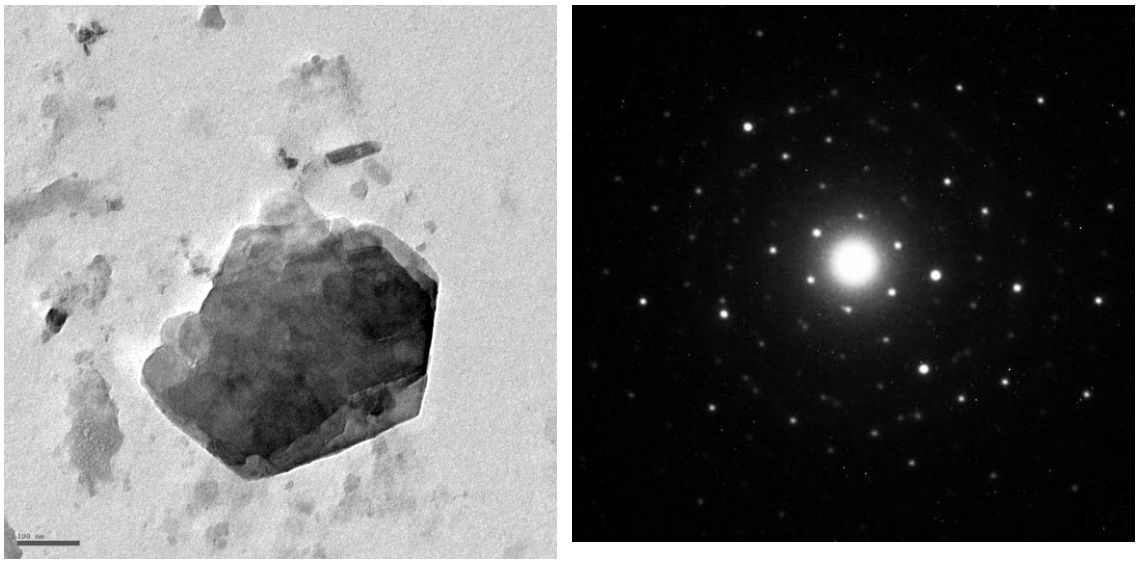

(a) **(b)**

Figure A1: (a) TEM image of a $Eu(tta)_3 \cdot H_2O$ nanocrystals (scale bar is 100 nm) and (b) Its SAED pattern

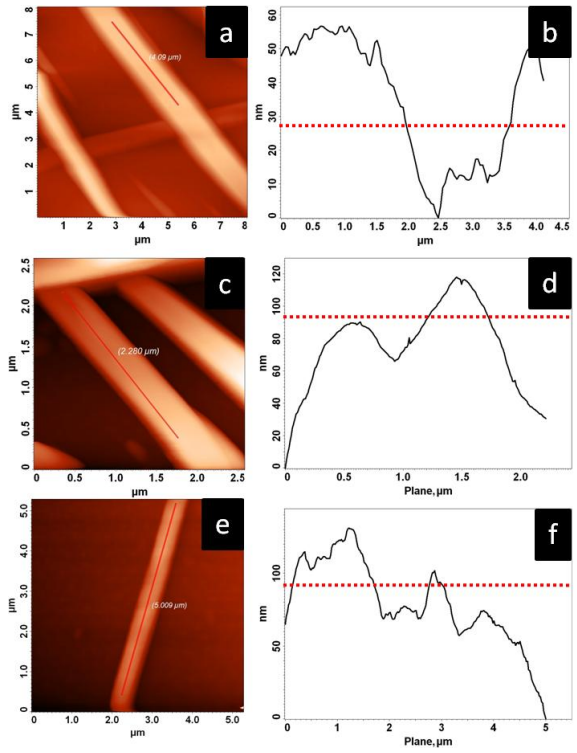

Figure A2: Tapping mode AFM images of rectangular tubes a, c and e and their corresponding profile b, d and f respectively, along the tube axis (red line).

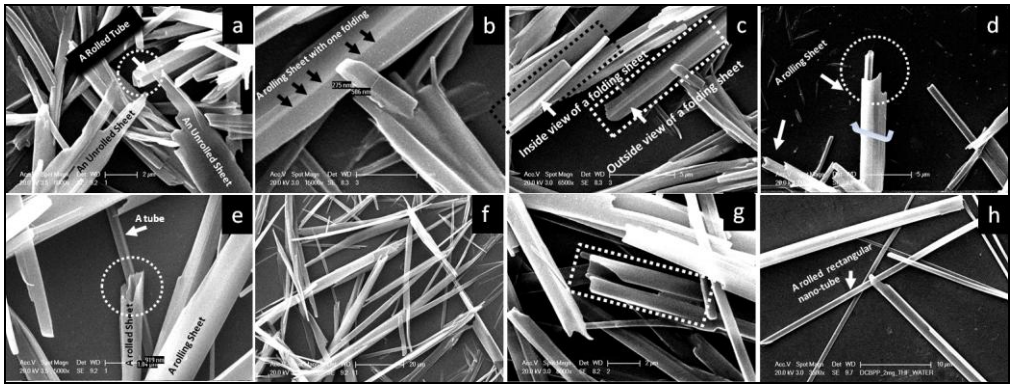

Figure A3: SEM micrographs of ***L5*** showing growth mechanism in THF/water. a) Sheet-like structures. White dotted circle: a rolled tube with rectangular cross section b) folded sheets. c) Black dotted rectangular box: an inside view of a folded sheet. White dotted rectangular box: an outside view of a folded sheet, d) White dotted circle: a rolled sheet forming a tubular morphology e) White arrow: a tube. White dotted circle: a rolled sheet with a rectangular cross section with tubular morphology. f) A collection of rolled sheets (before seaming process) g) White dotted rectangular box: seaming process involved in the rectangularly folded sheet with rectangular cavity. h) White arrow: a rolled tube with narrow cross-sections compared to the folding sheet with broader cross sections.

5

White Light Emitting Films from Eu(III) Complexed Copolymers of Alternating Fluorene and Bispyrazolylpyridine Derivatives

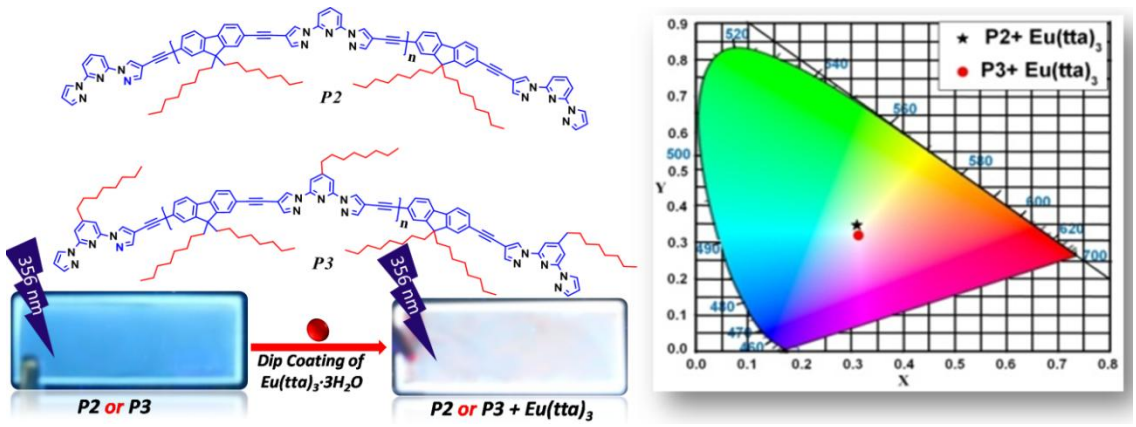

*This chapter is adapted from:

S. Basak, YSLV Narayana, M. Baumgarten, K. Müllen, and R. Chandrasekar* *Macromolecules* **2013,** *46,* 362.

5.1 Abstract

4-Ethynyl-2,6-bispyrazolylpyridine (BPP) end capped fluorene (FO) homo (P1) and FO-BPP main chain copolymers (P2 and P3) with ($\overline{M_n}$) around 10 kDa were successfully prepared. The optical band gap of P1-P3 copolymers were 2.69, 2.88 and 2.90 eV, respectively. Spin coated P2 and P3 thin films displayed blue and green dual emissions giving a mixed cyan color light under UV irradiation. By exploiting the metal coordinating ability of main chain tridentate BPP units, a red emitting Eu(III) ion coordinated conjugated polymer $[FO\text{-}(BPP(Eu(tta)_3))]_n$ layer was formed on top of the P2 and P3 thin films via dip coating technique to achieve white colour radiant films displaying triple emission with maxima at 425, 543, 614 nm and 428, 543, 611 nm for P2 and P3, respectively. The CIE (Commission internationale de l'Eclairage) coordinates were found to be (0.31, 0.35) and (0.31, 0.32) for white emitting films made from P2 and P3 respectively. These values are very close to the designated coordinates for a perfect white light emission (x = 0.33; y= 0.33).

5.2 Introduction

Metal containing conjugated polymers (MCCP)[1-3,8-12] have attracted immense interest among polymer and material scientists, since they offer the possibility for colour tunability through metal coordination with photoluminescent transition metal (Ru^{3+}, Ir^{3+})[2] and lanthanide (Ln^{3+})[3] ions. Particularly white light emitting MCCP are of interest due to their potential applications in light-emitting diodes, backlights for liquid-crystal displays or flat-panel displays, full-colour flat-panel displays and solid state lighting devices.[4-7] One way to achieve pure white colour with prescribed CIE coordinates in MCCP consists of incorporating two (blue and orange) or three emission chromophores (blue, green and red) in appropriate ratios covering the visible regions from 400 to 700 nm. Till now most of the reported luminescent MCCPs were made by incorporation of metal coordinating bidentate and tridentate ligands such as bipyridine[8], terpyridine[9] derivatives and benzimidazole.[10] The metal ions can be incorporated into the polymer chains by three different ways: (i) tethering of the metal ions into the polymer via long alkyl chains carrying ligands,[1h,10] (ii) construction of the conjugated polymers via metal-ditopic ligand self-assembly[11] i.e., metallo-supramolecular polymers and (iii) coupling of the metal ions directly to the conjugated polymer back bone containing ligand.[12] There are numerous

papers reported on the metal containing polymers synthesized by using methods (i) and (ii). Only a few articles reported to adopt the third method,[12] because the syntheses of conjugated polymers having fluorescent ligands (particularly tridentate type) in their backbone is still not a trivial task. Only one method described the electro polymerization of thiophene substituted BPP coordinated to Ru(II).[12a] Moreover, after metal incorporation most of the known conjugated polymers showed bad solubility in organic solvents and thus poor processability.

In order to address these solubility, processability, and multicolor emission issues, we have envisioned building alternating copolymers composed of FO and BPP units. It has been known for a long time that the blue emitting fluorene based homo polymers and

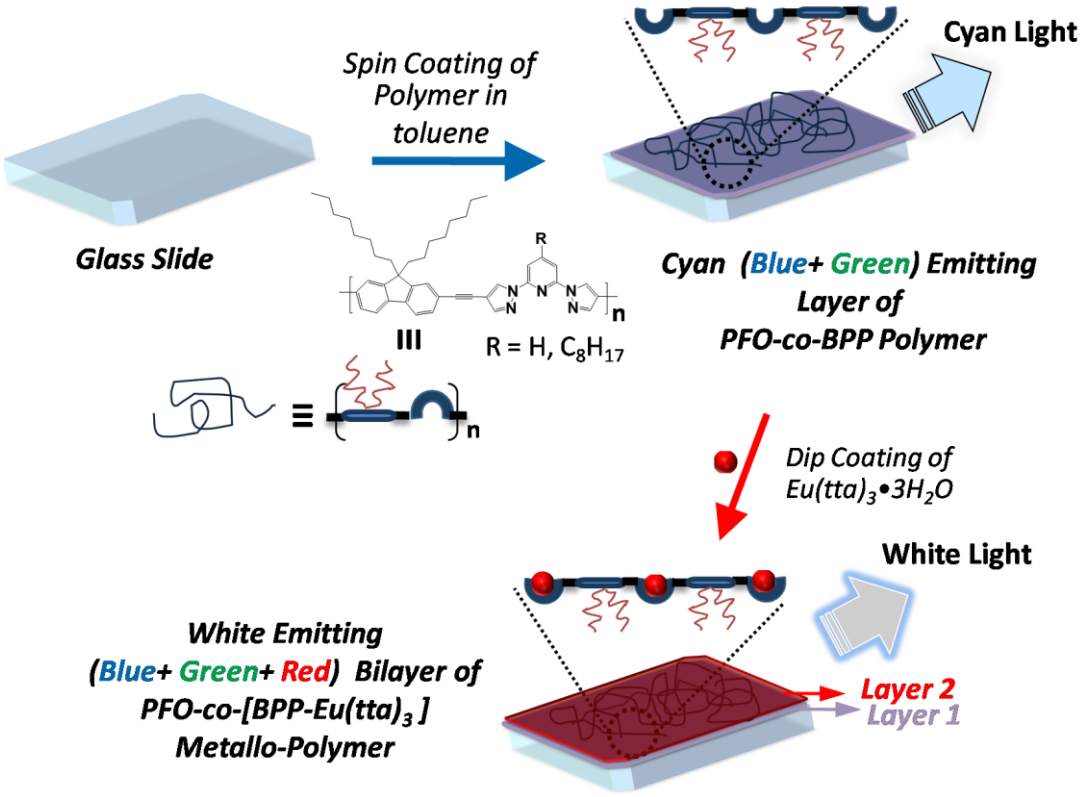

Scheme 5.1 Illustration of the technique involved in the preparation of white emitting polymer films from $Eu(tta)_3$ coordinated co-polymers **P2** and **P3.**

copolymers also show green emission due to fluorenone/excimer formation and ketone defects.[13] Taking advantage of the dual emissions, we thought that copolymerization of BPP with FO would combine some of the superior properties such as solubility, color tunability and processability of poly(9,9-dioctyl-9H-fluorene-2,7-diyl (PFO) and coordinating[14] ability of BPP derivatives with red phosphorescence metal ions to achieve white color emitting MCCPs films after correct color combinations.

In this chapter we report the syntheses of model compounds (**M1-M3**) and their corresponding homo and co-polymers namely, i) BPP end capped PFO homo polymer (**P1**), ii) alternating PFO-BPP copolymer (**P2**) end-capped with BPP units, and iii) copolymer **P3** from alternating PFO and octylated BPP units end capped with alkylated BPP units. We also show a method to achieve equal intensity ratios of the blue and green emissions by controlling the layer thickness of copolymers to get a mixed cyan color light.

Additionally, incorporation of the red emitting $Eu^{III}(tta)_3$ complex onto the blue-green emitting PFO-BPP thin film via metal coordination to generate white color light with CIE coordinates close to perfect white light will also be discussed (Scheme 5.1). The energy transfer process involved from polymer backbone to nine coordinated Eu(III) center will be presented. Detailed characterization of model compounds and polymers were performed using NMR, FTIR, and, UV-Vis spectroscopy, mass spectrometry, gel permeation chromatography (GPC), and thermo gravimetric analysis (TGA) techniques.

Results and Discussion

5.3.1 Synthesis of Polymers, Monomers and Model Compounds:

Syntheses:

2-bromo-9,9-dioctyl-9H-fluorene[15d], 2-ethynyl-9,9-dioctyl-9H-fluorene[15a] (**34**), 2,7-diiodo-9,9-dioctyl-9H-fluorene[15a] (**33**), 2,7-diethynyl-9,9-dioctyl-9H-fluorene[15a] (**32**), 2-(4-iodo-1H-pyrazol-1-yl)-6-(1H-pyrazol-1-yl)pyridine[15b] (**27**), 2,6-bis(4-iodo-1H-pyrazol-1-yl)pyridine[15b] (**24**) and 4-iodo-2,6-di(1H-pyrazol-1-yl)pyridine[15c] (**26**) were prepared according to literature procedure.

2-(4-iodo-1H-pyrazol-1-yl)-6-(1H-pyrazol-1-yl)pyridine (27:. 2,6-di(1H-pyrazol-1-yl)pyridine (1.0 g, 4.74 mmol) was charged in a round-bottomed flask containing AcOH (5 mL) and aq H_2SO_4 (30%, 0.5 mL). A deep-violet aqueous solution (50 mL) containing HIO_3 (0.55 g, 3.17 mmol), I_2 (1.55 g, 6.1 mmol) and two drops of concentrated H_2SO_4 was prepared. This solution was added drop wise to the mixture and the reaction was monitored constantly by TLC to maximize the amount of mono iodinated product. The reaction was stopped by adding aq $Na_2S_2O_3$ solution to destroy any excess iodine. The mixture was quenched with saturated aq $NaHCO_3$ followed by aqueous Na_2CO_3 solution

until pH ~ 8 was reached. The white precipitate that formed was extracted with $CHCl_3$ (3 × 50 mL), dried over $MgSO_4$ and evaporated under vacuo. The crude solid mixture was column chromatographed on silica gel using 5% EtOAc/Hexane to get compound **27** in 75% yields (1.2 g). ^{1}H NMR (400 MHz, $CDCl_3$-d_1) δ: 8.61 (s, 1 H), 8.56-8.55 (d, 1H) 7.94 - 7.87 (m, 2H), 7.81-7.74 (m, 3H), 6.5 (q, 1H). ^{13}C NMR (100 MHz, $CDCl_3$-d_1) δ: 150.02, 149.10, 147.0, 142.54, 141.58, 131.52, 127.04, 109.96, 108.86, 108.14, 60.11 ppm. FTIR (KBr disc; ν in cm^{-1}): 3150, 3101, 2925, 2843, 1610, 1582, 1517, 1473, 1391, 1319, 1204, 1139, 1029, 958, 936, 799. LCMS analysis: m/z calcd 337.12, found = 338.45 (positive mode). Anal. Calcd for $C_{11}H_8IN_5$: C, 39.19; H, 2.39; N, 20.77. Found: C, 39.26; H, 2.31; N, 20.65.

2-(4-iodo-1H-pyrazol-1-yl)-4-octyl-6-(1H-pyrazol-1-yl)pyridine (30:. 4-octyl-2,6-di(1H-pyrazol-1-yl)pyridine **29** (1.96 g, 4.36 mmol) was charged in a round-bottomed flask containing AcOH (5 mL) and H_2SO_4 (30%, 1.0 mL). A deep-violet aqueous solution (65 mL) containing HIO_3 (0.52 g, 2.95 mmol), I_2 (1.43 g, 5.63 mmol) and two drops of concentrated H_2SO_4 was prepared. This solution was added drop wise to the above solution and the reaction was monitored constantly by TLC to maximize the amount of mono iodinated product. The reaction was stopped by adding aqueous $Na_2S_2O_3$ solution to destroy any excess iodine. The mixture was quenched with aqueous sat. $NaHCO_3$ and then with aqueous Na_2CO_3 solution until pH ~ 8 was reached. The white precipitate that formed was extracted with $CHCl_3$ (3 × 50 mL), dried over $MgSO_4$ and evaporated under vacuo. The crude solid mixture was column chromatographed on silica gel using 5% EtoAc/Hexane to isolate compound **30** as the second fraction. Yield 650 mg (24%). ^{1}H NMR (400 MHz, $CDCl_3$-d_1) δ: 8.79 (s, 1H), 8.61 (s, 1H), 8.00 - 7.74 (m, 3H), 7.65 (s, 1H), 6.5 (s, 1H), 2.91 (t, 2H), 1.72 (t, 2H), 1.7-1.2 (m, 10H), 0.96 (t, 3H). ^{13}C NMR (100 MHz, $CDCl_3$-d_1) δ: 158.64, 150.03, 149.16, 146.78, 142.30, 131.67, 127.18 109.98, 108.93, 107.94, 59.80, 35.91, 31.83, 30.18, 29.35, 29.27, 29.16, 22.65, 14.10 ppm. FTIR (KBr disc; ν in cm^{-1}): 3126, 2924, 2855, 1616, 1572, 1520, 1462, 1398, 1381, 1259, 1203, 1173, 1041, 970, 941, 916, 893, 854, 767, 640, 608. LCMS analysis: m/z calcd 449.33, found = 450.25 (positive mode). HR-MS: *m/z* calcd 450.25, found 472.1 [M^+ + Na]. Anal. Calcd for $C_{19}H_{24}IN_5$: C, 50.79; H, 5.38; N, 15.59. Found: C, 50.68; H, 5.48; N, 15.41.

4-(oct-1-ynyl)-2,6-di(1H-pyrazol-1-yl)pyridine (28:. A Schlenk tube was charged with 4-iodo-2,6-di(1H-pyrazol-1-yl)pyridine **26** (1 g, 2.96 mmol) together with $Pd(PPh_3)_2Cl_2$, (104 mg, 0.148 mmol), triphenylphosphene (50 mg, 0.19 mmol) and CuI (50 mg, 0.262

mmol). Freshly distilled and anhydrous diisopropylamine (20 mL) and THF (10 mL) was added to it. The Schlenk tube was carefully degassed by several freeze and thaw cycles. To this 1-octyne (0.65 mL, (d = 0.746 g/mL; 4.45 mmol) was injected under argon by a syringe, and the resulting mixture was heated to 80 °C for 6 h. It was then cooled to room temperature and left for stirring for an additional hour. The mixture was filtered through filter paper and washed with THF. The filtrate was evaporated to get a dark brown solid which was column chromatographed on silica (100-200 mesh) using (8:92) EtOAc/Hexane to get desired compound **28** as a white crystalline solid. Yield 0.7 g (74%). ^{1}H NMR (400 MHz, $CDCl_3$-d_1) δ: 8.54 (s, 2H), 7.83 (s, 2H), 7.76 (s, 2H), 6.49 (m, 2H), 2.45 (t, 2H, *J* = 7.2), 1.66-1.26 (m, 5H), 0.94-0.91 (t, 3H) ppm. ^{13}C NMR (100 MHz, $CDCl_3$-d_1) δ: 150.08, 142.42, 137.69, 127.07, 111.65, 108.01, 97.41, 78.31, 31.35, 28.60, 28.31, 22.55, 19.51, 14.10 ppm. FTIR (KBr disc; ν in cm^{-1}): 3447, 2930, 2859, 2239, 1730, 1611, 1553, 1524, 1462, 1396, 1259, 1205, 1113, 1014, 955, 933, 791, 758. LC-MS m/z calcd 319.18, found 320.10 (positive mode). HR-MS: *m/z* calcd 319.18, found 342.17 [M^+ + Na]. Anal. Calcd for $C_{19}H_{21}N_5$: C, 71.45; H, 6.63; N, 21.39. Found: C, 71.64; H, 6.51; N, 21.85.

4-octyl-2,6-di(1H-pyrazol-1-yl)pyridine (29): To a degassed solution of 4-(oct-1-ynyl)-2,6-di(1H-pyrazol-1-yl)pyridine **28** (0.700 g, 2.19 mmol) in EtOAc (200 mL) was added 10% Pd/C (0.300g), and the mixture was stirred under H_2 balloon pressure. After 4 d the mixture was filtered through a celite plug to remove activated Pd/C. Afterwards the plug was washed with 100 mL of EtOAc and collected filtrate was concentrated to afford yellowish gummy oil. Yield 0.70 g (99%). ^{1}H NMR (400 MHz, $CDCl_3$-d_1) δ: 8.52 (d, 2H), 7.72 (s, 2H), 7.67 (s, 2H), 6.44 (s, 2H), 2.69 (t, 2H), 1.70-1.65 (q, 2H), 1.33-1.23 (m, 10H), 0.87-0.84 (t, 3H). ^{13}C NMR (100 MHz, $CDCl_3$-d_1) δ: 158.3, 149.9, 142.1, 127.1, 109.4, 107.7, 35.9, 31.8, 30.2, 29.4, 29.3, 29.2, 22.7, 14.1 ppm. FTIR (KBr disc; ν in cm^{-1}): 3484, 3152, 2926, 2855, 1769, 1728, 1618, 1572, 1522, 1466, 1398, 1261, 1207, 1111, 1041, 955, 918, 862, 787, 758, 642, 609. LCMS analysis: m/z calcd 323.44, found = 324.50 (positive mode). HR-MS: *m/z* calcd 323.44, found 346.201 [M^+ + Na]. Anal. Calcd for $C_{19}H_{25}N_5$: C, 70.56; H, 7.79; N, 21.65. Found: C, 70.42; H, 7.71; N, 21.48.

2,6-bis(4-iodo-1H-pyrazol-1-yl)-4-octylpyridine (31): 4-octyl-2,6-di(1H-pyrazol-1-yl)pyridine **29** (0.7 g, 2.16 mmol) in a round-bottomed flask was treated under argon with acetic acid (4 mL) and H_2SO_4 (30% in water, 0.5 mL) and heated to 60 °C. A separately prepared deep violet aqueous solution (H_2O, 10 mL) containing HIO_3 (0.29 g, 1.68

mmol), I_2 (0.85 g, 3.37 mmol) and two drops of concentrated H_2SO_4 was slowly added to the solution in such way that the iodine was consumed before addition of the next drop. After adding half of this solution (5 mL), the remaining 5 mL was completely dropped into the reaction mixture. At this time the reaction mixture appeared heterogeneous due to the presence of a white flocculate, which was left under argon atmosphere at 60 °C for a further 7 h. After the cooling the mixture to room temperature, enough aq. $Na_2S_2O_3$ was added to quench the pale rose color. A $NaHCO_3/Na_2CO_3$ (1:1 in H_2O) solution was used to neutralize the acetic acid/H_2SO_4 mixture (pH = 7–8) and the product 2,6-bis(4-iodo-1H-pyrazol-1-yl)-4-octylpyridine **31** was extracted with portions of $CHCl_3$. The $CHCl_3$ fractions were subsequently evaporated to get a glossy off white solid. The solid was washed with MeOH to get remove the colored impurities to get a white solid of **31** in 1.3 g yield (99%). ^{1}H NMR (400 MHz, $CDCl_3$-d_1) δ: 8.59 (s, 2H), 7.74 (s, 2H), 7.67 (s, 2H), 2.76-2.72 (t, 2H, *J* = 7.6), 1.73-1.67 (q, 2H), 1.33-1.26 (m, 10H), 0.89-0.86 (t, 3H). ^{13}C NMR (100 MHz, $CDCl_3$-d_1) δ: 159.0, 149.1, 146.9, 131.7, 109.5, 60.0, 35.9, 31.8, 30.2, 29.3, 29.2, 29.1, 22.6, 14.1 ppm. FTIR (KBr disc; ν in cm^{-1}): 2918, 2851, 1620, 1574, 1514, 1462, 1379, 1259, 1186, 1147, 1080, 1051, 968, 943, 858, 812, 788, 638, 596. LCMS analysis: m/z calcd 575.23, found = 575.55 (positive mode). HR-MS: *m/z* calcd 575.23, found 597.99 [M^+ + Na]. Anal. Calcd for $C_{19}H_{23}I_2N_5$: C, 39.67; H, 4.03; N, 12.17. Found: C, 39.65; H, 4.12; N, 12.28.

2-(4-((9,9-dioctyl-9H-fluoren-2-yl)ethynyl)-1H-pyrazol-1-yl)-6-(1H-pyrazol-1-yl)pyridine (M2): A dried 100 mL two neck round-bottomed flask was charged with 2-ethynyl-9,9-dioctyl-9H-fluorene **34** (0.200 g, 0.48 mmol), 2-(4-iodo-1H-pyrazol-1-yl)-6-(1H-pyrazol-1-yl)pyridine **27**, (0.162g, 0.48 mmol), $Pd(PPh_3)_2Cl_2$, (24 mg, 0.024 mmol), and CuI (10 mg, 0.012 mmol). The flask was evacuated and filled with nitrogen and charged with freshly distilled triethylamine (30 mL) and THF (20 mL). The resulting mixture was heated to 80 °C overnight. After cooling to room temperature the solvent from the mixture was evaporated under vacuo to afford pale yellowish oil. The product was further purified on a silica column with EtOAc/hexane (1:10) mixture to obtain **M2** as a fine yellowish oil (174 mg, yield 60%). ^{1}H NMR (400 MHz, $CDCl_3$-d_1, 25 ^{o}C) δ/ppm: 8.79 (s, 1H), 8.61 – 8.60 (d, 1H), 7.99 -7.87 (m, 4H), 7.8 (s, 1H), 7.73 -7.69 (m, 2H), 7.54 – 7.52 (m, 2H), 7.36 – 7.33 (m, 3H), 6.55 – 6.54 (s, 1H), 2.01-1.64 (m, 4H), 1.59 (s, 4H), 1.24-1.07 (m, 19H), 0.91-0.80 (m, 6H) ppm. ^{13}C NMR (100 MHz, $CDCl_3$-d_1, 25 ^{o}C) δ/ppm: 150.1, 144.5, 142.5, 141.5, 140.4, 130.4, 129.2, 127.5, 127.0, 126.9,

125.8, 122.9, 121.2, 119.9, 109.9, 109.5, 108.1, 106.0, 92.6, 55.1, 40.4, 31.8, 30.0, 29.2, 23.7, 22.6, 14.0. FT-IR (KBr) ν in cm^{-1}: 2928, 2854, 2318, 1713, 1605, 1522, 1473, 1391, 1339, 1207, 1146, 1076, 1034, 960, 937, 912, 833, 802, 754, 694, 654, 594, 571, 542, 515, 457, 408. LCMS analysis m/z: experimental value: 623.0, calculated value: 623.87. Elemental analysis: experimental value: C, 80.68; H, 7.85; N, 11.31. calculated value: C, 80.86; H, 7.92; N, 11.23.

Synthesis of compound M3: A dried 100 mL two neck round-bottomed flask was charged with 2-ethynyl-9,9-dioctyl-9H-fluorene **34** (0.180 g, 0.43 mmol) , 2-(4-iodo-1H-pyrazol-1-yl)-4-octyl-6-(1H-pyrazol-1-yl)pyridine **30** (0.194, 0.434 mmol), $Pd(PPh_3)_2Cl_2$ (30 mg, 0.043 mmol), and CuI (10 mg, 0.04 mmol). The flask was evacuated and backfilled with nitrogen and charged with freshly distilled diisopropylamine (30 mL) and anhydrous THF (20 mL). The resulting mixture was heated to 80 °C overnight. It was then cooled to room temperature and the mixture was evaporated under vacuo to afford pale yellowish oil. The product was further purified on a silica column (SiO_2) with an EtOAc/hexane (1:10) mixture to get an yellowish oil (195 mg, yield 62%). ^{1}H NMR (400 MHz, $CDCl_3$-d_1, 25 ^{o}C) δ/ppm: 8.79 (s, 1H), 8.61 – 8.60 (d, 1H), 7.94 (s, 1H), 7.79-7.78 (m, 5H), 7.73 -7.70 (m, 3H), 7.54 – 7.52 (m, 3H), 7.36 – 7.33 (m, 3H), 6.56 – 6.52 (s, 1H), 2.78 (t, 2H), 2.02 (t, 4H), 1.98 (s, 2H), 1.37-1.08 (m, 45H), 0.91-0.85 (m, 11H), 0.65-0.64 (m, 5H). ^{13}C NMR (100 MHz, $CDCl_3$-d_1, 25 ^{o}C) δ/ppm: 158.6, 151.1, 150.8, 150.0, 149.4, 144.3, 142.3, 141.4, 140.4, 130.3, 129.3, 127.6, 127.1, 126.9, 125.8, 122.9, 121.2, 120.0, 119.7, 109.9, 109.5, 107.9, 105.8, 92.5, 79.9, 55.1, 40.4, 35.9, 31.86, 31.84, 31.4, 30.24, 30.21, 30.0, 29.2, 29.1, 23.7, 22.68, 22.62, 14.0. FT-IR (KBr) ν in cm^{-1}: 3447, 2926, 2855, 1728, 1620, 1572, 1522, 1466, 1396, 1205, 1040, 955, 916, 862, 789, 758. LCMS analysis m/z: experimental value: 736.15, calculated value: 736.0. Elemental analysis: experimental value: C, 81.85; H, 8.26; N, 9.75.calculated value: C, 81.59; H, 8.90; N, 9.51.

Synthesis of P1: 4-iodo-2,6-di(1H-pyrazol-1-yl)pyridine **26** (30.73 mg, 0.091 mmol), 2,7-diethynyl-9,9-dioctyl-9H-fluorene **32** (200 mg, 0.455 mmol), 2,7-diiodo-9,9-dioctyl-9H-fluorene **33** (263 mg, 0.41 mmol), THF (10.0 mL), and diisopropylamine (20.0 mL) were taken in a two-neck round-bottom flask, and the solution was purged with nitrogen for 20 min. Afterwards the reaction mixture was deaerated by a repeated sequence of freeze-pump-thaw cycles. $PdCl_2(PPh_3)_2$ (16.0 mg, 0.02 mmol), PPh_3 (20.0 mg, 0.07 mmol) and CuI (20.0 mg, 0.1 mmol) were added to the reaction under nitrogen atmosphere and the

mixture was stirred at 60 °C overnight. After 16 h, a small excess of **26** (15.3 mg, 0.045 mmol) was added, and the reaction mixture was stirred for additional 6 h. The hot suspension was poured into a saturated aqueous EDTA solution (200 mL) and the mixture was stirred for 1 h. The organic layer was separated, and the aqueous layer was extracted with $CHCl_3$. The combined organic layers were washed with deionized water, and the volume was reduced under vacuo. The concentrated organic layer was redissolved in $CHCl_3$ and MeOH was added to precipitate the polymer. The white colored precipitate was filtered and washed with boiling MeOH, EtOH, CH_3CN followed by cold hexane and $CHCl_3$ and then by soxhlet extraction by a series of solvent like acetone, MeOH and $CHCl_3$. The acetone and MeOH fraction was discarded, the $CHCl_3$ fraction was collected and the polymer was precipitated by adding excess MeOH. The compound was dried in air at room temperature to yield **P1** as a light yellow powder (270 mg). X_n = 16, M_n = 7400 by ^{1}H NMR end group analysis. ^{1}H-NMR (400 MHz, $CDCl_3$-d_1, 298 K) δ: 8.60 (d, 4H, end group), 8.03 (s, 4H, end group), 7.81 (s, 4H, end group), 7.75-7.71 (t, 32H), 7.61-7.55 (m, 64H), 6.58 (d, 4H, end group) 2.04 (m, 25H), 1.27-1.10 (m, 380H), 0.9-0.82 (m, 132H), 0.65 (s, 52H). GPC (THF): M_n = 15.1 KDa, M_w= 29 KDa, PDI = 1.9. FTIR (KBr disc; ν in cm^{-1}): 2924, 2849, 1609, 1549, 1464, 1256, 1097, 1024, 887, 820, 754.

Synthesis of P2: The procedure is same as for **P1**. 2-(4-iodo-1H-pyrazol-1-yl)-6-(1H-pyrazol-1-yl)pyridine **27** (30.7 mg, 0.091 mmol), 2,7-diethynyl-9,9-dioctyl-9H-fluorene **32** (200 mg, 0.456 mmol), 2,6-bis(4-iodo-1H-pyrazol-1-yl)pyridine **24** (190mg, 0.41 mmol), THF (10.0 mL), and diisopropylamine (20.0 mL). After degassing, $Pd(PPh_3)_2Cl_2$ (16.0 mg, 0.02 mmol), PPh_3 (20.0 mg, 0.07 mmol) and CuI (20.0 mg, 0.1 mmol) were added. **P2** was obtained as a light yellow powder in 200 mg. X_n = 12, M_n = 8000 by ^{1}H NMR end group analysis. ^{1}H-NMR (400 MHz, $CDCl_3$-d_1, 298 K) δ: 8.80 (s, 18H), 8.69 (s, 2H, end group), 8.59 (s, 2H, end group), 7.98 (m, 56H), 7.88 (m, 6H, end group), 7.70 (m, 24H), 7.55 (s, 50H), 6.52 (s, 2H), 2.01 (s, 47H), 1.62 (s, 16H), 1.22-1.09 (m, 245H), 0.86 (m, 84H), 0.65 (t, 47H). GPC (THF): M_n = 8 KDa, M_w = 26 KDa , PDI = 3.25. FTIR (KBr disc; ν in cm^{-1}): 2924, 2853, 1605, 1582, 1522, 1470, 1396, 1352, 1286, 1192, 1144, 1088, 1038, 1003, 962, 862, 800, 654, 613.

Synthesis of P3: The procedure same as for **P1**. 2,6-bis(4-iodo-1H-pyrazol-1-yl)-4-octylpyridine **31** (236 mg, 0.41 mmol), 2-(4-iodo-1H-pyrazol-1-yl)-4-octyl-6-(1H-pyrazol-1-yl)pyridine **30** (40.97 mg, 0.09 mmol 1st time/ 20.45 mg, 0.045mmol 2nd time), compound **32** (200 mg, 0.45 mmol), $PdCl_2(PPh_3)_2$ (16.0 mg, 0.02 mmol, 5 mol %), PPh_3

(20.0 mg, 0.07 mmol) and CuI (20.0 mg, 0.1 mmol): yield 230 mg*; X_n* = 12, M_n = 9000 by ^{1}H NMR end group analysis. ^{1}H-NMR (400 MHz, $CDCl_3$-d_1, 298 K) δ: 8.82-8.79 (d, 18H), 8.60 (s, 2H, end group), 8.59 (s, 2H, end group), 7.95-7.94 (d, 20H), 7.78-7.70 (m,

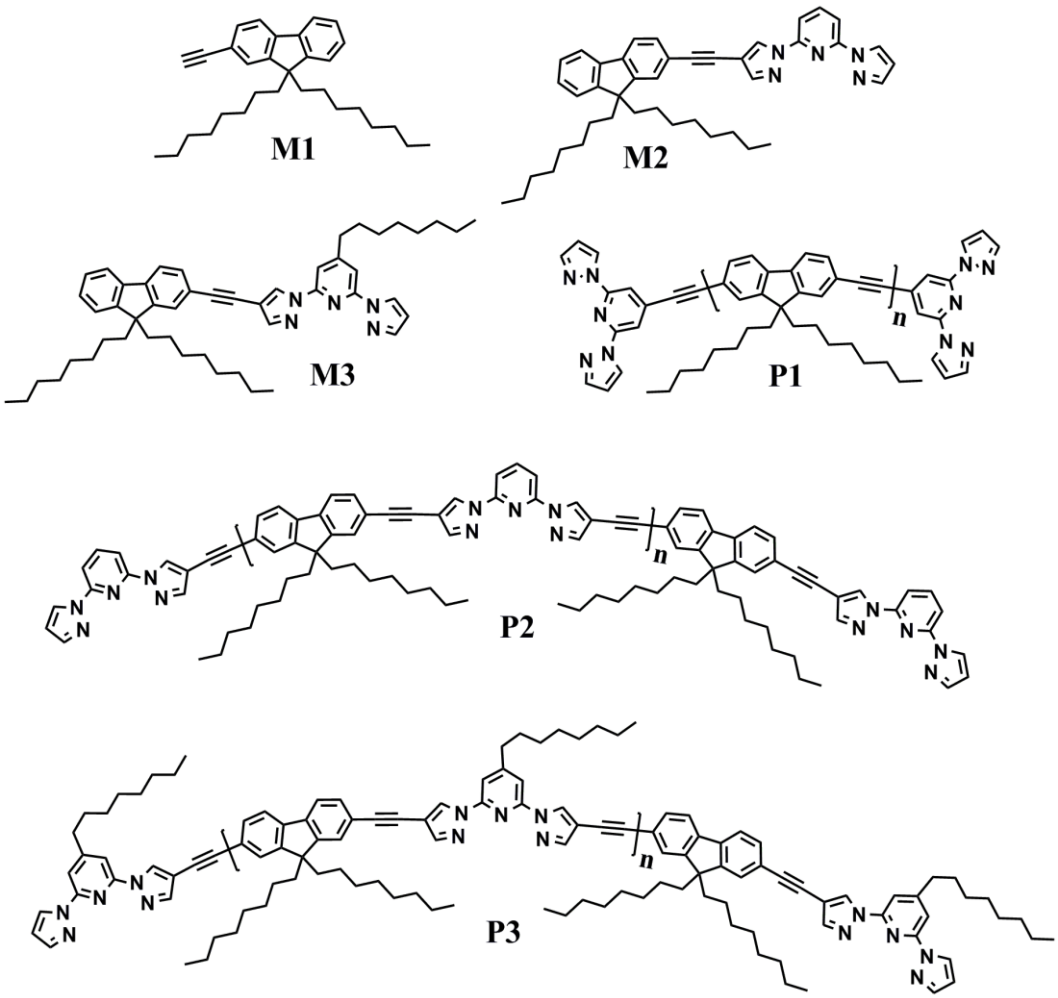

Chart 5.1 Chemical structures of model compounds (**M1-M3**) and homo and copolymers (**P1-P3**).

54H), 7.54 (s, 52H), 6.52 (s, 2H, end group), 2.79 (s, 24H), 2.02 (s, 47H), 1.76 (s, 29H), 1.61 (s, 19H), 1.4-1.1 (m, 415H), 0.91-0.81 (m, 138H), 0.66 (t, 54H). GPC (THF): M_n = 10 KDa, M_w = 26 KDa, PDI = 2.6. FTIR (KBr disc; ν in cm^{-1}): 2923, 2952, 1618, 1570, 1462, 1186, 1003, 968, 862, 817, 792.

Model compound **M1** was prepared as reported previously.[15a] **M2** and **M3** were synthesized under Sonogashira cross-coupling conditions by reacting monoalkynylated fluorine (**34)** with 2-(4-iodo-1H-pyrazol-1-yl)-6-(1H-pyrazol-1-yl)pyridine (**27**) for **M2** and compound **34** with 2-(4-iodo-1H-pyrazol-1-yl)-4-octyl-6-(1H-pyrazol-1-yl)pyridine (**30**) for **M3** in ca. 60% yields. Compound **27** was prepared by controlled monoiodination

of BPP in 75% yield. Octylated monoiodo BPP **30** was prepared from 4-iodo-2,6-di(1H-

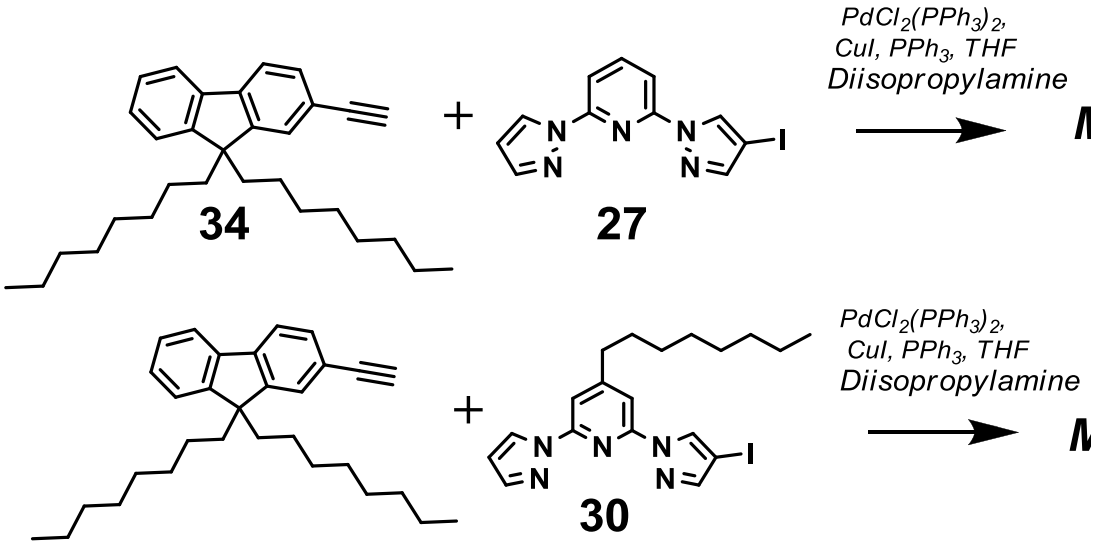

Scheme 5.2 Syntheses of model compounds (**M2** and **M3**).

pyrazol-1-yl)pyridine (**26**)[15c] in three steps. Firstly, 1-octyene was attached to **26** via Sonogashira cross-coupling reaction to get 4-(oct-1-ynyl)-2,6-di(1H-pyrazol-1-yl)pyridine (**28**) in 74% yield. Secondly, the triple bond in **28** was successfully reduced by using Pd/C/H_2 conditions to isolate 4-octyl-2,6-di(1H-pyrazol-1- yl)pyridine (**29**) as an oil in 99% yield. Subsequently, controlled iodination of **29** yielded both mono and diiodinated compounds 2,6-bis(4-iodo-1H-pyrazol-1-yl)-4-octylpyridine (**31**) and 2-(4-iodo-1H-pyrazol-1-yl)-4-octyl-6-(1H-pyrazol-1-yl)pyridine **30** in 99% and 24% yields, respectively. PFO polymer end-capped with 4-ethynyl BPP (**P1**) was prepared via Sonogashira cross-coupling reaction of 2,7-diiodo-9,9-dioctyl-9H-fluorene (**33**)[15d] and 2,7-diethynyl-9,9-dioctyl-9H-fluorene (**32**),[15a] using compound **26** as an end-capper (Scheme 5.3). The number-average degree of polymerization, $X_n \leq 18$ was maintained by controlling the molar ratio of two bifunctional monomers **32** and **33**. The polyconden-

Table 5.1 Physical properties of polymer (**P1-P3**)

Polymer	M_n (*by ^1H NMR*)	M_n by GPC (*after Soxhlet extraction*)	M_w by GPC	PDI	T_D (°C) (*by TGA*)
P1	7400	15100	29000	1.92	371
P2	8000	8000	26000	3.25	377
P3	9000	10000	26000	2.60	385

-sation reaction was performed using $Pd(PPh_3)_2Cl_2$/CuI catalysts in a mixture of tetrahydrofuran and diisopropylamine stirring at 80 ^oC.[16] An excess of end-capper **26** was added at the end of the reaction with an objective to maximize end-capping of polymer **P1**. The excess metal salts were removed by adding a saturated EDTA solution and then washing the polymer with a series of solvents like boiling MeOH, EtOH, and CH_3CN, followed by soxhlet extraction with a series of solvents like acetone, MeOH and $CHCl_3$. The acetone and MeOH ractions were discarded, and the $CHCl_3$ soluble fraction was collected and the polymer was precipitated by adding an excess MeOH. By following a similar methodology copolymer **P2** was synthesized by using **32**, 2,6-bis(4-iodo-1H-

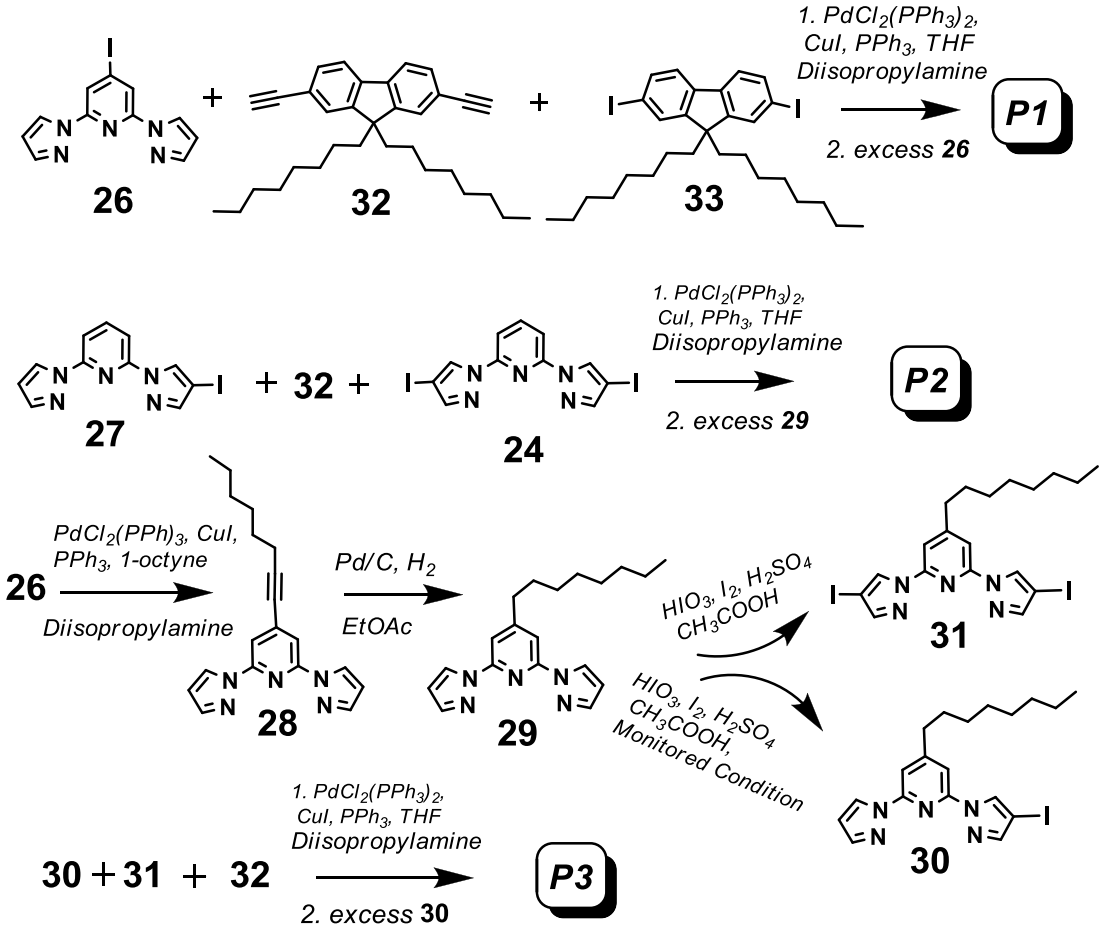

Scheme 5.3 Syntheses of Polymers (**P1-P3**).

pyrazol-1-yl)pyridine (**24**)[15b] and 2-(4-iodo-1H-pyrazol-1-yl)-6-(1H-pyrazol-1-yl) pyridine (**27**) as an end capping unit. Here the end capping unit (**27**) was used to determine the number average molecular weight ($\overline{M_n}$) of **P2** from the ^1H NMR spectrum by taking the pyrazole proton chemical shift (δ ~ 6.6 – 6.4 ppm) as a reference. To improve the solubility of **P2**, 2,6-bis(4-iodo-1H-pyrazol-1-yl)-4-octylpyridine (**31**) and **32**

were copolymerized using Sonogashira cross-coupling reaction with **30** as an end capping agent to obtain polymer **P3**. The ^{1}H NMR spectra proved the intact structure of the prepared polymers. ^{1}H NMR end-group analyses of polymers **P1** showed the ratio of the proton on fluorine (marked by "e") to *bpp* (marked by "a") is 16:2, but for a corresponding monomer (i.e. having one fluorine unit) the ratio is 2:4. This show there are sixteen repeating fluorine moiety in the polymer, and the calculated ($\overline{M_n}$) value becomes 7.4 KDa. Similarly for **P2** the ratio of the proton on fluorine (marked by "e") to *bpp* (marked by "a") is 25:2, but for a corresponding monomer the ratio is 1:1. This show there are *ca.* twelve repeating moiety in the polymer, and the calculated ($\overline{M_n}$) value becomes ~ 8 KDa (Fig. 5.1). Similarly calculation for **P3** shows the molecular weight is ~ 9 KDa. Additionally the obtained polymers were subjected to Soxhlet extraction to remove low molecular weight polymers and to isolate thin film forming higher molecular weight fractions. The GPC analysis showed improved ($\overline{M_n}$) in the range of 15 KDa, 8 KDa, and 10 KDa for **P1**-**P3**, respectively (Table 5.1).

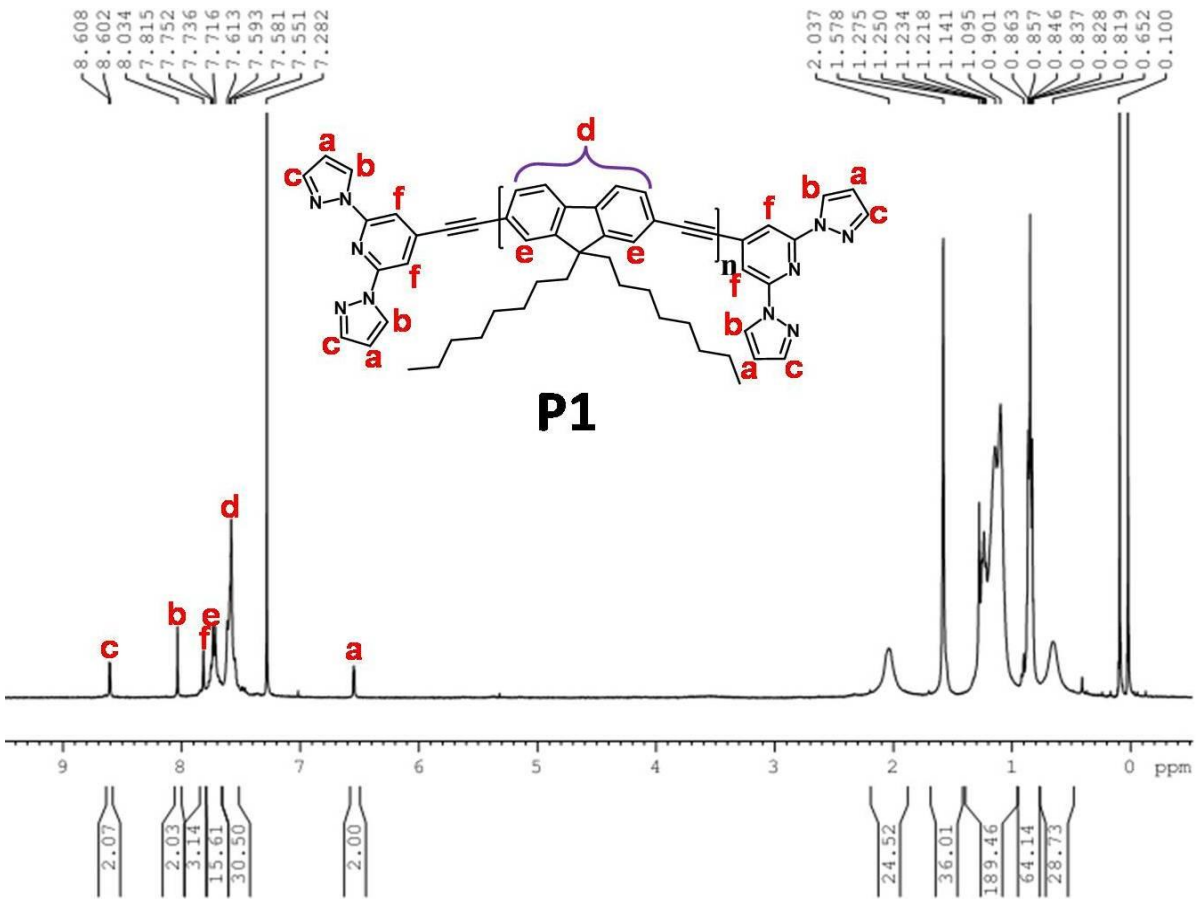

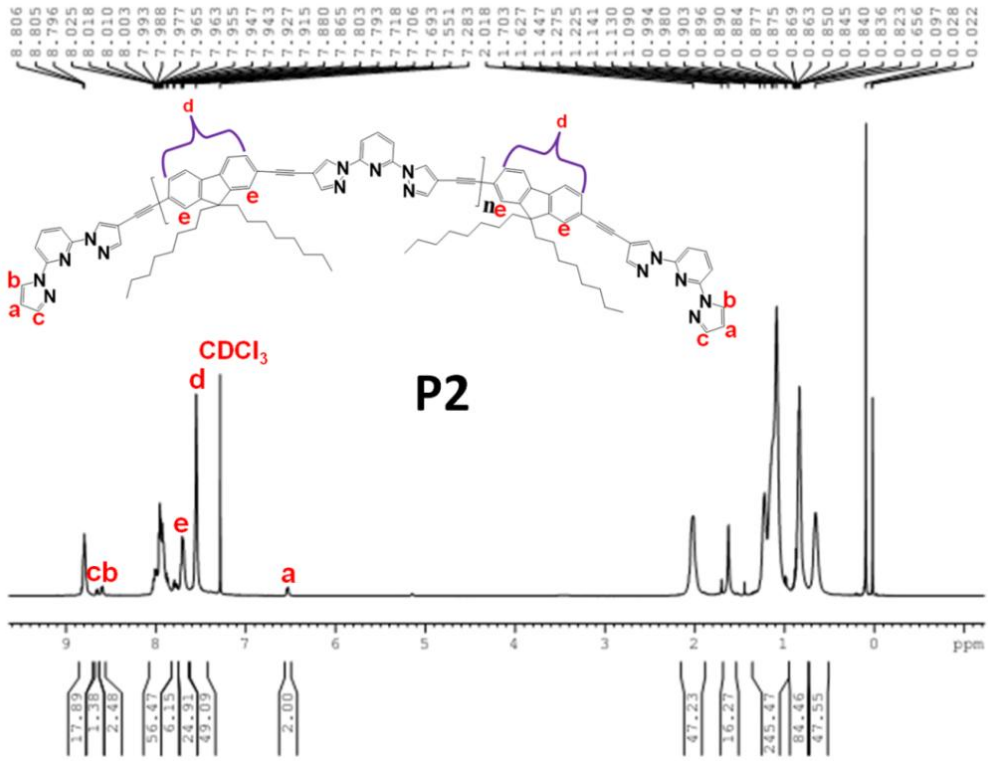

Figure 5.1 ^{1}H-NMR spectra of **P1** and **P2**

The decomposition temperature (T_D) of polymers **P1-P3** was 371 °C, 377 °C and 385 °C, respectively (Fig. 5.2). These data demonstrated that the incorporation of BPP units within the PFO main chain increased the thermal stability of the resultant BPP-PFO copolymers due to probable hindered polymer chain mobility.

5.3.2 Optical Properties of Polymers in Solution: The photo physical characteristics of the polymers were studied both in $CHCl_3$ solution and in spin-casted thin films; all spectroscopic data are summarized in Table 5.2, and absorption and emission spectra of polymers **P1-P3** are shown in (Fig. 5.3). All the polymers **P1-P3** exhibited two absorption bands in solution due to π-π*

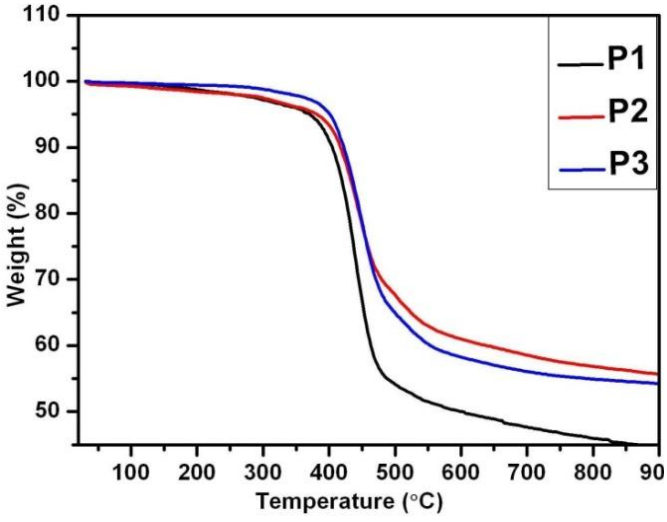

Figure 5.2 TGA analyses of polymers (**P1-P3**).

transition, with the absorption maxima at 411/393, 330/235, 317/238 nm, respectively.

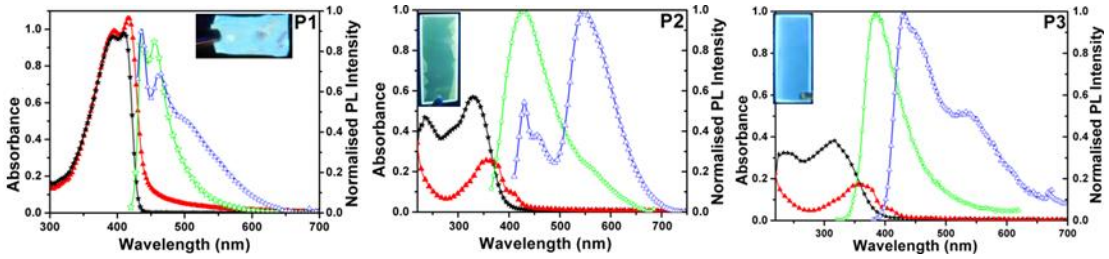

[a]Quinine sulfate as reference (Q_{ref} = 0.577). [b]Estimated from the onset wavelength of optical absorption in the solid state film.

Figure 5.3 Optical properties of **P1**-**P3**. Absorption spectra in $CHCl_3$ solution (—★—), spin casted film (—▲—), and PL spectra in $CHCl_3$ solution (—☆—), spin casted film (—△—).The insets show the emission colors of the polymer films under UV light.

Optical excitation of the polymers in solution caused intense blue fluorescence. The emission spectrum of polymer **P1** displayed two well-resolved bands near 436 and 455 nm which are characteristic for conjugated polyfluorene. Polymer **P2** exhibited an intense emission at 427 nm and a low intense shoulder at 563 nm, which probably occurs due to possible excimer/ketone formation,[13d] while polymer **P3** showed a blue shifted single band at 383 nm compared to **P2**. This is probably due to the decrease of the planarity of successive aromatic units caused by the octylated BPP units in the polymer **P3** backbone, which reduces the electronic conjugation leading to an increased band gap of ca. 2.90 eV.[17]

Table 5.2 Solution and solid state optical absorption and photo luminescent data of **P1-P3.**

	Solution ($CHCl_3$)				**Thin Film**			
Polymer	*Absorption λ_{max} (nm)*	*Excitation λ_{ex} (nm)*	*Emission λ_{max} (nm)*	*Φ_f^a*	*Absorption λ_{max} (nm)*	*Emission λ_{max} (nm)*	*Excitationλ_{ex} (nm)*	*Optical band Gap[b]/eV*
P1	393, 411	411	436, 455	61%	395, 417	436, 464, 506	417	2.69
P2	235, 330	330	427,563 (weak)	55%	358, 407	430, 455, 546	354	2.88
P3	238, 317	317	383	36%	352, 407	431, 456, 534	352	2.90

5.3.3 Optical Properties of Pristine Films and Eu(III) Coordinated Thin Films: All polymers were readily processed into homogeneous films of good optical quality by spin-

coating from toluene (for **P1**) and $CHCl_3$ (for **P2-P3**) solution (~10^{-5} M for **P1**, ~ 0.2 M for **P2**, ~0.1 M for **P3**) at 6000 rpm on clean quartz substrates. The absorption spectra of spin-casted copolymer films (**P1 - P3**) showed slightly red shifted and broadened bands at (395, 417), (358, 407), and (352, 407) nm, respectively, when compared to solution state

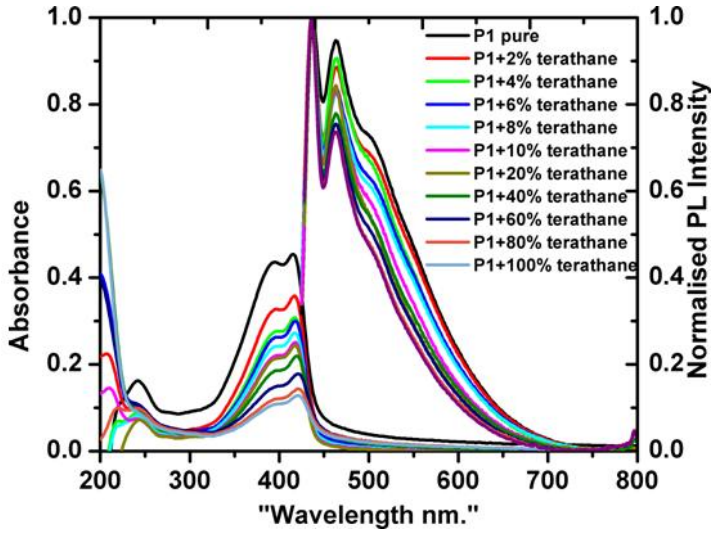

Figure 5.4 Spin cast films of polymer **P1** in terathane from $CHCl_3$ solution. Films were excited at 417 nm. Spectrum were normalised at 435 nm. It is clear that with solid state dilution of the film the green (excimer) emission goes down. With further dilution of the film may behave like a solution.

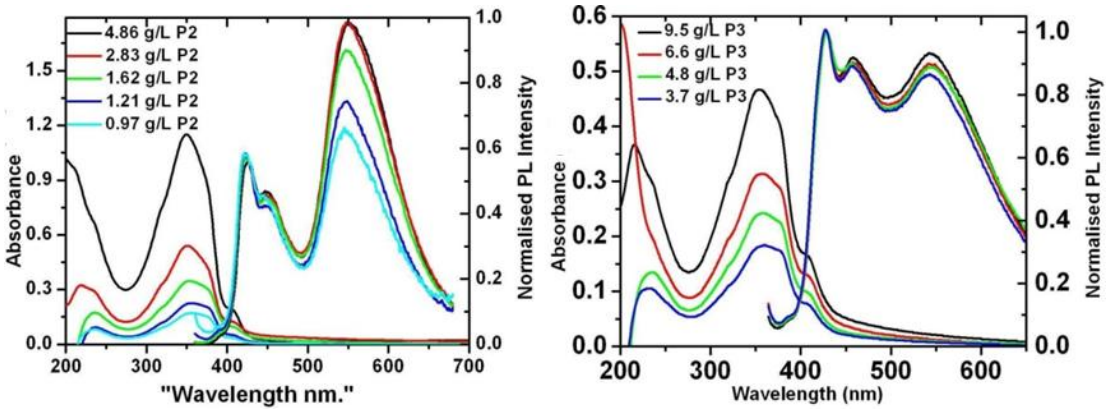

Figure 5.5 Absorption and emission spectra of **P2** and **P3** polymer films prepared by spin coating from a $CHCl_3$ solution at different concentration. Absorption and Emission spectrum was collected from films prepared by spin coating from a $CHCl_3$ solution of **P2** and **P3.** The film thickness was varied by changing the concentration of the solution and keeping the injection amount (200 µL), spin coating time (10 sec) and rpm (6000) same for each cases. With decrease of the thickness of the film the absorbance decreases according to Lambert- Beer's law.

absorptions (Fig. 5.3). These features are characteristic of chain aggregation and pronounced interchain interactions.[18] Polymer **P1** showed two blue emission bands at 436 nm and 455 nm in solution, whereas in the solid film the 455 nm band shifted to 464 nm with reduced intensity and a new band appeared at 506 nm with a long tail which

continued up to 650 nm displaying green color. This broad emission can be attributed to excimer-like behavior.[13] To confirm this, solid solution of **P1** was prepared with a non emissive poly(tetrahydrofuran) polymer matrix (terathane 2900), (Fig. 5.4) and interestingly with dilution i.e. with increase of terathane/**P1** ratio the solid film showed a decreased green emission due to the segregation of polymer chains. At 1:1 ratio the solid film showed a blue emission from the film and with further increase of terathane loading the solid polymer film behaves almost like a solution.

The solid film of polymer **P2** provided an emission at 430 nm along with an appearance of an intense broad emission at 546 nm which continued up to 710 nm due to excimer/aggregate formation. The ratio of I_{430}/I_{546} depends on the polymer film thickness (Fig. 5.5). Similar behavior was observed in case of **P3** but the band responsible for excimer emission (low energy band) is 12 nm blue shifted compared to **P2** which is attributed to the incorporation of octylated BPP unit which reduces the intermolecular interaction leading to a blue shifted emission.[17] Since the overall color of the **P2** polymer film depends on the accumulative intensity of the two bands viz. at 430 nm due to an excited state (A*) emission and at 546 nm because of excimer/aggregate like (AA*) nature. The appearing color of the **P2** polymer film under UV light can be controlled by various factors such as polymer film thickness,[19] temperature of the film and diluting with non emissive polymer matrix. In our case the emission intensity of I_{430}/I_{546} was adjusted by tuning the polymer film thickness in such a way that a cyan color light was obtained. We found that spin coating of a $CHCl_3$ solution of concentration of 0.97 g/L of **P2** emitted a brilliant cyan color with $I_{430}/I_{546} \sim 1$ (Fig. 5.5). Furthermore by utilizing the metal coordination ability of main chain BPP units present in polymers **P2** and **P3** incorporation of red emitting $Eu(tta)_3$[14a,21] was envisioned to achieve a final white color light. Therefore the **P2** film was dipped in a 20 mL methanol solution containing 1 mg $Eu(tta)_3$ complex for one hour. Here the amount of $Eu(tta)_3$ complex formation was optimized to control the intensity of the Eu(III) centered red phosphorescence [$^5D_0 \rightarrow {}^7F_J$ (J= 0–4) transitions] according to the intensity of I_{430}/I_{546} emissions to attain good quality white color. Exposure of **P2** film surface coordinated with $Eu(tta)_3$ complex under UV light showed a brilliant white color light due to the mixing of 430/546/613 emissions (Fig. 5.6). Similarly for **P3** white light was obtained by controlling the polymer film thickness (c = 9.5 g/L; $CHCl_3$ spin coating) and $Eu(tta)_3$ (1 mg in 20 mL of MeOH) concentration. The purity of the emitted white-light was examined by chromaticity

diagram (Fig. 5.6c) for which the CIE coordinates[3b] were found to be (0.31, 0.35) and (0.31, 0.32) for films made from **P2** and **P3**, respectively. The x and y coordinates obtained for our polymers are very close to the designated coordinates for perfect white-light (x = 0.33; y = 0.33).

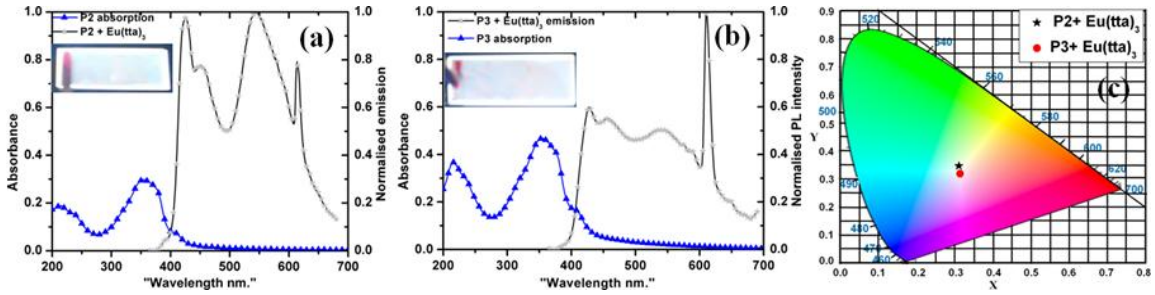

Figure 5.6 a) and b) Optical absorption and emission spectra of white emitting Eu(tta)$_3$ coordinated **P2** and **P3** films, respectively. c) Emission color of Eu(tta)$_3$ coated **P2** and **P3** film in a CIE 1931 2° Standard observer chromaticity diagram. The insets in (a) and (b) show the white emitting thin films under UV excitation.

Additionally the involvement of any energy transfer process between the coordinated Eu(III) centre and the polymer backbone in the white emitting **P2** film was examined (Fig. 5.7). Excitation of white light emitting Eu(tta)$_3$ coordinated **P2** polymer at 353 nm (corresponding to the absorption maximum of **P2**), showed a collective luminescence bands of pristine polymers together with features corresponding to Eu(tta)$_3$[$^5D_0 \rightarrow {}^7F_J$; see visible J = 2 transition at 613 nm] (Fig. 5.7c and d). While direct

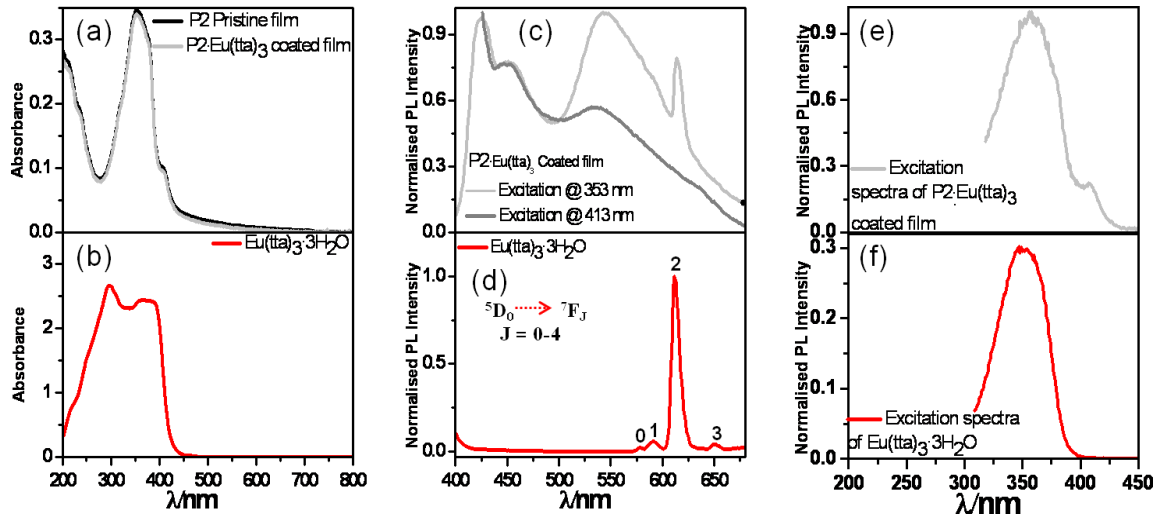

Figure 5.7 (a) Absorption: **P2** (▬) and Eu(tta)$_3$ coordinated film (▬). (c) Emission: Eu(tta)$_3$ coordinated film, λ_{exc} = 353 nm(▬); λ_{exc} = 413 nm (▬) (e) Excitation: Eu(tta)$_3$ coordinated film, λ_{em} = 613 nm (▬).(b) Absorption, (d) emission (λ_{exc} = 413 nm) and (f) excitation (λ_{em} = 613 nm) spectra of Eu(tta)$_3$·3H$_2$O.

excitation of the same polymer at 413 nm (corresponding to the absorption of $Eu(tta)_3 \cdot 3H_2O$) exhibited no Eu(III) centered emission (Fig. 5.7c), but excitation at this wavelength pure $Eu(tta)_3 \cdot 3H_2O$ showed red emission (Fig. 5.7d). This result confirmed the coordination of $Eu(tta)_3$ with polymer and formation of $[FO\text{-}(BPP(Eu(tta)_3))]_n$ layer. Additionally, the excitation spectrum of white light emitting $Eu(tta)_3$ coordinated **P2** polymer film monitored at λ_{em} of 613 nm (J = 2 transition) resulted in a profile with two maxima at 358 and 407 nm, assignable to the absorption of pristine **P2** film (Fig. 5.7e), thus indicating an energy transfer from the polymer backbone to Eu(III) center[11a, 22].

5.4 Conclusions

In conclusion a BPP end capped fluorene homo polymer and two novel BPP-Fluorene copolymers have been prepared. Because of their excimer like behavior a dual emission[20] was obtained from the copolymers displaying a mixed cyan color. Furthermore using the coordinating ability of the polymer main chain tridentate BPP units, a layer of $[FO\text{-}(BPP(Eu(tta)_3)]$ complex was formed on the surface of the polymer film to generate almost pure white light emission. Additionally the involvement of energy transfer process from polymer chain to coordinated Eu(III) center was demonstrated. The presented technology of generating the white light is very simple, unprecedented and promising for potential future development in the field of optoelectronic applications.

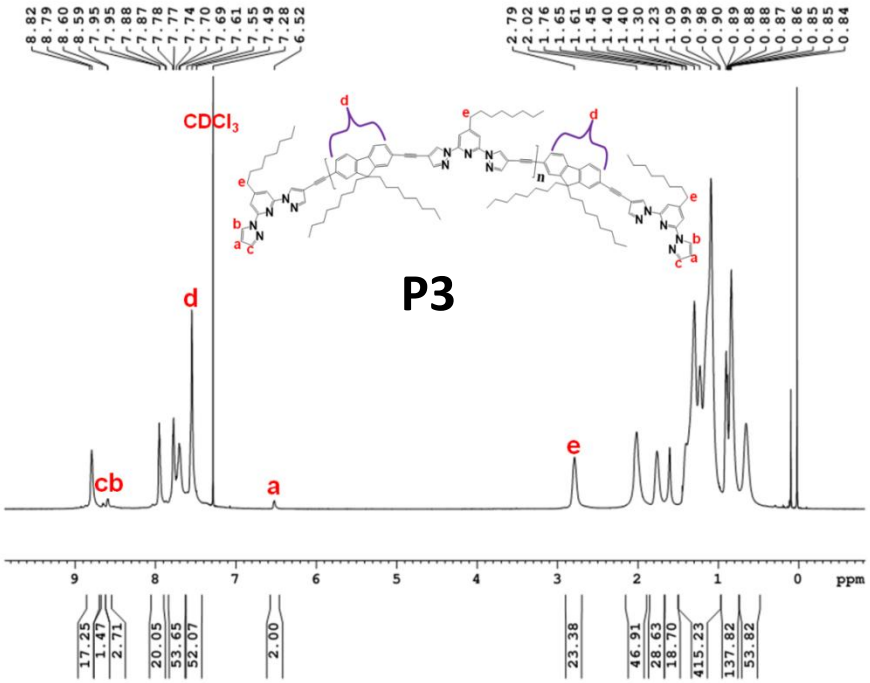

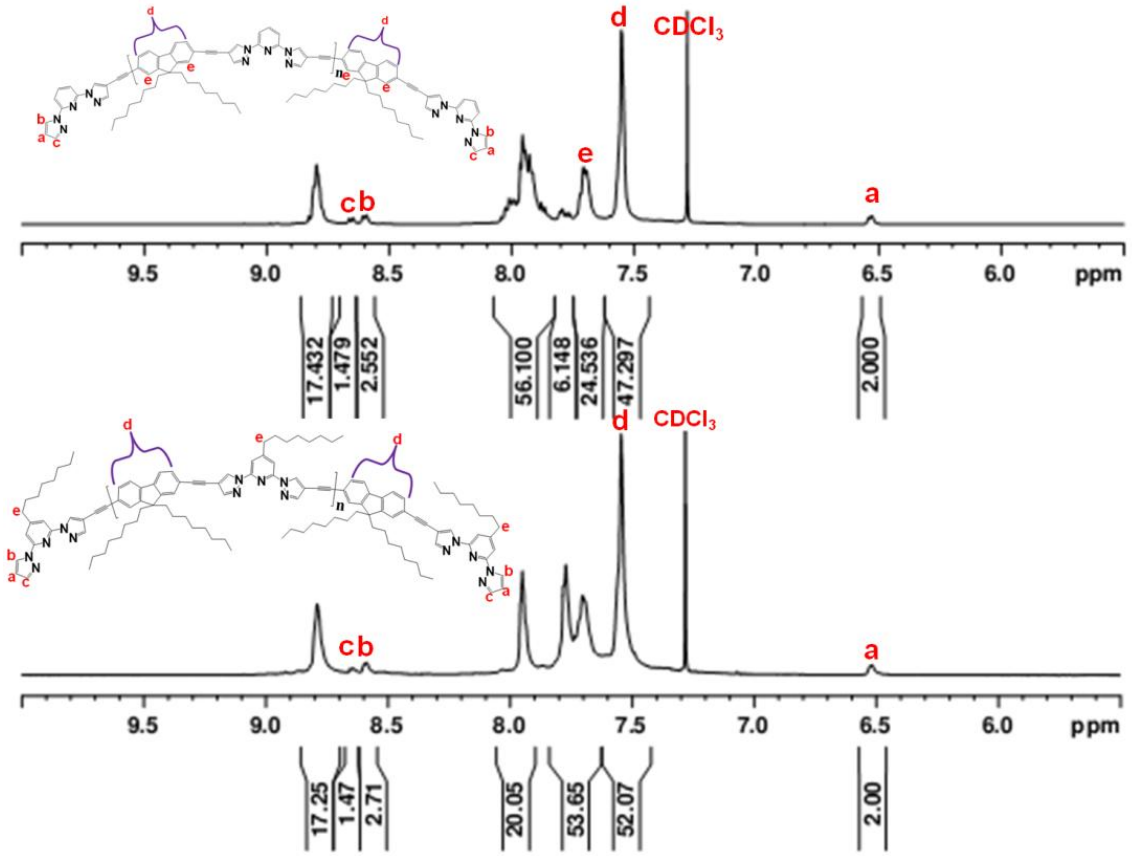

References

1. (a) Lehn, J.-M. *Supramolecular Chemistry*; VCH: Weinheim, **1995**. (b) Samori, P.; Cacialli, F. *Functional Supramolecular Architectures*; Wiley-VCH, **2011**. (c) Zhu, S. S.; Swager, T. M. *J. Am. Chem. Soc.* **1997**, *119*, 12568. (d) Constable, E. C.; Ward, M. D. *J. Chem. Soc., Dalton Trans*. **1990**, 1405. (e) Collin, J. P.; Laine, P.; Launay, J.-P.; Sauvage, J.-P.; Sour, A. *J. Chem. Soc., Chem. Commun*. **1993**, 434. (f) Chelucci, G; Thummel, R. P. *Chem. Rev*. **2002**, *102*, 3129. (g) Constable, E. C. *Chem. Soc. Rev.* **2007**, *36*, 246. (h) Schubert, U. S.; Hofmeier, H.; Newkome, G. R. *Modern Terpyridine Chemistry*; Wiley-VCH: Weinheim, **2006**; *69*. (i) Whittell, G. R.; Hager, M. D.; Schubert, U. S.; Manners, I. *Nat. Mater*. **2011**, *10*, 176. (j) Wolf, M. O. *J. Inorg. Organomet. Polym*. **2006**, *16*, 189.

2. (a) Qin, T.; Ding, J.; Baumgarten, M.; Wang, L.; Müllen, K. *Macromol. Rapid Commun.* **2012**, *33*, 1036. (b) Park, M. J.; Kwak, J.; Lee, J.; Jung, I. H.; Kong, H.; Lee, C.; Hwang, D. H.; Shim, H. K. *Macromolecules,* **2010**, *43*, 1379. (c) Grimsdale, A. C.; Chan, K. L.; Martin, R. E.; Jokisz, P. G.; Holmes, A. B. *Chem. Rev.* **2009**, *109*, 897. (d) Mishra, S. P.; Krishnamoorthy, K.; Sahoo, R.; Kumar, A. *J. Mater. Chem*. **2006**, *16*, 3297.

3. (a) Shunmugam, R.; Tew, G. N. *J. Am. Chem. Soc*. **2005**, *127*, 13567. (b) He, G.; Guo, D.; He, C.; Zhang, X.; Zhao, X.; Duan, C. *Angew. Chem. Int. Ed.* **2009**, *48*, 6132. (c) Balamurugan, A.; Reddy, M. L. P.; Jayakannan, M. *J. Phys. Chem. B,* **2009**, *113*, 14128. (d) Harrison, B. S.; Foley, T. J.; Bouguettaya, M.; Boncella, J. M.; Reynolds, J. R. *Appl. Phys. Lett.* **2001**, *79*, 37703.

4. D'Andrade, B. W.; Forrest, S. R. *Adv Mater.* **2004**, *16*, 1585.

5. Misra, A.; Kumar, P.; Kamalasanan, M. N.; Chandra, S. *Semicond Sci Technol*, **2006**, 21, R35-R47.

6. Sun, Y. R.; Giebink, N. C.; Kanno, H.; Ma, B. W.; Thompson, M. E.; Forrest, S. R. *Nature* **2006**, *440*, 908.

7. Schwartz, G.; Pfeiffer, M.; Reineke, S.; Walzer, K.; Leo, K. *Adv Mater,* **2007**, *19*, 3672.

8. (a) Metera, K. L.; Sleiman, H. *Macromolecules* **2007**, *40*, 3733. (b) Kokil, A.; Yao, P.; Weder, C. *Macromolecules* **2005**, *38*, 3800. (c) Walters, K. A.; Trouillet, L.; Guillerez, S.; Schanze, K. S. *Inorg. Chem*. **2000**, *39*, 5496. (d) Thomas, K. R. J.; Lin, J. T.; Lin, H. M.; Chang, C. P.; Chuen, C. H. *Organometallics* **2001**, *20*, 557. (e) Trouillet, L.; Nicola, A. D.; Guillerez, S. *Chem. Mater*. **2000**, *12*, 1611. (f) Pefkianakis, E. K.; Tzanetos, N. P.; Kallitsis J. K. *Chem. Mater*. **2008**, *20*, 6254. (g) Tian, L.; Zhang, W.; Yang, B.; Lu, P.; Zhang, M.; Lu, D.; Ma, Y.; Shen, J. *J. Phys. Chem. A*, **2005**, *109*, 6944. (h) Pautzsch, T.; Klemm, E. *Macromolecules* **2002**, *35*, 1569.

9. (a) Schlutter, F.; Wild, A.; Winter, A.; Hager, M. D.; Baumgaertel, A.; Friebe, C.; Schubert, U. S. *Macromolecules* **2010**, *43*, 2759. (b) Maier, A.; Rabindranath, A. R.; Tieke, B. *Chem. Mater*. **2009**, *21*, 3668. Hong, Y.; Chen, S.; Leung, C. W. T.; Lam, J. W. Y.; Liu, J.; Tseng, N. W.; Kwok, R. T. K.; Yu, Y.; Wang, Z.; Tang, B. Z. *ACS Appl. Mater. Interfaces* **2011**, *3*, 3411.

10. (a) Fox, J. D.; Rowan, S. J. *Macromolecules* **2009**, *42*, 6823. (b) Kumpfer, J. R.; Wie, J. J.; Swanson, J. P.; Beyer, F. L.; Mackay, M. E.; Rowan, S. J. *Macromolecules* **2012**, *45*, 473. (c) Kumpfer, J. R.; Jina, J.; Rowan, S. J. *J. Mater. Chem.* **2010**, *20*, 145. (d) Burnworth, M.; Tang, L.; Kumpfer, J. R.; Duncan, A. J.; Beyer, F. L.; Fiore, G. L.; Rowan, S. J.; Weder, C. *Nature* **2011**, *472*, 334.

11. (a) Pal, R. R.; Higuchi, M.; Kurth, D. G. *Org. Lett*. **2009**, *11,* 3562. (b) Dobrawa, R.; Würthner, F. *Chem. Commun*. **2002**, 1878. (c) Dobrawa, R.; Lysetska, M.; Ballester, P.; Grune, M.; Würthner, F. *Macromolecules* **2005**, *38*, 1315. (d) Basak, S.; Hui, P.; Boodida, S.; Chandrasekar, R. *J. Org. Chem*. **2012**, *77*, 3620. (e) Chandrasekhar, N.; Chandrasekar, R. *J. Org. Chem.* **2010***, 75,* 4852. (f) Benniston, A. C.; Harriman, A.; Li, P.; Sams, C. A. *J. Am. Chem. Soc.* **2005**, *127*, 2553.

12. (a) Zhu, X. J.; Holliday, B. J. *Macromol. Rapid Commun.* **2010***, 31,* 904. (b) Xu, H.; Zhu, R.; Zhao, P.; Huang, W. *J. Phys. Chem. C.* **2011**, *115*, 15627.

13. (a) Kim,Y.; Bouffard, J.; Kooi, S. E.; Swager, T. M. *J. Am. Chem. Soc.* **2005**, *127*, 13726. (b) Satrijo, A.; Kooi, S. E.; Swager, T. M. *Macromolecules* **2007**, *40*, 8833. (c) Gaal, M.; List, E. J. W.; Scherf, U. *Macromolecules* **2003**, *36*, 4236. (d) Scherf, U.; List, E. J. W. *Adv. Mater.* **2002**, *14*, 477.

14. (a) Stanley, J. M.; Zhu, X.; Yang, X.; Holliday, B. J. *Inorg. Chem*. **2010**, *49*, 2035. (b) Stanley, J. M.; Holliday, B. J. *Coord. Chem. Rev.* **2012**, *256*, 1520.

15. (a) Liu, L.; Wong, W. Y.; Lam, Y. W.; Tam, W. Y. *Inorg. Chim. Acta* **2007**, *360*, 109. (b) Zoppellaro, G.; Baumgarten, M. *Eur. J. Org. Chem*. **2005**, 2888. (c) Rajadurai, C.; Schramm, F.; Brink, S.; Fuhr, O.; Ghafari, M.; Kruk, R.; Ruben, M. *Inorg. Chem*, **2006**, *45*, 10019. (d) Tang, S.; Liu, M. R.; Lu, P.; Xia, H.; Li, M.; Xie, Z. Q.; Shen, F. Z.; Gu, C.; Wang, H. P.; Yang, B.; Ma, Y. G. *Adv. Funct. Mater*. **2007**, *17*, 2869.

16. Sanechika, K.; Yamamoto, T.; Yamamoto, A. *Bull. Chem. Soc. Jpn*. **1984**, *57*, 752.

17. Schlüter, A. D. *J. Polym. Sci., Part A: Polym. Chem*. **2001**, *39*, 1533.

18. (a) Halkyard, C. E.; Rampey, M. E.; Kloppenburg, L.; Studer-Martinez, S. L.; Bunz, U. H. F. *Macromolecules* **1998**, *31*, 8655. (b) Levitus, M.; Schmieder, K.; Ricks, H.; Shimizu, K. D.; Bunz, U. H. F.; Garcia-Garibay, M. A. *J. Am. Chem. Soc.* **2001**, *123*, 4259. (c) Beck, B. J.; Kokil, A.; Ray, D.; Rowan, S. J.; Weder, C. *Macromolecules* **2002**, *35*, 590.

19. Tekin, E.; Wijlaars, H.; Holder, E.; Egbe, D. A. M.; Schubert, U. S. *J. Mater. Chem*. **2006**, *16*, 4294.

20. King, S. M.; Perepichka, I. I.; Perepichka, I. F.; Dias, F. B.; Bryce, M. R.; Monkman, A. P. *Adv. Funct.*

Mater. **2009**, *19*, 586.

21. Basak, S.; Chandrasekar, R. *Adv. Funct. Mater.,* **2011**, *21*, 667.

22. (a) Binnemans, K.; Lenaerts, P.; Driesen, K.; Görller-Walrand, C. *J. Mater. Chem.* **2004**, *14* , 191. (b) Li, J.; Song, F.; Wang, L.; Jiao, J.; Cheng, Y.; Zhu, C. *Macromol. Rapid Commun*. **2012**, *33*, 1268. (c) McGehee, M. D.; Bergstedt, T.; Zhang, C.; Saab, A. P.; O'Regan, M. B.; Bazan, G. C.; Srdanov, V. I.; Heeger, A. J. *Adv. Mater.* **1999**, *11*, 1349.

Appendix

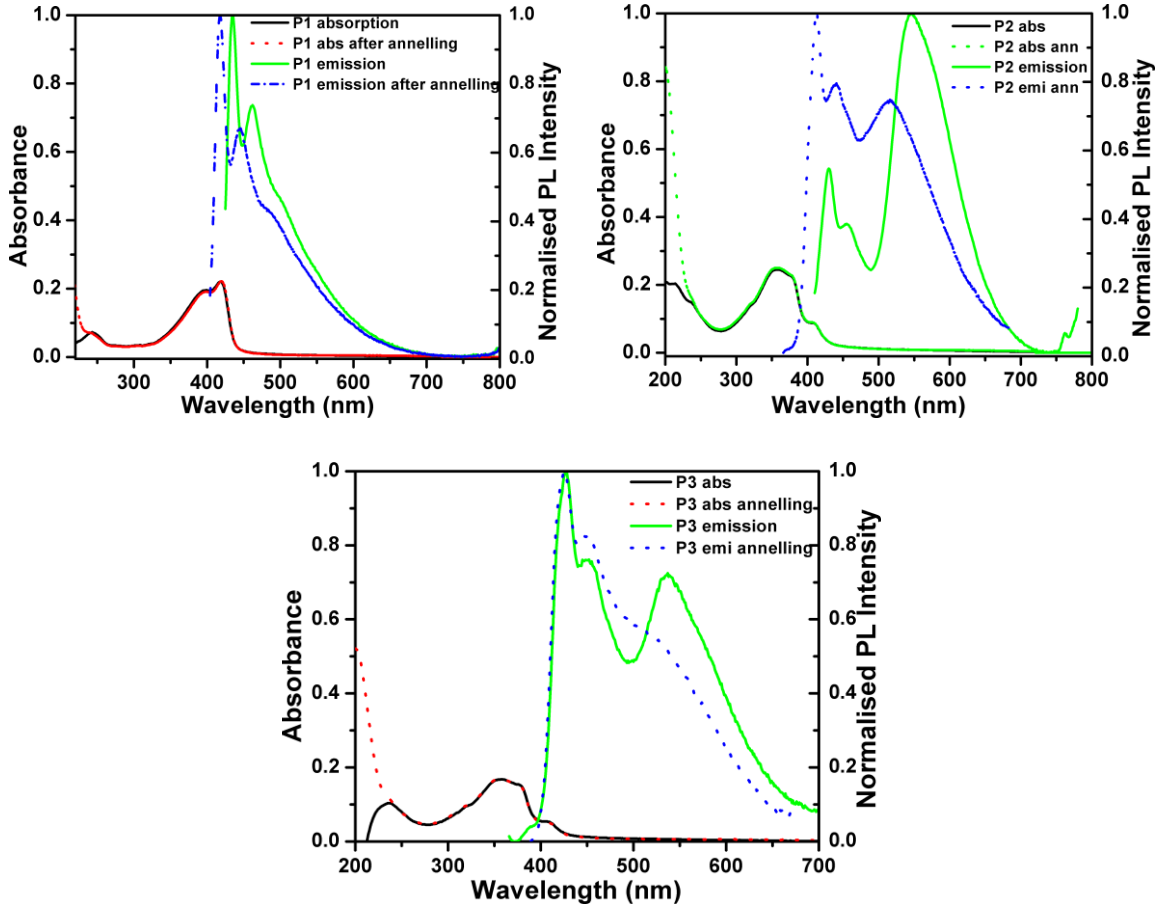

Figure A1. Annealing experiment of polymers **P1, P2** and **P3.**

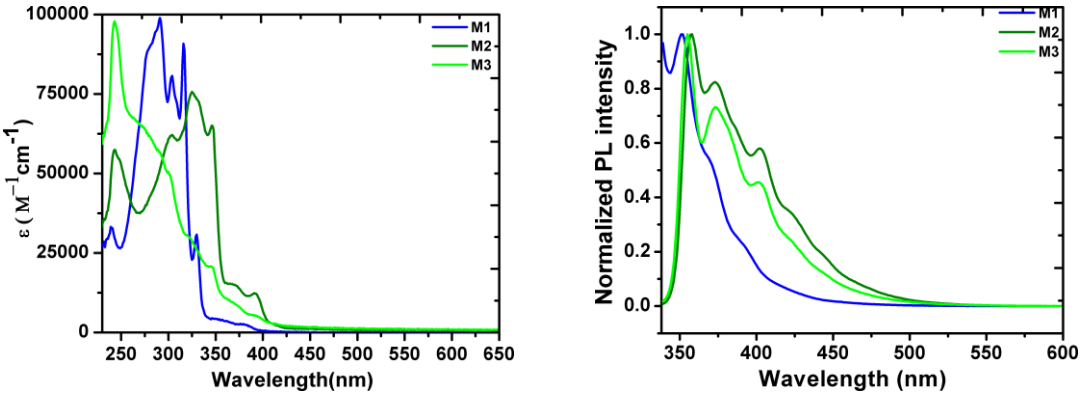

Figure A2. Absorption and emission spectra of **M1, M2,** and **M3** in $CHCl_3$ (C =1.0 × 10^{-6} M)

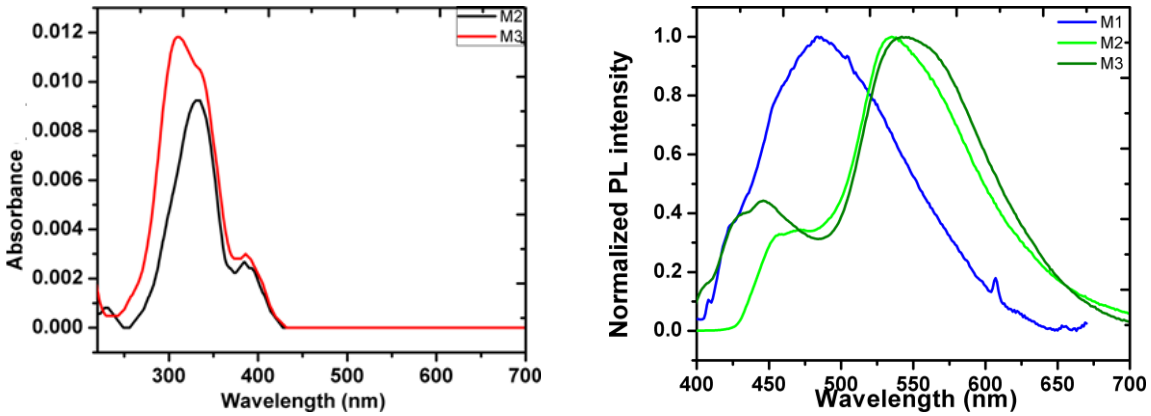

Figure A3. Solid state emission spectra of **M1, M2,** and **M3**.

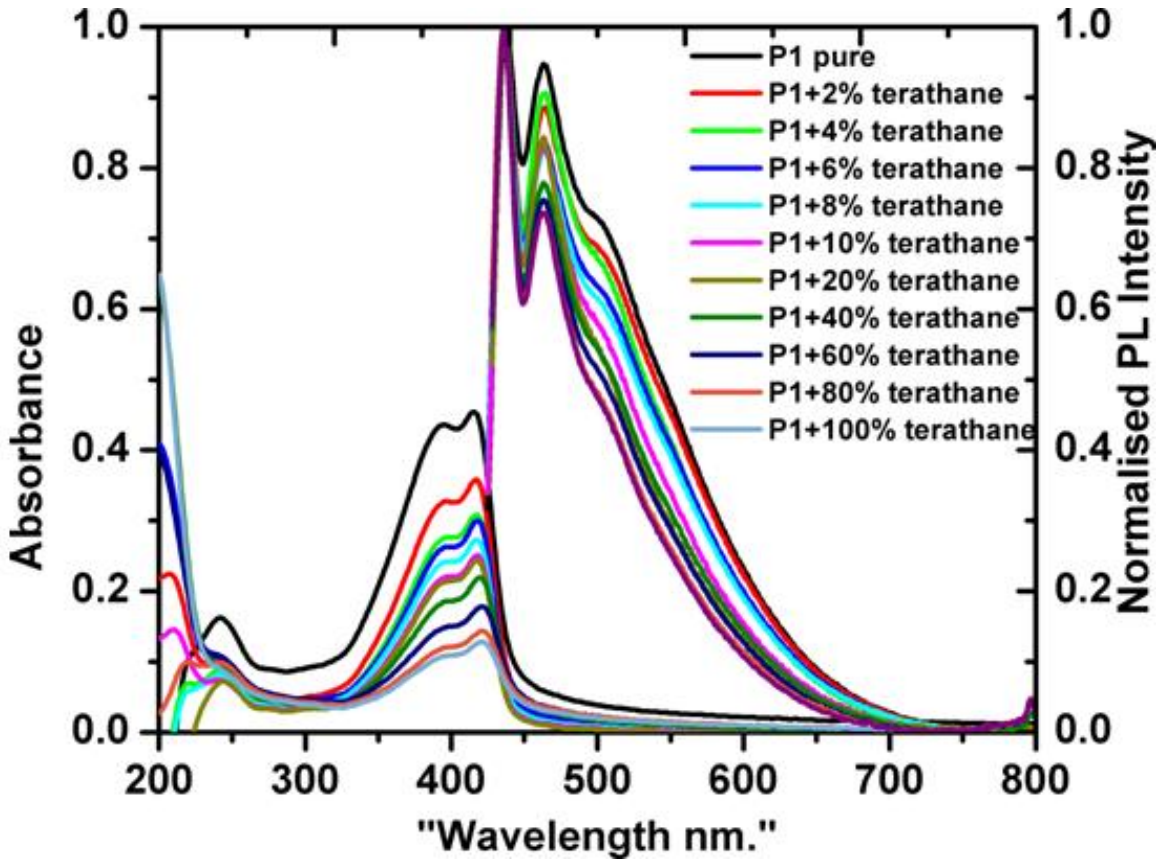

Figure A4. Excimer like behavior from a spin coated film of **M2.** The thickness of the film was monitored as mentioned before. The emission spectrum was normalized at 423 nm. With the decreasing thickness of the film the intensity of 522 nm band decreases, this can be attributed due to the excimer like nature. The corresponding absorbance of the film decreases as usual due to Lambert- Beer's law.

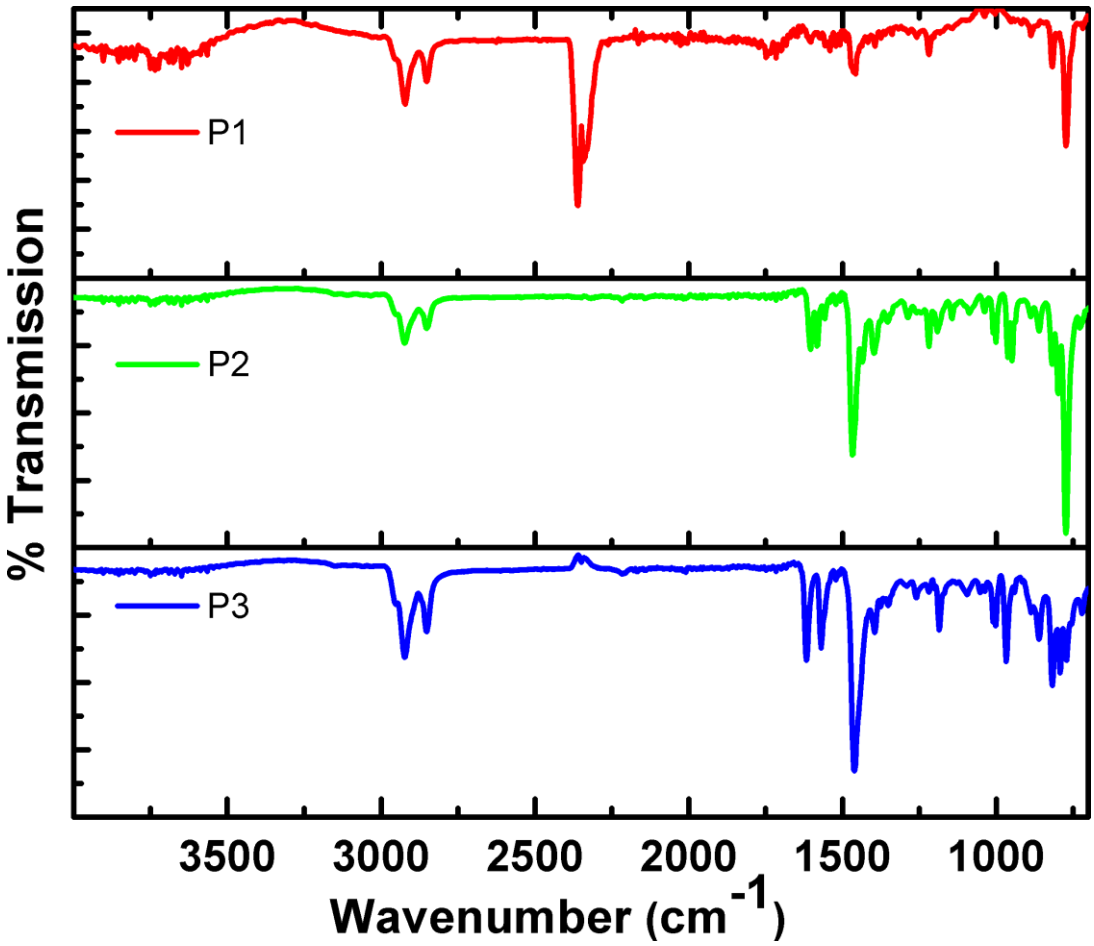

Figure A5. Comparative FTIR spectra for **P1**, **P2** and **P3.**

6

Parallelepipedic Passive Organic Optical Wave Guides: Laser Cutting, Controlling Guided Light Propagation Lengths and Out-Put Efficiency

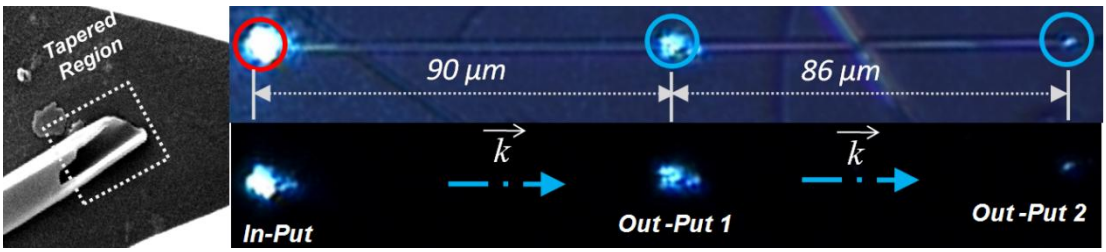

*This chapter is adapted from:

S. Basak, R. Chandrasekar*
J. Mater. Chem. C. **2013**, Revised.

6.1 Abstract

In this chapter we have exploited laser ablation/cutting technique to precisely control the longitudinal dimension of self-assembled organic nanotubes to create tailor-made lengths. Since these organic nanotubes show passive optical wave guiding tendency, the presented cutting technique is quite useful to exactly control the light propagation distance and to create multiple optical outputs. The estimated wave guiding efficiency (WGE) of a randomly selected tube with appropriate laser coupling is >47%. The efficiency of a tube is also dependent on its wall thickness, lengths and defect density. A tube not in contact with the substrate also guides the optical wave indicating its true wave guiding nature.

6.2 Introduction

Nanoscale optical wave guides are one of the important components of miniaturized nano-photonics devices.[1-7] In particular, one dimensional (1D) organic solids are useful to manipulate and guide optical waves within the nano/submicro/micro domains, because the refractive index (n) of the organic solid (n~1.6) is usually higher than the surrounding air medium (n=1).[8-13] Based on the type of light an 1D solid propagates, organic optical wave guides are classified into *active*- and *passive-waveguides*. In active wave guides,[10-25] the molecular building block of the organic solid is electronically excited and the coupled exciton-polariton propagates to the output end as luminescence. Although this area is relatively young, a few excellent examples reported for

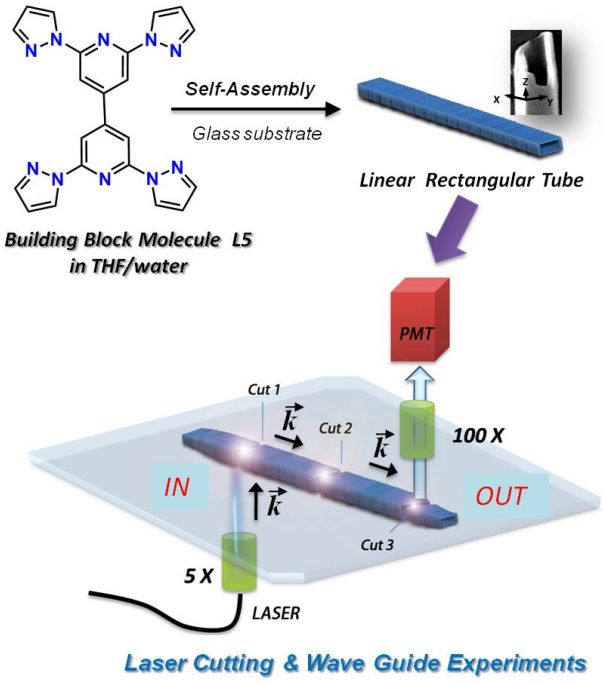

Scheme 6.1 Top figure: Formation of parallelepipedic organic nanotubes from ***L5*** via self-assembly. Bottom figure: Experimental set-up used for the tube cutting and wave guiding studies. PMT stands for photo multiplier tube.

this type of exciton-polariton based active wave guides.[10-23] On the other hand, passive organic wave guides function almost similar to commercial optical fibers and other dielectric-based guided wave structures, i.e., here the input light directly propagates along the organic medium to the output end. Chandrasekar and co-workers have recently reported for the first time on the passive wave guiding tendency of self-assembled organic submicrotubes and rods.[26-30] The potential utility of the guided laser light along the submicrotubes to remotely excite a porphyrine nano-sheet positioned 20 microns away from the source laser was also demonstrated.[28] Additonally, Raman scattering interaction of the propagating passive light with the molecular building blocks of the tube was used to pin-point nano/micro scale defect sites inherited during the self assembly process.[28,29]

6.3 Results and Discussion

Importantly, to exploit organic optical waveguides as components for future nano-photonic device applications,[1,2] it is imperative to precisely control the optical signal propagation distance from the input point to out point(s) of our choice. Additionally, it is essential to comprehend the correlation between transverse dimensionality of 1D organic nanostructures and the wave guiding propensity. Regrettably, though the science of self-assembled 1D organic nanostructures are known for a long time, still it is impossible to exactly control their growth length during self-assembly. To date, no experimental methods reported in the literatures on externally controlling the longitudinal dimensions of organic wave guiding solids (tube, rod and fiber), thereby precisely controlling optical wave propagation distance. Hence, performing length "*cutting*" operation on extended nano/micro scale organic solids is crucial step to assemble them as components in miniaturized organic nano-photonic devices.

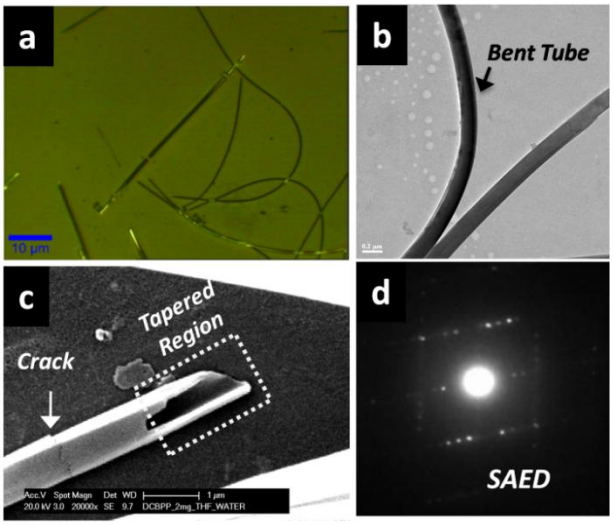

Figure 6.1 a) Confocal microscopy image of linear and curved parallelepipedic organic nanotubes. b) TEM image of tubes. c) SEM image displaying tapered open end of a tube (see dotted rectangle). d) Selected area electron microscopy image of a crystalline tube.

6.3.1 Optical Wave Guiding Studies:

In Chapter 4, fabrication and thorough characterization of self-assembled crystalline organic parallelepipedic nanotubes obtained from heterocyclic molecule ***L5*** is presented (Scheme 6.1).[31] We have found that the optical wave guiding tendency of these organic nanotubes is dependent on the tube transverse dimension i.e. height and width. In this chapter we would like to present three original general methodology on tuning organic waveguides towards photonic device applications: (i) submicro scale resolution laser cutting of organic parallelepipedic nanotubes at defined positions, ii) precise control of optical wave propagation distance along the nanotubes and generation of multiple optical outputs, and iii) estimation/control of the optical wave transmission efficiency. In this experiment, a combined laser confocal Raman/atomic force microscopy set-up was employed, the former to perform laser ablation/cutting operation and to do wave guiding experiments and the latter to investigate dimension of the ablated tube.

Building block molecule ***L5*** forms parallelepipedic nanotubes upon slow evaporation conditions from THF/water on glass substrate.[31] On the substrate some of the longer tubes bent and produced curved structures indicating their flexible nature[28] (Fig. 6.1 a,b). A closer look at the tube ends revealed *tapered* regions (Fig. 1c). The selected area electron diffraction (SAED) pointed out the crystalline nature of the tubes (Fig. 6.1 d). The solid state absorbance band of ***L5*** showed that there is no possible molecular absorbance above $\lambda \sim 420$ nm. Initially, to study the passive wave guiding behavior of these organic nanotubes, a confocal Raman/AFM microscope (*back scattering mode*) was employed. A longer wavelength (λ) visible light (Ar^+ 488 nm) was used for the optical waveguide experiments to circumvent any molecular electronic absorption and resultant fluorescence. Orthogonal direct laser illumination (Ar^+ 488 nm; 100× objective; N.A. 0.95) at one of the open ends of a tube (tapered region) showed *no* output light at the opposite open end in the bright field image. Similar behavior was observed for irradiation performed at the other end and middle of the tube (Fig 6.2 a). The corresponding dark field images without and with 488 long pass edge filter (LPEF) presented in Fig 6.2 b and Fig 6.2 c, respectively also show similar trend. One can interpret this results in two ways: (i) the light is not coupled to the tube at the tapered ends possibly due to their much smaller transverse dimension (less than $\lambda/2$) in comparison to λ of the input light. (ii) the light can be

coupled in the middle of the tube and possibly confined within the tube with out outcoupling due to tapered ends.

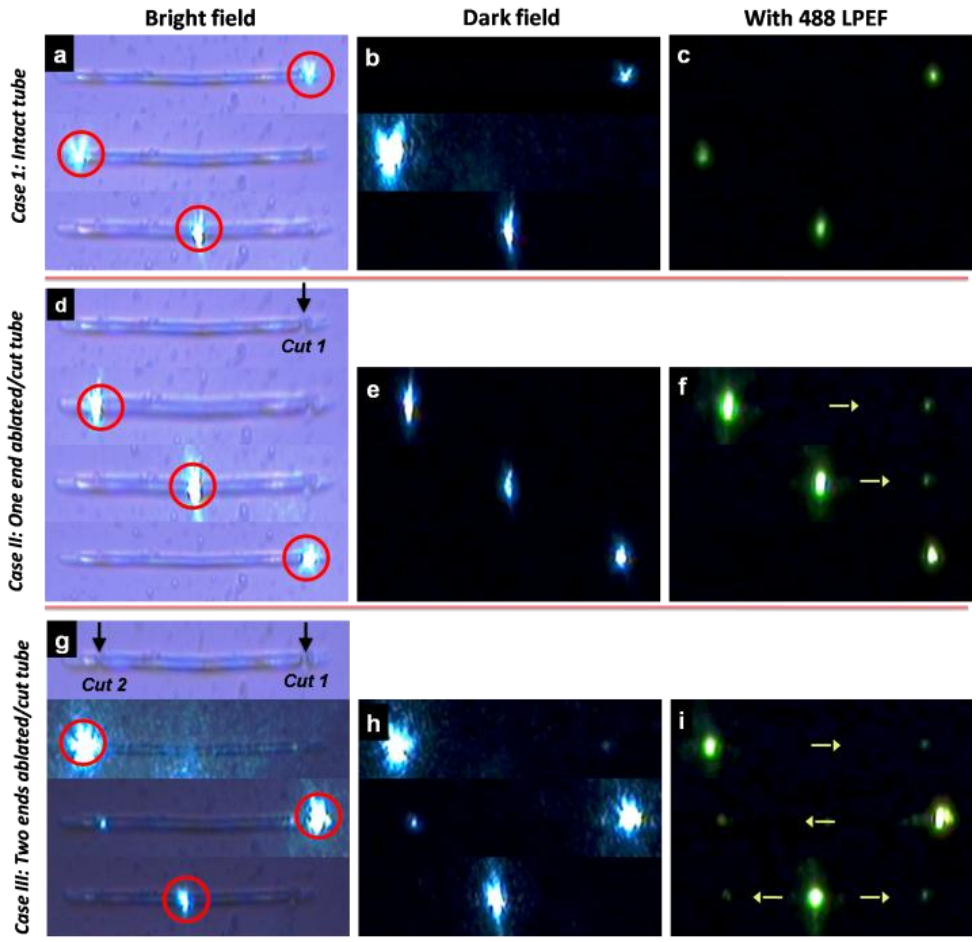

Figure 6.2 a) Bright field image of a tube illuminated with 488 Ar^+ laser. b and c) the corresponding a dark field images without and with LPEF, respectively. d) The same tube ablated/cut with 488 Ar^+ laser (see *Cut 1*); e and f) the corresponding dark field images without and with LPEF, respectively. g) The same tube ablated/cut with 488 Ar^+ laser at the left side (see *Cut 2*); h and i) the corresponding dark field images without and with LPEF, respectively.

6.3.2 Laser Ablation/Cutting of Photonic Tubes:

To clearly understand the coupling of light with the tube and to observe any possible out coupled light in the bright and dark field images, a confocal Raman/AFM microscope (*back scattering mode*) set-up was employed to perform laser ablation or cutting on the tube at selected positions and AFM analysis of the ablated area as well. For tube cutting, a CW 488 nm Ar^+ ion laser (40 mW) was point focused through 100× objective on the right side of the tube slightly away from the tapered area to burn the molecules using source laser heat (see *cut 1*; Fig. 6.2 d). Here the CW laser power is kept constant; hence the depth of cutting is dependent upon the laser ablation

time. Afterwards, coupling of laser light to the left side (slightly away from the tapered area) or middle of the tube showed *no perceptible* out coupled light at the opposite end(s) in the bright and dark field images. Whereas the same dark field images with 488 LPEF showed weak and clear out put signals at the ablated area (see arrow marks toward *cut 1*; Fig. 6.2 f). As expected coupling of laser light at *cut 1* showed no out coupled light at the opposite end, indicating complete confinement of light within the tube due to tapered output ends. To verify further, the tube was again ablated at the opposite side (*cut 2*) slightly away from the tapered area (Fig. 6.2 g). Now coupling of laser light at *cut 1*, *cut 2* and middle of the tube display out coupled light at the opposite laser ablated areas. But still the laser-tube coupling efficiency in the middle part of the tube was rather weak, which was apparent from the bright and dark field images (Fig. 6.2 g,h). These experiments demonstrate that the laser is not coupled to the tapered region and hence the tube was not able to act as a wave guide. When the laser was coupled *away* from the tapered end the tube shows wave guiding behaviour. To find a correlation between the tube transverse dimensions and laser-tube coupling tendency/propagation efficiency a selected tube was scrutinized by AFM technique.

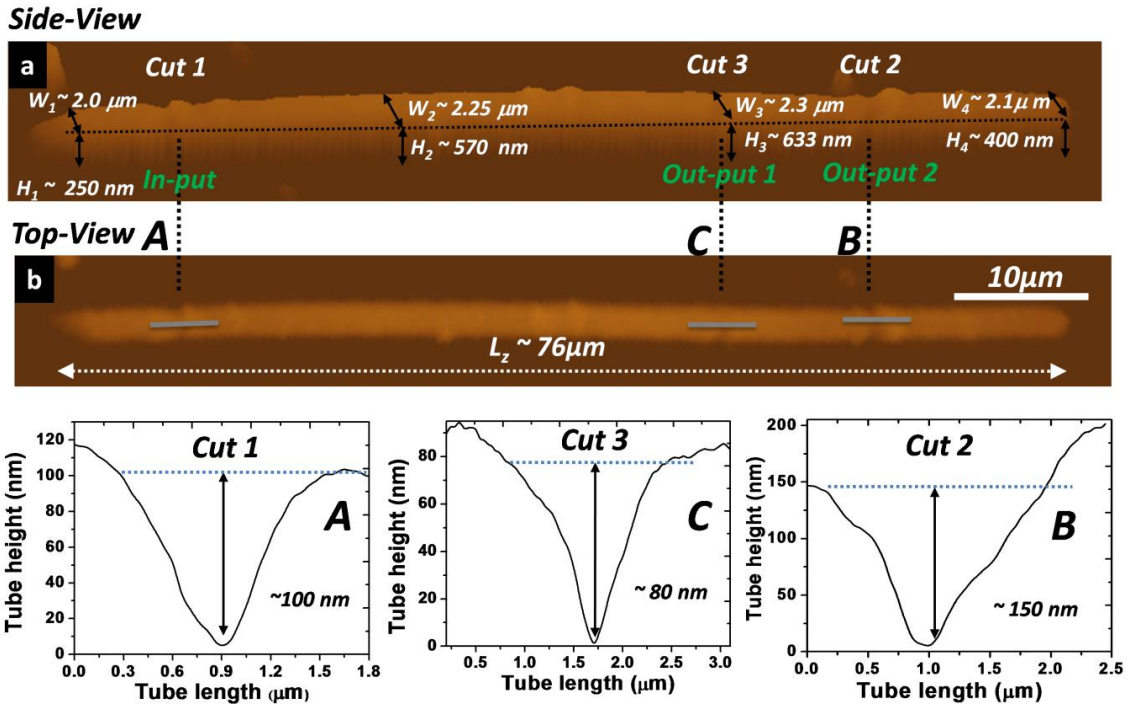

Figure 6.3 AFM images of (a) side and (b) top view of a laser ablated/cut tube at positions *A* (*Cut 1*), *B* (*Cut 2*) and *C* (*Cut 3*). H and W stand for height and width profiles, respectively. The corresponding depth profile of the cut regions are shown in the bottom figures.

As expected the height (H) and width (W) profiles were not same all over the tube, particularly at the tube ends. For example, the $H_x \times W_x$ (x = 1- 4) profiles at four different regions (x = 1- 4) varied in the range of ~250 nm × ~2 μm, <570 nm × ~2.25 μm, ~633 nm × ~2.3 μm, and 400 nm × ~2.1 μm, respectively (see Fig. 6.3). The length of the tube was ca. 76 μm. Here, the variation of H × W transverse profile at the tapered tube ends arises during the growth process, for example Fig 6.1 c clearly shows that the top (W) and side walls (H) of the *tapered* region is not grown as much as the bottom wall (W), leading to a decrease of the tube height. To study transverse dimension (H and W) dependent wave guiding tendency of a tube, the same tapered tube was used. Here, the λ of the laser line (488 or 532) is almost close to one of the transverse dimensions (λ ≤ H) of the tube from *A* to *B* and it is around λ/2 ≥ H in the tapered regions 1 and λ < H in region 4 (see Fig. 6.3 labels).

Initially two laser cuts (*Cut-1* and *Cut-2*) were made by point illumination of

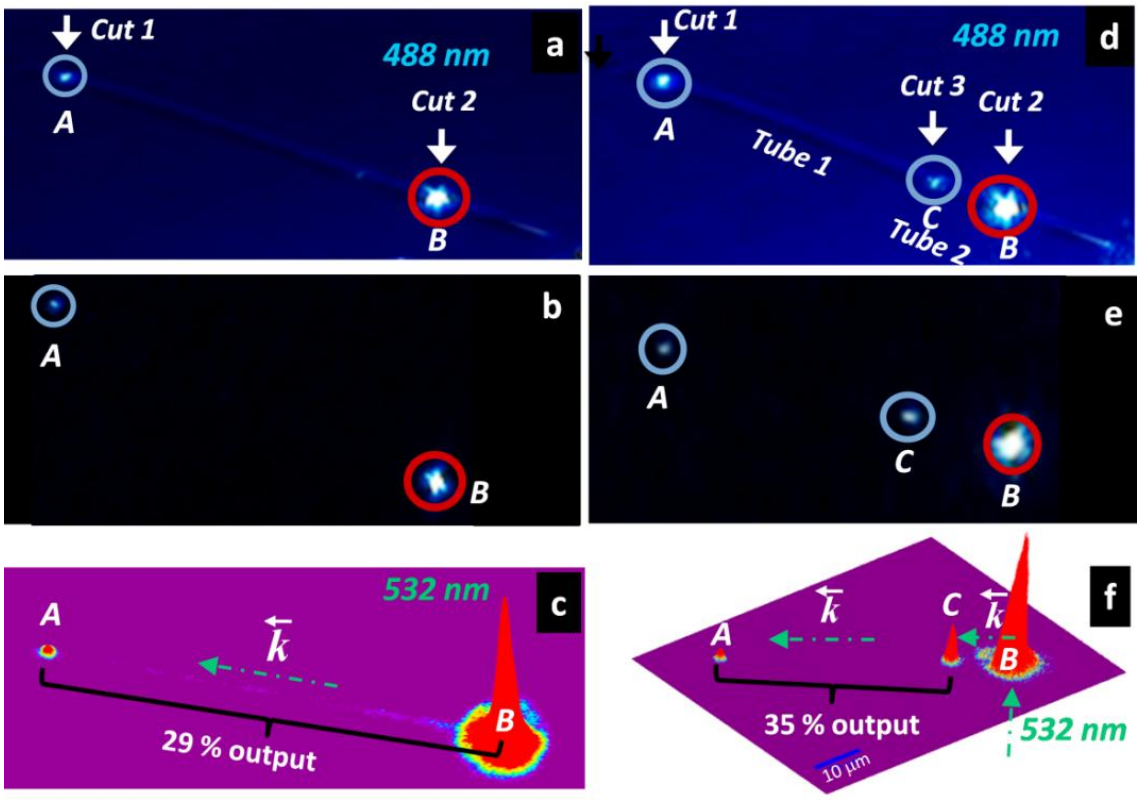

Figure 6.4 a) A laser ablated tube [*A* (*Cut 1*) and *B* (*Cut 2*)] shown in Fig. 6.3 irradiated with 488 nm laser at *B*; (b) the corresponding dark field image; (c) PMT image of 532 nm wave guiding tubes displaying 29% output; d) Ablation of tube shown in Fig. 6.4a at position *C* (*Cut 3*), followed by irradiated with 488 nm laser at *B*; e) The corresponding dark field image; f) PMT image of a wave guiding tube with two out puts. The calculated optical transmission efficiency of tube 1 (from *C* to *A*) is ca. 35%. The red and blue circles stand for laser irradiation and output points, respectively.

488 light at positions *A* (H: 530 nm; W: 2.12 μm) and *B* (H: 540 nm; W: 2.35 μm) (see Fig. 6.3 and Fig. 6.4 a). AFM examination of a cut tube showed that the ablation was about 100 nm deep with the separation ca. 1 μm between the two pieces of a tube (Fig. 6.1). The optical wave guiding experiments on the tube was performed on laser confocal Raman/AFM microscope set-up (*transmission mode*) connected to a photo multiplier tube (PMT) (Scheme 6.1). Here a Nd:YAG 532 nm laser was bottom fix illuminated through a 5× objective at point *A* and the output light position of the output light signal was detected by scanning the entire area of the tube using a top 100× objective and sent to a photomultiplier (PMT) detector. Illumination of laser at point *B* (*Cut-2*) exhibited a clear out put light at point *A* (*Cut-1*) (Fig. 6.4 a, b). The 3D mapping of the PMT counts clearly showed the output signal transmission efficiency at point *B* is *ca.* 29% (*B*/*A*). One should remember the fact that for calculating optical transmission efficiency the present light–tube coupling geometry is not appropriate since the source laser light couple to the tube in an orthogonal manner, which leads to unwanted scattering at the input point thus increasing optical loss. Hence to couple the light directly (*longitudinal*) to the tube (within the acceptance angle), another laser cut (*Cut-3*) was made at point *C* (H: 597 nm; W: 2.52 μm) there by producing two wave guiding tubes, *1* and *2* (see Figures 6.3 and 6.4 e). AFM profile analysis showed that the depth of cutting was ca. 75 nm.

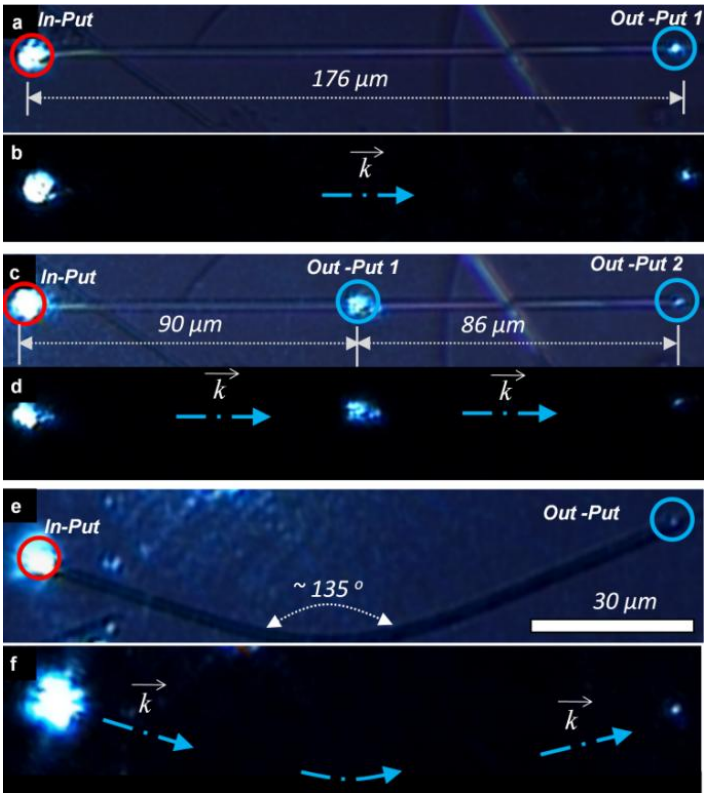

Figure 6.5 a and b) Bright and dark field images of a passive wave guiding tube ablated/cut with laser at tapered open ends, respectively. c and d) Bright and dark field images of the tube cut by laser into two sections to control the light propagation lengths and efficiency, respectively. The red and blue circles stand for laser irradiation and output points, respectively. e and f) Bright and dark field images of a bent tube displaying wave guiding tendency.

The separation between Tube *1* and *2* was ca. 1 μm (Fig. 6.3). Orthogonal illumination of 532 nm laser at point *B* showed remarkable propagation of light from point *B* to *C* and then to *A*. As expected the out coupled light intensity at point *A* was lower than the output at point *C* due to leakage at *Cut-3*. Nevertheless, the direct orientation of tubes *1* and *2* is an ideal geometry for improved estimation of optical transmission efficiency from tube *2*. By ignoring the minor scattering losses at the coupling point *C* the estimated optical guiding effectiveness was >35% (*A*/*C*). Further to demonstrate the use of this technology to precisely control the light propagation length scale and to create multiple outputs along the wave guide, a 176 μm long was identified. At first, the tapered tip ends of the tube were removed by laser ablation. Subsequently, the tip polished tubular wave guide (Fig. 6.5 a,b) was exactly laser cut to create two wave guiding tubes of lengths 90 μm and 86 μm. Launching of laser light at the input clearly showed two output signals at a distance of 90 μm and 86 μm (Fig. 6.5 c,d). Similarly, a tips polished bent tube (bent angle of ~ 135^{o}) also guide the input light to the output end confirming the true optical wave guiding tendency of the tubes (Fig. 6.5 e,f).

To prove light guiding tendency in a bent tube having acute turn, a tube forming a loop was laser polished to produce a U-shaped tube (Fig. 6.6 a). Laser

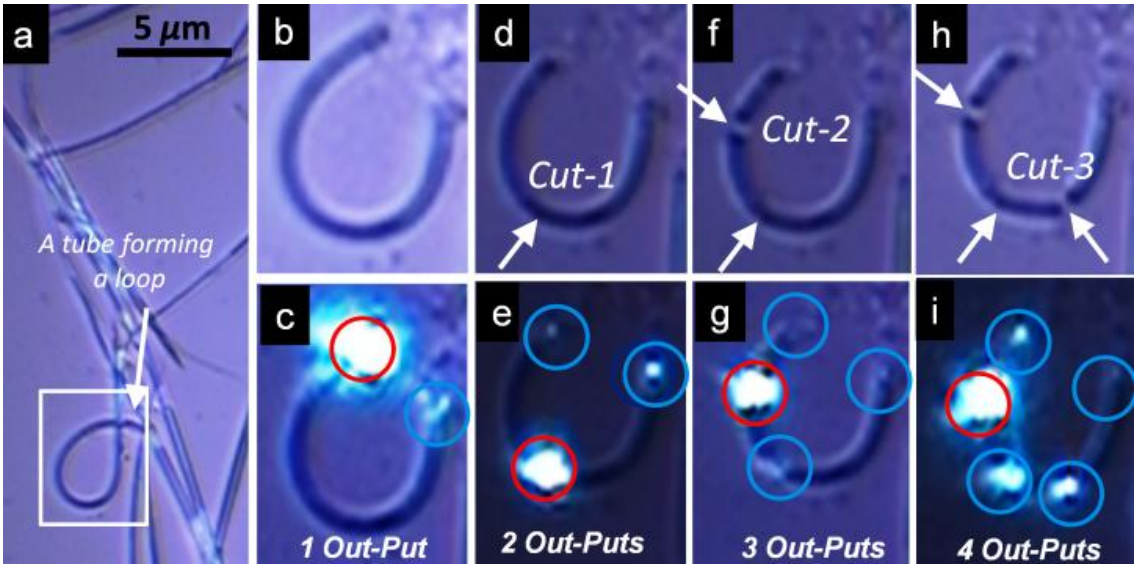

Figure 6.6 a) A tube forming a loop. b and c) U-shaped tube produced from the loop via laser ablation displaying passive wave guiding tendency even at acute turns. d and e) U-shaped tube laser ablated in the middle (cut 1) shows 2 out puts. f and g) U-shaped tube laser ablated at cut 2 shows 3 out puts. h and i) U-shaped tube laser ablated in the middle (cut 3) shows 4 out puts. The red and blue circles denote laser input and output points, respectively. An Ar+ 488 laser was used for laser ablation and wave guiding studies.

coupling at one of the ends of a tube showed clear out put at the opposite end indicating an efficient propagation of guided laser light even at sharp turns (Fig. 6.6 b, c). Further to produce multiple optical out puts, the U shaped tube was laser ablated successively to create *Cut-1*, *Cut-2* and *Cut-3* (Fig. 6.6 d,f,h) and to emanate 2, 3 and 4 optical outputs, respectively (Fig. 6.6 e,g,i).

To rule out any substrate influence on the wave guiding tendency of tubes, it is important to demonstrate the wave guiding nature of an organic tube surrounded only by air medium (no substrate contact). For this experiment an AFM tip was used to lift a tube from the substrate and the cantilever carrying the tube was inverted and used for the optical wave guiding studies (Fig. 6.7). Note that during lifting, the tube surrounded by the air medium was broken and bent slightly. Orthogonal laser

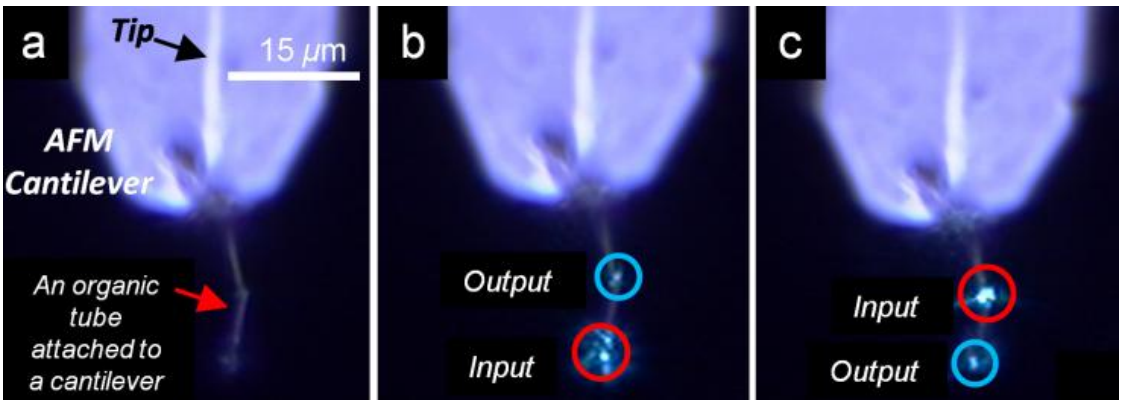

Figure 6.7 a) A broken tube attached to an inverted AFM cantilever. b) and c) Optical wave guiding property of a bent tube surrounded by air. An Ar+ 488 laser was used for wave guiding studies. The red and blue circles denote laser input and output points, respectively.

coupling one of the ends of the tube evidently showed guided light propagation to the respective opposite end (Fig. 6.7 b,c). This experiment clearly supported the true wave guiding character of the organic tube.

6.4 Conclusions

We have presented an innovative method to fabricate extended 1D organic solids with tailor made lengths using simple laser ablation/cutting technique. Additionally, we have also demonstrated the transverse dimension dependent optical wave guiding behaviour of parallelepipedic organic nanotubes. We have also established a better method to estimate optical transmission efficiency of wave guiding organic tubes using appropriate optical coupling geometry. It is also important to note that the optical

transmission efficiency of the tubes is dependent upon the tube lengths, wall thickness and defects. The true wave guiding behaviour of a tube surrounded only by the air medium has also been demonstrated as well. This laser ablation methodology can be used to make tailor made nanophotonic organic wave guides with multiple outputs and to precisely control the guided optical wave propagation length scales.

References

1. Hunsperger, R. G. *Integrated Optics: Theory and Technology*, 5th ed.; Springer: Berlin, **2002**.
2. Ohtsu, M. *Nanophotonics and Nanofabrciation*, Wiley-VCH: Weinheim, **2009**.
3. Maier, S. A.; Kik, P. G.; Atwater, H. A.; Harel, E.; Koel, B. E.; Requicha, A. A. G. *Nat. Mater.* **2003**, *2*, 229.
4. Bozhevolnyi, S. I.; Volkov, V. S.; Devaux, E.; Laluet, J. Y.; Ebbesen, T. W. *Nature* **2006**, *440*, 508.
5. Lipson, M. J. *Lightwave Technol.* **2005**, *23*, 4222.
6. Jalali, B.; Fathpour, S. J. *Lightwave Technol*. **2006**, *24*, 4600.
7. Barrelet, C. J.; Greytak, A. B.; Lieber, C. M. *Nano Lett*. **2004**, *4*, 1981.
8. Zhang, C.; Zhao, Y. S.; Yao, Y. *Phys. Chem. Chem. Phys*., **2011**, *13*, 9060.
9. Zhao, Y. S.; Fu, H.; Peng, A.; Ma, Y.; Liao, Q.; Yao, J. *Acc. Chem. Res.* **2010**, *43*, 409.
10. Yan, Y.; Zhang, C.; Yao, J.; Zhao, Y. S. *Adv. Mater*. **2013**, *225*, 3627.
11. Yanagi, H.; Morikawa, T. *Appl. Phys. Lett.* **1999**, *75*, 187.
12. Takazawa, K.; Kitahama, Y.; Kimura, Y.; Kido, G. *Nano Lett*. **2005**, *5*, 1293.
13. Balzer, F.; Bordo, V. G.; Simonsen, A. C.; Rubahn, H. –G. *Appl. Phys. Lett.* **2003**, *82*, 10.
14. Balzer, F.; Bordo, V. G.; Simonsen, A. C.; Rubahn, H.-G. *Phys. Rev. B*, **2003**, *67*, 115408.
15. Zhao, Y. S.; Xu, J. J.; Peng, A. D.; Fu, H. B.; Ma, Y.; Jiang, L.; Yao, J. N. *Angew. Chem. Int. Ed.* **2008**, *47*, 7301.
16. Schiek, M.; Balzer, F.; Al-Shamer, K.; Brewer, J. R.; Lutzen, A.; Rubahn, H.-G. *Small* **2008**, *4*, 176.
17. Zhao, Y. S.; Xu, J. J.; Peng, A. D.; Fu, H. B.; Ma, Y.; Jiang, L.; Yao, J. N. *Angew. Chem. Int. Ed.* **2008**, *47*, 7301.
18. Zhao, Y. S.; Fu, H. B.; Peng, A. D.; Ma, Y.; Xiao, D. B.; Yao, J. N. *Adv. Mater.* **2008**, *20*, 2859.
19. Zhang, C.; Zou, C. L.; Yan, Y. L.; Hao, R.; Sun, F. W.; Han, Z. F.; Zhao, Y. S.; Yao, Y. N. *J. Am. Chem. Soc.* **2011**, *133*, 7276.
20. Kim, F. S.; Ren, G. Q.; Jenekhe, S. A. *Chem. Mater*. **2011**, *23*, 682.
21. Takazawa, K.; Inoue, J.; Mitsuishi, K.; Takamasu, T. *Phys. Rev. Lett.* **2010**, *105*, 067401.
22. Bao, Q. L.; Goh, B. M.; Yan, B.; Yu, T.; Shen, Z. A.; Loh, K. P. *Adv. Mater.* **2010**, *22*, 3661.
23. Cheng, C. W.; Luo, Y. *Micro Nano Lett*. **2012**, *7*, 397.
24. O'carroll, D.; Lieberwirth, I.; Redmond, G. *Nat. Nanotech,* **2007**, *2*, 180.
25. Tessler, N.; Denton, G. J.; Friend, R. H.; *Nature*, **1996**, *382*, 695.

26. Chandrasekhar, N.; Chandrasekar, R. *Chem. Commun.* **2010**, *46*, 2915.

27. Chandrasekhar, N.; Chandrasekar, R. *Angew. Chem. Int. Ed.* **2012**, *51*, 3556; *Angew. Chem.* **2012**, *124*, 3616.

28. Chandrasekhar, N.; Mohiddon, Md. A.; Chandrasekar, R. *Adv. Optical Mater.* **2013**, *1*, 305.

29. Hui, P.; Chandrasekar, R. *Adv. Mater.* **2013**, *25*, 2963.

30. Basak, S.; Botacha, A. K.; Ansari, Md. T.; Chandrasekar, R. *Ind. J. Mater. Sci.* **2013**, in press.

31. Basak, S.; Chandrasekar, R. *Adv. Funct. Mater*. **2011**, *21*, 667.

7

Conclusions and Future Prospects

7.1 Conclusions

This thesis entitled "*Novel Molecular and Metallo-Supramolecular Nano-Materials: Design, Synthesis, Processing and Functional Aspects*" describes the synthesis of several monomeric and polymeric 2,6-bis(pyrazol-1-yl)pyridine (BPP) derivatives and exploitation of their self-assembling properties to create nano/micro scale molecular tubes, arrays and patterns possessing unique photonic properties and magnetically bistability. The ultimate aim of the thesis is to create molecular solids down to nano/micro domains. Hence in the beginning much attention has been paid to synthesize solution and solution processable monomeric and metallo-supramolecular polymeric BPP analogues, which are described in *chapters 2*, *3* and *5*.

Later we have adopted *top-down* and *bottom-up* nano technological approaches to achieve our goal. Initially by following *top-down* technique we have developed a methodology to fabricate fluorescent μ-patterns and magnetically bistable nano/micro patterns and arrays embedded within an optically transparent polymer film towards future flexible memory device applications, which are discussed in *chapters 2* and *3*, respectively. *Chapter 4* provides a general bottom-up approach for one-pot fabrication of organic/inorganic hybrid parallelepipedic tubes with rectangular cavities displaying dual luminescence using the *surface selective coordination chemistry* on ligand nano tubes.

Using this technique a blue emitting tube was coated with red emitting Eu(III) ions to achieve blue and red dual emissions.

Later on in *chapter 5*, to combine the metal coordinating ability of BPP Ligand with the luminescent property of conjugated polymers, for the first time BPP units incorporated within the main chain of poly-fluorene [i.e., Poly(BPP-fluorene) type copolymers] were successfully synthesized by Sonogashira cross-coupling methods. These polymers were used to achieve white light emission, by exploiting polymer dual emission (blue and green) due to excimer/aggregate formation and by coordinating red emitting Eu(III) ion with the main chain BPP units. This novel and simple technique can be used as prototype to achieve multi-colour emissions suitable for several solid state device applications.

At last in *chapter 6*, an original and innovative technique to probe the optical wave guiding tendency of the tubes described in *chapter 4*, is presented. Additionally, laser ablation was employed as a tool to precisely cut, thereby control the longitudinal dimension of self-assembled organic nanotubes. The general cutting technique of the tubes can be successfully used to control the light propagation length scales and to create multiple optical outputs in organic nanotubes. The true wave guiding nature of the tubes were demonstrated by nano manipulating a tube with an AFM tip and performing wave guiding experiments on a tube not in contact with the substrate.

7.2 Future Prospects

A series of further investigations can be envisaged based on the work presented in this thesis which is described below.

The *back-to-back* coupled ligand developed in *chapter 2* can be further modified for enhanced functional properties. Exploration of known and new molecules with active functionalities and development of fabrication procedures to assemble them into hybrid nanostructures with superior luminescent properties are interesting and challenging problems. Some of these issues are currently being actively pursued in our laboratory. The examples are shown below (Fig. 7.1). The molecule (**i**) is very useful for the interaction with carbon nanotubes, which can directly wrap the carbon nanotube through its π-π interaction to generate luminescent carbon nanotubes. Once the wrapping with the ligand molecule is complete the coordination cite can be filled with lanthanide metal ions.

This simple strategy allows us to generate multiluminescent carbon nanotubes which are highly desirable for the future application in the field of carbon nanotubes based

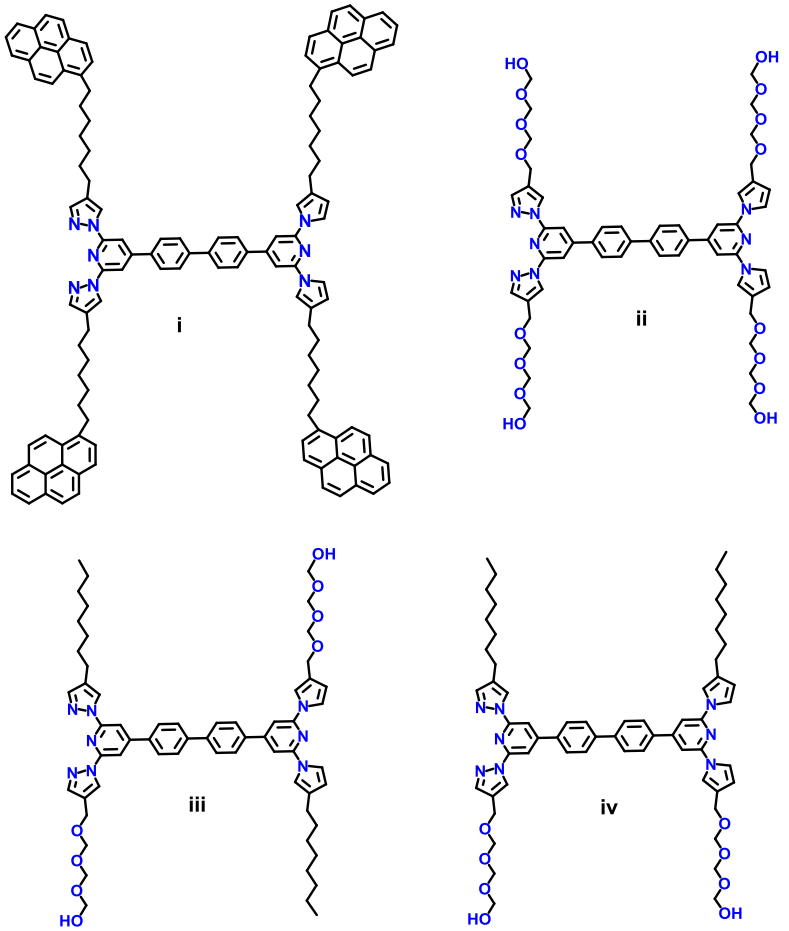

Figure 7.1 Future functional molecules based on ***L2.***

materials. Presently in our lab is investigating the effect of electrical conductivity of pristine nanotubes wrapped with porphyrin based polymers. It is also very interesting to study the self-assembly properties of the molecule (**ii**) (Fig. 7.1) which is preassembly water soluble, and the Janus type Ligand molecules e.g. (**iii**) and (**iv**) (Fig. 7.1). We have

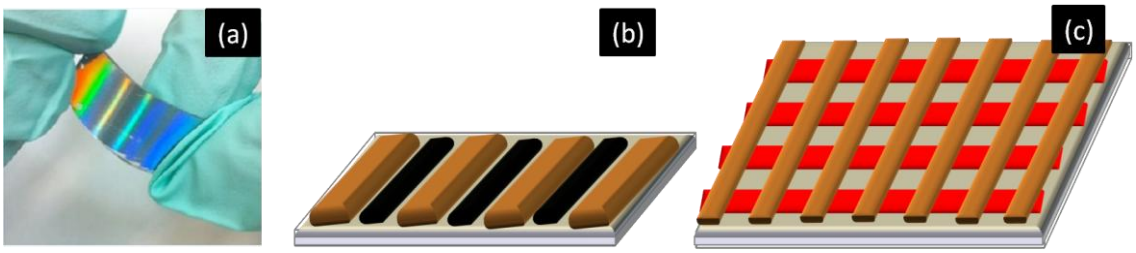

Figure 7.2 (a) A film having nano/micro patterns, (b) Proposed alternate patterning of two different spin-crossover compounds, (c) Proposed grid like structure formed from two spin-crossover compounds.

also found that the molecules ***L1-L3*** can form 1-D metallo-supramolecular spin crossover coordination polymers upon coordination with $Fe(BF_4)_2$. Interestingly one of the metallo-polymer shows formation of chain like structure, when deposited on a mica substrate. It would be a rewarding to investigate the spin state transition of the chain like structures by variable temperature Raman spectroscopy on a single chain. Structurally the molecules are very attractive for self-assembly. For a materials chemist it is very easy to predict the self assembly of molecule viz. ***L1*** will be a one dimensional structure. Depending on the solvent polarity the self-assembly can be tuned to form 1-D→0-D. 1-D and 0-D dimensional structures can also be obtained simultaneously by modification of solvent environment.

The patterning methodology to achieve flexible devices discussed in *chapter 3* can be further extended to fabricate a multi-component channel patterns (Fig. 7.2). Presently, we are trying to extend our proposed methodology to fabricate stacked 3-D multilayer memory devices. Here each layer is made of several SCO compounds having different progressive $T_{1/2}$ temperatures. Mario and coworkers developed the electric field control over the spin states of a molecule.[1] The each layer consists of the 3-D multilayer stacked device can be connected with the electric field and the spin can be manipulated to erase or create memory based on their spin states. It is further interesting to fabricate a bio compatible mold to bring the environment-friendly devices in electronic industry.

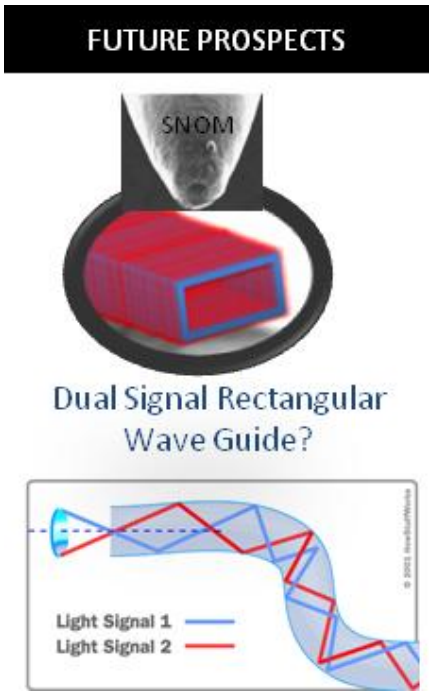

Scheme 7.1 Schematic representation of a dual optical waveguide.

We have proposed an elementary model to explain the formation of parallelepipedic nanotubes designed from a ditopic molecule ***L5***. This simple methodology to perform surface selective coordination chemistry on the ligand nano tube can be extended to fabricate various hybrid metal/organic luminescent nanostructures. One exciting design might be to fabricate Er coated nanotubes which can emit at NIR region (λ_{em} = 1.5 μm) for organic NIR fiber lasers and interferometers. Our present study shows the parallelepipedic tubes can act as a passive optical

waveguide which can launch laser light (λ = 488 nm) several tens of micron away from the laser source. This simple and innovative method enables us to separate the heat associated with the laser source, which has a great significance to study biological samples. The hybrid nanotubes used in our study have the absorption window in the UV range. In the simple sense both the ***L5*** molecule and the complex ***C4*** can absorb UV light and emits in the blue region at 420 nm for ***L5*** and at the red region at 613 nm for the complex ***C4***. This property enables the hybrid nanotube to act as a dual signal rectangular waveguide (Scheme 7.1). On a single shot of UV laser at one end can generate two optical signals (blue + red) propagate to the other opposite end. Some of the other studies like assembling the nanotubes, filling the cavity with conducting polymer to make a core shell type electrical wire are underway.

Synthesis of the conjugated polymer containing metal ion in their backbone leads to numerous ideas. The monomer **31** shown in *chapter 5* is useful for the preparation of homopolymer. The homopolymer must be preassembly blue emitting and using our developed concept of surface selective coordination chemistry with $Eu(tta)_3$ and $Tb(acac)_3$, one can readily fabricate grid like cross-patterns where the junction of the grid can emit white light.

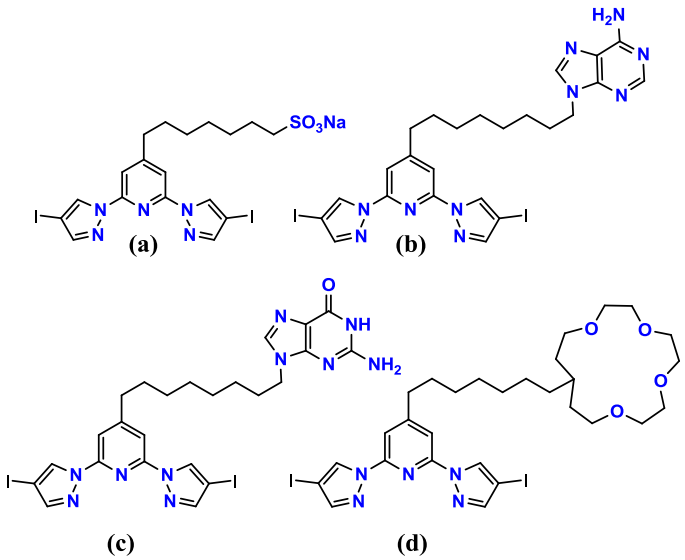

Figure 7.3 Proposed structures of monomers to develop new functional polymers.

A series of further rational design can be envisaged based on the monomer **31**. The alkyl chain can be functionalized by ionic sulphonate groups to form water soluble polymers (Fig**.** 7.3 a). Alternatively the chain can be terminated with nucleobases like adenine or guanine (Fig. 7.3 b and c) to make bio-compatible polymers. Another simple

idea one can think is to functionalize the long chain with crown ethers which will allow diverse supramolecular interactions as well as to incorporate more than one metal ion in the polymer backbone (Fig. 7.3 d).

Synthesis of polymers described in this thesis involved only coupling of the metal ions directly to the conjugated polymer backbone containing ligand. Alternate methods like tethering of the metal ions into the polymer via long alkyl chains carrying ligands (Fig. 7.4 A), incorporation of platinum(II) to synthesize thermally stable polyyne polymers of the type $[-C\equiv C-Pt(PBu_3)_2-C\equiv C-X-]_n$ can also be extended to their closest neighbours, viz, gold(I)[2] and mercury(II)[3] . The predicted macromonomer shown in **A** can form metallo-supramolecular polymer upon coordination with Fe(II) ion. The polymer can be readily solution processed to form a free standing magnetically bistable thin film. The film can be used to read and write memory applications and it is further possible to manipulate the memory by simply varying the temperature.

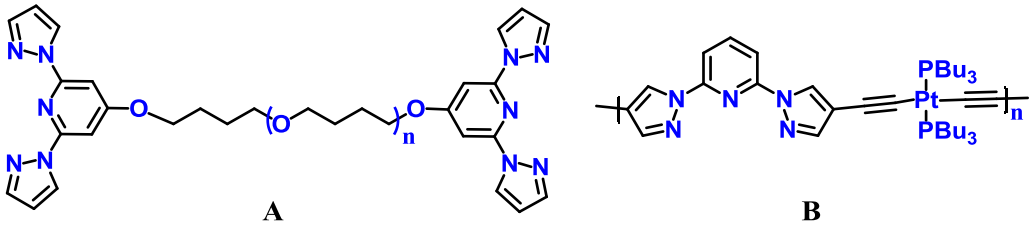

Figure 7.4 (A) A macromonomer to fabricate a free standing SCO film. (B) A polyyne polymer.

We believe that the apart from the main scope of this thesis i.e., investigation to fabricate flexible optically transparent SCO patterns/arrays, multicolour displaying hybrid organic nanotubes and white light emitting polymers, the proposed ideas and future directions outlined above will open up new avenues for promising materials research in future.

References

1. Wagner, S.; Kisslinger, F.; Ballmann, S.; Schramm, F.; Chandrasekar, R.; Bodenstein, T.; Fuhr, O.; Secker, D.; Fink, K.; Ruben, M.; Weber, H. B. *Nat. Nanotech.* **2013**, *3*, 575.

2. (a) Chao, H.-Y.; Lu, W.; Li, Y.; Chan, M. C. W.; Che, C.-M.; Cheung, K.-K.; Zhu,N. *J. Am. Chem. Soc.* **2002**, *124*, 14696. (b) Lu, W.; Xiang,H.-F.; Zhu, N.; Che, C.-M. *Organometallics* **2002**, *21*, 2343.

3. (a) Wong, W.-Y. *Coord. Chem. Rev.* **2007**, *251*, 2400. (b) Wong, W.-Y.; Liu, L.; Shi, J.-X. *Angew. Chem. Int. Ed.* **2003**, *42*, 4064. (c) Zhou, G.; Wong, W.-Y.; Ye, C.; Lin, Z. *Adv. Funct. Mater.* **2007**, *17*, 963. (d) Zhou, G.; Wong, W.-Y.; Lin, Z.; Ye, C. *Angew.Chem. Int. Ed.* **2006**, *45*, 6189.

Appendix A

Materials

$[Pd(PPh_3)_4]$	Aldrich, 99%
Citrazinicacid	Aldrich, 98%
Cu(I)I	Avra Synthesis Pvt. Ltd. 98%
$Eu(tta)_3 \cdot 3H_2O$	Acros, 98%
$Fe(BF_4)_2$	Aldrich, 97%
$Fe(ClO_4)_2$	Aldrich, 98%
HIO_3	Sigma Aldrich, 99.5%
I_2	Finar Reagents, 99.5%
KI	Merck Chemicals Pvt. Ltd. 99%
LiOH	Avra Synthesis Pvt. Ltd. 98%
NaN_3	Avra Synthesis Pvt. Ltd. 98%
$NaNO_2$	Merck Chemicals Pvt. Ltd. 99%
$POCl_3$	Avra Synthesis Pvt. Ltd. 98%
PPh_3	Avra Synthesis Pvt. Ltd. 98%
Pyrazole	Aldrich, 98%
trifloro acetic acid	Aldrich, 99%
$(COCl)_2$	Avra Synthesis Pvt. Ltd. 98%
$Pd(PPh_3)_2Cl_2$	Aldrich, 99%
1-Octyne	Aldrich, 97%

Appendix B

Instrumentation

Nuclear Magnetic Resonance Spectroscopy

^{1}H and ^{13}C NMR spectra were recorded on a Bruker 400 MHz NMR spectrometer. Spectra were recorded using the solvent peaks as the internal standard.

Mass Spectroscopy

Shimadzu LC-MS 2010A equipment was used to record the mass spectra of the isolated compounds following atmospheric pressure chemical ionization (APCI) technique.

Elemental Analysis

Elemental analysis was carried out on a Thermo Finnigan Flash EA-1112 series) CHNS analyzer.

Melting Point

Melting temperatures of solids were determined using Büchi made electro-thermal melting point apparatus and values reported are uncorrected.

Infrared Spectroscopy

FT-IR spectra were recorded on a JASCO FT/IR-5300 or Nicolet 5700 FT-IR. Solid samples were recorded as KBr pellets and liquid samples as thin films between NaCl plates.

Absorption Spectroscopy

Absorption spectra were recorded on a Shimadzu UV-3600 UV-Vis-NIR Spectrophotometer or Cary 100 Bio UV-Visible spectrophotometer.

Fluorescence Spectroscopy

Steady state fluorescence emission and excitation spectra were recorded on a Jobin Yvon Horiba model Fluoromax-3 spectrofluorimeter.

Transmission Electron Microscopy

TEM images were obtained on a TECNAI G2 FEI F12 TEM at an accelerating voltage of 120 kV. Samples were prepared by placing a drop of the samples on a polymer (polyvinyl formvar) − coated copper grid (200 mesh) and air drying.

Scanning Electron Microscopy

SEM and FESEM images were recorded on a Philips XL30 ESEM and a HITACHI S-4300SE/N FESEM respectively using beam voltages of 20 kV. The samples were fixed on aluminum platforms using carbon tapes; a conducting connection was made between samples and aluminum platform by silver paint. Samples were coated with a thin layer (3 − 5 nm) of sputtered gold prior to imaging.

Atomic force microscopy

Atomic Force Microscopy (AFM) imaging was carried out on NT-MDT Model Solver Pro M microscope using a class 2R laser of 650 nm wavelength having maximum output of 1 mW. All calculations and image processing was carried out by a software NOVA 1.0.26.1443 provided by the manufacturer. The images were recorded in a semi-contact mode using a noncontact mode tip purchased from NT-MDT, Moscow. The dimensions of the tip are as follows: Cantilever length = 95 (±5) μm, Cantilever width 30 (±5) μm, and Cantilever thickness = 1.5-2.5 μm, Resonate frequency = 140-390 kHz, Force constant = 3.1-37.6 N/m, Chip size = 3.4×1.6×0.3 mm, Reflective side = Au, Tip height = 14-16 μm, Tip curvature radius = 10 nm, and Aspect ratio 3:1-5:1.

Spin-coating

Laurell Technologies Corporation Model WS-400B-6NPP/LITE/8K spinner was used for the fabrication of thin polymer films.

Thermogravimetric analysis

(TGA) of samples were carried out on a (Netzsch STA 409PC) TG-DTA instrument from 30 to 800°C with a scanning rate of 10° C/min.

Confocal laser scanning microscopy

The luminescence behavior of the samples was observed with a Leica Laser scanning confocal microscope, Germany [model No - TCS – SP2 (spectral confocal microscope)] equipped with an Acousto-Optical Beam Splitter (AOBS) emission filter. The wavelength and amplitude of the ultrasound can be changed (programmed) to deflect certain band of wavelength and its amount passing through the field to collect emissions in high efficiency. The topographic structural data were directly coupled with the spectroscopic properties of the specimen. The emission spectral curves were recorded in XYλ (spectral scan mode) scan mode, and the images were recorded in XYT mode (time scan mode). Argon-ion Laser (Power- 280 mW) was used as UV excitation source. Scanning was done by a 20.0X optical lens, later it was further magnified by a factor 3.45 using digital magnification by the Leica confocal software (LCS). The data were recorded with a (Continuous scan) scanning speed of 400 Hz (image lines per second) with a scan format of 512 pixel × 512 pixel resolution. The active emission colors were detected using the different color detection channels of the photomultiplier tube (PMT). The pinhole size was 36 μm and six frames were taken to make an average of the final frame.

Confocal Raman micro spectroscopy Studies

Raman spectra of the samples were recorded on a WI-Tec confocal Raman spectrometer equipped with a Peltier-cooled CCD detector. Using a 600 grooves/mm grating BLZ = 500 nm, the integration time was typically 2.0000 s. Ten accumulations was performed for acquiring a single spectrum. For imaging the integration time was typically 2.000 s, keeping in mind that the x or y resolution is ~250 nm four points per line and four line per image was taken for imaging of a 1μm × 1μm area. A He-Ne 633 nm or Argon-Ion 488nm laser was used as an excitation source for the Raman scattering. All measurements were done at ambient conditions.

Bulk Magnetic Studies

The temperature dependent magnetic susceptibility of complexes in the powder state was measured on a Quantum Design vibrating sample magnetometer (VSM-SQUID) setup in the temperature range of 340↔2 K at continuous cooling (↓) and heating (↑) cycles with an applied direct current (DC) magnetic field of 0.5 T. Heating and cooling rate of the sample was kept at a 10 K interval in sweep mode.

Electron Spin Resonance Spectroscopy (EPR) Studies.

X-band EPR spectra were recorded on a Bruker-ER073 spectrometer equipped with an EMX microX source. For data analysis Xenon 1.1b.60 software provided by the manufacturer was used. During the liquid helium measurement the temperature was controlled by a temperature controller supplied by Oxford instruments (ITC 503S).

Single Crystal X-ray Diffraction: Data Collection, Solution and Refinement

The X-ray intensity data of crystals were collected on a Bruker Nonius SMART APEX CCD area detector system equipped with a graphite monochromator and a MoKα fine-focus sealed tube (λ = 0.71073 Å) operated at 1750 W power (50 kV, 35 mA). All data were collected at 298K. The detector was placed at a distance of 6.003 cm from the crystal; exposure time (10-20 sec/frame) was set based on the data quality. The frames were integrated with the Bruker SAINT Software package using a narrow-frame integration algorithm. Data were corrected for absorption effects using the multi-scan technique (SADABS). The structure was solved and refined using the direct method analysis in Bruker SHELXTL Software Package.

Publications

1. **Basak, S.**; Hui, P.; Chandrasekar, R Regio-Selective Synthesis of Brominated and Iodinated 2′,6′-Bispyrazolyl Pyridine Units.
   Synthesis, **2009**, *23*, 4042-4048.

2. **Basak, S.**; Chandrasekar, R Multi-Luminescent Organic/Inorganic Hybrid Nanotubes: One-Pot Fabrication of Tricolor (Blue-Red-Purple) Luminescent Rectangular Organic Nanotubes Grafted with Eu(III) Complexes.
   Adv. Funct. Mater. **2011**, *21*, 667-673.

3. **Basak, S.;** Hui, P.; Boodida, S.; Chandrasekar, R Micro-Patterning of Metallo-Polymers: Syntheses of Back-to-back Coupled Octylated 2,6- Bis(pyrazolyl)pyridines Ligands and their Solution Processable Coordination Polymers.
   J. Org. Chem. **2012**, *77*, 3620-3626.

4. **Basak, S.**; Narayana, YSLV.; Baumgarten, M.; Müllen, K.; Chandrasekar, R White Light Emitting Films from Eu(III) Complexed Copolymers of Alternating Fluorene and Bispyrazolylpyridine Derivatives.
   Macromolecules **2013**, *46,* 362-369.

5. Narayana, YSLV.; **Basak, S**.; Baumgarten, M.; Müllen, K.; Chandrasekar, R White-Emitting Organic/Inorganic Hybrid Spheres: Phenylethynyl and 2,6 -Bis(pyrazolyl)pyridine Copolymer Coordinated to $Eu(tta)_3$.
   Adv. Funct. Mater. **2013**, DOI: 10.1002/adfm.201301476.

6. **Basak, S.**; Hui, P.; Chandrasekar, R Flexible and Optically Transparent Polymer Embedded Nano/Micro Scale Spin Cross-Over Fe(II) Complex Patterns/Arrays.
   Chem. Mater. **2013**, *25*, 3408-3413.

7. **Basak, S.**; Botcha, A. K.; Ansari, M. T. Chandrasekar, R Optical Waveguiding Organic Nano-Rods Coated with Reversibly Switchable Fe(II) Spin Transition Nanoparticles.
   Indian J. Mater. Sci. **2013**, in press.

8. **Basak, S.**; Chandrasekar, R Parallelepipedic Passive Organic Optical Wave Guides: Laser Cutting, Controlling Guided Light Propagation Lengths and Out-put.
   J. Mater. Chem. C. **2013**, Revised.

Presentations in Conferences and Symposiums

1. **Basak, S.**; Chandrasekar, R.
   Coordination Chemistry on the Surface of the Ligand Nano Super-Structure.
   Poster presented at the XX International Conference on the Chemistry of Organic Solid State (ICCOSS-XX), Bangalore, India, June 26-30, 2011.

2. **Basak, S.**; Chandrasekar, R.
   Nano-Photonics: Coordination Chemistry on the Surface of the Ligand Nanotubes.
   Poster presented at the Modern Trends in Inorganic Chemistry (MTIC-XIV), University of Hyderabad, Hyderabad, India, December 10–13, 2011.

3. **Basak, S.**; Chandrasekhar, N.; Chandrasekar, R.
   Poster presented in Chemfest-2011, 8th Annual In-House Symposium held at University of Hyderabad.

4. **Basak, S.**
   White Emitting Eu(III) Ion Coordinated Ethynyl Linked Fluorene/2,6(Bispyrazolylpyridine) Copolymer Films.
   Delivered an oral presentation at Frontiers in Chemical Sciences (FICS-2012) held at IITG on December 2-4, 2012.

5. **Basak, S.**; Narayana, Y. S. L. V.; Chandrasekar, R.
   White Light Emitting Films from Eu(III) Complexed Copolymers of Alternating Fluorene and Bis(pyrazolyl)pyridine Derivatives.
   Delivered an oral presentation as well as a poster presentation in Chemfest-2013 held in University of Hyderabad.

6. **Basak, S.**
   Top Down and Bottom Up Approaches for the Fabrication of Functional Molecular Nano/Micro Structures.
   Oral presentation at Dr. K. V. Rao 8th Annual Research Award Program, Hyderabad, India, on April 22, 2008. (Received "1st *RUNNER UP AWARD*")

7. **Basak, S.**; Chandrasekar, R.
   Nano/Micro Scale Functional (Photonic & Magnetic) Patterns, Arrays and Tubes.
   Poster presented at the Indo-US Symposium on Molecular Materials held in IISc during 15-17 July 2013.